# NEAR THRESHOLD NEUTRAL PION ELECTROPRODUCTION AT HIGH MOMENTUM TRANSFERS

By

Puneet Kumar Khetarpal

A Thesis Submitted to the Graduate

Faculty of Rensselaer Polytechnic Institute

in Partial Fulfillment of the

Requirements for the Degree of

DOCTOR OF PHILOSOPHY

Major Subject: PHYSICS

Approved by the
Examining Committee:

_____
Paul Stoler, Thesis Adviser

_____
Gary Adams, Member

_____
Vladimir Braun, Member

_____
Valery Kubarovsky, Member

_____
James Napolitano, Member

_____
William Siegmann, Member

Rensselaer Polytechnic Institute
Troy, New York

August 2010
(For Graduation August 2010)

## CONTENTS

## LIST OF TABLES

## LIST OF FIGURES

## ACKNOWLEDGMENT

This work acknowledges the contribution and assistance from the members of the CLAS collaboration, Jefferson Lab and RPI, *viz.*, François-Xavier Girod, Kijun Park, Maurizio Ungaro and many others who are too numerous to list them all here. In addition, I am grateful to Inna Aznauryan for assisting in the extraction of the S-wave multipoles for the near threshold process and am especially thankful to Vladimir Braun for assisting in the theoretical interpretation of the experimental results. Also, I am grateful to the members of the thesis committee, Paul Stoler, Gary Adams, Vladimir Braun, Valery Kubarovsky, James Napolitano and William Siegmann, for advising me throughout the experiment.

An extra special word of thanks goes to Paul Stoler and Valery Kubarovsky who have guided me throughout my graduate school experience both professionally and personally. I couldn't have asked for better advisors. I thank them both from the bottom of my heart.

Additionally, my endless love and gratitude to my family, friends and relatives for repeatedly asking the two fundamental questions of my life and for providing both encouragement and hope.

And lastly, this work is dedicated to my forebears under whose perennial shadow I continue to grow.

"No word is true until it is eaten"

- *36 Lessons of Vivec, Sermon 27*

## ABSTRACT

Pion photo- ($\gamma p \to \pi N$) and electroproduction ($\gamma^* p \to \pi N$) close to threshold have been the subject of experimental and theoretical study since the 1950s. The predictions for near threshold cross sections have been studied for momentum transfers $Q^2 < 1\,\mathrm{GeV}^2/\mathrm{c}^2$ theoretically via the Low Energy Theorems (LETs). Additionally, these LETs give predictions for the axial form factor $G_A(Q^2)$ via the charged pion process near threshold. The LETs provide transition amplitude predictions for both neutral and charged pion reactions using chiral symmetry and current algebra arguments near threshold. Previous experimental measurements from Saclay, Mainz and others have shown consistency with the LET predictions at low momentum transfers $Q^2 < 1\,\mathrm{GeV}^2/\mathrm{c}^2$.

Recently, new extensions to these LETs at high $Q^2$ have been introduced by Pobylista *et al* (2001) and then by Braun *et al* (2008). In the work of Braun *et al*, the near threshold pion electroproduction transition amplitudes are written in terms of new form factors. These new generalized form factors $G_1^{\pi N}(Q^2)$ and $G_2^{\pi N}(Q^2)$ are obtained on the current quark basis and have been predicted using light cone sum rules (LCSRs) in the chiral limit ($m_\pi \to 0$) for the reactions $ep \to eN\pi$ in the $Q^2$ range of $1 - 10\,\mathrm{GeV}^2/\mathrm{c}^2$. Additionally, the predictions include a prescription to access the axial form factor $G_A$ near threshold at these high momentum transfers for the charged pion reaction.

An experiment at Jefferson Lab was conducted using the CLAS detector to measure near threshold neutral pion electroproduction $ep \to ep\pi^0$ as a function of $Q^2$. This is the first measurement of this process in the near threshold region of $W$ from 1.08 to 1.16 GeV and at momentum transfers $Q^2 \approx 2 - 5\,\mathrm{GeV}^2/\mathrm{c}^2$. The differential angle integrated cross sections were measured and the associated structure functions and S-wave multipoles were extracted. The cross section, extracted multipole amplitudes and generalized form factors $G_1^{\pi^0 p}(Q^2)$ and $G_2^{\pi^0 p}(Q^2)$ are presented along with the predictions from Braun *et al*.

# 1. Introduction and Historical Review

In this thesis, we will study the differential cross sections and the structure of the pion-nucleon system for the reaction $ep \to ep\pi^0$. This reaction is studied using data collected in Hall B of the Thomas Jefferson National Accelerator Facility (Jefferson Lab) using the CLAS[1] detector. The $e1$-6 experiment measured the angular distribution of the process in the near threshold region $W \in (1.08, 1.16)$ GeV and at high $Q^2 \approx 2 - 5\,\mathrm{GeV}^2/c^2$.

## 1.1 Formalism

### 1.1.1 Kinematic Definitions

The reaction of interest, shown schematically in Fig. 1.1(a), is

$$e(l_\mu) + p(P_\mu) \to e(l'_\mu) + N(P'_\mu) + \pi(k_\mu). \tag{1.1}$$

Here, $e$ and $p$ refer to electron and proton target; $N$ is either a neutron ($n$) or a proton ($p$) and $\pi$ is either neutral ($\pi^0$) or charged ($\pi^+$). So, we have two possible reactions:

$$e(l_\mu) + p(P_\mu) \quad \to \quad e(l'_\mu) + p(P'_\mu) + \pi^0(k_\mu) \tag{1.2}$$

$$e(l_\mu) + p(P_\mu) \quad \to \quad e(l'_\mu) + n(P'_\mu) + \pi^+(k_\mu). \tag{1.3}$$

In this thesis, we will focus on the analysis concerning only the neutral pion channel. In this experiment, we assume the incident electron interacts with the target proton via exchange of a single virtual photon. In this approximation, we also assume that the electron mass is negligible ($m_e \approx 0$) compared to the overall kinematics of the reaction.

The 4-momentum of the particles are defined using the Minkowski spacetime metric, $g^{\mu\nu} = diag(1, -1, -1, -1)$. If we have two 4-vectors $a^\mu = (E_a, \mathbf{p_a})$ and $b^\mu = (E_b, \mathbf{p_b})$, their inner product in this metric is $a \cdot b = a^\mu b^\nu g_{\mu\nu} = a^\mu b_\mu = a^0 b^0 - \mathbf{a} \cdot \mathbf{b}$. We can also define the invariant quantity $a \cdot a = a^\mu a_\mu = E_a^2 - |\mathbf{p_a}|^2 = m_a^2$, which is the mass of the particle and is invariant under Lorentz transformations.

In the lab frame,

- $l_\mu = (E_e, E_e\hat{\mathbf{z}})$ is the 4-momentum of the incident electron beam

[1] **C**ontinuous Electron Beam Accelerator Facility's (CEBAF) **L**arge **A**cceptance **S**pectrometer

- $l'_\mu = (E'_e, \mathbf{p'_e})$ is the 4-momentum of the scattered electron with $\mathbf{p'_e} = (p'_e, \theta'_e, \phi'_e)$
- $P_\mu = (M_p, \mathbf{0})$ is the 4-momentum of the target proton at rest with $M_p$ as the mass of the proton
- $P'_\mu = (E'_p, \mathbf{p'_p})$ is the 4-momentum of the recoiled nucleon (neutron or proton) with $\mathbf{p'_p} = (p'_p, \theta'_p, \phi'_p)$
- $k_\mu = (E_\pi, \mathbf{p}_\pi)$ is the 4-momentum of the emitted pion ($\pi^0$ or $\pi^+$) with $\mathbf{p}_\pi = (p_\pi, \theta_\pi, \phi_\pi)$
- $q_\mu = l_\mu - l'_\mu = (\omega, \mathbf{q})$ is the 4-momentum of the virtual photon ($\gamma^*$).

Using the above kinematic definitions and approximations, we can define other kinematic quantities for the reaction. One of the quantities of interest is the 4-momentum squared of the virtual photon, $Q^2$, which defines the amount of 4-momentum transferred from the incident electron to the target proton:

$$Q^2 \equiv -q^2 = -\omega^2 + |\mathbf{q}|^2 = 4E_e E'_e \sin^2(\theta'_e/2). \tag{1.4}$$

Another kinematic quantity of interest is the invariant mass of the virtual photon-proton system

$$s = W^2 = (q+p)^2 = M_p^2 + 2\omega M_p - Q^2. \tag{1.5}$$

The threshold energy is the minimum energy required to create the particles in the final state ($p\pi^0$) in this system and this energy is directly related to the quantity $W = M_p + m_\pi$.

### 1.1.2 Cross Section and Multipole Definitions

For neutral pion electroproduction $ep \to ep\pi^0$, the transition amplitude can be separated in terms of the leptonic and hadronic currents, if one assumes a one-photon exchange approximation:

$$T = \frac{4\pi\alpha}{Q^2} L_{\mu\nu} M^{\mu\nu} \tag{1.6}$$

where $\alpha$ is the electromagnetic fine-structure constant

$$\alpha = \frac{e^2}{4\pi\hbar c} \approx \frac{1}{137} \tag{1.7}$$

and

$$L_{\mu\nu} = [\bar{u}(l')\gamma_\mu u(l)][\bar{u}(l)\gamma_\nu \bar{u}(l')] \tag{1.8}$$

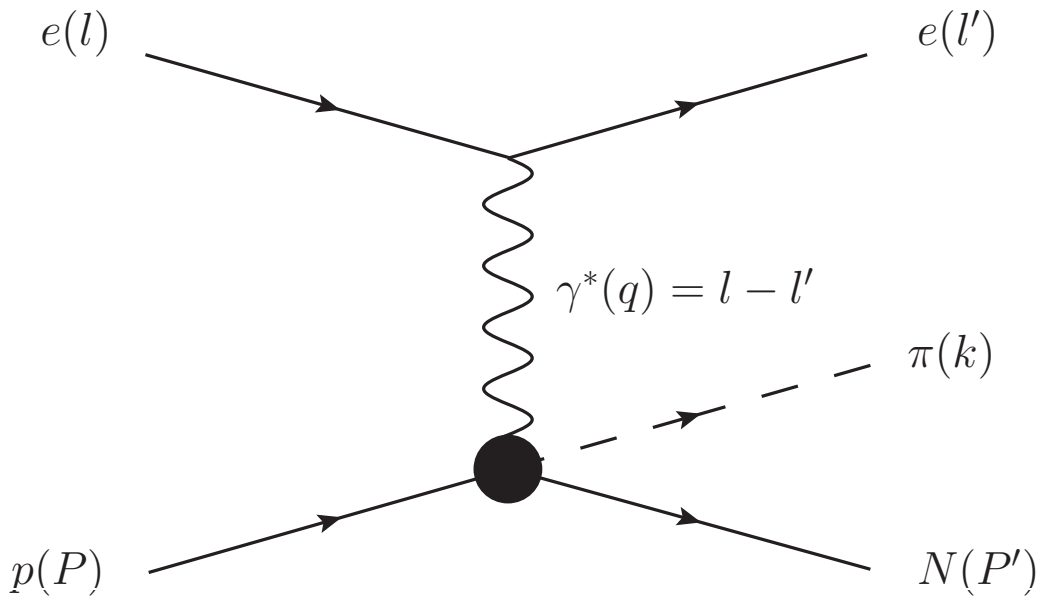


(a)

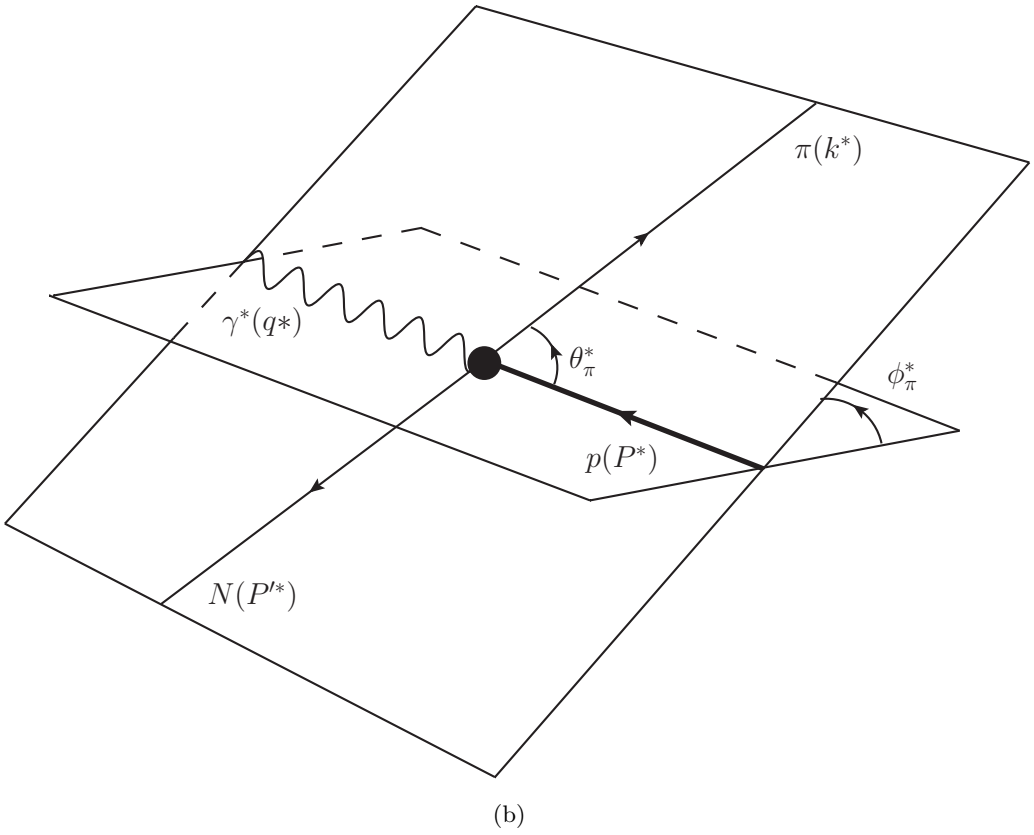


(b)

**Figure 1.1: (a) Schematic diagram of pion electroproduction. (b) Pion electroproduction kinematics in virtual photon-proton center of mass system.**

is the tensor describing the interaction at the leptonic vertex. Here, $u$ and $\bar{u}$ represent the Dirac spinors for the incoming and outgoing lepton, respectively, and $\gamma_\mu$ is the Dirac matrix satisfying the Dirac equation [1].

For the hadronic interaction, we have

$$M_{\mu\nu} = \langle p\pi|j_\mu(x)|p\rangle\langle p|j_\nu^\dagger(x)|p\pi\rangle \tag{1.9}$$

where we imply sum and average over polarizations; the electromagnetic current

$$j_\mu(x) = e_u\bar{u}(x)\gamma_\mu u(x) + e_d\bar{d}(x)\gamma_\mu d(x). \tag{1.10}$$

In the above equation, $u(x)$ and $d(x)$ are Dirac spinors and $e_u$ and $e_d$ are fractional charges for the up and down quarks, respectively.

We can then write the five-fold differential cross section for the reaction in terms of the cross section for the subprocess $\gamma^* p \to p\pi^0$ [2], which depends only on the matrix elements of the hadronic interaction from Eq. 1.9:

$$\frac{d^5\sigma}{dE'_e d\Omega'_e d\Omega^*_\pi} = \Gamma\frac{d^2\sigma_{\gamma^* p\to p\pi^0}}{d\Omega^*_\pi}. \tag{1.11}$$

Here, $d\Omega'_e = d\cos\theta'_e d\phi'_e$ is the differential solid angle for the scattered electron in the lab frame; $d\Omega^*_\pi = d\cos\theta^*_\pi d\phi^*_\pi$ is the differential solid angle for the pion in the virtual photon-proton ($\gamma^* p$) center of mass frame. The $\gamma^* p$ center of mass (CM) system and associated variables can be seen in Fig. 1.1(b). On the other side, we have

$$\Gamma = \frac{\alpha}{2\pi^2}\frac{E'_e}{E_e}\frac{W^2 - M_p^2}{2M_pQ^2}\frac{1}{1-\varepsilon}, \tag{1.12}$$

which is the *virtual photon flux* and depends entirely on the matrix elements of the leptonic interaction Eq. 1.8. The virtual photon flux depends on the *transverse polarization* of the virtual photon

$$\varepsilon = \left(1 + 2\frac{|\mathbf{q}|^2}{Q^2}\tan^2\frac{\theta_e}{2}\right)^{-1}. \tag{1.13}$$

Similarly, the *longitudinal polarization* of the virtual photon can be defined as

$$\varepsilon_L = \frac{Q^2}{\omega^2}\varepsilon. \tag{1.14}$$

For unpolarized beam and target the reduced cross section from Eq. 1.11 can be expanded in terms of the hadronic structure functions:

$$\frac{d\sigma_{\gamma^* p\to p\pi^0}}{d\Omega_\pi^*} = \frac{p_\pi^*}{k_\gamma^*}\left(\frac{d\sigma_T}{d\Omega_\pi^*} + \varepsilon_L\frac{d\sigma_L}{d\Omega_\pi^*} + \varepsilon\frac{d\sigma_{TT}}{d\Omega_\pi^*}\cos 2\phi_\pi^* + \sqrt{2\varepsilon_L(\varepsilon+1)}\frac{d\sigma_{LT}}{d\Omega_\pi^*}\cos\phi_\pi^*\right). \quad (1.15)$$

Here, $p_\pi^*$ is the pion momentum in the CM frame, and $k_\gamma^*$ is the virtual photon equivalent energy in the CM frame that can be written as

$$k_\gamma^* = \frac{W^2 - M_p^2}{2W}. \quad (1.16)$$

The structure functions are related to the hadronic matrix elements (Eq. 1.9).

- $d\sigma_T/d\Omega_\pi^*$ is the structure function giving the part of the reaction cross section due to the transverse component for unpolarized virtual photons,
- $d\sigma_L/d\Omega_\pi^*$ is the structure function giving the part of the reaction cross section due to the longitudinal component,
- $d\sigma_{TT}/d\Omega_\pi^*$ is the structure function that describes the interference between the transverse-transverse components of the virtual photon cross section,
- $d\sigma_{LT}/d\Omega_\pi^*$ describes the interference between the longitudinal and transverse components of the virtual photon cross section.

These structure functions can be expanded in terms of Legendre polynomials and fitted to extract the Chew-Goldberger-Low-Nambu (CGLN) [3] multipoles. To understand the nature of these multipoles, let us take a look at the differential cross sections from another viewpoint. The reduced differential cross section can be written in terms of relativistic invariant functions

$$\frac{d\sigma_\gamma^*}{d\Omega_\pi^*} = \frac{p_\pi^*}{k_\gamma^*}|\varepsilon_\mu\mathcal{M}^\mu|^2 \quad (1.17)$$

where $\varepsilon_\mu$ is the polarization vector of the virtual photon and $\mathcal{M}^\mu$ are the transition matrix elements. The general amplitude can be represented in terms of six invariant functions $F_n$ that are defined by the expansion [2]:

$$\mathcal{M}_\mu\varepsilon^\mu = \sum_{n=1}^{6} F_n(W, Q^2, \cos\theta_\pi^*)I_n. \quad (1.18)$$

Here, the $I_n$ are six basic scalars that are formed by the most general combinations of all the vectors that can play a role in describing this meson-baryon reaction. These six scalars are defined as:

$$\begin{aligned} I_1 &= i\boldsymbol{\sigma}\cdot\mathbf{b} \\ I_2 &= (\boldsymbol{\sigma}\cdot\hat{\mathbf{q}}^*)(\boldsymbol{\sigma}\cdot\hat{\mathbf{k}}^*\times\mathbf{b}) \\ I_3 &= i(\boldsymbol{\sigma}\cdot\hat{\mathbf{k}}^*)(\mathbf{b}\cdot\hat{\mathbf{q}}^*) \\ I_4 &= i(\boldsymbol{\sigma}\cdot\hat{\mathbf{q}}^*)(\mathbf{b}\cdot\hat{\mathbf{q}}^*) \\ I_5 &= -i\boldsymbol{\sigma}\cdot\hat{\mathbf{k}}^* b_0 \\ I_6 &= -i\boldsymbol{\sigma}\cdot\hat{\mathbf{q}}^* b_0. \end{aligned} \tag{1.19}$$

In the above equations, $\hat{\mathbf{k}}^*$ and $\hat{\mathbf{q}}^*$ are the unit vectors defining the direction of the pion and the virtual photon in the center of mass frame. Also, $\boldsymbol{\sigma}$ is a "vector" containing the Pauli matrices $\boldsymbol{\sigma} = \{\sigma_1, \sigma_2, \sigma_3\}$ and $b^\mu$ contains the polarization vector dependence:

$$b^\mu = \varepsilon^\mu - \frac{\boldsymbol{\varepsilon}\cdot\mathbf{q}^*}{|\mathbf{q}^*|}q^\mu. \tag{1.20}$$

The coefficients of the expansion in Eq. 1.18, $F_n$, are the Lorentz invariant complex functions that are known as the CGLN amplitudes. The $F_1$, $F_2$, $F_3$ and $F_4$ describe transitions generated by transverse photons and $F_5$ and $F_6$ are those generated by longitudinal photons. They are functions of $W$, $Q^2$ and $\cos\theta_\pi^*$. These functions, in turn, can be expanded in terms of the Legendre polynomials and the derivatives of Legendre polynomials:

$$\begin{aligned} F_1 &= \sum_l \left[P'_{l+1}(x)E_{l+} + P'_{l-1}(x)E_{l-} + P'_{l+1}(x)M_{l+} + (l+1)P'_{l-1}(x)M_{l-}\right] \\ F_2 &= \sum_l \left[(l+1)P'_l(x)M_{l+} + lP'_l(x)M_{l-}\right] \\ F_3 &= \sum_l \left[P''_{l+1}(x)E_{l+} + P''_{l-1}(x)E_{l-} - P''_{l+1}(x)M_{l+} + P''_{l-1}(x)M_{l-}\right] \\ F_4 &= \sum_l \left[-P''_l(x)E_{l+} - P''_l(x)E_{l-} + P''_l(x)M_{l+} - P''_l(x)M_{l-}\right] \\ F_5 &= \sum_l \left[-(l+1)P'_l(x)S_{l+} + lP'_l(x)S_{l-}\right] \\ F_6 &= \sum_l \left[(l+1)P'_{l+1}(x)S_{l+} - lP'_{l-1}(x)S_{l-}\right]. \end{aligned} \tag{1.21}$$

Above, $P(x)$ are the Legendre polynomials and $P'(x)$ and $P''(x)$ are the first and second

derivatives of the Legendre polynomials, respectively, with $x = \cos\theta^*_\pi$. The coefficients of these Legendre polynomials are the CGLN multipoles $E_{l\pm}$, $M_{l\pm}$ and $S_{l\pm}$, where $E$, $M$ and $S$ describe the electric, magnetic and scalar multipoles, respectively. Also, $l$ indicates the orbital angular momentum of the pion-nucleon system and $\pm$ describes the proton spin state such that the total spin of the final pion-nucleon state is $l \pm \frac{1}{2}$.

These CGLN multipoles are functions of $W$ and $Q^2$ for a reaction. In this experiment, we are particularly interested in the S-wave multipoles, *i.e.*, $E_{0+}$ and $S_{0+}$ and will be discussed in detail in the upcoming sections. In Chapter 6 a procedure to extract these multipoles from the structure functions is discussed.

## 1.2 Historical Review

Pion photo- and electroproduction $\gamma N \to \pi N$, $\gamma^* N \to \pi N$ close to threshold has been studied extensively since the 1950s both experimentally and theoretically. Exact predictions for the threshold cross sections and the axial form factor were pioneered by Kroll and Ruderman in 1954 for $Q^2 = 0$, *i.e.*, photo-production [4]. This was the first of the low energy theorems (LETs) to appear but not without limitations. This LET provided model independent predictions of cross sections for pion photoproduction in the threshold region by applying gauge and Lorentz invariance [5]. The predictions of this LET were restricted only to charged pions and the $\pi^0$ contribution was shown to vanish in the 'soft pion' limit ($m_\pi \sim p_\pi$). Additionally, these cross section predictions were limited to diagrams with contributions in the pion-nucleon mass ratio to $O(m_\pi/m_N)$. In later years, using vanishing pion mass chiral symmetry ($m_\pi \to 0$) these predictions were extended to pion electroproduction for both charged and neutral pions [6, 7].

To better understand the axial form factor one can first look at the electromagnetic form factors for the proton. By probing the proton at rest with an electromagnetic current, in the case of electron-proton scattering, one can study the charge distribution in the proton. The Fourier transform of this charge distribution is the electromagnetic form factor in the infinite momentum frame. Similarly, the axial form factor measures the axial charge distribution in the proton. The axial form factor is normally accessed in neutrino scattering experiments using a parity violating weak current as a probe.

Now of course, vanishing pion mass doesn't relate to the observed mass of the pion $m_\pi/m_N \sim 1/7$. So, higher order finite mass corrections to the LET were conducted in late sixties and early seventies before the appearance of QCD. These also included

contributions to the non-vanishing neutral pion amplitudes for the cross section.

In the late eighties and early nineties experiments at Saclay [8] and Mainz [9] obtained threshold pion photo-production data on $\gamma p \to \pi^0 p$. The theoretical predictions of LETs at the time were inconsistent with the data at low photon energies. With the emergence of chiral perturbation theory ($\chi$PT), the scattering amplitudes and other physical observables were systematically expanded in the low energy limit in powers of pion mass and momentum. Using this framework LETs were re-derived to include contributions to the amplitudes from certain loop diagrams, which were lost in the expansion in the pion mass in the earlier works [10, 11]. Further experiments at NIKHEF [12] on $\gamma^* p \to \pi^0 p$ with photon virtuality $Q^2 \sim 0.05 - 0.1\,\mathrm{GeV}^2$ provided good agreement with $\chi$PT predictions.[2]

These soft-pion theorems or LETs [4, 6, 7, 10, 11] are not applicable for $Q^2 \gg \Lambda_{QCD}^3/m_\pi$, where $\Lambda_{QCD} \sim 1$ GeV is a typical hadronic scale. In the case of asymptotically large momentum transfers ($Q^2 \to \infty$) perturbative QCD (pQCD) factorization techniques [13, 14, 15] have been used to obtain predictions for cross section amplitudes and axial form factors near threshold. In this technique, 'hard' ($Q^2 \gg \Lambda_{QCD}$) and 'soft' ($k \sim \Lambda_{QCD}$) momentum contributions to the scattering amplitude can be separated cleanly and each contribution can be theoretically calculated using pQCD and LETs, respectively, if possible.

Furthermore, Braun *et al* in Refs. [16, 17] suggest a method to extract new baryon form factors for $Q^2 \sim 1 - 10\,\mathrm{GeV}^2$ using light cone sum rules (LCSR). Additionally, the sum rules can be extended to the lower $Q^2 \sim 1\,\mathrm{GeV}^2$ regime and the LET are recovered to $O(m_\pi)$ accuracy. This approach provides a bridge between the low and high $Q^2$ regimes. Predictions for the axial form factor and the generalized form factors are also obtained.

In the following paragraphs we take a closer look at chiral symmetry, low energy theorems and the approach used by Braun *et al*. We will also look at some of the principles and consequences of chiral symmetry such as the partial conservation of axial current (PCAC) and the famous Goldberger-Treiman relation. These concepts are crucial in our understanding of the predictions in the high $Q^2$ regime.

### 1.2.1 Chiral Symmetry

Let us consider the $SU(2)_R \times SU(2)_L$ Lorentz group, where $SU(2)_R$ and $SU(2)_L$ are spin (rotational) groups for the right and left handed fermions. The $R$ and $L$ generators

[2] For convenience, we use units where $c = \hbar = 1$ throughout the document unless noted otherwise

of these groups are defined as [18]

$$\begin{aligned} R_i &= \frac{1}{2}(J_i + iK_i) \\ L_i &= \frac{1}{2}(J_i - iK_i) \end{aligned} \tag{1.22}$$

and they satisfy the following commutation relations

$$\begin{aligned} [R_i, R_j] &= i\epsilon_{ijk}R_k \\ [L_i, L_j] &= i\epsilon_{ijk}L_k \\ [L_i, R_j] &= 0. \end{aligned} \tag{1.23}$$

Here, $J_i$ and $K_i$ are the angular momentum and boost operators for the Lorentz group. The right and left generators separately satisfy the angular momentum algebra. The fundamental representations for these groups are given by the spinors $\chi_R \sim (\frac{1}{2}, 0)$ and $\chi_L \sim (0, \frac{1}{2})$. The rotation and boost generators can be written in terms of the left and right handed generators

$$\begin{aligned} J_i &= R_i + L_i = \sigma_i/2 \\ K_i &= i(-R_i + L_i) = -i\sigma_i/2 \end{aligned} \tag{1.24}$$

where $\sigma_i$ are the Pauli matrices.

The Lagrangian for a free nucleon ($p$ or $n$) in the Weyl representation can be written in terms of the left and right handed spinors

$$\mathcal{L} = i\chi_R^\dagger \sigma^\mu \partial_\mu \chi_R + i\chi_L^\dagger \bar{\sigma}^\mu \partial_\mu \chi_L + m(\chi_L^\dagger \chi_R + \chi_R^\dagger \chi_L). \tag{1.25}$$

Here, $\sigma^\mu = (1, \sigma)$, $\bar{\sigma}^\mu = (1, -\sigma)$, $\partial_\mu$ is the derivative of a four-vector and $m$ is the mass of the nucleon. This Lagrangian is Hermitian, Lorentz invariant and conserves the fermion number. It can be re-written in the standard form as

$$\mathcal{L} = i\bar{\psi}\gamma^\mu \partial_\mu \psi + m\bar{\psi}\psi. \tag{1.26}$$

Here we have a four component spinor

$$\psi = \psi_R + \psi_L = \begin{pmatrix} \chi_R \\ 0 \end{pmatrix} + \begin{pmatrix} 0 \\ \chi_L \end{pmatrix} = \begin{pmatrix} \chi_R \\ \chi_L \end{pmatrix} \tag{1.27}$$

with the four-component chiral fermions $\psi_L$ and $\psi_R$.

A two-component isospinor for the fundamental representation of isospin group SU(2) can be written for the two flavors $u$ and $d$

$$\psi = \begin{pmatrix} u \\ d \end{pmatrix}. \tag{1.28}$$

Here, $u$ and $d$ are each four-component spinors such that

$$\psi = \psi_R + \psi_L = \begin{pmatrix} u_R \\ d_R \end{pmatrix} + \begin{pmatrix} u_L \\ d_L \end{pmatrix} = \begin{pmatrix} u_R + u_L \\ d_R + d_L \end{pmatrix} = \begin{pmatrix} \chi_R^u \\ \chi_L^u \\ \chi_R^d \\ \chi_L^d \end{pmatrix}. \tag{1.29}$$

This gives us the free Lagrangian

$$\mathcal{L} = \bar{\psi}(i\partial\!\!\!/ - m)\psi. \tag{1.30}$$

In this representation, $m$ is a diagonal $2 \times 2$ mass matrix in the isospin space

$$m = \begin{pmatrix} m_u & 0 \\ 0 & m_d \end{pmatrix}. \tag{1.31}$$

The right or left chiral transformations are written as

$$\psi_R \to e^{ir}\psi_R, \psi_L \to e^{il}\psi_L \tag{1.32}$$

with $r = \mathbf{t} \cdot \mathbf{r}$ and $l = \mathbf{t} \cdot \mathbf{l}$; $\mathbf{t} = \tau/2$ are the generators of the SU(2) Lorentz group. One can define isospin right and left currents that are associated with these transformations

$$\begin{aligned} R_\mu^a &= \bar{\psi}_R \gamma_\mu t^a \psi_R \\ L_\mu^a &= \bar{\psi}_L \gamma_\mu t^a \psi_L. \end{aligned} \tag{1.33}$$

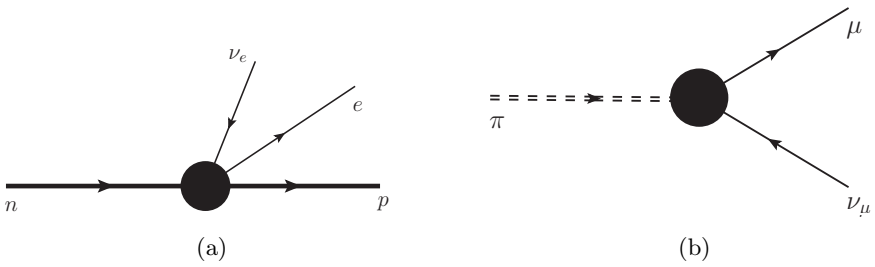


**Figure 1.2: (a) Weak decay of the neutron. (b) Weak decay of the pion.**

Additionally, one can define the isospin vector and axial-vector currents

$$\begin{aligned} V_\mu^a &= R_\mu^a + L_\mu^a = \bar{\psi}\gamma_\mu t^a \psi \\ A_\mu^a &= R_\mu^a - L_\mu^a = \bar{\psi}\gamma_\mu\gamma_5 t^a \psi. \end{aligned} \tag{1.34}$$

The currents $V_\mu$ and $A_\mu$ are exactly the electromagnetic and axial currents, respectively, that are of interest in our experiment. By probing the nucleon via the electromagnetic current, one has access to the electromagnetic form factors $F_1(Q^2)$ and $F_2(Q^2)$ and by probing the nucleon via the axial current, one has access to the axial form factor $G_A(Q^2)$. In the chiral limit of $m \to 0$, both of these currents are conserved under vector and axial-vector transformations

$$\begin{aligned} \psi \to e^{iv}\psi &= \begin{pmatrix} e^{iv}u_R + e^{iv}u_L \\ e^{iv}d_R + e^{iv}d_L \end{pmatrix} \\ \psi \to e^{ia\gamma_5}\psi &= \begin{pmatrix} e^{ia}u_R - e^{ia}u_L \\ e^{ia}d_R - e^{ia}d_L \end{pmatrix}. \end{aligned} \tag{1.35}$$

Here, $v = \mathbf{t}\cdot\mathbf{v}$, $a = \mathbf{t}\cdot\mathbf{a}$ with vector and axial vector parameters $\mathbf{v}$ and $\mathbf{a}$. For finite masses, neither of these currents are conserved. But in the isospin limit, $m_u = m_d$, only the vector current is conserved, the axial-vector is not.

This broken approximate chiral symmetry entails the existence of an approximately massless Goldstone boson with the same quantum numbers as the broken symmetry generator of the axial-current $A_\mu^a$. The pion satisfies this requirement as a state of negative parity, spin zero, isospin one, and zero baryon number and strangeness.

### 1.2.2 Goldberger-Treiman Relation and PCAC

Interestingly enough, the electromagnetic and axial currents $V_\mu^a$ and $A_\mu^a$ of our strong interactions also appear in weak interactions such as the nuclear beta decay. For this reaction, $n \to p + e^- + \bar{\nu}$, the nucleon matrix element of the axial-vector current can be written as [19]

$$\langle p|A^\mu(x)|n\rangle = \frac{e^{iq\cdot x}}{(2\pi)^3}\bar{u}_p\left[-i\gamma^\mu\gamma_5 f(q^2) + q^\mu\gamma_5 g(q^2)\right]u_n. \tag{1.36}$$

Here, $u_{p,n}$ are the Dirac spinors for the proton and neutron, $f(q^2)$ and $g(q^2)$ are the two form factors, and $q = p_n - p_p$. The $f(q^2)$ is known as the axial form factor and is usually written as $G_A(q^2)$. The relationship between $f(q^2)$ and $g(q^2)$ can be seen in the following way. If we assume that we have exact $SU(2)_R \times SU(2)_L$ symmetry, then the conservation of axial current requires that

$$q_\mu\langle p|A^\mu(x)|n\rangle = 0. \tag{1.37}$$

Using the Dirac equations for nucleons with $m_N$ as the mass of the nucleon

$$\bar{u}_p(i\not{p}_p + m_N) = 0,\ (i\not{p}_n + m_N)u_n = 0 \tag{1.38}$$

one obtains

$$2m_N f(q^2) = q^2 g(q^2). \tag{1.39}$$

In the limit $q^2 \to 0$, $f(0)$ is measured experimentally to be positive definite and is usually called $g_A$. It has a value of $\approx 1.26$ [20, 21]. So, we have in Eq. 1.39 neither $m_N$ nor $f(0)$ to be small. This implies that for $SU(2)_R \times SU(2)_L$ symmetry to be exact $g(q^2)$ must have a pole as $q^2 \to 0$:

$$g(q^2) \to \frac{2m_N g_A}{q^2}. \tag{1.40}$$

A requirement of the spontaneous breaking of an exact $SU(2)_R \times SU(2)_L$ symmetry is the creation of a massless pion that gives us this pole.

For the decay of a charged pion, $\pi^+ \to \mu^+ + \nu_\mu$, the primary interaction is via the exchange of a weak boson ($W^+$). But at low energies compared to the mass of the weak boson, the interaction takes the form $J_\mu J^\mu$ with $J^\mu = J_h^\mu + J_l^\mu$. Here, $J_l^\mu$ and $J_h^\mu$ refer to the leptonic and hadronic currents, respectively. The transition matrix of this process

can thus be written as

$$T \sim \langle \mu\nu | J_\mu J^\mu | \pi(k) \rangle = \langle \mu\nu | J^l_\mu | 0 \rangle \langle 0 | J^\mu_h | \pi(k) \rangle. \tag{1.41}$$

The hadronic part of the process can be described by the axial-vector current $A^a_\mu(x)$ because the pion carries the negative parity for the process:

$$\langle 0 | A^a_\mu(x) | \pi^b(k) \rangle = i k_\mu \delta^{ab} f_\pi(k^2) e^{ik\cdot x}. \tag{1.42}$$

Here, $k_\mu$ is the four vector for the pion momentum and $f_\pi(k^2)$ is the pion form factor. When $k^2 = m_\pi^2$, *i.e.* on mass shell, $f_\pi(k^2)$ is defined to be pion decay constant $f_\pi$. The derivative of Eq. 1.42 is

$$\langle 0 | \partial^\mu A^a_\mu(x) | \pi^b(k) \rangle = -k^2 \delta^{ab} f_\pi(k^2) e^{ik\cdot x}. \tag{1.43}$$

In the chiral limit, $m_\pi = 0$, the axial-vector current is conserved. But, when we have a small pion mass, $k^2 = m_\pi^2 \neq 0$, we can introduce a pion field $\phi^a(x)$ such that

$$\langle 0 | \phi^a(x) | \pi^b(k) \rangle = \delta^{ab} e^{ik\cdot x}. \tag{1.44}$$

This gives us the partially conserved axial current (PCAC) relation,

$$\partial^\mu A^a_\mu(x) = -m_\pi^2 f_\pi \phi^a(x). \tag{1.45}$$

To conserve the axial current Eq. 1.45 only vanishes if the pion decay constant $f_\pi \to 0$ (a stable pion), or the pion field $\phi^a(x)$ vanishes, or if the pion has no mass. This PCAC relation plays an important role in the derivation of the low energy theorems (next section).

Now, going back to our beta decay reaction, we can see that from Eq. 1.42

$$A^a_\mu = f_\pi \partial_\mu \phi^a \tag{1.46}$$

to lowest order in $\phi^a(x)$. This gives us

$$\langle p | A^a_\mu(x) | n \rangle_{\pi-pole} = i f_\pi q_\mu \langle p | \phi^a(x) | n \rangle. \tag{1.47}$$

The strong coupling constant $G_{\pi N}(q^2)$ can be defined by [19]

$$\langle p|\phi^a(x)|n\rangle = \frac{ie^{iq\cdot x}}{(2\pi)^3 q^2} G_{\pi N}(q^2)\bar{u}_p\gamma_5 u_n. \tag{1.48}$$

Hence,

$$\langle p|A^a_\mu(x)|n\rangle_{\pi-pole} = -f_\pi \frac{e^{iq\cdot x}}{(2\pi)^3}\frac{q_\mu}{q^2} G_{\pi N}(q^2)\bar{u}_p\gamma_5 u_n. \tag{1.49}$$

Comparing the above equation with Eq. 1.36, we can see that one-pion exchange gives the function $g(q^2)$ a pole

$$\lim_{q^2\to 0} g(q^2) = \frac{G_{\pi N} f_\pi}{q^2} \tag{1.50}$$

and thus combining with Eq. 1.40

$$G_{\pi N} = \frac{2m_N g_A}{f_\pi}. \tag{1.51}$$

This is the famous Goldberger-Treiman relation [22]. The important thing to note here is that the strong interaction coupling between the pion-nucleon $G_{\pi N}$ has been related to the weak reaction coupling constant $g_A$. The Goldberger-Treiman relation will appear later in the description of the predictions by Braun *et al* for near threshold pion electroproduction at high $Q^2$.

### 1.2.3 Low Energy Theorem

In this section we take a look at one of the low energy theorems for photoproduction that involves the Kroll-Ruderman contact term and the use of chiral symmetry and PCAC. To lowest order in electromagnetic interaction, $J$, the transition matrix elements for the pion photoproduction ($Q^2 = 0$) reaction $\gamma(q) + N(p) \to \pi^a(k) + N(p')$ is given by [5]

$$S \sim -i \int \mathrm{d}^4x\, e^{-iqx}\varepsilon^\mu(q)\langle N'\pi^a|J_\mu(x)|N\rangle \tag{1.52}$$

where $\varepsilon^\mu$ is the photon's polarization vector. Using translation invariance and other simplification techniques such as PCAC (Eq. 1.45) one can write the scattering amplitude $\mathcal{M}$ for the reaction:

$$\mathcal{M} = \frac{k^2 - m_\pi^2}{f_\pi m_\pi^2}\int \mathrm{d}^4x\, e^{ikx}\langle N'|T(\partial^\mu A^a_\mu(x)\varepsilon\cdot J(0))|N\rangle. \tag{1.53}$$

Using integration by parts, we obtain two terms contributing to our amplitude

$$\mathcal{M} = \frac{k^2 - m_\pi^2}{f_\pi m_\pi^2} \int \mathrm{d}^4x\, e^{ikx} \{\delta(x_0)\langle N'|[A_0^a(x), \varepsilon \cdot J(0)]|N\rangle + ik^\mu \langle N'|T(A_\mu^a(x), \varepsilon \cdot J(0))|N\rangle\}. \tag{1.54}$$

The first term in the above equation was obtained by differentiating on the plane wave and the second by differentiating on the step functions ($\Theta(x_0)$ and $\Theta(-x_0)$) that are contained implicitly in the time ordering operator. Additionally, the first term, which contains the equal time commutators (ETC) of the axial charge and the electromagnetic current, will yield the Kroll-Ruderman term (Fig. 1.3(d)) that dominates the threshold production for $\pi^\pm$ but vanishes for $\pi^0$. This Kroll-Ruderman term describes the contact interaction between the photon and the proton.

But we still have a problem with Eq. 1.54. The time ordering product term would vanish in the limit $k^2 \to m_\pi^2$ for physical pions if it were not for the hidden pion pole term in the product. To overcome this problem we first look at the contribution of the axial current of the pion. The axial current for the hadronic system (pion and nucleon) is given by some additional terms in Eq. 1.46

$$A_\mu^a = J_\mu^{N,a} + f_\pi \partial_\mu \phi^a + J_\mu^{\mathrm{int},a} = f_\pi \partial_\mu \phi^a + \tilde{J}_\mu^a, \tag{1.55}$$

where $\tilde{J}_\mu^a$ contains contributions from the nucleon and interaction current. So, placing this into Eq. 1.54 and integrating by parts we have

$$\begin{aligned} \frac{f_\pi m_\pi^2}{-k^2 + m_\pi^2}\mathcal{M} &= \int \mathrm{d}^4x\, e^{ikx} \{\delta(x_0)\langle N'|[A_0^a, \varepsilon \cdot J]|N\rangle - i\omega_\pi f_\pi \delta(x_0)\langle N'|[\phi^a, \varepsilon \cdot J]|N\rangle \\ &\quad + ik^\mu \langle N'|T(\tilde{J}_\mu^a \varepsilon \cdot J)|N\rangle + f_\pi k^2 \langle N'|T(\phi^a \varepsilon \cdot J)|N\rangle\}. \end{aligned} \tag{1.56}$$

If one compares the above equation with Eq. 1.53 one may note that the last term on the RHS of the above equation is simply $\mathcal{M}$ multiplied by $f_\pi k^2/(-k^2 + m_\pi^2)$. So, combining this term with the LHS of above we get rid of the pole structure.

And we obtain our final result:

$$\begin{aligned} \mathcal{M} &= \frac{1}{f_\pi} \int \mathrm{d}^4x\, e^{ikx} \{\delta(x_0)\langle N'|[A_0^a, \varepsilon \cdot J]|N\rangle - i\omega_\pi f_\pi \delta(x_0)\langle N'|[\phi^a, \varepsilon \cdot J]|N\rangle \\ &\quad + ik^\mu \langle N'|T(\tilde{J}_\mu^a \varepsilon \cdot J)|N\rangle\}. \end{aligned} \tag{1.57}$$

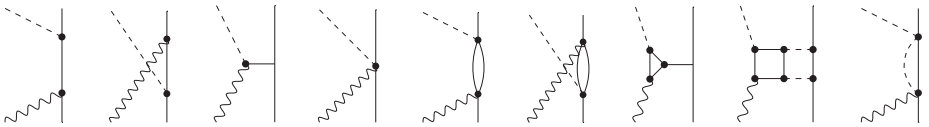


**Figure 1.3: Diagrams for pion photoproduction: (a) $s$-channel, (b) $u$-channel, (c) $t$-channel, (d) Kroll-Ruderman term, (e)-(i) higher order diagrams. Diagrams (e) and (f) are the ones recovered from $\chi$PT.**

Again, the first term is the Kroll-Ruderman term and the second term contributes to the $t$-channel photoproduction at threshold. The third term, to lowest order gives us the $s$ and $u$-channel contributions to the pion nucleon coupling (Fig. 1.3). The higher order contributions from this term, which can be computed perturbatively, give us one-loop and higher corrections to threshold production and can be expressed in powers of pion mass. These one loop contributions (Figs. 1.3 (e) and (f)) were exactly what were missing from the naive expansion in pion mass in the earlier approaches to LET derivation. This approach is known as the chiral perturbative approach ($\chi$PT).

The neutral pion photoproduction cross sections provide a good insight into the validity of $\chi$PT derivation of the low energy theorems. This can be observed in the data obtained from Saclay and Mainz [8, 23]. Data from Saclay indicated that the naive expansion about the pion mass can lead to omission of certain one loop diagrams when done to higher order [8].

A similar calculation can be performed to obtain the electroproduction cross sections and predictions for the neutral pion reaction for $Q^2 < 1\,\mathrm{GeV}^2$ [24].

### 1.2.4 Braun *et al* Predictions

For the $Q^2$ range of $1-10\,\mathrm{GeV}^2$, Braun *et al* [17] have a new prescription to describe the threshold physics. For the $\gamma^* p \to N\pi$ reaction, the transition matrix elements exactly at *threshold* can be written as

$$\langle N(P')\pi(k)|J_\mu|p(P)\rangle = -\frac{i}{f_\pi}\bar{N}(P')\gamma_5\left[(\gamma_\mu q^2 - q_\mu \not{q})\frac{G_1^{\pi N}(Q^2)}{m_N^2} - \frac{i\sigma_{\mu\nu}q^\nu}{2m_N}G_2^{\pi N}(Q^2)\right]p(P). \tag{1.58}$$

Here, $J_\mu$ is the electromagnetic interaction current for the reaction, $N(P')$ and $p(P)$ are the spinors for the nucleon in the final and initial state, respectively, $f_\pi$ is the pion decay constant, $m_N$ is the mass of the nucleon and $q = P - P'$. Also, $G_1^{\pi N}(Q^2)$ and $G_2^{\pi N}(Q^2)$

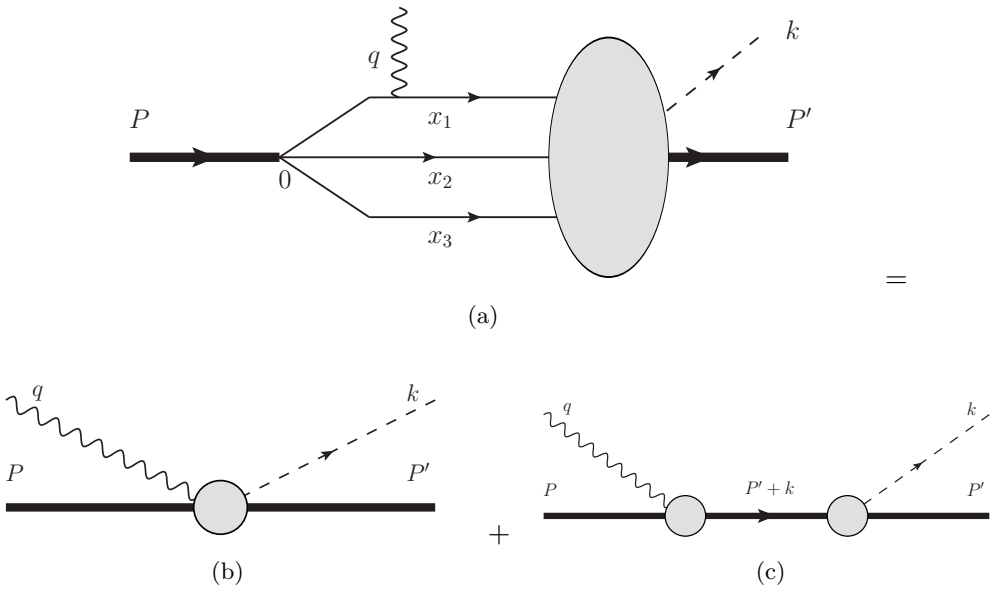


**Figure 1.4: The feynman diagrams describing the threshold pion electroproduction at high $Q^2$ per Braun *et al.* (a) The total pion electroproduction process that includes two terms: (b) the Kroll-Ruderman term and (c) the nucleon pole term. The contributions from these terms are computed using different techniques for different ranges of $Q^2$.**

are the generalized form factors for the pion-nucleon system that describe the 'blob' in the Kroll-Ruderman process in Fig. 1.4(b).

The last term in this equation is the helicity non-conserving form factor and is similar to the elastic electromagnetic form factor $F_2(Q^2)$ for the nucleon. This is because in the elastic scattering process $ep \to ep$, the matrix elements of the hadronic current are related to [25]

$$\langle N|J_\mu|p\rangle = e\bar{N}\left(\gamma_\mu F_1(Q^2) + \frac{i\sigma_{\mu\nu}q^\nu}{2m_N}F_2(Q^2)\right)N. \tag{1.59}$$

One may observe a parallel between the last term in Eq. 1.58 and Eq. 1.59. The difference is only in the presence of $\gamma_5$ and modulo a few factors. Both terms contain the antisymmetric tensor $\sigma_{\mu\nu}$, which gives us the non-helicity conservation of the current. Additionally, in the elastic case if the nucleon were a point particle, then the form factor $F_2 = 0$. Similarly, we can say that $G_2 = 0$ if the nucleon were a point particle.

Also, now let's take a look at the first term in both equations. We see a term containing $\gamma_\mu$ and its associated form factors $G_1$ and $F_1$. This term is related to the helicity conservation of the current. The difference comes in the presence of the additional gauge term in Eq. 1.58, *i.e.*, $q_\mu \not{q}$. This is to make the overall axial-vector term $\gamma_5\gamma_\mu$ gauge

invariant.

With this in mind, we expect the generalized form factors to be somehow related to the elastic electromagnetic form factors. We look at the neutral pion channel [17]:

$$\begin{aligned} \frac{Q^2}{m_N^2} G_1^{\pi^0 p} &= \frac{g_A}{2} \frac{Q^2}{(Q^2 + 2m_N^2)} G_M^p \\ G_2^{\pi^0 p} &= \frac{2 g_A m_N^2}{Q^2 + 2m_N^2} G_E^p. \end{aligned} \tag{1.60}$$

Here, $g_A$ is the axial coupling constant obtained from weak interactions and $G_E^p$ and $G_M^p$ are the Sachs electromagnetic form factors for the proton that are linear combinations of $F_1$ and $F_2$:

$$\begin{aligned} G_E &= F_1 - \frac{Q^2}{4m_p^2} F_2 \\ G_M &= F_1 + F_2. \end{aligned} \tag{1.61}$$

For the charged pion case, $\pi^+$, the generalized form factors can also be related to the electromagnetic form factors for the neutron. Additionally, there is a way to access the axial form factor $G_A$ via these form factors:

$$\begin{aligned} \frac{Q^2}{m_N^2} G_1^{\pi^+ n} &= \frac{g_A}{\sqrt{2}} \frac{Q^2}{(Q^2 + 2m_N^2)} G_M^n + \frac{1}{\sqrt{2}} G_A \\ G_2^{\pi^+ n} &= \frac{2\sqrt{2} g_A m_N^2}{Q^2 + 2m_N^2} G_E^n. \end{aligned} \tag{1.62}$$

Here, $G_M^n$ and $G_E^n$ are the Sachs form factors for the neutron.

Let's examine Eq. 1.60 a little bit in detail. These expressions are obtained in the chiral limit, $m_\pi = 0$ and are valid exactly at threshold. For low energies, *i.e.*, $Q^2 \to 0$, we observe

$$\begin{aligned} \lim_{Q^2 \to 0} G_1^{\pi^0 p} &= \frac{g_A}{4} G_M^p \\ \lim_{Q^2 \to 0} G_2^{\pi^0 p} &= g_A G_E^p. \end{aligned} \tag{1.63}$$

Although we expect a relationship between the elastic form factors and the generalized form factors, we did not expect the involvement of the $g_A$. As mentioned earlier, this coupling constant is involved in weak interactions where we also see the presence of $\gamma_5$. So, we finally see the culprit here. The overall difference in the two currents comes from

the presence of $\gamma_5$. It changes the current in an axial manner, *i.e., a chiral rotation.* It essentially takes an electromagnetic current and "chirally" rotates it. This $\gamma_5$ object describes the presence of the pion in the final state of the reaction.

These transition amplitudes or cross sections are directly related to the CGLN multipoles as discussed in Section 1.1.2. In particular, at *threshold*, only the S-wave multipoles $E_{0+}$ and $L_{0+}$ contribute to the cross sections [2, 17]:

$$\left.\frac{d\sigma}{d\Omega_\pi^*}\right|_{\rm th} = \frac{2p_\pi^* W}{W^2 - M_p^2}\left[|E_{0+}|^2 + \varepsilon\frac{Q^2}{\omega^2}|L_{0+}|^2\right]. \tag{1.64}$$

Here, $p_\pi^*$ is the pion momentum in the CM system, $\varepsilon$ is the transverse polarization of the virtual photon and $\omega$ is the virtual photon energy in the CM frame. Here 0 in the subscript refers to the total angular momentum $l = 0$ of the pion relative to the proton and + represents the spin of the proton $+\frac{1}{2}$. Also, here the scalar multipole $S_{0+}$ has been redefined as $L_{0+} = \frac{\omega}{|\mathbf{q}^*|}S_{0+}$ with $|\mathbf{q}^*|$ as the momentum of the virtual photon in the CM frame. $E_{0+}$ can be thought of as the transverse coupling of the virtual photon to the nucleon spin and the $L_{0+}$ as the longitudinal coupling of the same.

Only these two multipoles contribute in the electroproduction of the pion at threshold and are known as the S-wave multipoles. These S-wave multipoles are in turn directly related to the generalized form factors $G_1$ and $G_2$ at threshold for high $Q^2$:

$$\begin{aligned} E_{0+} &= \frac{\sqrt{4\pi\alpha}}{8\pi f_\pi}\sqrt{\frac{(2m_N + m_\pi)^2 + Q^2}{m_N^3(m_N + m_\pi)^3}}\left(Q^2 G_1^{\pi N} - \frac{m_N m_\pi}{2}G_2^{\pi N}\right) \\ L_{0+} &= \frac{\sqrt{4\pi\alpha}}{8\pi f_\pi}\frac{m_N|\omega_\gamma^{th}|}{2}\sqrt{\frac{(2m_N + m_\pi)^2 + Q^2}{m_N^3(m_N + m_\pi)^3}}\left(G_2^{\pi N} + \frac{2m_\pi}{m_N}G_1^{\pi N}\right). \end{aligned} \tag{1.65}$$

Here, $\alpha$ is the electromagnetic coupling constant, $f_\pi = 93$ MeV is the pion decay constant and $\omega_\gamma^{th}$ is the photon energy at threshold in the CM frame and is given by the following relation:

$$\omega_\gamma^{th} = \frac{m_\pi(2m_N + m_\pi) - Q^2}{2(m_N + m_\pi)}. \tag{1.66}$$

Once we start to move away from threshold, the P-wave multipoles ($l = 1$) start contributing to the transition amplitude in addition to the S-wave multipoles. These multipoles are related to the nucleon pole process shown in Fig. 1.4(c). In this process, an off-shell nucleon interacts with the virtual photon, which then decays into an on-shell nucleon and a pion. The interaction of the virtual photon and the nucleon is described by

the electromagnetic form factors $F_1(Q^2)$ and $F_2(Q^2)$ represented by the first 'blob' in the figure. So, the total transition amplitude matrix elements can be written as

$$\langle N(P')\pi(k)|J_\mu|p(P)\rangle = -\frac{i}{f_\pi}\bar{N}\gamma_5\left[(\gamma_\mu q^2 - q_\mu \not{q})\frac{1}{m_N^2}G_1^{\pi N}(Q^2) - \frac{i\sigma_{\mu\nu}q^\nu}{2m_N}G_2^{\pi N}(Q^2)\right]p$$
$$+\frac{ig_A}{2f_\pi[(P'+k)^2 - m_N^2]}\bar{N}\not{k}\gamma_5(\not{P}' + m_N)\left[\left(\gamma_\mu - \frac{q_\mu \not{q}}{q^2}\right)F_1^p(Q^2) + \frac{i\sigma_{\mu\nu}q^\nu}{2m_N}F_2^p(Q^2)\right]p. \quad (1.67)$$

Above, in the second term, the strong coupling of the pion and the off-shell nucleon $G_{\pi N}$ is described in terms of the axial coupling constant $g_A$ and the pion decay constant $f_\pi$ per the Goldberger-Treiman relation Eq. 1.51. This is represented by the second 'blob' in Fig. 1.4(c) that describes the decay of the off-shell proton into an on-shell proton and a pion. Additionally, one sees the presence of the propagator to describe the off-shell nucleon $i/[(P'+k)^2 - m_N^2]$. The presence of the $\gamma_5$ object in front is included to conserve the overall parity of the process.

These electromagnetic form factors $F_1$ and $F_2$ are well known from elastic scattering experiments. The associated P-wave multipoles include $E_{1+}$, $M_{1-}$ and so on, which contribute to the transition amplitude once one starts to move away from threshold. The total process is shown in Fig. 1.4(a) that includes both S- and P-wave contributions.

These predictions for the transition amplitudes or cross sections only contain the S- and P-wave contributions. All higher order contributions such as D-waves are neglected in the predictions of Braun *et al* [17]. These multipole contributions can be related to the structure functions for the differential cross section as in Eq. 1.15. The $\sigma_T + \varepsilon_L\sigma_L$ structure functions are directly related to the S-wave multipoles and these are expected to dominate in the near threshold region. The S-wave is independent of $\phi_\pi^*$. The P-wave multipoles are related to the $\sigma_{LT}$ interference term and the contribution from this term near threshold is predicted to be smaller than the S-wave. The D-wave multipoles are related to the $\sigma_{TT}$ interference term and it is neglected in the predictions.

It is suspected that in the experiment, the P-wave contribution may be higher than is predicted by Braun *et al*. This is because the cross section predictions near threshold do not include energy dependence of the generalized form factors generated by the final state interaction. Additionally, it has not been tuned to include lower $Q^2$ and higher $W$ experimental results [17].

The predictions for $G_1$ and $G_2$ are obtained in this high $Q^2$ regime where 'soft' processes dominate. This kinematic region is beyond the regime of low energy theorems.

Also, perturbative techniques (pQCD) cannot be used to compute the form factors. Using a new approach, known as the Light Cone Sum Rules (LCSR) [14, 15, 26], Braun *et al* compute contributions from the 'soft' processes for the form factors. This method is similar to the Shifman-Vainshtein-Zakharov (SVZ) [27] sum rule approach. The generalized form factors are as such computed using this technique but only in the chiral limit, $m_\pi \to 0$. These predictions are consistent with the low energy theorem predictions for $Q^2 \to 0\,\mathrm{GeV}^2$. Additionally, there are predictions for the axial form factor $G_A$ that can be extracted for the charged pion reaction from the generalized form factors $G_1$ and $G_2$.

## 1.3 Experimental Goals

In this experiment, the neutral pion electroproduction reaction $ep \to ep\pi^0$ is studied for $W = (1.08 - 1.16)$ GeV and $Q^2 = (2 - 5)\,\mathrm{GeV}^2$. The aim of this experiment is to measure the differential and integrated cross sections for the reduced process $\gamma^* p \to p\pi^0$. The structure functions and the S-wave multipoles, $E_{0+}$ and $L_{0+}$, will be extracted from the measured cross sections. Additionally, the generalized form factors $G_1^{\pi^0 p}(Q^2)$ and $G_2^{\pi^0 p}(Q^2)$ will also be obtained. These form factors will then be compared with the predictions of Braun *et al*.

In the following chapters, we will discuss the the CLAS detector and the experimental conditions. The analysis process of obtaining these form factors is detailed in chapters 3, 4 and 5. The results of the measured cross sections, structure functions, multipoles and form factors along with the comparisons with the predictions are shown in chapter 6.

# 2. Experimental Apparatus

## 2.1 Overview of Experiment

The $e1$-6a experiment was conducted in Hall-B at Jefferson Lab. An incident electron beam with intensity of 7 nA and an average energy of 5.754 GeV was directed on a 5 cm long cylindrical liquid hydrogen target. A total charge of about 21 mC was collected with an average beam polarization of 70%. The target was placed -4 cm upstream from the CLAS center in the hall. In this chapter, we will describe the accelerator facility and CLAS detector system that was used to run the experiment.

## 2.2 Accelerator

The Continuous Electron Beam Accelerator Facility (CEBAF) provides upto 6 GeV electron and photon beams to study the structure of atomic nuclei and other subatomic particles. The electron beam can be sent simultaneously to three experimental Halls A, B and C. The schematic design of the accelerator facility and the three Halls is shown in Fig. 2.1 [28].

Two parallel superconducting continuous-wave (CW) linear accelerators are connected with magnetic recirculation arcs. The parallel accelerators are composed of 338 five-cell superconducting niobium cavities that operate at an average temperature of about 2K. These cavities provide an average energy gain of 5 MeV/m.

The electron beam is introduced into the accelerator from the injector at one end and is recirculated for up to five times. A radio frequency separator can be used to extract every third bunch from each of the first four passes. This extracted electron beam with an energy of $\frac{N_{pass}}{5} \times E_{\max}$ can then be delivered to one of the three experimental halls. The beam can be split into three parts at the end of the fifth pass to be simultaneously sent to three halls. On average, the beam energy resolution of the facility is $\Delta E/E \leq 10^{-4}$ and the beam size is in the order of about a few hundred micrometers [29].

## 2.3 Beam Line Instrumentation

Three beam position monitors (BPMs) are used to continuously measure electron beam position. The BPMs consist of three RF cavities and the monitors are placed 36.0, 24.6, and 8.2 m upstream of CLAS target. The measurements from the BPMs are used

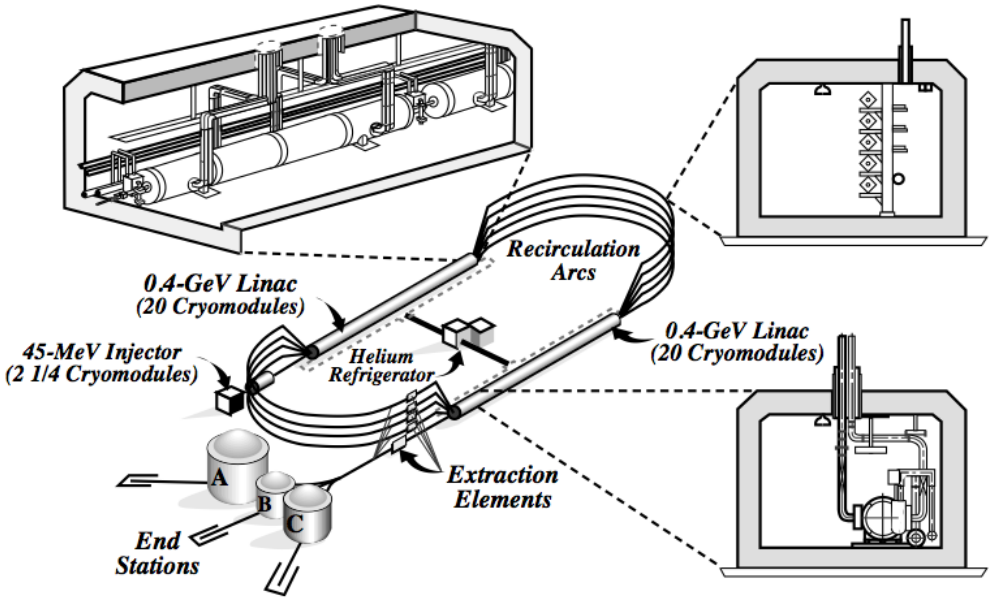


**Figure 2.1: Schematic design of the CEBAF accelerator.**

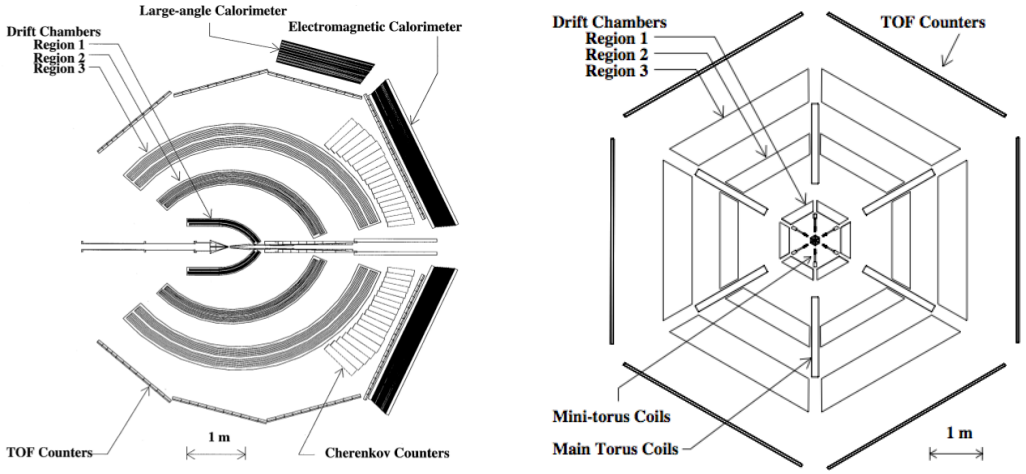


(a) (b)

**Figure 2.2: (a) A slice of the CLAS detector shown cut through its midplane. The electron beam enters from the left. (b) Another view of the CLAS detector shown as a cut through the target. The cryostats of the superconducting magnet are shown which slice the detector into six sectors. Also shown are the mini-torus coils surrounding the target.**

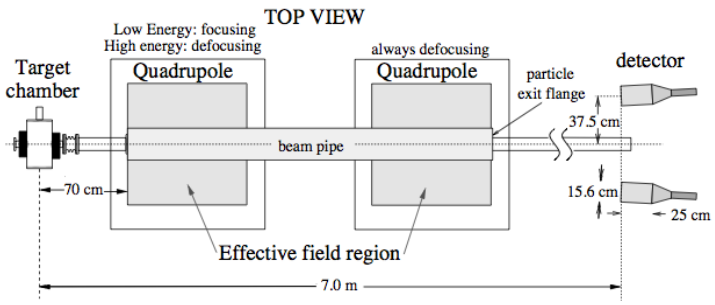


**Figure 2.3: A schematic layout of the Møller polarimeter.**

to center the beam on the target.

A Faraday cup is used to measure the total charge collected for a given run period. It is composed of 4000 kg lead (75 radiation lengths) and is located 29 m downstream of the target. It is also used to measure the charge variation as a function of helicity for experiments that require polarized electrons.

A Møller polarimeter is used to measure the beam polarization. It measures the electron-electron (Møller) scattering asymmetry to determine the polarization. It is located upstream of the bremsstrahlung tagging system and consists of a target chamber, two quadrupole magnets and two detectors in the horizontal plane on either side of the beamline as shown in Fig. 2.3. The target is made of 25 $\mu$m thick permendur foil. The quadrupoles separate the scattered electrons from the unscattered beam. The electrons are then received at two lead/scintillation fiber composites placed 7 m downstream of the target. The polarization is determined to about 1% statistical uncertainty.

## 2.4 Cryogenic Target

The targets are positioned inside CLAS using support structures as in Fig. 2.4(a). A superconducting magnet, the 1 K refrigerator, the microwave and NMR systems, and the target module system comprise the target. These subsystems including the pumping system are attached to a rail mounted cart that allows the entire assembly to be rolled in and out of CLAS.

The $e$1-6a target (Fig. 2.4(b)) is a 5 cm long and 1.4 cm diameter Kapton cell. It is positioned -4 cm upstream from the CLAS center and filled with liquid hydrogen.

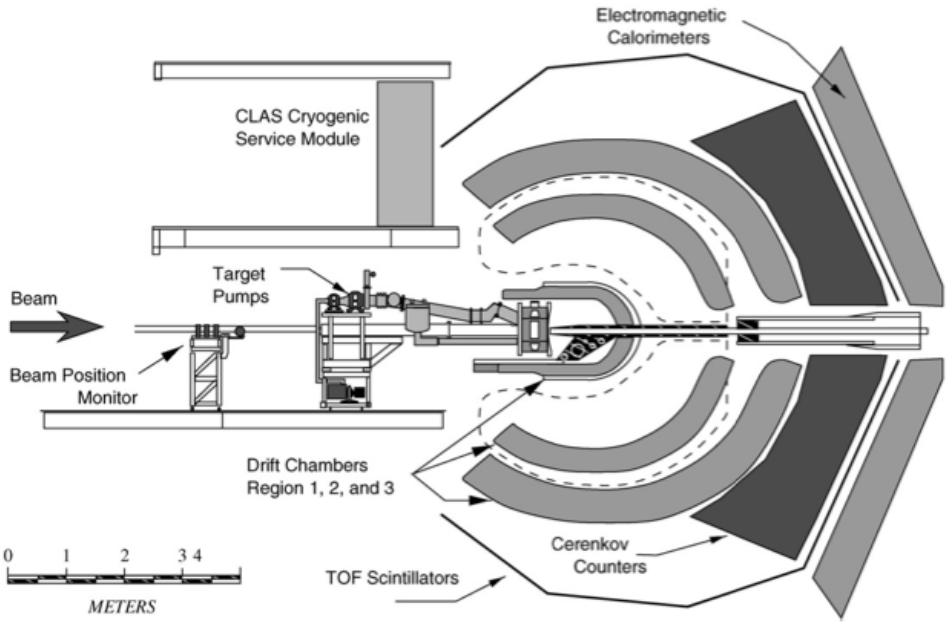


(a)


(b)

**Figure 2.4: (a) A schematic overview of target position in relation to all major CLAS systems. Dashed lines indicate projections of torus cryostats onto the midplane. (b) The $e$1-6a target cell.**

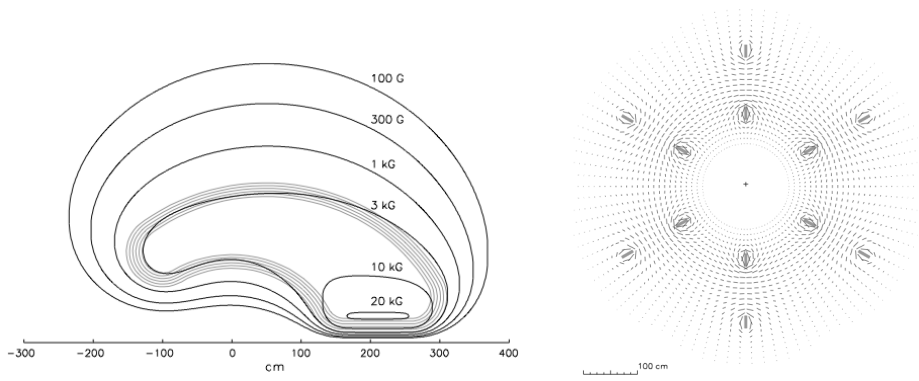


(a) (b)

**Figure 2.5: (a) Constant magnetic field contours for the CLAS toroid in the midplane between two coils. The coil projections are shown for reference. (b) The six magnetic coils shown along with their respective magnetic field vectors transverse to the beam on a plane centered on the target.**

## 2.5 Torus Magnet

Six superconducting coils arranged in a toroidal geometry are used to generate a magnetic field around the electron beam line. The magnetic field bends the negatively (or positively) charged particles toward (or away from) the beam line and the deflection of the particle's track is used to reconstruct its momentum.

The coils separate the CLAS detector into six sectors. Each of the coils is composed of 4 layers of 54 turns of aluminum-stabilized NbTi/Cu conductor. The coils are kept cool by supplying super-cool helium through cooling tubes located at the edges. The coils are shaped like kidneys. The orientation and layout of the coils and the strength of the generated magnetic fields is shown in Figs. 2.5(a)-2.5(b).

The coils are designed to handle upto 3860 A of current, which generates upto about 2.5 Tm magnetic field in the forward direction and as low as 0.6 Tm at the scattering angle of 90°. The primary component of the magnetic field is in the azimuthal $\phi$ direction, but close to the coils there is contribution to the $\theta$ component. The effect of this contribution is minimized by the circular inner shape of the coils [28].

## 2.6 Mini Torus

In addition to the main torus, CLAS also houses a mini torus that is not superconducting. It surrounds the target and prevents low momentum particles produced from Møller scattering in the target from reaching the innermost drift chambers. This mini torus

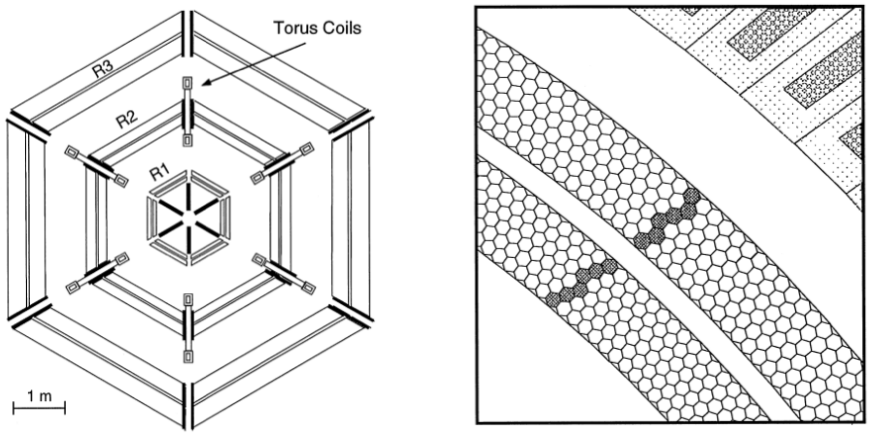


(a) (b)

**Figure 2.6: (a) Three regions of drift chambers shown through a vertical cut transverse to the beam line at the target. (b) Two superlayers of R3 sector are shown. The sense wires are at the center of each hexagon and the field wires are at the vertices. The fired drift cells are highlighted as the charged particle passes through the superlayers. The Cerenkov detector is shown in the upper right hand corner.**

is installed only for use in electron beam experiments. For photon beam experiments, this mini-torus is replaced by a scintillator start counter for triggering purposes. Figure 2.2(b) shows the placement of the mini-torus with respect to other CLAS components.

## 2.7 Drift Chambers

The drift chambers (DC) in CLAS are designed primarily to track the trajectories of charged particles. The charged particles are tracked as they are bent toward or away from the beam axis, depending on the particle's charge, due to the magnetic field created by the toroidal magnet. The tracks are measured at three different locations in each of the six sectors with an accuracy of 100 $\mu$m in the direction parallel to the magnetic field plane and an accuracy of about 1 mm in the direction perpendicular to the magnetic field plane. There are a total of 18 drift chambers with 3 regions in each sector.

The Region 1 (R1) drift chambers surround the target where the magnetic field is low. The Region 2 (R2) drift chambers are larger and are between the magnetic coils. They are in the region where the magnetic field strength is highest. The third region of drift chambers, Region 3 (R3), is largest and lies outside the magnetic coils as seen in Fig. 2.6(a).

The 130,000 wires in the drift chamber are arranged in layers of concentric circles,

which are in turn grouped into two "superlayers" for redundancy in tracking and pattern recognition. One of the superlayers is arranged in the direction parallel to the magnetic field and the other is tilted at a 6° stereo angle around the radius of each layer for azimuthal measurement. As shown in Fig. 2.6(b) six layers of drift cells usually comprise each superlayer. The wires are arranged in a quasi-hexagonal pattern where six field wires surround one 20-$\mu$m diameter gold-plated tungsten sense wire. The field wires are made of 140-$\mu$m diameter gold-plated aluminum 5056 alloy.

This hexagonal configuration allows for measuring drift time and distances easily for tracks entering at different angles. It also provides for a simpler sense wire location resolution for individual tracks. Furthermore, the electrostatic forces are reduced, thereby reducing the tensions in the wires, and thus requiring thinner endplates for support. The thin endplates prevent material from the torus from projecting out of the torus shadow, which affects the geometric acceptance of the spectrometer.

The drift chambers are filled with a 90% argon - 10% $CO_2$ gas mixture. This mixture provides low multiple scattering and has an operating voltage plateau of several hundred volts before breakdown occurs.

Here, charged particle tracks are reconstructed in two stages: 1) *hit-based* tracking and 2) *time-based* tracking. For hit-based tracking, within each superlayer the data are combined into track segments that are linked together to form tracks across three drift chamber regions in the sector. The momentum of the tracks can be reconstructed with about 3-5% resolution. For the time-based tracking stage, the drift times are converted to drift distances using a lookup table. For each drift cell the track positions are fit to determine the final track parameters. The identities and speeds of the particles are obtained from other detectors in CLAS. The average single-wire resolution in the middle portion of the cell for each Region is about 200 to 250 $\mu$m at the time of construction. The whole-cell average resolution is about 310, 315, and 380 $\mu$m for R1, R2, and R3, respectively [30].

## 2.8 Cerenkov Detector

As an electron passes through a material where its speed is greater than the speed of light in that medium it gives off radiation. This light (or Cerenkov radiation) can be collected using Cerenkov detectors (CC) to trigger on electrons and separate electrons from pions. For each sector these detectors provide polar angle coverage from $\theta = 8°$ to

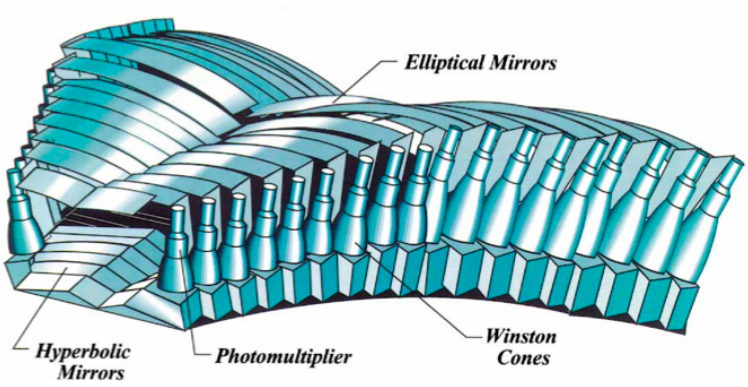


(a)

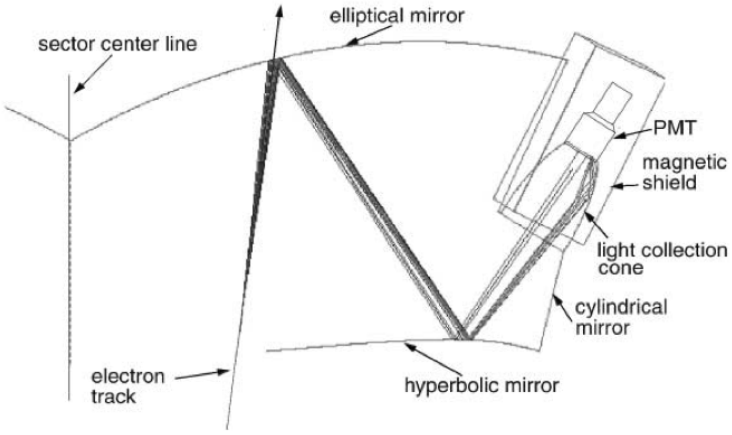


(b)

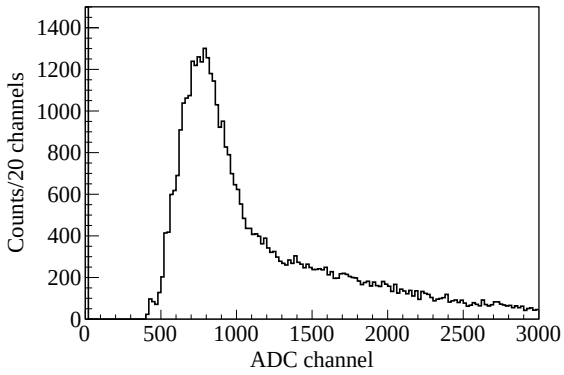


(c)

**Figure 2.7: (a) A schematic diagram of the optical modules array in a sector for the large angle Cerenkov detector. (b) Optical and light collection components are shown for one of the optical modules in the Cerenkov detector. Light from a typical electron track is shown as it bounces inside the mirrors and is collected in the PMT. (c) A typical ADC spectrum from the $e$1-6a experiment.**

45°.

For each sector, the Cerenkov detector is divided into 18 regions of $\theta$ called segments. Each segment is divided in two modules along the midplane of the sector, *i.e.*, bisecting the sector along the azimuthal $\phi$ direction. A "Winston" light collection cone and photomultiplier tube (PMT) is placed at the end of each module. The light from electrons is focused into the PMT using a series of mirrors arranged in a manner as shown in Fig. 2.7(a) and Fig. 2.7(b).

The 216 PMTs are placed in the azimuthal regions obscured by the torus magnet coils. To protect the PMTs from the magnetic fields produced by the coils, the PMTs are surrounded with high permeability multi-layered magnetic shields.

The Cerenkov gas of choice is $C_4F_{10}$ (perfluorobutane) because of its high refraction index of 1.00153 and its relative transparency to UV light (Cerenkov light is mostly in this range). This provides for electrons giving off Cerenkov light with momentum as low as 9 MeV while eliminating pions of momentum less than 2.5 GeV/c. This gives a nice separation between electrons and pions, thereby providing a means to trigger on electrons.

Beyond the edges of the mirrors the optical collection efficiency for the Cerenkov light drops rapidly. There are also spots along the midplane of the detector where the efficiency is low because of large gaps between the mirrors and imperfect optics in those regions. The electron efficiency in the region of fiducial acceptance is nominally about 99%. A typical ADC spectrum of the single photoelectron peak from a PMT is shown in Fig. 2.7(c)[31].

## 2.9 Scintillation Counters

A scintillation counter (SC) measures ionization radiation. When a charged particle strikes a scintillator, which is a transparent crystal (usually plastic), some of the atoms in the material get excited and emit ionization radiation. This radiation is absorbed into neighboring atoms which in turn get excited and emit multiple lower energy photons. This process repeats until the light is collected into the PMTs at the edge of the material.

The scintillation counters are used to measure the time of flight of particles for identification and triggering purposes. It can also be used for energy loss measurements and velocity determination. Additionally, it can be used to determine energies for slow moving particles such as the neutron. It is used primarily for timing, velocity, etc., and only secondarily for energy loss of slow hadrons.

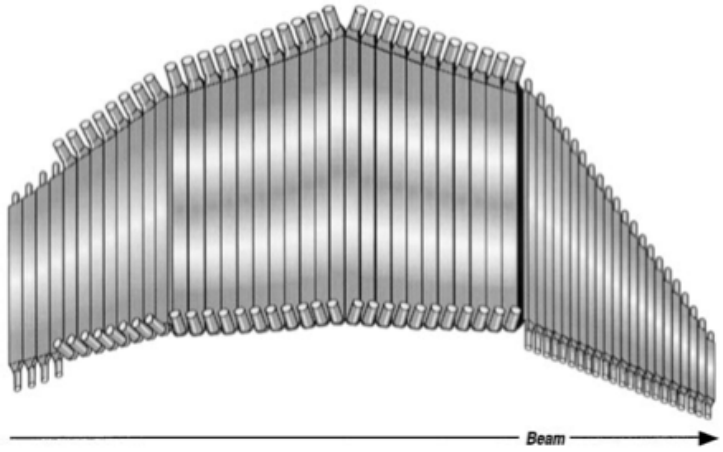


(a)

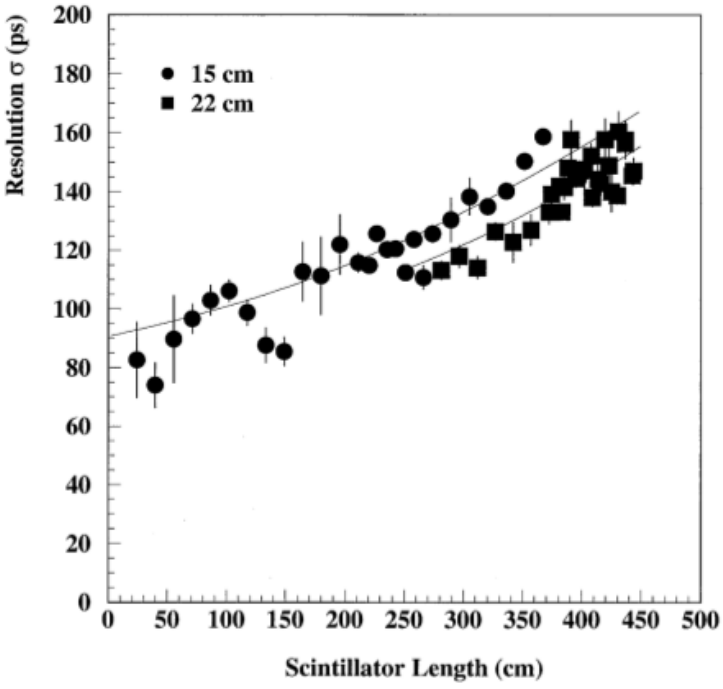


(b)

**Figure 2.8: (a) View of the time of flight counters in one sector showing the groupings into four panels. (b) Time resolutions of TOF counters determined using cosmic rays.**

The time of flight counters cover the entire azimuthal angle range $\phi$ and the polar angle range from 8° and 142°. They lie between the Cerenkov detectors and the electromagnetic calorimeters as shown in Fig. 2.2(a). Each scintillator is of uniform thickness of 5.08 cm and is positioned such that it forms a straight line from the central target position. Each counter has an acceptance of 1.5° of scattering angle. The forward counters at $8° < \theta < 45°$ are 15 cm wide and the rest are 22 cm wide. The ends of each scintillator counter are capped with PMTs to collect the signal from ionization radiation (Fig. 2.8(a)).

The time resolution of each counter can be determined using cosmic ray studies (Fig. 2.8(b)). The resolution depends on single photoelectron response of the scintillator and PMT, path length variations in light collection, and the length of the counter itself; it ranges from 100-200 ps [32].

## 2.10 Electromagnetic Calorimeters

The forward electromagnetic calorimeter (EC) works under the following principle. The calorimeter contains alternating scintillator and lead sheets. When a hadron hits the lead layer it creates a shower of secondary particles that are viewed in the scintillator layer and collected in a PMT.

The forward electromagnetic calorimeter in CLAS serves three primary functions: 1) detection and triggering of electrons with energies greater than 0.5 GeV, 2) detection of photons with energies more than 0.2 GeV and 3) detection of neutrons. The photon detection is useful in reconstruction of $\pi^0$ and $\eta$ as these mesons primarily decay into $2\gamma$s. The neutron is distinguished from the photon using time of flight measurements. For each sector, the calorimeter can detect particles in the polar angle range of $8° < \theta < 45°$.

The sampling calorimeter is composed of alternating scintillator and lead sheets with a total thickness of 16 radiation lengths. Each CLAS sector module has 40 cm of scintillator and and 8 cm of lead so that approximately one-third of the shower energy is deposited on the scintillator. Nearly all of the shower originates in the lead and is viewed in the scintillator.

Each lead-scintillator system is designed in an equilateral triangle shape. There are 39 layers of alternating 10 mm thick BC412 scintillator and 2.2 mm thick lead sheet. To minimize shower leakage at the edges and to minimize dispersion in signal arrival times that originate at different scintillator layers, each layer in the calorimeter has successively increasing area, giving it a "projective geometry."

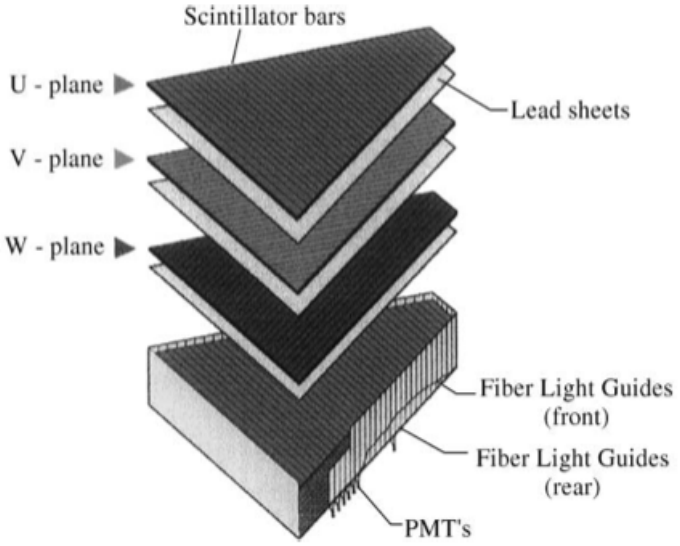


(a)

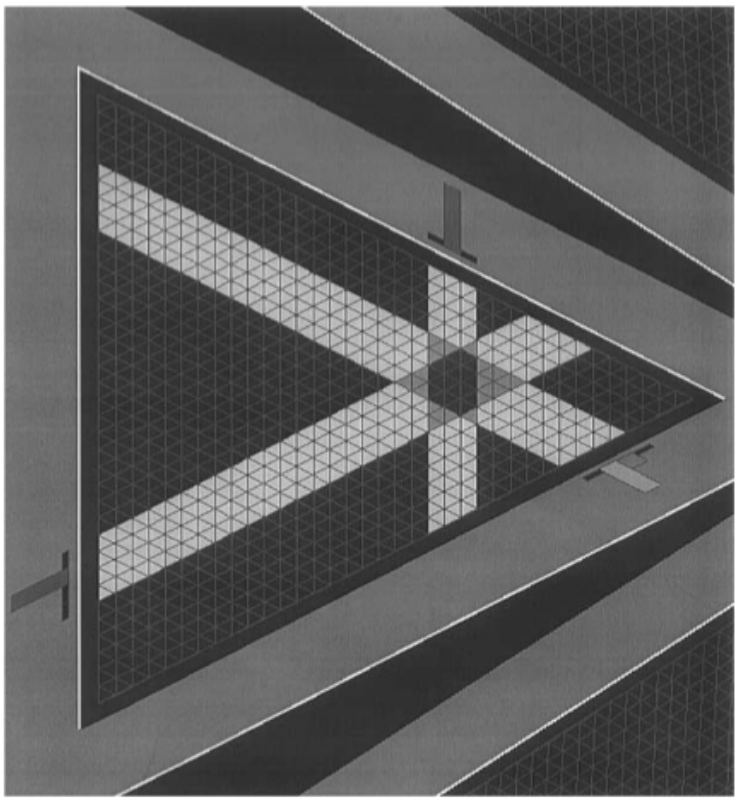

(b)

**Figure 2.9: (a) Segmented view of one of the six CLAS electromagnetic calorimeter modules. (b) Single event display of simulated EM shower in EC. Energy deposition profile of a charged particle is shown along each of the U, V, W views in the detector.**

Each scintillator layer has 36 strips that are parallel to one side of the triangle. These strips are rotated by 120° for each successive layer so that we have three views U, V, and W (Fig. 2.9(a)) that give us stereo information on the location of energy deposition (Fig. 2.9(b)). So, we have a total of 13 layers for each view. Additionally, each view is divided into an *inner* and an *outer* stack composed of 5 and 8 layers, respectively. These stacks provide longitudinal sampling for better hadron identification, especially for distinguishing minimum ionizing particles. For each module there are 216 PMTs to collect the light from the showers. Overall, there are 1296 PMTs and 8424 scintillator strips for the six EC modules.

This design provides a moderate resolution measurement of energy of particles. The resolution of the energy measurement depends on the sampling fraction, *i.e.*, the fraction of the incident particle energy deposited in the scintillators. The primary contribution to the energy resolution comes from fluctuations in the sampling of the number of secondary particle tracks. The sampling fraction resolution, $\sigma_{fs}$, can be parameterized as

$$\frac{\sigma_{fs}}{E} \propto \sqrt{\frac{t_s}{f_s}} \tag{2.1}$$

where $t_s$ is the sampling thickness measured in radiation lengths. Simulation studies estimate the resolution $\sigma_{fs}/E = 6\%/\sqrt{E(\text{GeV})}$ [33].

## 2.11 Trigger and Data Acquisition

CLAS employs a two-level hierarchical trigger system to collect events of interest. The Level 1 trigger system processes all PMT signals within 90 ns. These signals include information about the general location of hits in TOF detector, the signals in Cerenkov detector, and the energy deposited in the electromagnetic calorimeter. The signals from these detectors are selected based on lookup tables that are preloaded into memory.

Sometimes a Level 1 trigger can be set by cosmic-rays that do not have trajectories in the drift chambers. To reject these events, a Level 2 trigger system is used to find correlation between the tracks in the drift chambers and Level 1 signal.

The signals from the Level 1 and 2 triggers are placed inside the Trigger Supervisor (TS) board. There are 12 trigger inputs where the first eight are used for Level 1 triggers that can be prescaled. The remaining four are used for calibration purposes.

The primary trigger for the $e$1-6a experiment is a coincidence between the Cerenkov and the forward calorimeter (EC) to identify electrons. When this trigger is set the data

acquisition system takes a electronic snapshot of all information from the detectors and builds an "event" using the Event Builder system and passes it through the data pipelines to be stored in RAID disks. The data from these disks are periodically transferred to the computer center to be stored and accessed for analysis.

# 3. Data Analysis

## 3.1 Overview

In this chapter we discuss the particle identification procedures for the electron and proton, elastic event selection, kinematic corrections, fiducial cuts, and the pion identification process for the exclusive process $ep \rightarrow ep\pi^0$.

## 3.2 Particle Identification

The event reconstruction process involves taking a file containing BOS banks[3] that are produced by the DAQ system and producing a "cooked" file containing higher level information, such as four vectors. In addition to reconstruction of events, the cooking procedure also involves appropriate calibration of reconstructed data from different detector systems [34]. This process also includes a preliminary particle identification based on the reconstructed tracking information. To obtain a better identification of particles in our process, we perform our own identification.

For this experiment, in each event we detect an electron and a proton using the information from the CLAS detector. The pion is reconstructed by applying four-momentum conservation. Fig. 3.1 shows a typical event with electron and proton tracks as detected by CLAS. In the following paragraphs the electron and proton identification is discussed.

### 3.2.1 Electron

An *event* for this experiment involves a trigger on electrons. A good electron candidate is required to have the following properties:

- negative charge
- coincidence between Cerenkov counter (CC) and forward calorimeter (EC) in the same sector
- good geometrical hit status
- track in drift chambers (DC) for a negatively charged particle in the same sector
- hit in time of flight (TOF or SC) system in the same sector.

[3]Data banks containing raw hit information for each detector system for each event.

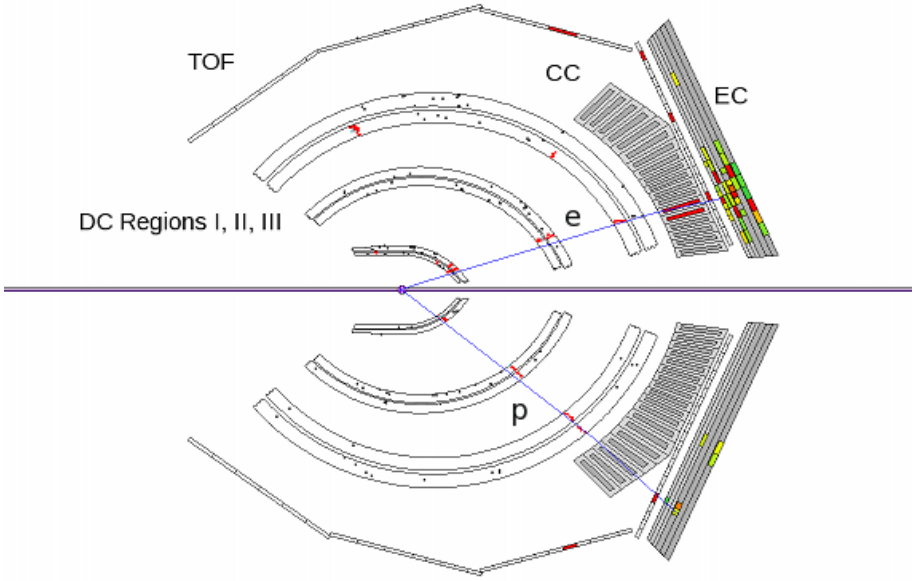


**Figure 3.1: A schematic representation of sectors 3 and 6 of the CLAS detector showing the electron (top) and proton (bottom) tracks from a typical near threshold event for the $e$1-6 experiment.**

For an electron track to have a good status (stat $> 0$) it must have geometrical matching in DC, EC and CC and also include viable timing information from SC. When information from a detector is incomplete or is missing for a track the corresponding detector bank value is set to zero. Please see Section 2.7 for track reconstruction procedures in DC.

The above requirements are necessary but not sufficient to clearly identify a track as an electron. There is additionally a significant contamination of minimum ionizing particles (MIPs) to the electrons, *i.e.*, $\pi^-$s. These particles can be isolated using information from EC.

As the electrons pass through EC they shower with a total energy deposition $E_{tot}$ that is proportional to their momentum $p$. Because of incorrect calculation and comparison with the drift chamber momentum this total energy is sometimes not equal to the sum of the energies in the inner $E_{in}$ and outer $E_{out}$ part of the calorimeter. So, we take the total energy as the one that is larger of either $E_{in} + E_{out}$ and $E_{tot}$.

The sampling fraction ($E_{tot}/p$) is plotted as a function of momentum for each sector after applying all the other electron identification cuts and preliminary cut on $W < 1.3$ GeV to focus on our kinematic region(s) of interest. Fig. 3.2(a) shows this distribution

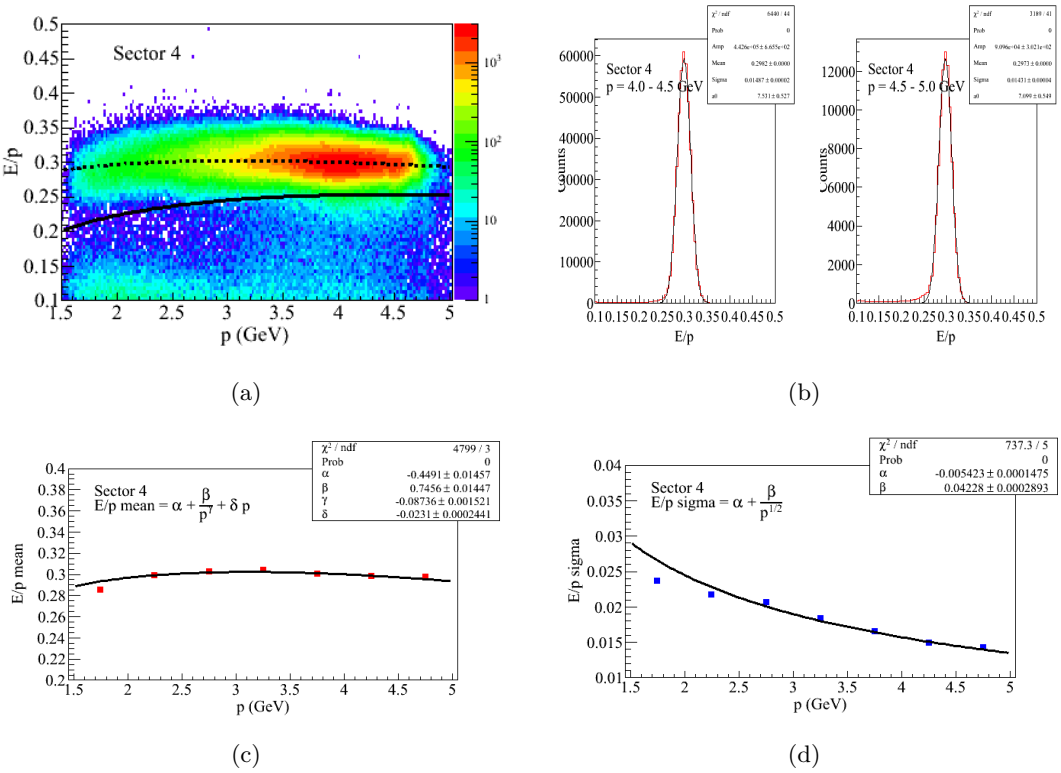


**Figure 3.2: (a) The sampling fraction $E/p$ is plotted as a function of the particle's momentum $p$ for electron candidates in Sector 4. The dashed curve shows the mean parameterization and the two solid curves indicate the cuts applied. (b) The sampling fraction $E/p$ projections for different slices in electron momentum $p$ for Sector 4. (c) Mean and (d) $\sigma$ of the sampling fraction for different momentum slices with associated fits (black curves).**

for one of the CLAS sectors. In the figure, one can note the MIPs contamination near the smaller values of $E/p$. The "good" electrons are mostly concentrated around $E/p \approx 0.3$. Ideally, the "good" electrons should not show any dependence on momentum, but in reality there is a slight momentum dependence.

So, to isolate these electrons we plot the sampling fraction for different momentum slices and fit with a Gaussian and a constant (Fig. 3.2(b)). The mean positions and resolutions from this fit are in turn fit as a function of momentum using the following parameterizations [35]:

$$\begin{aligned} \mu(p) &= \alpha + \frac{\beta}{p^{\gamma}} + \delta p \\ \sigma(p) &= \alpha + \frac{\beta}{p^{1/2}}. \end{aligned} \tag{3.1}$$

Here, $\alpha$, $\beta$, $\gamma$ and $\delta$ are parameters of the fit and $\mu(p)$ and $\sigma(p)$ are the mean and resolution of the $E/p$ distribution as a function of momentum. The results of these fits are shown in Figs. 3.2(c) and 3.2(d) for one of the CLAS sectors. Using these parameters we select electrons with $3\sigma < (E/p - \mu(p))$. Since the $\pi^-$s are below the electrons we only apply a cut to reject events from the bottom. Please refer to Appendix A.1 for a complete list of all parameters and cuts for all sectors.

### 3.2.2 Proton

A good proton candidate has the following characteristics:

- it is positively charged,
- it has good geometrical hit status, and
- it has a hit in the TOF system.

Using this as a start, we select a particle to be a proton whose measured time is closest to the time we expect for a real proton, *i.e.*,

$$\Delta t = t_{measured} - t_{calculated} = t_{SC} - \left( t_{tr} + \frac{l}{\beta_{calc} c} \right). \tag{3.2}$$

In the above equation, $t_{SC}$ is the time measured from the TOF counters after correction (see Section 3.4.2), $l$ is the distance from the target center to the TOF paddle of hit, and $t_{tr}$ is the event start time calculated from the RF corrected electron time from the TOF measurement:

$$t_{tr} = t_e - \frac{l_e + (z_e - z_0)}{c}. \tag{3.3}$$

Here, $l_e$ is the path length of the electron track from its vertex, $z_e$, to its TOF hit and $z_0 = -4$ cm is the position of the center of the target in the $z$-axis for the experiment. Also, in Eq. 3.2

$$\beta_{calc} = \frac{p}{\sqrt{M_{pdg}^2 + p^2}}. \tag{3.4}$$

Here $\beta_{calc}$ is computed using the PDG [36] value of the mass of the proton $M_{pdg}$ and the momentum of the particle $p$. Fig. 3.3(a) shows the measured $\beta$ of all proton candidates as a function of momentum for one of the sectors in CLAS.

We look at the $\Delta t$ as a function of momentum slices (Fig. 3.3(b)). These distributions are fit with a Gaussian and first degree polynomial. The resulting mean positions

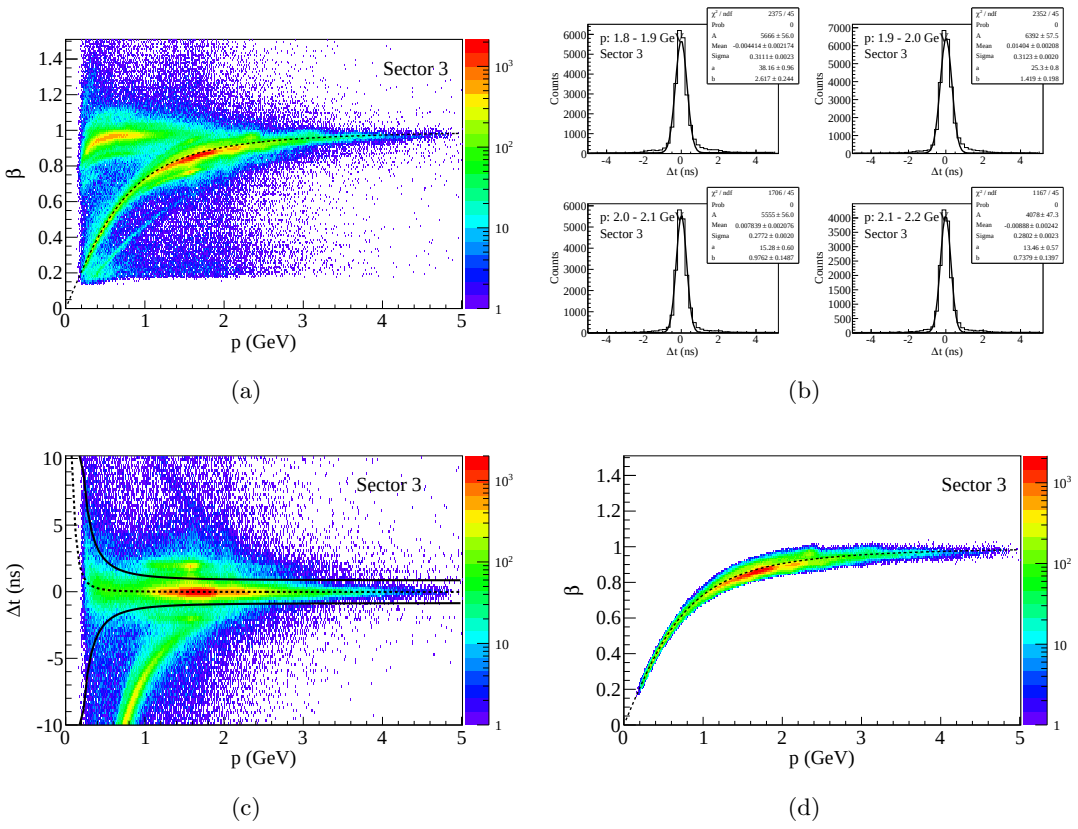


**Figure 3.3: (a) Measured $\beta$ as a function of $p$ for all possible proton candidates for sector 3. The dashed curve is the expected theoretical proton profile. (b) $\Delta t$ projections for selected $p$ slices for sector 3 fitted with a Gaussian and a first order polynomial. (c) $\Delta t$ as a function of $p$ with curves of fit showing $\pm 3.5\sigma$ cut (solid lines) from the mean fit (dashed line). (d) The measured $\beta$ as a function of $p$ after proton selection for sector 3. The dashed curve is the expected theoretical proton profile.**

and resolutions are fit as a function of momentum using the following parameterization:

$$\Delta t(p) = a + \frac{b}{p^c}. \tag{3.5}$$

Here, $p$ is the momentum of the proton candidates and $a$, $b$ and $c$ are the parameters of the fit. Next we made a $\pm 3.5\sigma$ cut on the above parameterization and obtained our protons as shown in Fig. 3.3(c). We select the proton that has the minimum time difference with the mean parameterization of the distributions. If no particles satisfy either of the above conditions then the event is rejected. Fig. 3.3(d) shows the measured $\beta$ distributions as a function of momentum after proton selection. Please refer to Appendix A.2 for parameters of the fits used in the selection and distributions for all sectors.

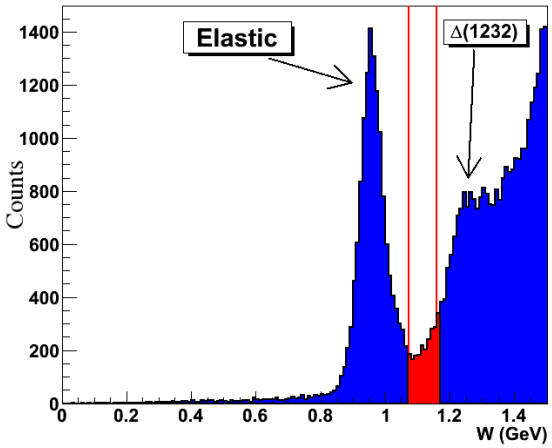


**Figure 3.4: The invariant mass, $W$, for $ep \to eX$ reaction showing the kinematic region of interest (red) flanked by the elastic and $\Delta(1232)$ resonance channels.**

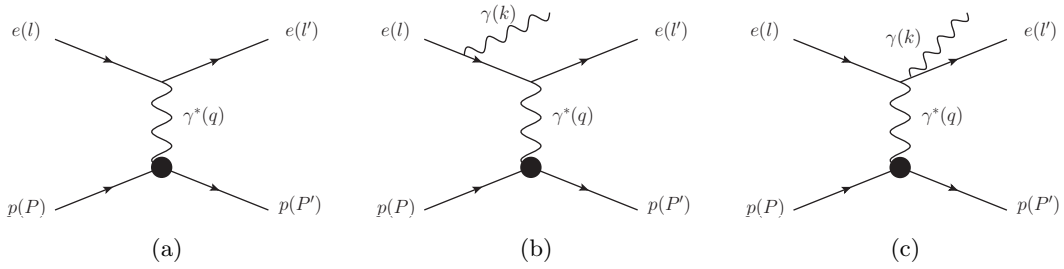


**Figure 3.5: (a) Elastic process $ep \to ep$. (b) Pre-radiative and (c) Post-radiative Bethe-Heitler process $ep \to ep\gamma$.**

## 3.3 Elastic Event Selection

In this section, we take a look at the elastic scattering process $ep \to ep$ and its associated radiative process $ep \to ep\gamma$. The elastic process is very close to our kinematic region of interest as shown in Fig. 3.4. This plot shows the invariant mass distribution, $W$, for the inclusive process $ep \to eX$ where only the electron is detected in the final state. The invariant mass distribution then shows us the two primary nucleon resonance regions for the electron-proton scattering, *viz.*, elastic ($ep$) and $\Delta(1232)$ ($ep\pi^0$) with the near threshold region sandwiched in between.

Fig. 3.5(a) shows the Feynman diagram of the elastic scattering process ($ep \to ep$) and Figs. 3.5(b) and 3.5(c) show the Feynman diagrams for the pre- and post-radiative elastic Bethe-Heitler processes ($ep \to ep\gamma$). These two diagrams give the highest order contributions to the radiative cross section amplitude. This radiative process is also the

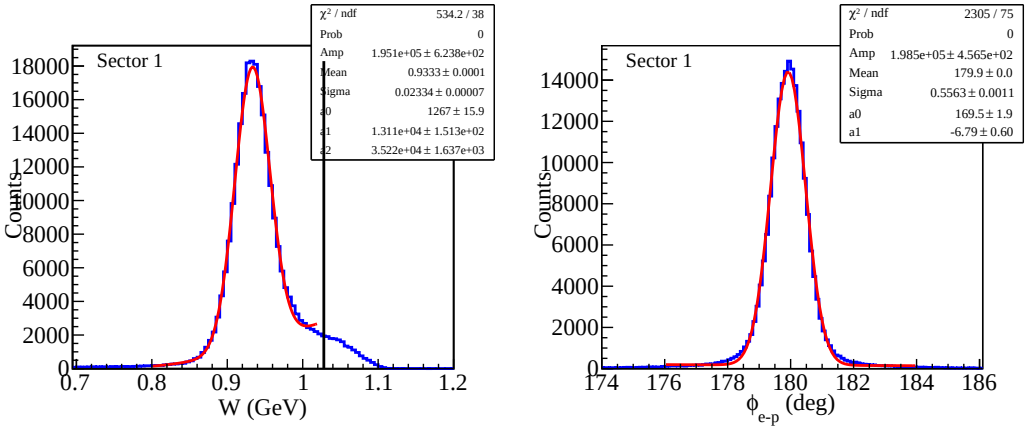


**Figure 3.6: Kinematic cuts applied to select elastic events from sector 1: (Left)** $(W - M_p) < 3.5\sigma$ **and (Right)** $|\phi_{e-p} - 180°| < 3\sigma$**.**

source of highest contamination for all electron scattering reactions, especially for near threshold pion production. The Bethe-Heitler contamination subtraction is discussed in Section 3.6 for this analysis.

To select elastic events, we select the electrons and protons as described in Sections 3.2.1 and 3.2.2 and we apply some cuts and constraints (Fig. 3.6):

1. $(W - M_p) < 3.5\sigma$ GeV
2. $|\phi_{e-p} - 180°| < 3\sigma$

The first cut on $W$ is used to select all events with $3.5\sigma$ from the expected elastic peak position. For the elastic process, the scattered electron and the recoiled proton are expected to be antiparallel (180°) in the azimuthal direction. This provides us with another constraint to select elastic events; we select events within $3\sigma$ of the azimuthal angular difference between the electron and proton.

This constitutes our elastic event selection. These events will be used for making kinematic and acceptance corrections in the following sections. Additionally, we will use the same events for normalization studies in later chapters.

## 3.4 Kinematic Corrections

Even though the subsystems of CLAS detector have been calibrated certain reconstructed kinematic quantities still have to be corrected to match up with expectations. For example, we expect our detected particles to conserve 4-momentum in the appropriate kinematic regime. In the following paragraphs we will describe

- vertex corrections for electrons and protons,
- time of flight corrections for protons,
- angle corrections for electrons and protons, and
- momentum corrections for electrons.

### 3.4.1 Vertex

For an ideal experiment, one would expect the incident electron beam to be centered at $(v_x, v_y) = (0, 0)$ cm at the target position. But due to misalignment the electron beam was found to be at $(0.090, -0.345)$ cm as shown in Fig. 3.7(a) [37]. The vertex position

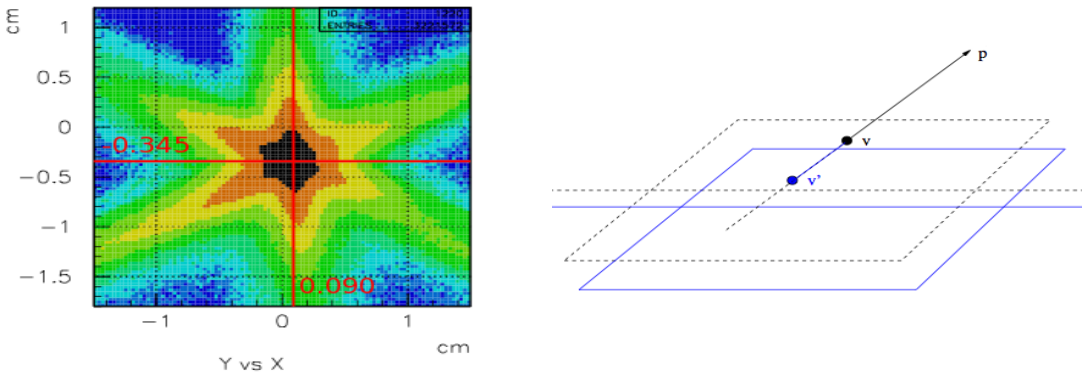


(a) (b)

**Figure 3.7: (a) The $y$ versus $x$ position of the vertex at the target window. The beam spot is centered at $(0.090, -0.345)$ cm. (b) The uncorrected vertex position $\vec{v}$ of the track with momentum $\vec{p}$ is contained within the original midplane (dashed). The corrected vertex position $\vec{v}'$ is obtained by intersecting the track with the midplane containing the measured beamline $(0.090, -0.345, z)$ cm (solid blue).**

of each track has to be corrected to reflect this deviation. The new vertex position was calculated by intersecting the track of particles with the midplane of a sector.

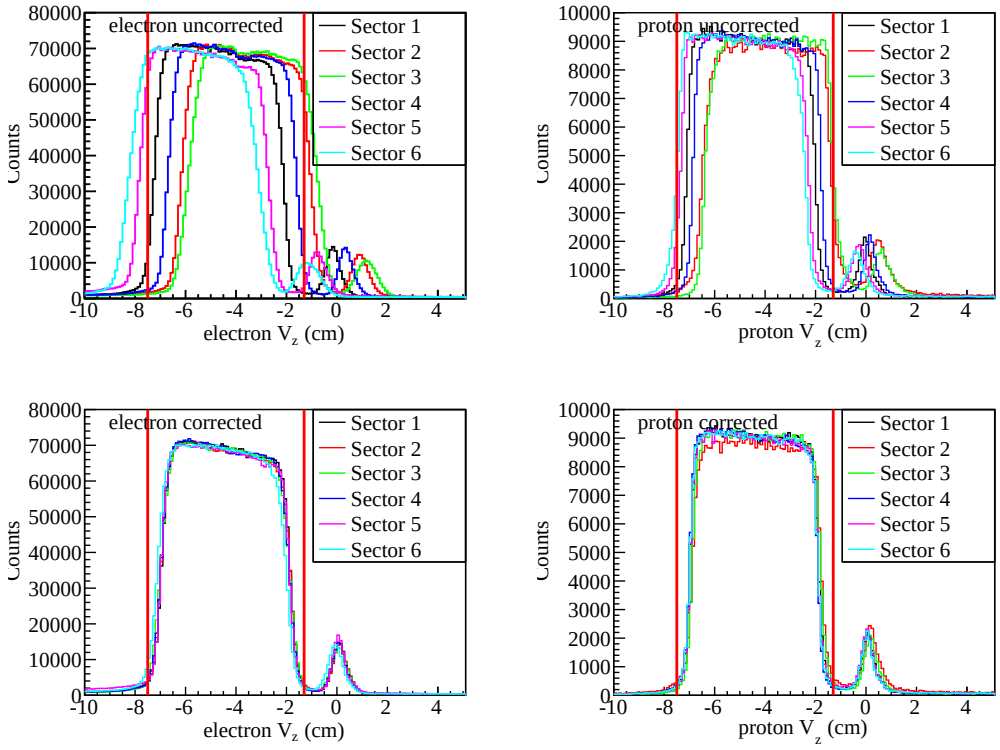


**Figure 3.8: Top: Vertex positions ($v_z$) for electrons (left) and protons (right) for 6 sectors before vertex correction. Bottom: Vertex positions for same after vertex corrections. Red lines indicate the cuts applied after corrections.**

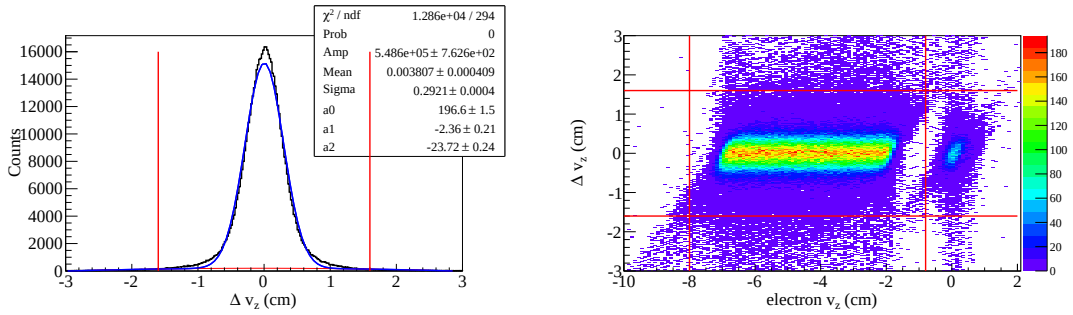


(a) (b)

**Figure 3.9: (a) Electron and proton z-vertex difference ($\Delta v_z$) distribution fitted with Gaussian and a polynomial of second order. Red lines indicate the $5.5\sigma$ cut applied. (b) Electron and proton z-vertex difference as a function of electron z-vertex after corrections. Red lines indicate the cuts applied.**

The midplane of a sector is a plane that divides the sector in half with the beamline at $(0, 0, z)$. The vertex positions are shifted appropriately such that the midplanes contain the measured beamline as shown in Fig. 3.7(b). The definitions of the original and new midplanes are determined and the vertex is corrected by intersecting the track of the particle of momentum $\mathbf{p}$ with these midplanes:

$$\mathbf{v}' = \mathbf{v} + \boldsymbol{\Delta}\mathbf{v}(\mathbf{p}). \tag{3.6}$$

Here $\mathbf{v}'$ is the corrected vertex position 3-vector, $\mathbf{v}$ is the uncorrected vertex position 3-vector, and $\Delta\mathbf{v}(\mathbf{p})$ is the correction factor that depends on the momentum of the track.

Fig. 3.8 shows the result of the correction on electrons and protons for each sector in CLAS. To select events inside the target cell we introduce a cut on the z-vertex of electrons and protons:

$$v_z \in (-8.0, -0.8)\,\text{cm}. \tag{3.7}$$

Additionally, we make a cut on the z-vertex difference between the electrons and protons to ensure event coincidence.

$$|\Delta v_z| < 1.6\,\text{cm}. \tag{3.8}$$

This is a $5.5\sigma$ cut based upon a Gaussian and polynomial fit on the z-vertex difference distribution as shown in Fig. 3.9(a).

### 3.4.2 Proton Timing

For the kinematics of the process in consideration it is found that some of the TOF paddles require corrections to properly identify a proton. For the possible proton candidates we observe that some of the paddles do not have $\Delta t$ (Eq. 3.2) centered around 0 ns as shown for one of the paddles for Sector 6 in Fig. 3.10(b).

To correct this we project each of these distributions onto the Y-axis and fit it using a Gaussian and a constant. The mean position of this peak is used as an offset to the measured TOF to obtain corrected time:

$$t_{corrected} = t_{measured} - t_{offset}. \tag{3.9}$$

To see the effect of this correction, we look at the mean position of the $\Delta t$ for different $p$ slices and the corresponding resolutions as functions of the particle's momenta

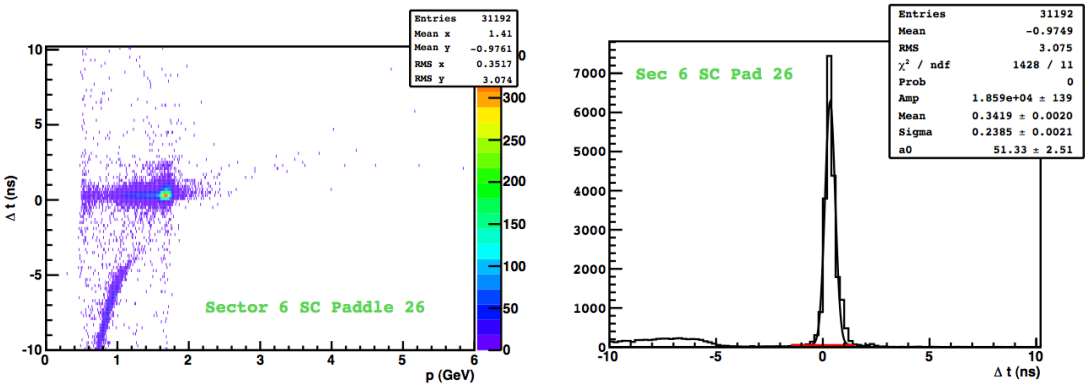


(a) (b)

**Figure 3.10: (a) $\Delta t$ of proton candidates as a function of $p$ for TOF paddle 26 in sector 6. (b) Projection of (a) on the Y-axis. This distribution has been fitted with a Gaussian and a constant. The events in both plots at $\Delta t < -5$ ns are from $\pi^+$ and are not included in the correction and proton identification process. Note the shift in the proton peak from the expected value of 0 ns.**

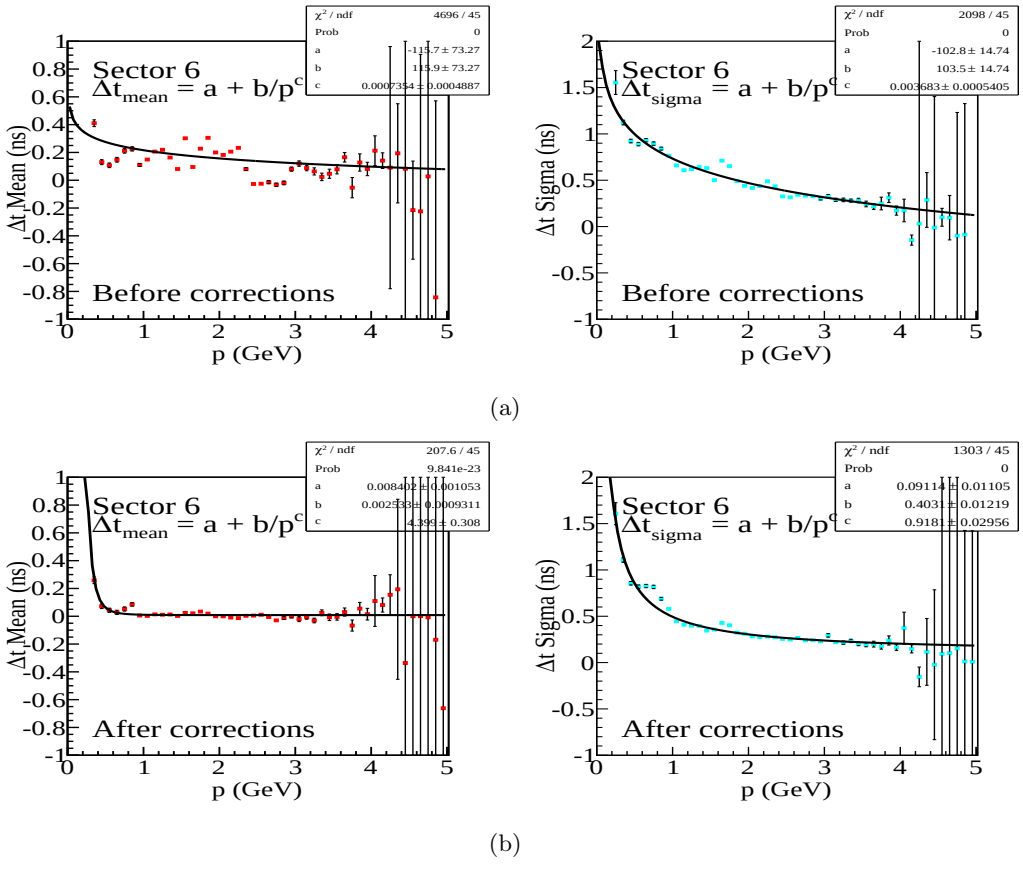


(a)

(b)

**Figure 3.11: (a) The mean and $\sigma$ of $\Delta t$ as functions of particle momenta for proton candidates in sector 6 for all TOF paddles before TOF corrections. (b) The same distributions after TOF corrections.**

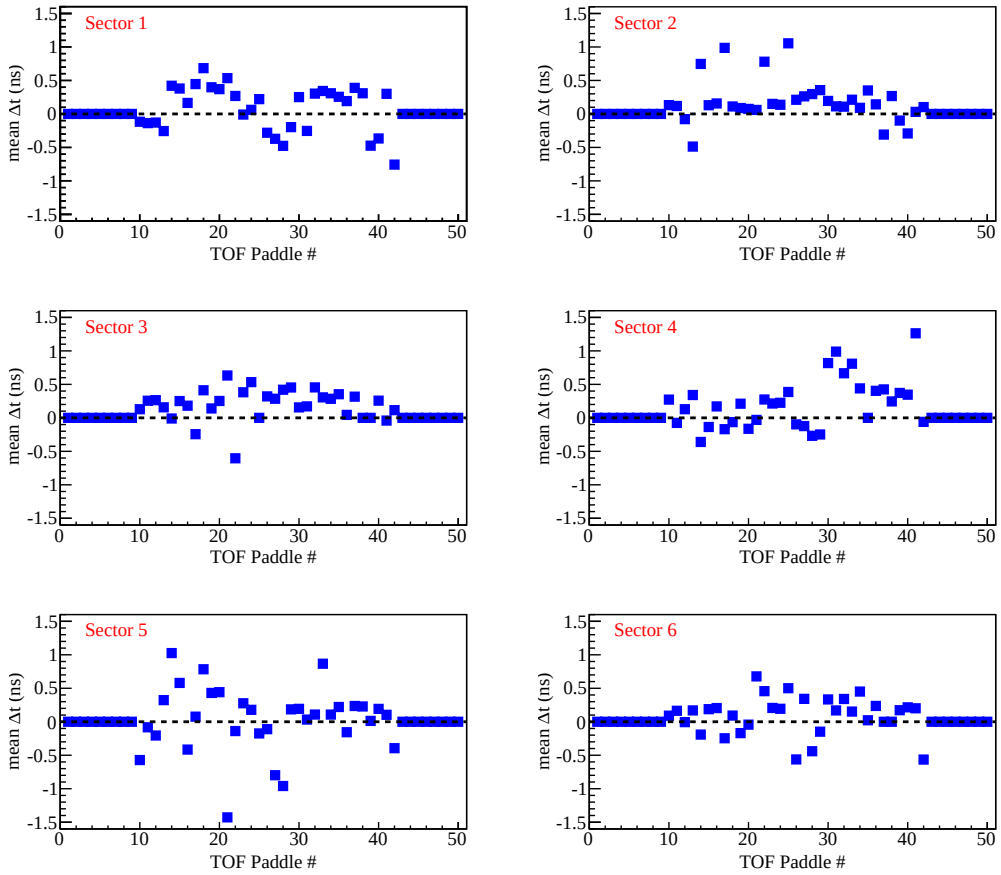


**Figure 3.12: The mean position of the fits to the $\Delta t$ distributions for each TOF paddle for each sector. Because of limited statistics offsets for some TOF paddles are not computed. The mean values for each paddle are used as offsets to the measured time for proton candidates.**

(Fig. 3.11(a)). These distributions have been fit using the parameterization from Eq. 3.5. One can observe that the distributions show fluctuations as functions of momenta. After the corrections have been applied the fluctuations are minimized (Fig. 3.11(b)). For the effect of corrections on all sectors, please see Appendix A.4. The offsets are obtained for all TOF paddles for each sector as shown in Fig. 3.12.

### 3.4.3 Electron and Proton Angle

The measured polar angles for the electron and proton in the lab frame, $\theta_e$ and $\theta_p$, should be independent of the azimuthal angle, $\phi_e$ and $\phi_p$. However, due to misalignments of the drift chambers in CLAS a dependence on the azimuthal angle is observed for these kinematic variables. To study this dependence we look at events from elastic scattering reaction, *i.e.*, $ep \to ep$.

For elastic scattering, the electron and proton polar angles are theoretically correlated via the incident electron beam energy, $E$:

$$E_{calc} = \frac{M_p}{\tan(\theta_e/2)\tan(\theta_p)} - M_p. \tag{3.10}$$

Fig. 3.13(a) shows this correlation for several incident electron beam energies. The red curve shows the correlation for the nominal beam energy for the $e$1-6a experiment, $E =$ 5.754 GeV.

This beam energy can be computed from the measured angles of the electron and proton for each event. We can then look at the deviation of this calculated energy, $\Delta E$, from the nominal, $E_{nom}$:

$$\Delta E = E_{nom} - E_{calc} \tag{3.11}$$

and obtain a correction to apply to the angles. For a given measurement of $\theta_e$ and $\theta_p$, we can find the minimum distance to the theoretical curve as shown in Fig. 3.13(b). The corresponding deviations, $\Delta\theta_e$ and $\Delta\theta_p$, for electron and proton angles, respectively, can thus be obtained and be used as corrections.

The correction, $\Delta\theta$, is parameterized as a function of $\theta$ and $\phi$ [38]:

$$\Delta\theta = \sum_{i=0}^{4} a_i(\theta)\phi^i \tag{3.12}$$

where $a_i(\theta)$ are polynomials of second order in $\theta$. These parameterizations are obtained for each CLAS sector and applied to the electron. Fig. 3.14 shows the effect of this correction on $\Delta E$ as a function of $\phi$ for one of the CLAS sectors. One can observe that the $\phi$ dependence is suppressed after corrections. Please refer to Appendix A.5 for a full list of parameters and result of the corrections on other sectors.

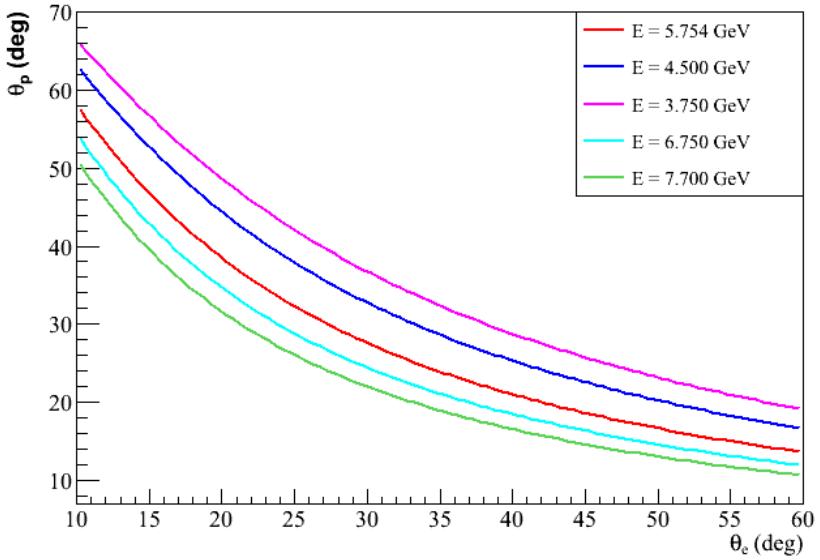


(a)

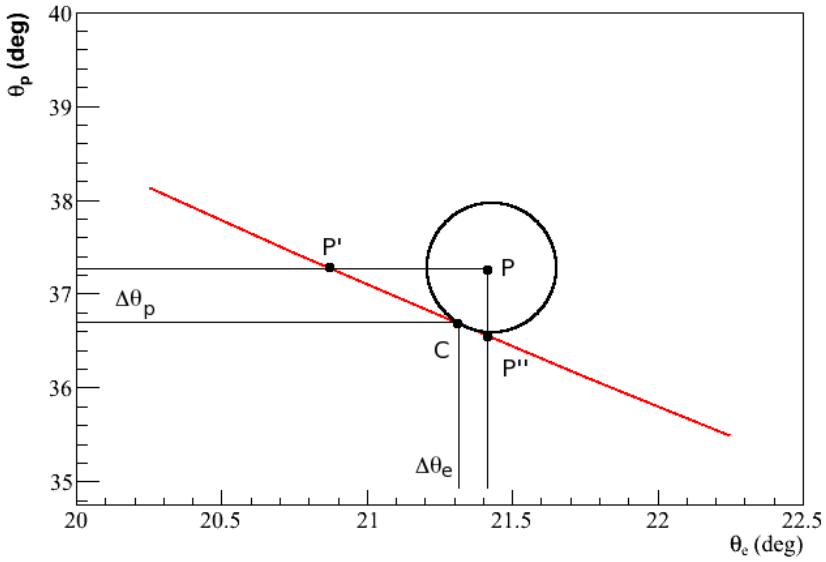


(b)

**Figure 3.13: (a) Theoretical correlation between the electron and proton polar angles for different values of incident electron beam energy, $E$. The nominal beam energy from $e$1-6a experiment is shown as a red curve. (b) The angle correction algorithm. The circle with center $P$ shows the measured $\theta_e$ and $\theta_p$ and $C$ is the point on the theoretical curve that is closest to $P$. $C$ is found by minimizing the radius of the circle that intersects the theoretical curve.**

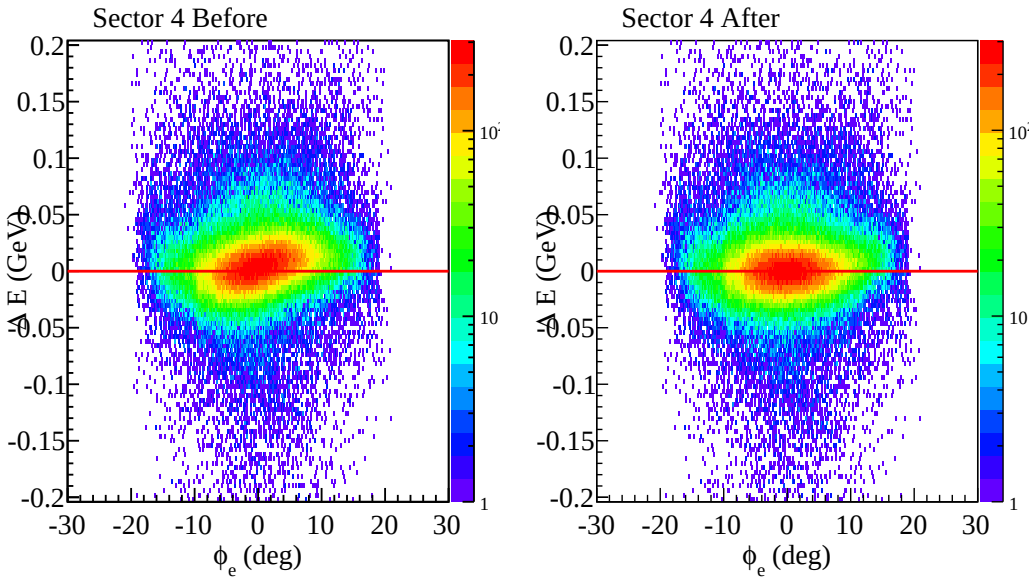


**Figure 3.14: The deviation of the calculated beam energy from the nominal value, $\Delta E$, as a function of $\phi_e$ for sector 4 before (left) and after (right) the electron $\theta_e$ corrections. Red line serves as a visual guide.**

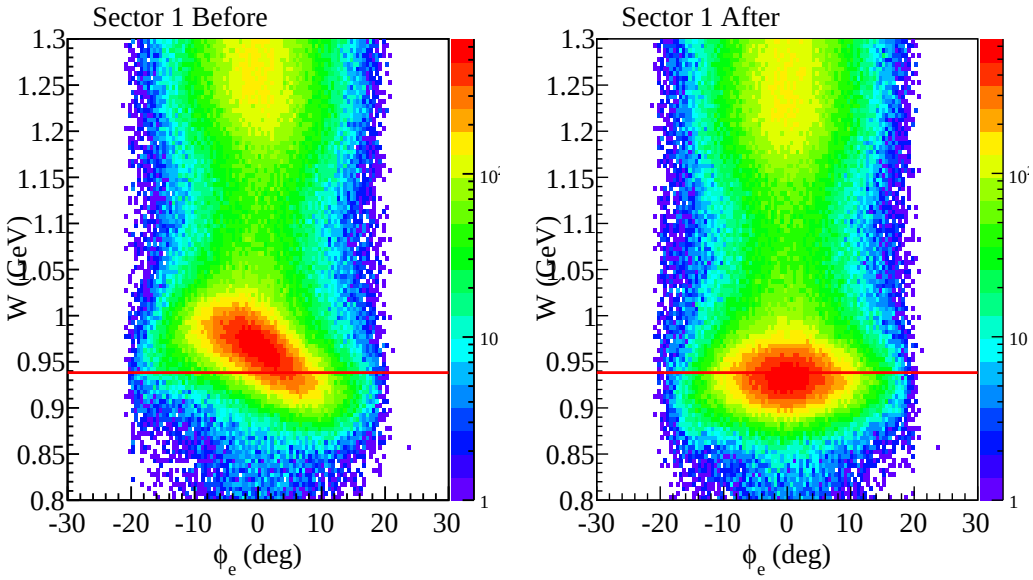


**Figure 3.15: $W$ vs $\phi_e$ distribution for sector 1 before (left) and after (right) electron momentum corrections. Red line indicates the expected elastic scattering peak position ($M_p$). Both plots show values after electron and proton angle corrections.**

### 3.4.4 Electron Momentum

For our reaction, $ep \to ep\pi^0$, the electron's kinematics are very close to those of the elastic scattering. As such, electrons have very high momenta depending on $Q^2$; any misalignments in the drift chambers and inaccurate values in the magnetic field maps result in its poor reconstruction. This is reflected in calculated values such as $W$ and missing mass. Fig. 3.15 (left) shows the deviation of the elastic scattering peak from its nominal position, *i.e.*, the mass of the proton, $M_p$, for one of the CLAS sectors.

This dependence can be corrected via the following prescription [39]:

$$\begin{aligned} \Delta p &= p_{meas} - p_{calc} \\ &= p_{meas} - \frac{E}{1 + E(1 - \cos\theta_e)/M_p}. \end{aligned} \tag{3.13}$$

Here, $p_{meas}$ is the measured momentum of the electron in CLAS, $E$ is the beam energy for the experiment, $M_p$ is the PDG mass of the proton, and $\theta_e$ is the polar angle of the electron after angle corrections have been applied. This $\Delta p$ is parameterized as a function of $\theta_e$ and $\phi_e$ [38]:

$$\Delta p = \sum_{i=0}^{3} a_i(\theta_e)\phi_e^i, \tag{3.14}$$

where $a_i(\theta_e)$ are polynomials of second order in $\theta_e$. These parameters are sector dependent. The effect of this correction is shown in Fig. 3.15 for one of the CLAS sectors where we see that the elastic peak's azimuthal dependence, $\phi_e$, is suppressed. Please refer to Appendix A.6 for a full list of parameters and result of the correction on other sectors.

## 3.5 Fiducial Cuts

There are regions in our detectors where we find dead wires, inefficient PMTs, detector edges, and regions where there are large variations in acceptance. In such regions we don't fully understand the geometrical acceptance of event reconstruction and consider the information as unreliable. These regions are isolated and those events reconstructed within are discarded. These cuts are known as fiducial cuts. In the following paragraphs we look at the fiducial cuts applied to the electrons and protons in the

- Electromagnetic Calorimeter
- Cerenkov Counters, and
- Drift Chambers.

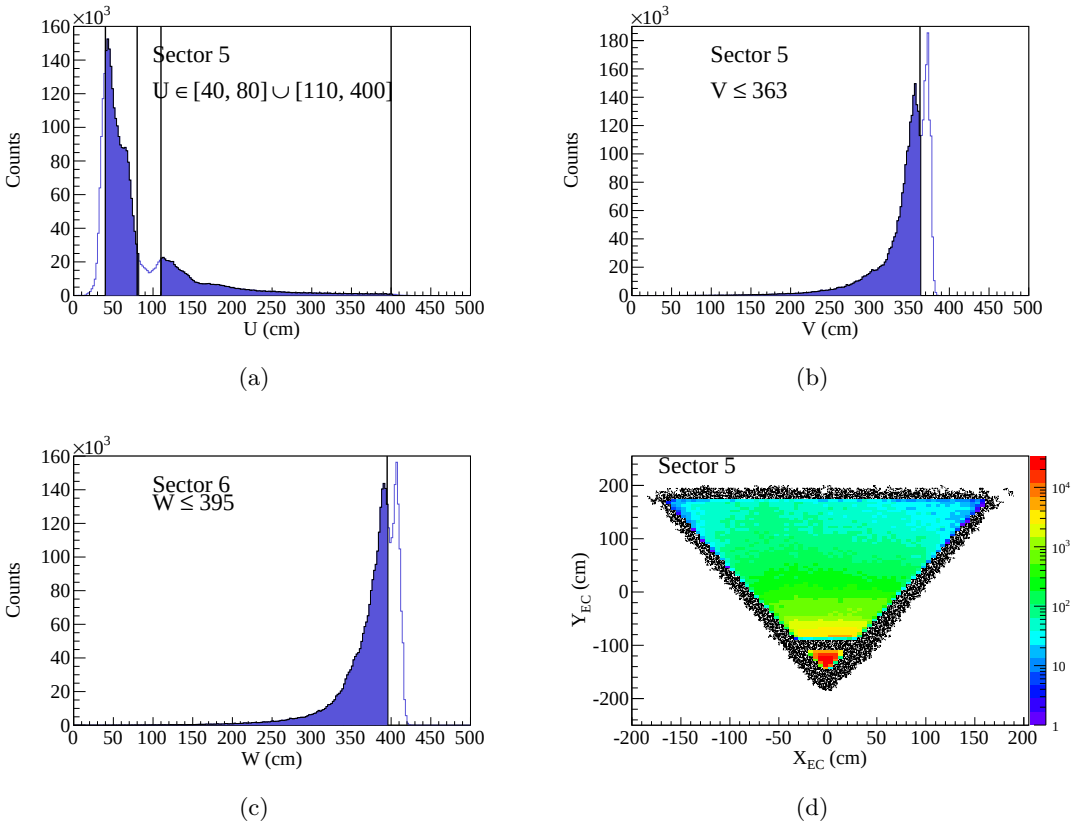


**Figure 3.16: (a)-(c) EC $U$, $V$ and $W$ coordinate distribution of hits for sector 5; shaded region indicates events retained after fiducial cuts (black lines). (d) The distribution of hits projected on the EC plane for sector 5. Black points indicate rejected events from applied fiducial cuts.**

### 3.5.1 Electromagnetic Calorimeter

The electrons start losing energy as they enter the calorimeter. The EC has been designed such that the electrons release all their energies in it. When the electrons shower near the edge of the calorimeter their shower is not fully contained and so their energies cannot be properly reconstructed. As such, we apply a fiducial cut on the track coordinates $U$, $V$ and $W$ of the electrons on the EC plane. These coordinates reflect the three orientations of the scintillator strips as discussed in Section 2.10. Please see Appendix B for transformation from CLAS coordinates to EC plane coordinates $(X_{EC}, Y_{EC}, Z_{EC})$ and $(U, V, W)$.

The cuts are selected to remove those tracks detected at the edge of the calorimeter. They are also selected to ensure azimuthal symmetry of the overall distribution of the tracks on the EC plane. The following cuts are made universally for all sectors to select

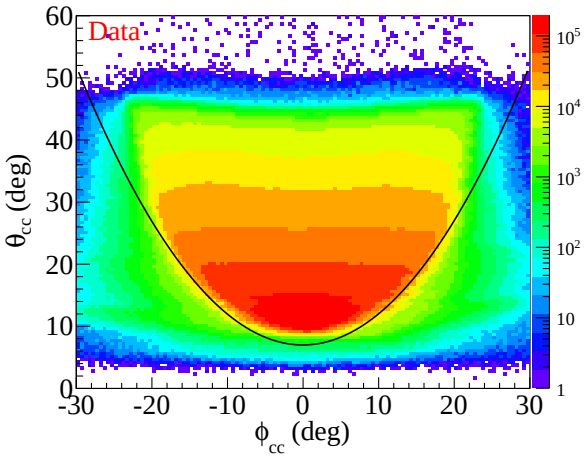


**Figure 3.17: The distribution of all hits in CC plane coordinates $\theta_{cc}$ and $\phi_{cc}$ integrated over all sectors. Black curve indicates a naive cut applied to remove the tracks entering the PMTs directly.**

the electron tracks:

$$\begin{aligned} 40 < U < 400\,\text{cm} \\ V \leq 363\,\text{cm} \\ W \leq 395\,\text{cm}. \end{aligned} \tag{3.15}$$

Additionally, we also remove a "bad" scintillator strip in $80 < U < 110$ cm for Sector 5 as shown in Fig. 3.16(a). The result of these cuts is shown in Fig. 3.16(d).

### 3.5.2 Cerenkov Counter

For the Cerenkov counters there is a similar problem to that of EC. Electrons give off Cerenkov light in CC which is collected in the PMTs on either side of the counters in each sector (Section 2.8). Sometimes, electrons hit the PMTs directly and their light is absorbed along with others coming in after bouncing from the mirrors. Here we have plotted the detected electron hits in "special-coordinates." These angle coordinates are measured from the center of CLAS and correspond to the intersection of the charged track with the CC plane given by [40]:

$$1 - 0.000784x - 0.00168z = 0. \tag{3.16}$$

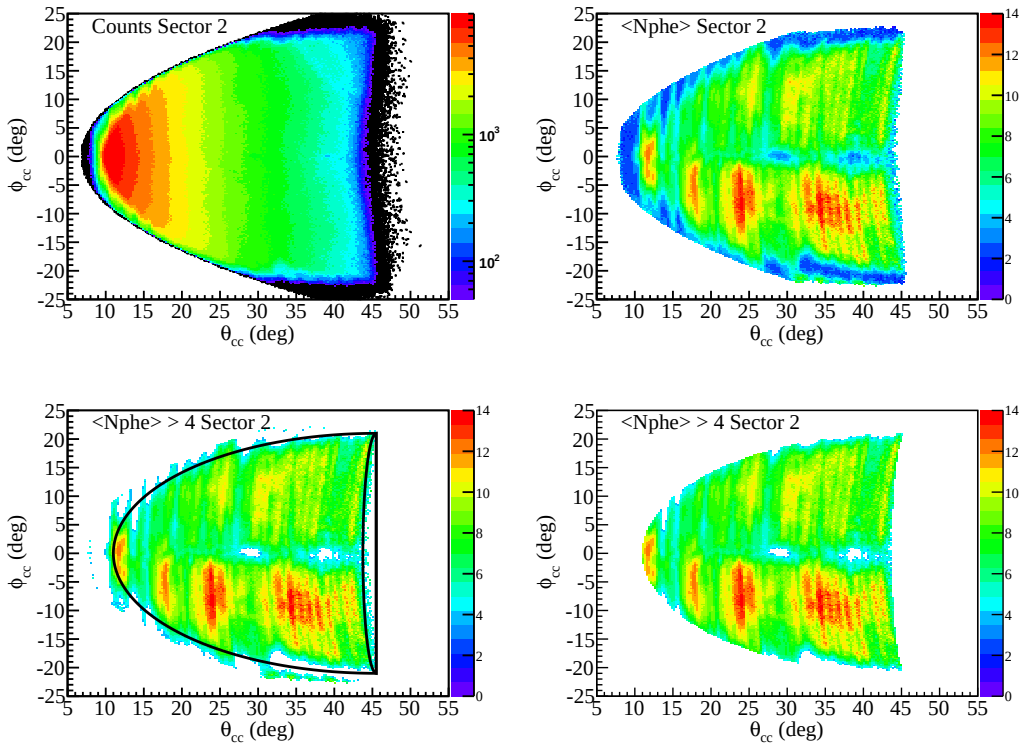


**Figure 3.18: (Top-Left) Sector 2 distribution of events on the CC plane with $z$-axis showing the number of charged tracks $N$ for each $\theta_{cc}$ and $\phi_{cc}$ bin. The black points indicate rejected bins with $N \leq 50$. (Top-Right) Sector 2 distribution of average number of photoelectrons $\langle Nphe \rangle$ for each bin. (Bottom-Left) Sector 2 distribution of $\langle Nphe \rangle > 4$ for each bin. Black curves are cuts applied to reject bins in the fringe of CC. (Bottom-Right) Sector 2 distribution of $\langle Nphe \rangle > 4$ after fringe cuts applied.**

We can put a naive cut on this distribution to remove the edges as shown in Fig. 3.17:

$$\theta_{cc} > 7.0 + 0.0032\phi_{cc} + 0.0499\phi_{cc}^2. \tag{3.17}$$

However, we still have a problem of dealing with inefficient bins on the CC plane.

Let's take a look at the average number of photoelectrons for each $\theta_{cc}$ and $\phi_{cc}$ bin (200x200 bins)

$$\langle Nphe \rangle = \frac{\sum_{i=1}^{N} nphe_i}{N}. \tag{3.18}$$

Here, $nphe_i$ is the number of photoelectrons for each event $i$ and $N$ is the total number of events (counts) for each bin. We want to look at those bins where we at least have 50

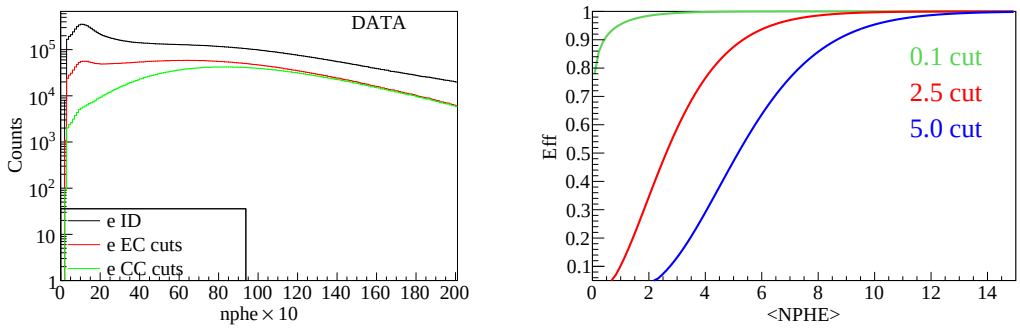


(a) (b)

**Figure 3.19: (a) Number of photoelectrons ($nphe \times 10$) after applying electron selection (black), after EC fiducial cuts (red) and after CC cuts (green) integrated over all sectors. (b) The efficiency of each $\theta_{CC}$ and $\phi_{CC}$ as a function of the $\langle Nphe \rangle$ for $nphe > 0.1$ (green), $nphe > 2.5$ (red), and $nphe > 5$ (blue).**

events so that we have good statistics to work with (Fig. 3.18 Top-Left).

This $\langle Nphe \rangle$ distribution is plotted for one of the sectors in CLAS (Sector 2) as shown in Fig. 3.18 (Top-Right). One expects this distribution to be uniform for all bins. But over time some PMTs lose their efficiency; these are seen as dark blue regions in the plot. This non-uniformity arises due to variations of the 36 mirrors in each sector, *viz.*, small optical misalignments, their overlap with each other and their shapes. We can make a cut

$$\langle Nphe \rangle > 4 \tag{3.19}$$

to remove those inefficient bins (Fig. 3.18 Bottom-Left). But, we still have some problems with the edges where we see some fringes where our acceptance isn't understood well. So, we apply a set of cuts to exclude the edges:

$$\begin{aligned} \left(\frac{\theta - 45.5^\circ}{34.5^\circ}\right)^2 + \left(\frac{\phi}{21^\circ}\right)^2 &\leq 1, \\ \left(\frac{\theta - 45.5^\circ}{1.75^\circ}\right)^2 + \left(\frac{\phi}{21^\circ}\right)^2 &> 1. \end{aligned} \tag{3.20}$$

So, we now have a 200x200 bin map of $\langle Nphe \rangle$ for each bin. We create similar maps for all six sectors and setup a look-up table for each bin. Using this table events can be selected that have $\langle Nphe \rangle > 4$ for the corresponding $\theta_{cc}$ and $\phi_{cc}$ bin[41].

Typically, a cut on the number of photoelectrons is applied $nphe > 2.5$ to eliminate the $\pi^-$ contamination. But after we apply our CC cuts, including both $\langle Nphe \rangle > 4$ and

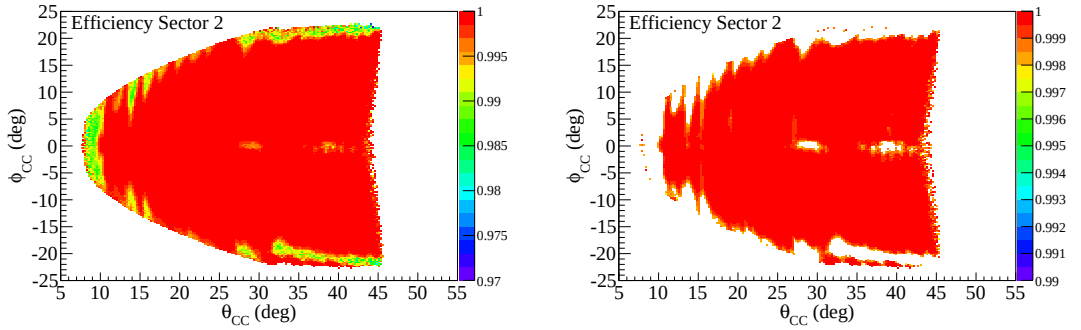


(a) (b)

**Figure 3.20: The efficiency of CC at each $\phi_{CC}$ and $\theta_{CC}$ bin (a) before any $\langle Nphe \rangle$ cuts and (b) after $\langle Nphe \rangle > 4$ cuts for sector 2 in CLAS.**

Eq. 3.20, this cut on *nphe* is no longer necessary (Fig. 3.19(a)). However, we still need to account for the inefficiency of the Cerenkov counters.

The *nphe* distribution for any $\theta_{CC}$ and $\phi_{CC}$ bin can be represented as a Poisson distribution. So, one can theoretically determine the efficiency of each bin by

$$Eff = \frac{\int_{x_0}^{\infty} P(x,\nu)dx}{\int_{0}^{\infty} P(x,\nu)dx} \tag{3.21}$$

where $P(x,\nu)$ is a Poisson distribution with the $\nu$ being the $\langle nphe \rangle$ and $x_0$ is cut on the *nphe* that is typically made in analysis, *e.g.*, $nphe > 2.5$. In this analysis, an inherent cut of $nphe > 0.1$ is present from hardware restrictions. Fig. 3.19(b) shows the computed efficiency based on this prescription as a function of $\langle Nphe \rangle$ for three different cuts on *nphe* distributions in analysis. As seen, if one has a cut on $nphe > 0.1$ and $\langle nphe \rangle > 4$, then the efficiency for each bin is about 99%. For a cut of $nphe > 2.5$ the efficiency is $\sim 80\%$.

Fig. 3.20(a) shows the efficiency for each $\theta_{CC}$ and $\phi_{CC}$ bin before any $\langle Nphe \rangle$ cuts are applied. One can see regions on the CC plane where the efficiency is less than the neighboring regions. These regions are removed after the cut on $\langle Nphe \rangle > 4$ is made as shown in Fig. 3.20(b).

### 3.5.3 Drift Chambers

To deal with edges, holes in drift chambers, and to remove dead or inefficient wires, a fiducial cut for both electrons and protons is applied [39].

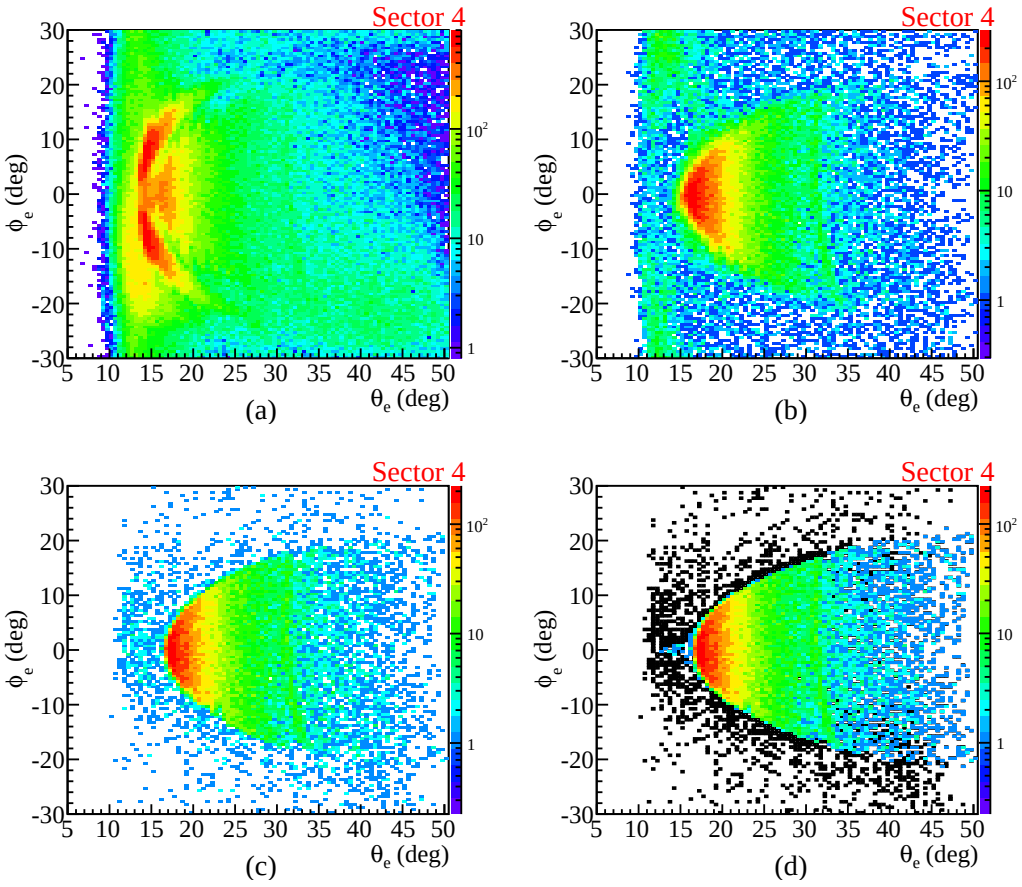


**Figure 3.21: Electron $\phi_e$ vs $\theta_e$ distribution for sector 4 integrated over $p_e$ (a) after electron selection, (b) after EC fiducial cuts, (c) after CC fiducial cuts, and (d) before and after DC fiducial cuts. Rejected tracks are shown in black.**

#### 3.5.3.1 Electrons

For each sector, we set up an empirical cut on electron's azimuthal angle $\phi$ as a function of electron momentum $p$ and polar angle $\theta$:

$$|\phi| \leq \Delta\phi(\theta, p). \tag{3.22}$$

The following fiducial cut parameterization was chosen to exploit the symmetry in $\phi$:

$$\Delta\phi = \alpha \left[ \sin\left(\theta - \left(\beta + \frac{\gamma}{p+\rho}\right)\right)\right]^{\kappa p^{\xi}}. \tag{3.23}$$

Here, $\alpha$, $\beta$, $\gamma$, $\rho$, $\kappa$ and $\xi$ are parameters of the cut. Please see Appendix A.3.1 for a full list of these parameters and their corresponding values for each sector.

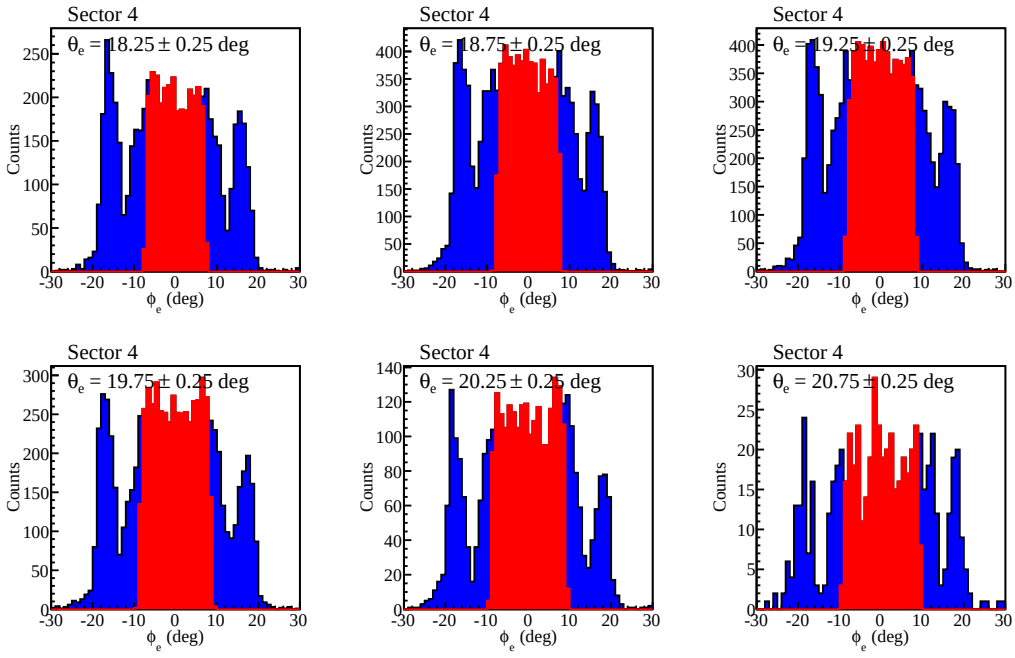


**Figure 3.22: Electron sector 4 $\phi_e$ distribution for $p_e = 4.1 \pm 0.1$ GeV shown for different $\theta_e$ slices. Blue curves show $\phi_e$ distribution after electron selection and red curves show $\phi_e$ distribution after applying electron DC fiducial cuts.**

Fig. 3.21 shows the $\phi$ versus $\theta$ distribution of electrons before and after the application of the fiducial cut for one of the CLAS sectors. This distribution is shown for all electrons within the kinematic region of interest, *i.e.*, $W \in (W_{th}, 1.16)$ GeV and is integrated over all $p$. Fig. 3.22 shows the $\phi$ distributions for electrons with $p = 4.1 \pm 0.1$ GeV for different slices of $\theta$. One can observe that these fiducial cuts keep those regions of $\phi$ that are uniform.

#### 3.5.3.2 Protons

As for electrons, we apply a fiducial on the proton's azimuthal angle $\phi$ as a function of its momentum $p$ and polar angle $\theta$. However, the edges of $\phi$ distributions are asymmetric for different slices of $\theta$. So, we parameterize this $\phi$ distribution for the protons using a trapezoidal function for each $\theta$ and $p$ slice as shown in Fig. 3.23(a).

From this parameterization we extract the upper and lower bound on the $\phi$ for the

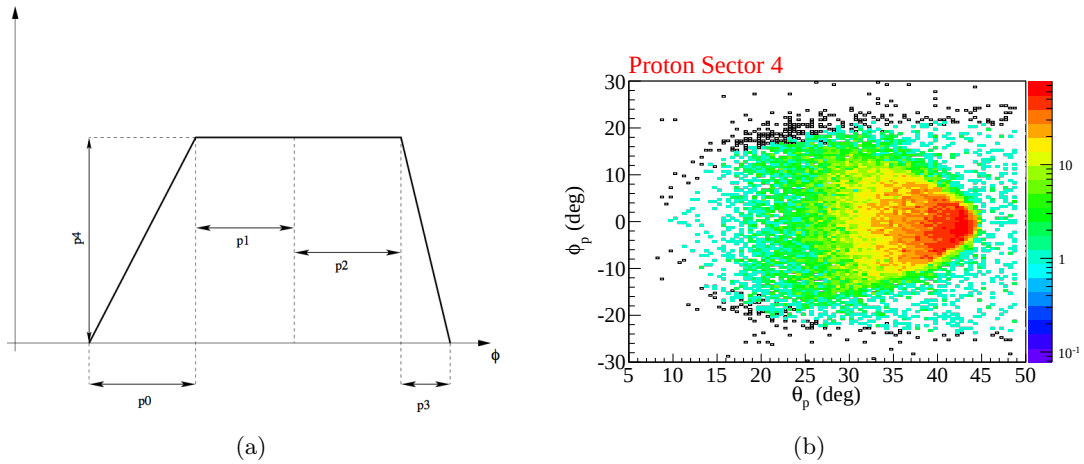


(a) (b)

**Figure 3.23: (a) The trapezoidal function used to fit the proton $\phi$ distribution. The parameters, $p_1$ and $p_2$ provide the limits for the proton DC fiducial cuts. (b) Proton $\phi_p$ vs $\theta_p$ distribution for sector 4 integrated over $p$ for sector 4. Rejected tracks are shown in black.**

fiducial cut. These limits can, in turn, be parameterized as functions of $\theta$ and $p$:

$$\begin{aligned} \phi_{min} &= \sum_{i=0}^{4} a_i(p)\theta^i \\ \phi_{max} &= \sum_{i=0}^{4} b_i(p)\theta^i \\ \phi_{min} \leq \quad \phi \quad &\leq \phi_{max}. \end{aligned} \tag{3.24}$$

Here, $\phi_{min/max}$ is parameterized as a function of $\theta$ to the fourth order polynomial and its coefficients $a_i(p)$ and $b_i(p)$ are second order polynomials as function of momentum of proton. Using this parameterization, we apply our fiducial cut. The result can be seen for one of the CLAS sectors in Fig. 3.23(b). Please refer to Appendix A.3.2 for a full list of the parameters for each sector.

## 3.6 Bethe-Heitler Subtraction

After the electron and proton has been selected for each event and all corrections and cuts have been applied, we now identify the neutral pions in our event. To do so, we use the conservation of 4-momentum and look at our missing mass squared distribution of the detected particles:

$$M_X^2(ep) = (l + P - l' - P')^2. \tag{3.25}$$

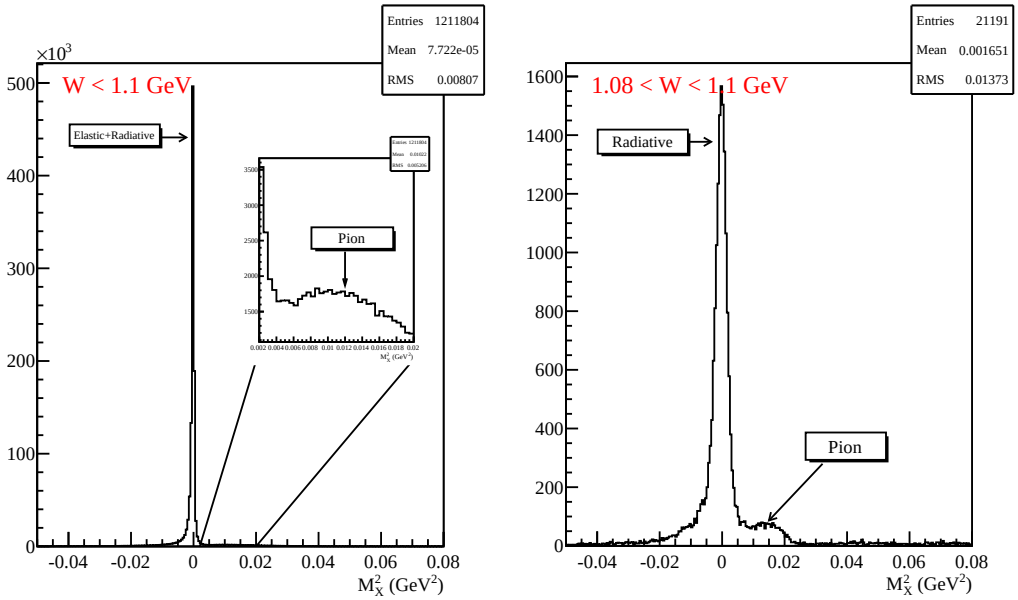


**Figure 3.24: (Left): $M_X^2$ for events with $W < 1.1$ GeV. Elastic and associated Bethe-Heitler events are centered around zero GeV$^2$. Inset plot shows the zoomed region with the neutral pion signal. (Right): $M_X^2$ for events with $1.08 < W < 1.1$ GeV. Elastic Bethe-Heitler events are centered around zero GeV$^2$.**

Here, $l$, $P$, $l'$ and $P'$ are 4-momenta of the incident and scattered particles as described in Section 1.1.1.

The plot of the $M_X^2$ for our events with $W < 1.1$ GeV is shown in Fig. 3.24 (Left). In this plot, we have the elastic ($ep \to ep$) and the associated Bethe-Heitler events ($ep \to ep\gamma$) centered around zero GeV$^2$. These events dominate the $M_X^2$ distribution and the $\pi^0$ signal near threshold is suppressed in comparison. A simple cut on $W$ can eliminate the elastic events as shown in Fig. 3.24 (Right). Here we have selected events for $1.08 < W < 1.1$ GeV, which is the $W$ bin closest to threshold. In this plot, the elastic events have been eliminated but some Bethe-Heitler and some multiple soft photon events are still present and centered around zero GeV$^2$. These events need to be removed so only the pion signal remains.

To do so, let's take a look at the two dominating Feynman diagrams for the Bethe-Heitler process $ep \to ep\gamma$. Fig. 3.25(a) shows the diagram with a pre-radiated photon (emission from an incident electron) and Fig. 3.25(b) shows the diagram with a post-radiated photon (emission from a scattered electron). These photons are emitted along the direction of the incident and scattered electron, respectively, in the peaking approximation

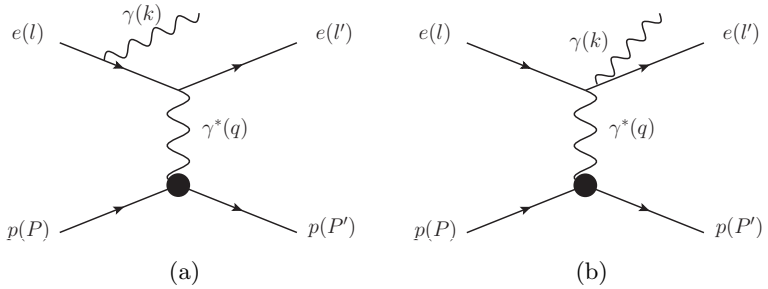


**Figure 3.25: The Bethe-Heitler process $ep \to ep\gamma$ diagrams for (a) a photon emitted from an incident electron (pre-radiation) and for (b) a photon emitted from a scattered electron (post-radiation).**

[42, 43]. When these photons are emitted the incident and scattered electrons lose energies. This feature of the Bethe-Heitler process can be exploited to our benefit.

For the elastic process $ep \to ep$, the proton angle can be computed independently of the incident and scattered electron energies:

$$\tan\theta_1^p = \frac{1}{\left(1+\frac{E'}{M_p - E'\cos\theta_e'}\right)\tan\frac{\theta_e'}{2}} \tag{3.26}$$

$$\tan\theta_2^p = \frac{1}{\left(1+\frac{E}{M_p}\right)\tan\frac{\theta_e'}{2}}. \tag{3.27}$$

Here, $\theta_1^p$ and $\theta_2^p$ are the proton angles computed independently of the incident and scattered electron energies, respectively. Also, $M_p$ is the mass of the proton, $\theta_e'$ is the angle of the scattered electron in the lab frame, and $E$ and $E'$ are the energies of the incident and scattered electron, respectively. We can calculate these angles for each event and look at its deviation ($\Delta\theta_{1,2}^p$) from the measured value ($\theta_{meas}^p$):

$$\Delta\theta_{1,2}^p \equiv \theta_{1,2}^p - \theta_{meas}^p. \tag{3.28}$$

Fig. 3.26(a) shows the $M_X^2$ plotted as a function of this deviation $\Delta\theta_1^p$ for one of the near threshold regions, $W = 1.09 \pm 0.02$ GeV. In the plot, we see two red spots along $M_X^2 = 0\,\mathrm{GeV}^2$. The one on the left is centered along $\Delta\theta_1^p = 0$ deg and it corresponds to the pre-radiated photon events. The other corresponds to the post-radiated photon events. Additionally, these radiative events extend toward the positive $M_X^2$ as fringes. These are the radiative events that we need to isolate from the pion signal as indicated by the red line in the plot.

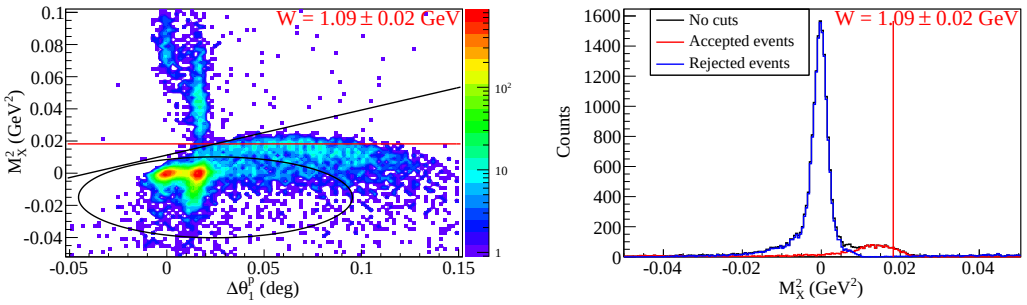


(a) (b)

**Figure 3.26: (a) $M_X^2$ vs $\Delta\theta_1^p$ for $1.08 < W < 1.1$ GeV. The red line indicates the expected pion peak position. The left red spot centered around zero degrees corresponds to the pre-radiative events and the one on the right to the post-radiative events. The two fringes extending toward positive $M_X^2$ are extensions of these radiative events. The ellipse and linear polynomial indicate the cuts applied to reject these events. (b) $M_X^2$ for events with $1.08 < W < 1.1$ GeV. Black curve shows events prior to any Bethe-Heitler subtraction cuts, blue curve shows events rejected from the cuts and red curve shows those events that survive the Bethe-Heitler subtraction cuts. Red line indicates expected pion peak position.**

To do so, we employ an elliptical and a linear polynomial as shown to reject these events. These cuts are parameterized as a function of $W$ and are defined as follows:

$$M_X^2 < b_0(W) + a_0(W)\Delta\theta_1^p \tag{3.29}$$

$$1 < \left(\frac{\Delta\theta_1^p - x_0}{r_1(W)}\right)^2 + \left(\frac{M_X^2 - y_0}{r_2(W)}\right)^2. \tag{3.30}$$

Here, $b_0$ and $a_0$ are linear functions of $W$ and are parameters of the linear polynomial; $x_0$ and $y_0$ are the coordinates of the center of the ellipse and are independent of $W$; $r_1$ and $r_2$ are the lengths of the semi-major and semi-minor axis of the ellipse and are parameterized as linear functions of $W$. The result of these cuts is seen in Fig. 3.26(b) with the accepted events after the cut shown in red as our pions and the rejected events in blue. Please see Appendix A.7 for the parameterization of these cuts and plots for other regions in $W$.

After the Bethe-Heitler subtraction cuts are applied, we select our pions by making a $\pm 3\sigma$ cut on the $M_X^2$ from the mean position of the distribution.

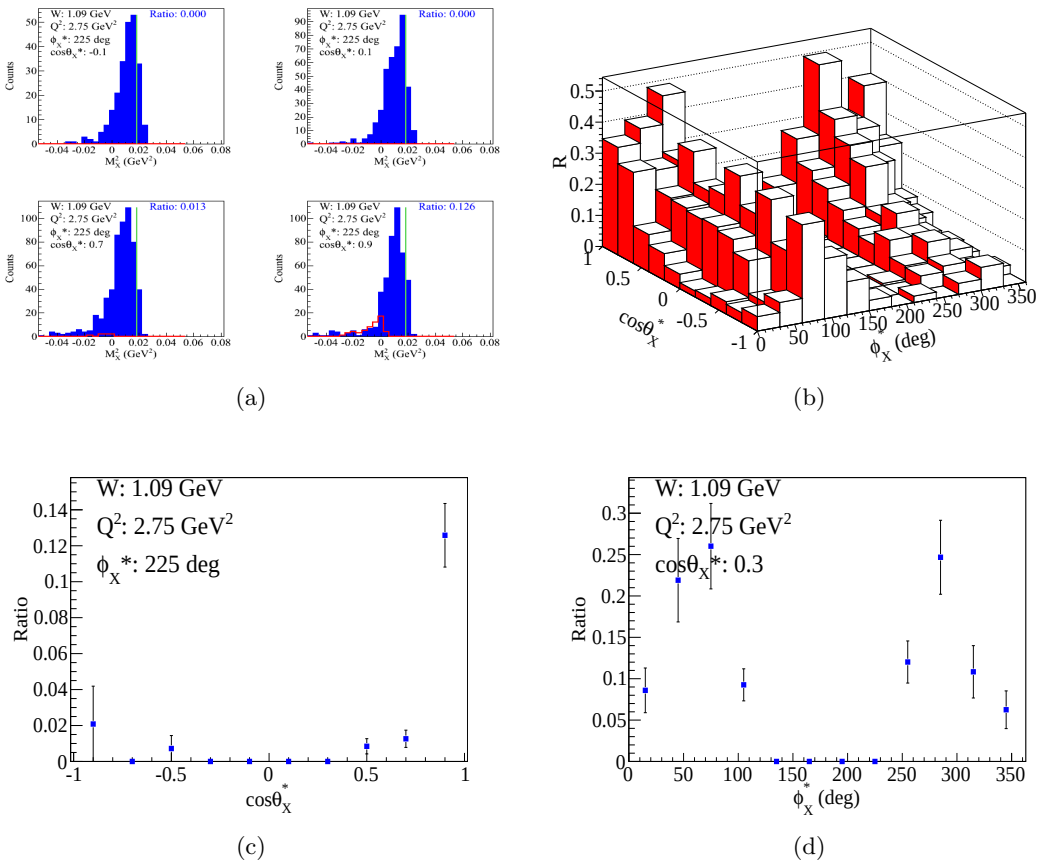


**Figure 3.27: (a) The $M_X^2$ for $W = 1.09$ GeV, $Q^2 = 2.75\,\mathrm{GeV}^2$, $\phi_X^* = 225°$ and $\cos\theta_X^* = \{-0.1, 0.1, 0.7, 0.9\}$ bins showing rejected (red) and accepted (blue) simulated events. Green line indicates the expected pion peak position. (b) The ratio of rejected events ($M_X^2 < m_\pi^2$) to total events for $W = 1.09$ GeV and $Q^2 = 2.75\,\mathrm{GeV}^2$ as a function of $\cos\theta_X^*$ and $\phi_X^*$ for simulation. (c) The ratio of pion loss for $\phi_X^* = 225°$ plotted as a function of $\cos\theta_X^*$. Statistical errors are shown for each bin. (d) The ratio of pion loss for $\cos\theta_X^* = 0.$ plotted as a function of $\phi_X^*$ with statistical errors.**

## 3.7 Pion Loss Estimation

The Bethe-Heitler cuts discussed in previous section might be too strong and might result in the loss of pion events. To estimate such a loss we can look at simulated events[4]. The process $ep \to ep\pi^0\gamma$ is considered and we look at the ratio of events rejected by the Bethe-Heitler subtraction cuts to those accepted.

Fig. 3.27(a) shows the simulated events that were rejected (red) and accepted (blue) from the Bethe-Heitler subtraction cuts for a particular $W$, $Q^2$, $\phi_X^*$ and for a few $\cos\theta_X^*$

[4]See Chapter 4 for discussion of simulated events

bins. Here, $\phi^*_X$ and $\cos\theta^*_X$ are angles for the missing particle (pion) in the virtual photon-proton center of mass frame. We look at the ratio, $R$, of the rejected events to the total events in the kinematic bin as shown in Fig. 3.27(b). When computing the ratio we only consider those rejected events with $M^2_X < m^2_\pi$ since the Bethe-Heitler events are only expected to be in this kinematic region. This gives us an estimate on the pion loss because of the subtraction cuts. This ratio is used as a correction on the cross section level and is applied for each kinematic bin:

$$\frac{d\sigma_{cor}}{dW dQ^2 d\Omega^*_\pi} = \frac{d\sigma}{dW dQ^2 d\Omega^*_\pi}(1+R). \tag{3.31}$$

Here, $\frac{d\sigma_{cor}}{dW dQ^2 \Omega^*_\pi}$ is the differential cross section after applying this correction. The correction is highest at the forward $\cos\theta^*_X$ and at $\phi^*_X$ around 0 or 360 degrees. Figs. 3.27(c) and 3.27(d) show corrections for a typical kinematic bin near threshold. The average correction over all bins is $\sim 18\%$.

# 4. Simulation

## 4.1 Overview

For this experiment, we simulate the reaction, $ep \rightarrow ep\pi^0\gamma$, using the standard CLAS simulation and reconstruction software. The following steps are used in the procedure:

- Generate events
- Simulate detector geometry and interaction using GEANT (GSIM)
- Simulate additional detector inefficiencies and resolutions using GSIM Post Processing (GPP)
- Reconstruct tracks.

These events are then sent through the same analysis process as the experimental data. In the following paragraphs these procedures will be described.

## 4.2 Monte Carlo Simulation

To determine the cross section of the reaction $ep \rightarrow ep\pi^0$, it is necessary to do a Monte Carlo (MC) study of what to expect from the experiment in the laboratory. As such, a good description of the physics model and the detector geometry is required.

### 4.2.1 Event Generation

Using a MAID model [44] to describe the physics of our experiment, events are generated for the reaction $ep \rightarrow ep\pi^0\gamma$. A photon in the final state is generated additionally to describe radiative effects in the cross section measurements and will be helpful later for radiative corrections[5].

The MAID2007 model is a Mainz unitary isobar model (UIM) [45] that describes the single pion electroproduction reaction. It uses phenomenological fit to previous photo- and electroproduction data. It describes nucleon resonances using Breit-Wigner forms and non-resonant backgrounds are described using Born terms and $t$-channel vector-meson exchange. To describe the threshold behavior, Born terms were included with a mixed

[5]See Section 5.4

| Variable | Range | Number of Bins | Width |
|---|---|---|---|
| $W$ (GeV) | 1.08 : 1.16 | 4 | 0.020 |
| $Q^2$ (GeV$^2$) | 2.0 : 4.5 | 5 | 0.5 |
| $\cos\theta^*_\pi$ | -1 : 1 | 10 | 0.2 |
| $\phi^*_\pi$ (deg) | 0 : 360 | 12 | 30 |

**Table 4.1: Kinematic bin selection.**

pseudovector[6]-pseudoscalar[7] $\pi NN$ coupling. While the pion electroproduction world data in the resonance region goes up to $Q^2 \sim 7\,\mathrm{GeV}^2$, there is no data near threshold for $Q^2 > 1\,\mathrm{GeV}^2$. The cross section amplitudes for $Q^2 > 1$ near threshold are described by extrapolations to fits to these data in the MAID2007 model.

The physics events are generated using the AAO_RAD software package that takes the MAID2007 model for the cross sections as input. For each kinematic bin events are thrown randomly in the azimuthal angle of the electron and proton in the lab frame since the physics is independent of this variable. Each event is generated within the phase space constraints. The total number of events in the bin is then normalized to the cross section from MAID model. The "RAD" in AAO_RAD stands for a radiated photon that is generated in addition to the electron, proton and the neutral pion in the final state. The energy of the radiated photon can be adjusted as an input to AOO_RAD.

Events are generated to cover the entire kinematic range described in Table 4.1 and a little bit beyond to account for resolution and bin migration effects. About 30 million events are generated for the 2400 kinematic bins.

### 4.2.2 GSIM

After the physics events are generated, their passage through the detector must be simulated using the GEANT based Monte Carlo (GSIM) program. This program simulates the geometry of the CLAS detector during the experiment and the interaction of the particles with the detector material. The program includes information on the following CLAS detector components:

- Liquid hydrogen target cell including support structures
- Beam line geometry
- Mini-torus magnet and its shielding

[6] $\bar{\psi}\gamma_\mu\gamma_5\psi$
[7] $\bar{\psi}\gamma_5\psi$

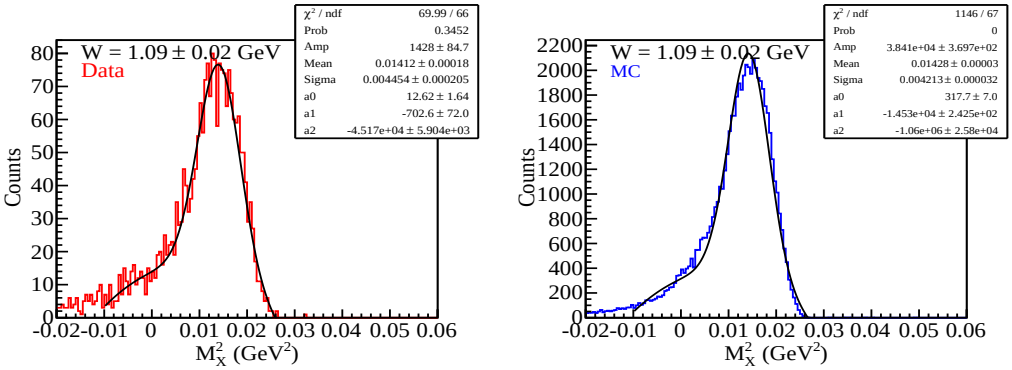


**Figure 4.1: Missing mass square for $W = 1.09 \pm 0.02$ GeV from experiment (red) and simulation (blue). The resolutions for both distributions are similar.**

- Main torus magnet and support structures
- Drift chambers
- Cerenkov counters
- Time of flight scintillators
- Electromagnetic calorimeters
- Structure of materials for all detectors

GSIM models the effects of multiple scattering of particles in the CLAS detector and geometric mis-alignments. The information for all interactions with the detectors is recorded in raw banks, which will be used for reconstruction of tracks later.

### 4.2.3 GSIM Post Processing

To incorporate the effects of tracking resolution in the drift chambers (DCs) and timing resolution of the TOF, additional processing (GPP) must be done on the simulated events. These effects are essential to incorporate into the simulation as they are tied to kinematic quantities such as missing mass resolutions that are involved in cuts in the analysis.

To include the effects of tracking resolution in the DCs, the distance-of-closest-approach (DOCA[8]) for each hit wire is smeared according to a parameterized residual function. These residuals are obtained from the CLAS data taken during the experiment.

[8]The distance from the sense wire to the track as determined from time based tracking.[46]

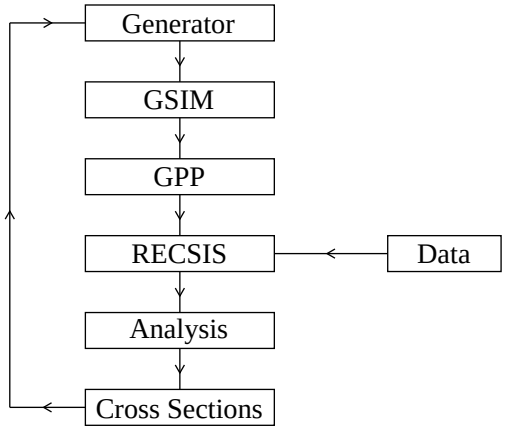


**Figure 4.2: The analysis process. Simulated events are generated, processed through GSIM and GPP. These events are cooked using RECSIS similar to experiment DATA and are analyzed to obtain the cross sections. The cross sections are then fed back into the generator as a model and the process repeats.**

The smeared DOCA are then converted into drift time and TDC values based on calibration. For the TOF, resolutions were incorporated into GPP using the fitting function based on cosmic ray tests for all scintillators as shown in Fig. 2.8(b).

Fig. 4.1 shows the comparison between the $M_X^2$ resolution for experiment ($\sigma = 0.0044\,\mathrm{GeV}^2$) and simulation ($\sigma = 0.0042\,\mathrm{GeV}^2$). The resolutions are similar and so the cuts on this variable can be consistently applied to both data and simulation.

In addition to the track resolutions, one also has to account for the dead wires in the DC. These dead wires and inefficient regions contribute to holes in the geometrical acceptance and reconstruction inefficiencies. During the run period these regions were studied and a MAP was created to describe the efficiency for each DC regions [47]. These maps are then supplied to GPP, which removes the dead channels and accounts for the inefficiencies.

### 4.2.4 Reconstruction

The output of GSIM and GPP contains just raw ADC and TDC hit information for each detector component. To obtain higher level information such as 4-momentum, position, timing, and so on, this information must go through a *cooking* procedure (RECSIS) that is exactly the same as for the experimental data as described in section 3.2.

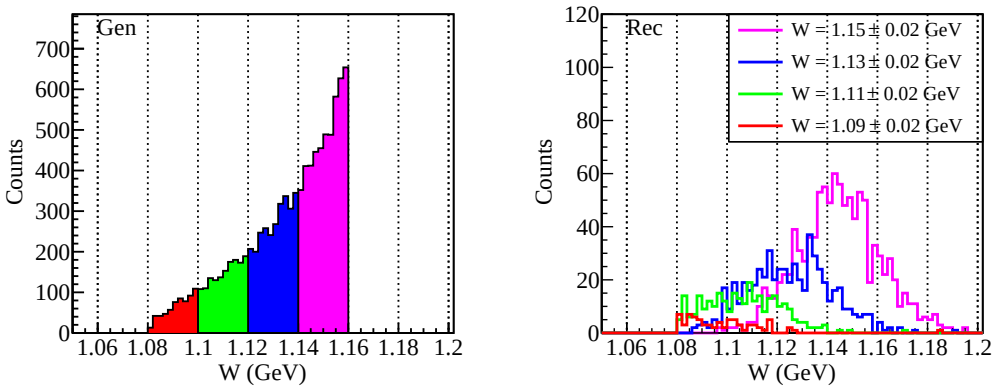


**Figure 4.3: Bin migration effect shown for some of the $W$ kinematic bins near threshold. The left plot shows generated events for four different $W$ bins and the right column shows the reconstructed events after passing all analysis cuts.**

After cooking, the simulated events are analyzed similarly to the experimental data and are used for acceptance corrections and so on to obtain cross sections and higher level physics information. The final measurements of the cross sections are then used as a model for input to AOO_RAD and the process repeats itself. Fig. 4.2 shows the process of obtaining Monte Carlo simulations.

## 4.3 Bin Migration

Bin migration is the effect where events are generated in a finite bin but are reconstructed in other neighboring bins. This can be a significant effect on the acceptance corrections if the reconstructed MC distributions are not reasonably close to the experimentally observed distributions.

An example of the bin migration effect can be observed in Fig. 4.3. The left column shows events generated in a specific $W$ bin using the MAID model. The right column shows events after reconstruction that have passed through all the analysis cuts. Some events from neighboring bins are reconstructed inside the generated bin and vice versa. So, there is an exchange of events over the bins and if the simulation model is reasonable then this should account for the same behavior as seen for the experiment.

# 5. Corrections and Normalizations

## 5.1 Overview

The simulated events are used to obtain the following corrections to the cross section:

- Acceptance corrections
- Bin Centering corrections
- Radiative corrections.

In addition to these corrections, we must check the consistency of our experiment with other known cross sections such as elastic scattering $ep \to ep$ and the $\Delta(1232)$ resonance. These corrections and procedures will be discussed in the following sections.

## 5.2 Acceptance Corrections

Acceptance corrections are applied to the experimental data to obtain the cross section for each kinematic bin. These corrections describe the geometrical coverage of the CLAS detector, inefficiencies in hardware and software, and resolution effects from track reconstruction.

By comparing the number of events in each kinematic bin from the physics generator and the reconstruction process, the corrections can be obtained as:

$$A = \frac{N_{rec}}{N_{gen}} \tag{5.1}$$

where $N_{rec}$ corresponds to those events that have gone through the entire analysis process including track reconstruction and all analysis cuts. $N_{gen}$ are those events that were generated using the physics generator AOO_RAD. These corrections are then applied to obtain the cross section

$$\sigma = \frac{N_{exp}}{A} \tag{5.2}$$

where $N_{exp}$ is the number of events as measured in experiment for each kinematic bin. Fig. 5.1 shows the acceptance as a function of $\phi_\pi^*$ for one of the kinematic bins in $W$, $Q^2$ and $\cos\theta_\pi^*$ near threshold. One can see that it is symmetric in $\phi_\pi^*$. The error bars increase for backward angles $\theta_\pi^*$ because of smaller generated statistics. Similar corrections are

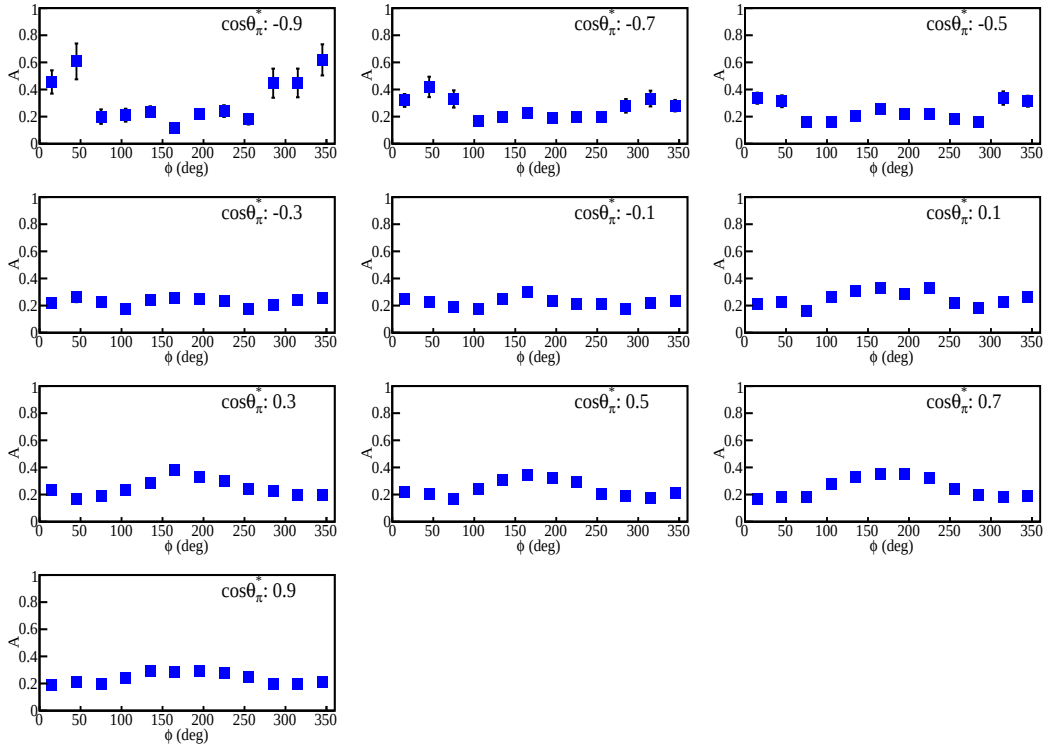


**Figure 5.1: Acceptance corrections for $W = 1.09$ GeV and $Q^2 = 2.75\,\mathrm{GeV}^2$ as a function of $\phi_\pi^*$. Each subplot shows corrections for different $\cos\theta_\pi^*$ bin.**

obtained for other bins. Acceptance corrections were obtained for all kinematic bins of interest and there were no bins with zero corrections.

## 5.3 Bin Centering Corrections

The kinematic bins have been selected to maximize the measured amount of counts within them. It is possible that the cross section might vary significantly within each kinematic bin. In such cases, reporting the cross section at the center of the bin may not be appropriate. Fig. 5.2(a) shows a typical kinematic binning where the average of the measured cross section $\sigma$ is not at the center of the bin but at $\bar{x}$, *i.e.*, the centroid for the bin that can be defined as

$$\bar{x} = \int_{x_1}^{x_2} x\sigma(x)dx. \tag{5.3}$$

Here, $x$ corresponds to a typical $W$, $Q^2$, $\cos\theta_\pi^*$ or $\phi_\pi^*$ kinematic bin.

To account for this discrepancy, a correction is made for each kinematic bin. Using a good model the centroid can be determined for each kinematic bin and the correction

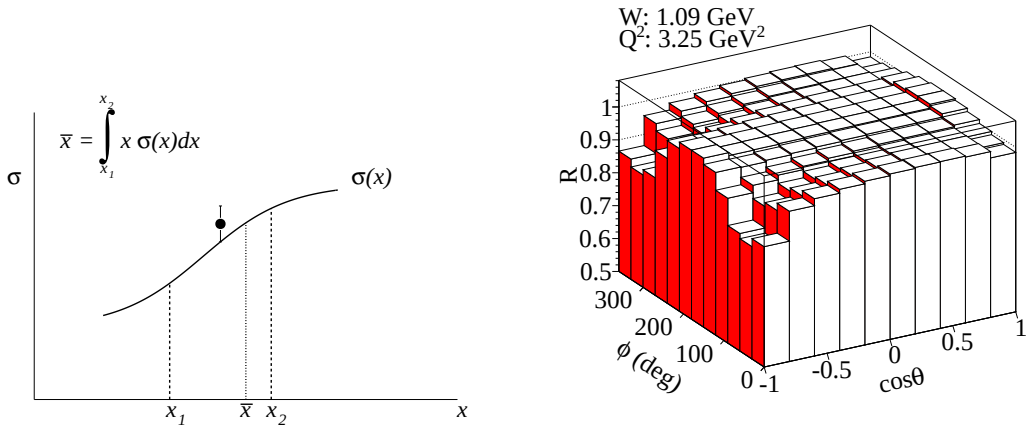


(a) (b)

**Figure 5.2: (a) A typical kinematic binning is shown. The measured cross section $\sigma$ is shown as a black point with error bars and the true value is shown as a function $\sigma(x)$. The average of the function is at $\bar{x}$. (b) Bin centering corrections for $W = 1.09$ GeV and $Q^2 = 3.25\,\mathrm{GeV}^2$ as a function of $\cos\theta^*_\pi$ and $\phi^*_\pi$.**

factor $R$ can be determined by the following prescription:

$$R(W, Q^2, \cos\theta^*_\pi, \phi^*_\pi) = \frac{\sigma_{center}}{\sigma_{centroid}}. \tag{5.4}$$

Here, $\sigma_{center}$ is the cross section as measured at the center of the kinematic bin and $\sigma_{centroid}$ is the value of the cross section determined at the centroid of the bin. The correction is applied to the measured cross section:

$$\sigma_{cor} = \frac{\sigma_{meas}}{R}. \tag{5.5}$$

Here, $\sigma_{cor}$ is the corrected cross section for a particular bin and $\sigma_{meas}$ is the measured uncorrected cross section at the bin.

Fig. 5.2(b) shows corrections for one of the kinematic bins in $W$ and $Q^2$ as a function of $\cos\theta^*_\pi$ and $\phi^*_\pi$. The correction is dependent on $\phi^*_\pi$ and is largest at $\cos\theta^*_\pi \to -1$. At backwards angle the cross section varies more rapidly than at other angles, which gives a larger correction to the cross section. The average correction over all kinematic bins is $\sim 3\%$.

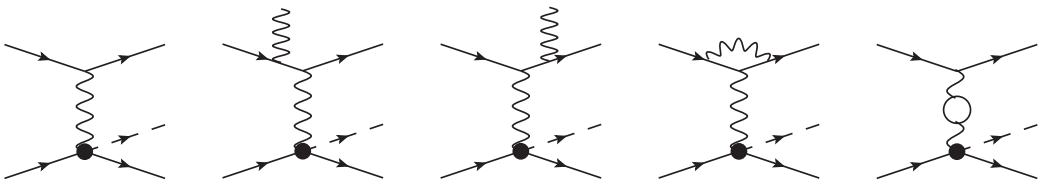


**Figure 5.3: Feynman diagrams contributing to the pion electroproduction cross section. (a) Born process, (b) and (c) Brehmsstrahlung, (d) Vertex correction, and (e) Vacuum polarization.**

## 5.4 Radiative Corrections

In section 3.6 the elastic Bethe-Heitler events were subtracted from the neutral pion process. However, additional corrections are required to the measured cross section to obtain results for $ep \to ep\pi^0$ process. This is because in the laboratory we measure not only the Born term, $ep \to ep\pi^0$, but also terms including the Bethe-Heitler $ep \to ep\pi^0\gamma$ and others as shown in Figs. 5.3(a)-(e).

These QED processes include radiation of photons that are not detected (Figs. 5.3(b)-(c)), vacuum polarization (Fig. 5.3(e)) and lepton-photon vertex corrections (Fig. 5.3(d)). The vacuum polarization refers to the process where the virtual photon temporarily creates and annihilates a lepton-anti-lepton pair. The lepton-photon vertex corrections are for processes where a photon is emitted by the incoming electron and is absorbed by the outgoing electron. These processes give the largest contribution to the cross section at the next-order level. These contributions can be calculated exactly from QED and the measured cross section can be corrected to extract the Born term [48]. These are the radiative corrections, $\delta$, for the experiment

$$\sigma_{Born} = \frac{\sigma_{meas}}{\delta}. \tag{5.6}$$

Here, $\sigma_{meas}$ is the observed cross section from experiment and $\sigma_{Born}$ is the desired cross section after corrections.

The correction is obtained using the software package EXCLURAD [49] that takes theoretical models, such as MAID, as input for the hadronic current. For this experiment, the same MAID model is used to determine the radiative corrections as the one used to generate the monte carlo events (Section 4.2.1). This is because the radiative corrections are closely related to the acceptance corrections. For each kinematic bin the differential

cross section can be written as:

$$\sigma = \frac{N_{meas}}{\mathcal{L}\,A}\frac{1}{\delta} \tag{5.7}$$

where $N_{meas}/\mathcal{L}$ is the number of events from experiment normalized by the integrated luminosity (with appropriate factors) before acceptance and radiative corrections. Also, $A = N_{rec}^{RAD}/N_{gen}^{RAD}$ is the acceptance correction for the bin and $\delta$ is the radiative correction. It should be noted that the events for the acceptance correction were generated with a radiated photon in the final state using the MAID2007 model.

EXCLURAD uses the same model to obtain the correction $\delta = N_{gen}^{RAD}/N_{gen}^{NORAD}$ where $N_{gen}^{NORAD}$ are events generated without a radiated photon in the final state. Thus

$$\sigma = \frac{N_{meas}}{\mathcal{L}}\left(\frac{N_{gen}^{RAD}}{N_{rec}^{RAD}}\right) \times \left(\frac{N_{gen}^{NORAD}}{N_{gen}^{RAD}}\right). \tag{5.8}$$

Using a good model such as MAID2007, one can expect the $N_{gen}^{RAD}$ terms to be identical for both the acceptance and radiative corrections. As such we can expect the terms to cancel each other in the above expression. But it might not be the case. To minimize the dependence of the radiative correction on the model, a missing mass cut is used as a parameter.

In the calculation of the correction, the missing mass cut restricts the maximum energy of the radiated photon that would otherwise go to the outgoing hadronic system. When no missing mass cut is applied, the cross section is computed by integrating from threshold to the $W$ bin of interest. For high enough $W$ this could introduce dependence on the model if no missing mass cut is applied. This missing mass cut parameter is known as the $v_{cut}$ parameter and is defined as:

$$v_{cut} = M_X^2 - m_\pi^2 \tag{5.9}$$

where $M_X$ is the desired missing mass cut and $m_\pi$ is the mass of pion. The corrections are thus computed for each kinematic bin $W$, $Q^2$, $\cos\theta_\pi^*$ and $\phi_\pi^*$.

Fig. 5.4(a) shows the radiative corrections calculated using $v_{cut} = 0.05\,\mathrm{GeV}^2$ for one of the kinematic bins as a function of the pion angles in CM system. One can observe that the corrections have a $\phi_\pi^*$ dependence. This is because the Brehmsstrahlung process only occurs on the leptonic plane, *i.e.*, at angles 0 or 180 degrees with respect to the hadronic plane. Also, one can notice that the correction increases with $\cos\theta_\pi^* \to -1$. This

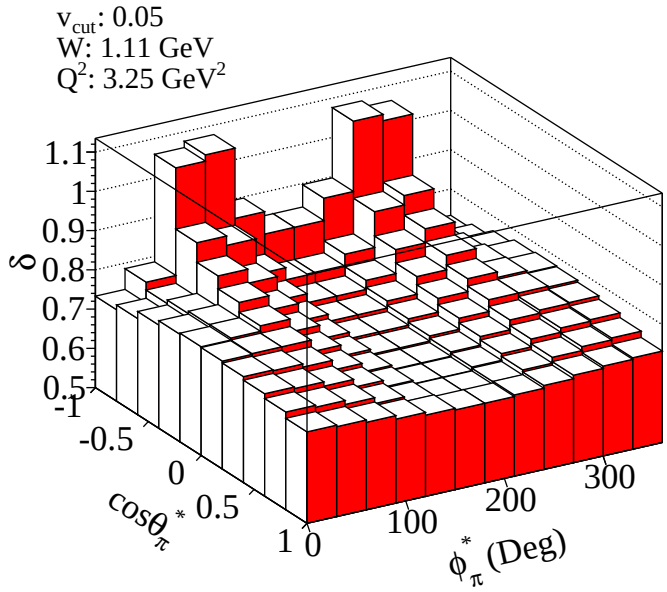


(a)

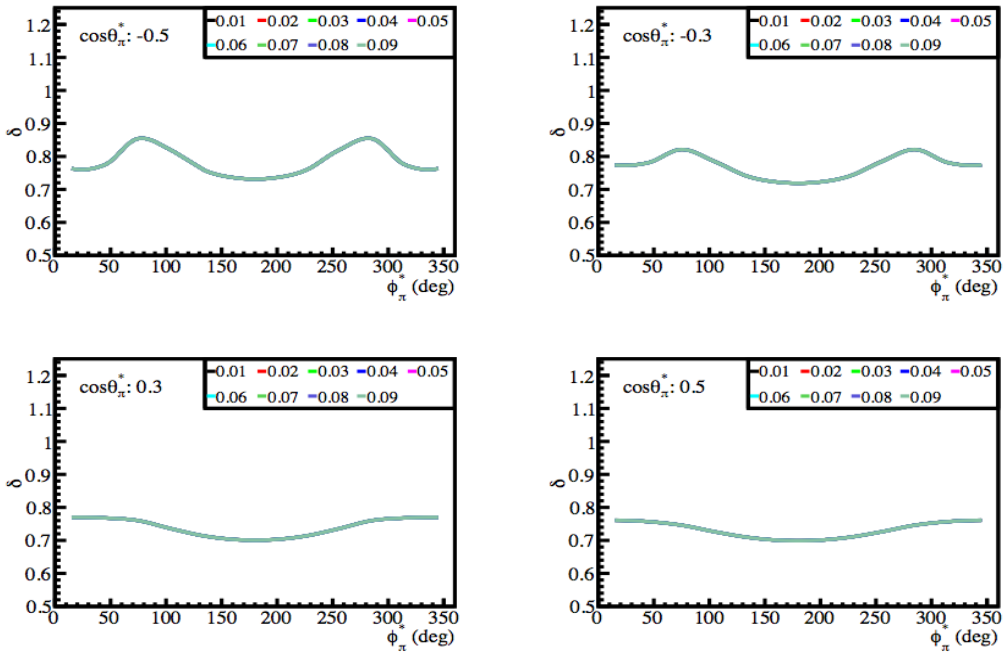


(b)

**Figure 5.4: (a) The radiative corrections for $W = 1.11$ GeV and $Q^2 = 3.25\,\mathrm{GeV}^2$ as a function of $\cos\theta^*_\pi$ and $\phi^*_\pi$ obtained from EXCLURAD using MAID2007 model with $v_{cut} = 0.05\,\mathrm{GeV}^2$. (b) The radiative corrections as a function of $\phi^*_\pi$ for $W = 1.11$ GeV, $Q^2 = 3.25\,\mathrm{GeV}^2$, and $\cos\theta^*_\pi = -0.5, -0.3, 0.3, 0.5$ for various values of $v_{cut}$ (different colors). The corrections are independent of $v_{cut}$ so the curves lie on top of each other.**

is because the cross section is expected to approach zero at backwards angles and that is the region where the Bethe-Heitler events dominate.

Fig. 5.4(b) shows the radiative corrections for the same kinematic bins as a function of $\phi_\pi^*$ calculated using various values of $v_{cut}$: 0.01, 0.02, 0.03, 0.04, 0.05, 0.06, 0.07, 0.08 and 0.09 GeV$^2$. The curves for each $v_{cut}$ overlap and no dependence on this parameter is observed for bins near threshold. This is because near threshold there isn't enough phase space for the photons to take energies away from the outgoing hadrons. So, for generality, a $v_{cut}$ value of $0.05\,\mathrm{GeV}^2$ is used to compute the corrections for all bins in this experiment. The average radiative correction over all kinematic bins is $\sim 25\%$.

## 5.5 Luminosity

The cross section of the reaction should be normalized to the integrated luminosity $\mathcal{L}$. Luminosity is the product of the number of particles hitting the target per unit area and per unit time and the total number of particles within the beam area [50]. Integrated luminosity is the integral of luminosity over the time of the experiment. The cross section is thus normalized to the integrated luminosity:

$$\sigma = \frac{N_{exp}}{\mathcal{L}} \tag{5.10}$$

where $\sigma$ is the normalized cross section and $N_{exp}$ is the number of events measured in a particular kinematic bin. As such, $\mathcal{L}$ should have the dimensions of $1/\mathrm{cm}^2$ or $1/\mathrm{nb}$.

To determine this quantity the total Faraday cup charge, $Q_{FCUP}$, collected during the entire *production* run period is calculated. There are times when the DAQ is busy recording an event and this fraction of the total time taken for the measurement is called *dead time*. The *live time* then is the total time when the DAQ is actually recording events. The total charge collected has to be factored by this *live time* to yield

$$Q_{FCUP} = 21.287\,\mathrm{mC}. \tag{5.11}$$

This charge is then used in the following equation to compute the integrated luminosity:

$$\mathcal{L} = N_e N_p = \left(\frac{Q_{FCUP}}{e}\right) \times \left(\frac{N_a l_{target} \rho}{amu}\right). \tag{5.12}$$

Here, $e$ is the charge of the electron in Coulombs, $N_a$ is Avogadro's number in 1/mol, $l_{target}$ is the length of the target (5.0 cm) and $amu$ is conversion factor to convert the

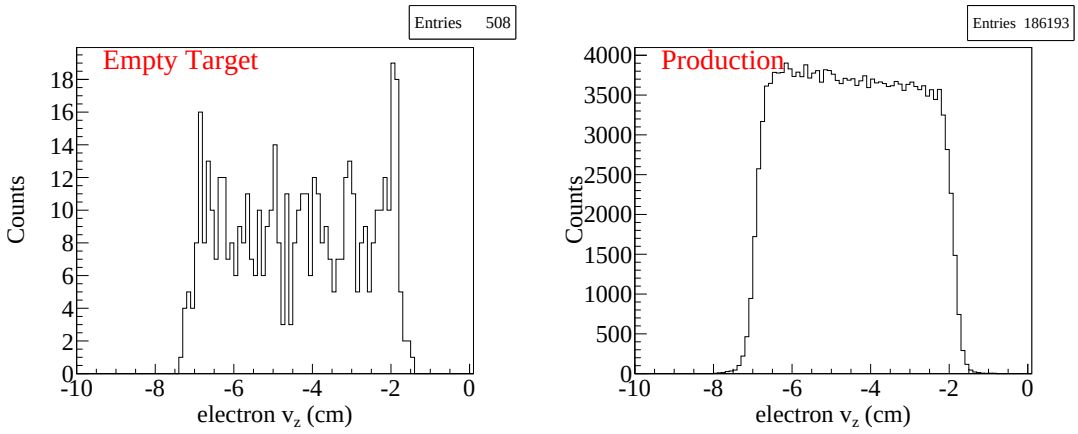


(a) (b)

**Figure 5.5: The electron z-vertex for (a) empty target and (b) production runs integrated over all $W$.**

density of the liquid hydrogen target $\rho$ from g/cm$^3$ to mol/cm$^3$.

The density of the liquid hydrogen target is checked for any variations as a function of temperature and pressure during the experiment. It was found that the density of the target remained stable throughout the run period under variations of temperature and pressure. The average density of the target was found to be 0.0708 g/cm$^3$ [51]. With these values the luminosity for the experiment was determined to be

$$\mathcal{L} = 2.81 \times 10^{40}\, 1/\text{cm}^2. \tag{5.13}$$

This value is then used in Eq. 5.10 for our absolute normalization of the cross section.

## 5.6 Target Cell Wall Contamination

It is expected that a fraction of events in the reaction $ep \to ep\pi^0$ are originating from the target cell walls. The 5 cm long target cell walls are made of 0.0127 cm thick Kapton. Even though the cell walls are thin they can be a source of contamination for our reaction of interest.

To estimate the level of contamination from this source, we look at events collected during the empty-target run period of the $e$1-6a experiment. These events are analyzed using the same process as those for the production run period. Figs. 5.5(a) and (b) show the electron z-vertex distribution for all events that passed through the analysis for both empty target and production events, respectively. The ratio of these two distributions as

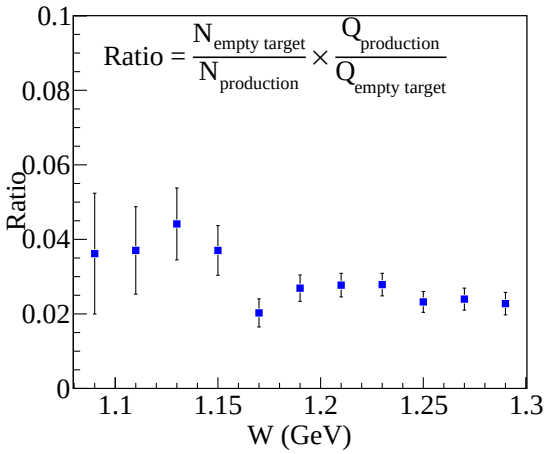


**Figure 5.6: The ratio of the events from empty target and production runs (normalized to the total charge collected) as a function of $W$.**

a function of $W$ is shown in Fig. 5.6. The total number of events is normalized to the total charge collected during the run periods:

$$R = \frac{N_{\text{empty target}}}{N_{\text{production}}} \frac{Q_{\text{production}}}{Q_{\text{empty target}}} \tag{5.14}$$

About 2.214 mC of total charge was collected for the empty target runs and about 21.287 mC for the production run period. The average contamination ranges from about 2-5% depending on the $W$ kinematic bin. This ratio of contamination is then applied as a correction factor to the measured cross section:

$$\sigma_{cor} = \sigma(1 - R). \tag{5.15}$$

Here, $\sigma_{cor}$ is the corrected cross section and $\sigma$ is the measured cross section for a particular bin in $W$.

## 5.7 Elastic Cross Section

To ensure the quality of the experimental measurement, we compare the cross section for the elastic scattering process ($ep \to ep$) to known values, such as the Bosted Form Factor parameterizations [52]. We study two topologies, (a) inclusive $ep \to eX$ and (b) exclusive $ep \to ep$. Monte carlo events are generated for the reaction $ep \to ep\gamma$ to obtain the cross sections. See Section 3.3 for a discussion on the elastic process.

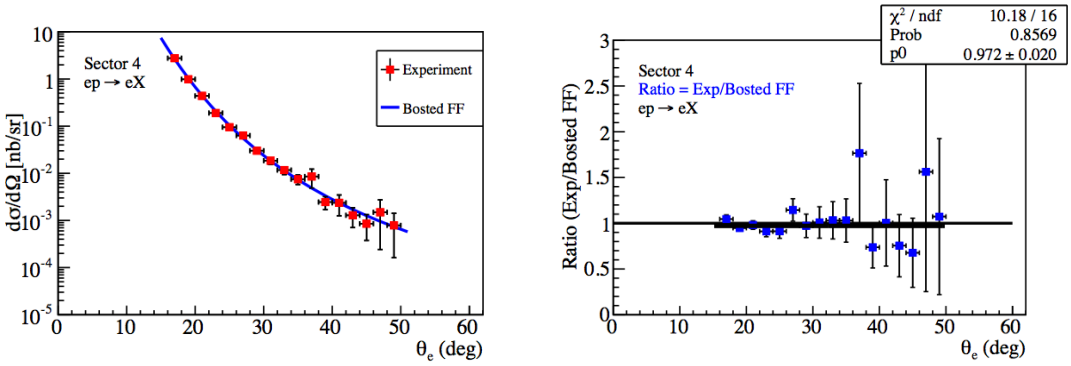


(a) (b)

**Figure 5.7: (a) The differential cross section (red) of the inclusive process $ep \to eX$ as a function of $\theta_e$ for sector 4. The blue curve is the expected cross section. The y-axis is in log scale. (b) The ratio of measured to expected differential cross section for sector 4. The thick black curve is the constant fit.**

### 5.7.1 Inclusive $ep \to eX$

For this topology, we select only the electron in the final state using the same procedure as Section 3.2.1. The appropriate angle and momentum corrections to the electron are applied and finally a cut on $W < 1.028$ is made to select elastic events as shown in Fig. 3.6 (left) for one of the CLAS sectors. The differential cross section for the reaction is then obtained for each CLAS sector as a function of $\theta_e$. These values are then compared with the form factor parameterizations of the elastic cross section.

Fig. 5.7(a) shows the differential cross section for the inclusive process as a function of $\theta_e$ for one of the CLAS sectors. The cross section shows fluctuations at high $\theta_e$ where we have poor statistics. Fig. 5.7(b) shows the ratio of the measured cross section to the expected values. The points are fitted with a constant to estimate the deviation from the expected ratio of 1. For this sector the cross section measurement is consistent with the expected value to within $\pm 5\%$.

The large error bars in the ratio at higher angles can be attributed to small statistics corresponding to higher $Q^2$. The small variation from the nominal cross section value can be attributed to inefficiencies in drift chambers and time of flight systems. But overall, the agreement is good. Other sectors show similar distributions. Please see Appendix C for distributions of other sectors.

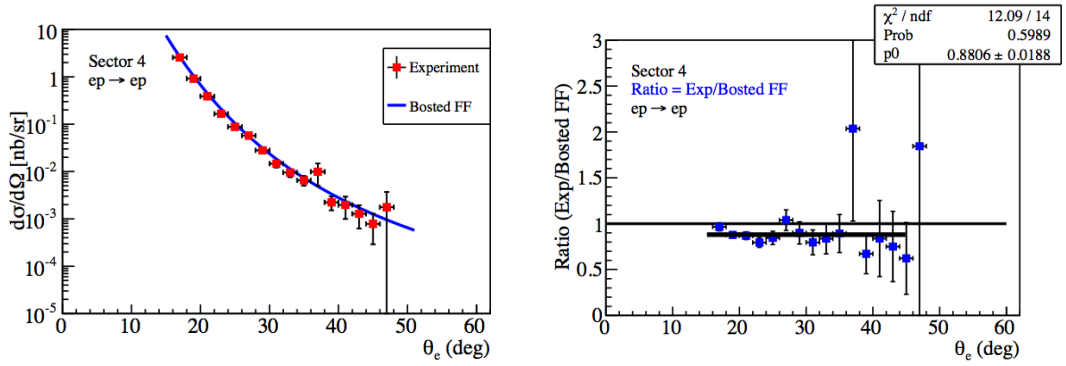


(a) (b)

**Figure 5.8: (a) The differential cross section (red) of the exclusive process $ep \to ep$ as a function of $\theta_e$ for sector 4. The blue curve is the expected cross section. The y-axis is in log scale. (b) The ratio of measured to expected differential cross section for sector 4. The thick black curve is the constant polynomial fit.**

### 5.7.2 Exclusive $ep \to ep$

For this topology, both electrons and protons are selected in the final state. All corrections and cuts appropriate for the particles is applied in the same manner as for the neutral pion process. Two cuts are applied to select the exclusive elastic events, *viz.*, $W < 1.028$ and $|\phi_{e-p} - 180^\circ| < 3\sigma$ as shown in Fig. 3.6 for one of the CLAS sectors. Once again, differential cross sections are obtained and compared with known values.

Fig. 5.8(a) shows the differential cross section for the exclusive process as a function of $\theta_e$ for one of the CLAS sectors. The cross section shows fluctuations at high $\theta_e$ where we have poor statistics. Fig. 5.8(b) shows the ratio of the measured cross section to the expected values. The points are fitted with a constant to estimate the deviation from the expected ratio of 1.

For the exclusive process, we see a significant deviation ($\sim 12\%$) from the expected value for this sector. A similar deviation is observed in other sectors as well. This result is quite surprising and its true nature is as of yet unknown. Previous CLAS analyses [53] have seen deviations for the exclusive process to the order of $\sim 5\%$ where such deviations have been attributed to proton detection inefficiencies in TOF and DC. But here, we observe twice the deviation for the same process.

To account for this discrepancy, we apply an overall normalization factor of $R_{elastic} = 0.89 \pm 0.02$ to the differential cross section for every kinematic bin. This factor is obtained

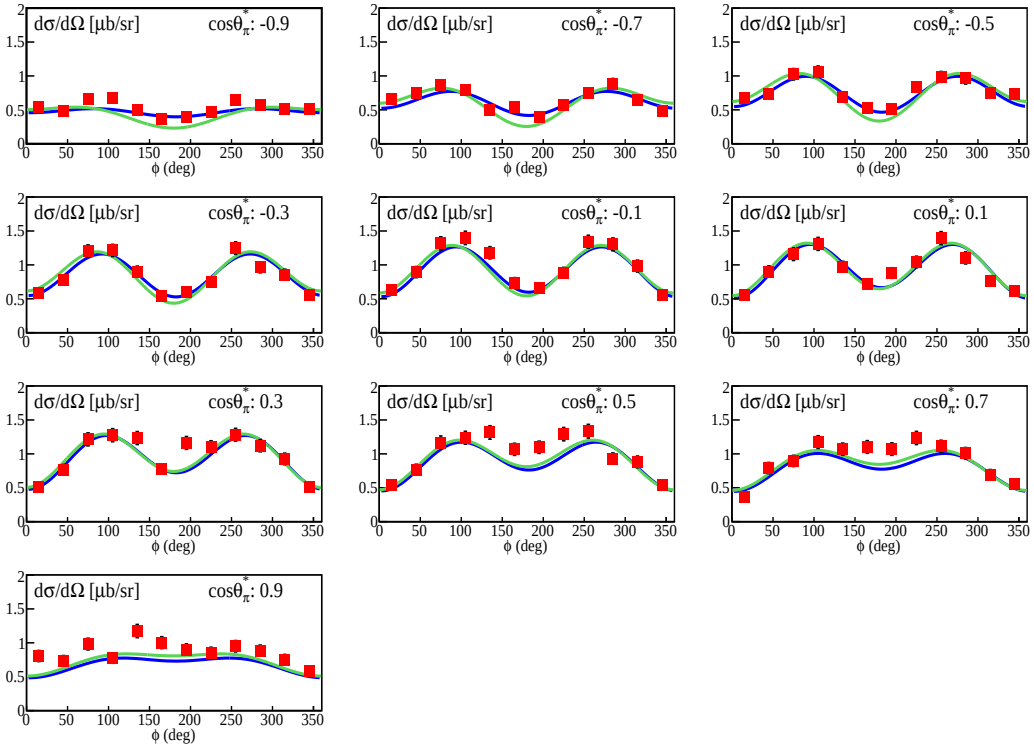


**Figure 5.9: The differential cross section for $ep \to ep\pi^0$ process in the Delta resonance region $W = 1.23$ GeV and $Q^2 = 2.75\,\mathrm{GeV}^2$ as a function of $\phi_\pi^*$. Each subplot shows different bin in $\cos\theta_\pi^*$. The blue curve represents the MAID2007 and the green curve represents Aznauryan *et al* (2009). Red points indicate results from this experiment. Only statistical errors are shown.**

as an average deviation for all the sectors and will account for our overall systematic uncertainty in the final measurements. The differential cross section will be corrected as follows

$$\sigma_{cor} = \sigma \frac{1}{R_{elastic}}. \tag{5.16}$$

This correction to the cross section also includes any detector inefficiencies and as such these inefficiencies will not be accounted for separately. Please see Appendix C for distributions of elastic cross section and ratios for other CLAS sectors.

## 5.8 Delta Resonance Cross Section

Another consistency check for the quality of the experiment is to look at the differential cross at the $\Delta(1232)$ resonance production for the reaction $ep \to ep\pi^0$. This reaction is similar to the near threshold neutral pion electroproduction except it has been studied previously [54, 55].

So, the analysis of the resonance process is the same and all cuts and corrections are extended to the resonance region. Fig. 5.9 shows the differential cross section of the reaction near the resonance region $W = 1.23$ GeV and for $Q^2 = 2.75\,\mathrm{GeV}^2$. The cross section is shown for different $\cos\theta^*_\pi$ bins and is plotted as a function of $\phi^*_\pi$.

Along with the measurements from this experiment two curves are also plotted. Both curves are fits to world data for this kinematic region. The blue curve represents values from MAID2007 [44] and green curve shows values from the parameterization by Aznauryan *et al* [55]. The parameterization by Aznauryan *et al* is also a unitary isobar model (UIM) similar to MAID. To compute the amplitudes at high energies this model uses a different parameterization and uses a different procedure to unitarize the amplitudes [56, 57]. Only statistical errors are shown for the measured values. The measurements are consistent with these parameterizations to within $\pm 10\%$.

# 6. Results

## 6.1 Overview

In this chapter, the differential and integrated cross sections and structure functions obtained from the experiment are shown along with theoretical predictions and extrapolations of fit to world data at higher $W$. A study of systematic uncertainties is also presented.

## 6.2 Differential Cross Sections

The reduced differential cross section for the reaction are computed for each kinematic bin. This cross section includes all corrections and normalization factors discussed

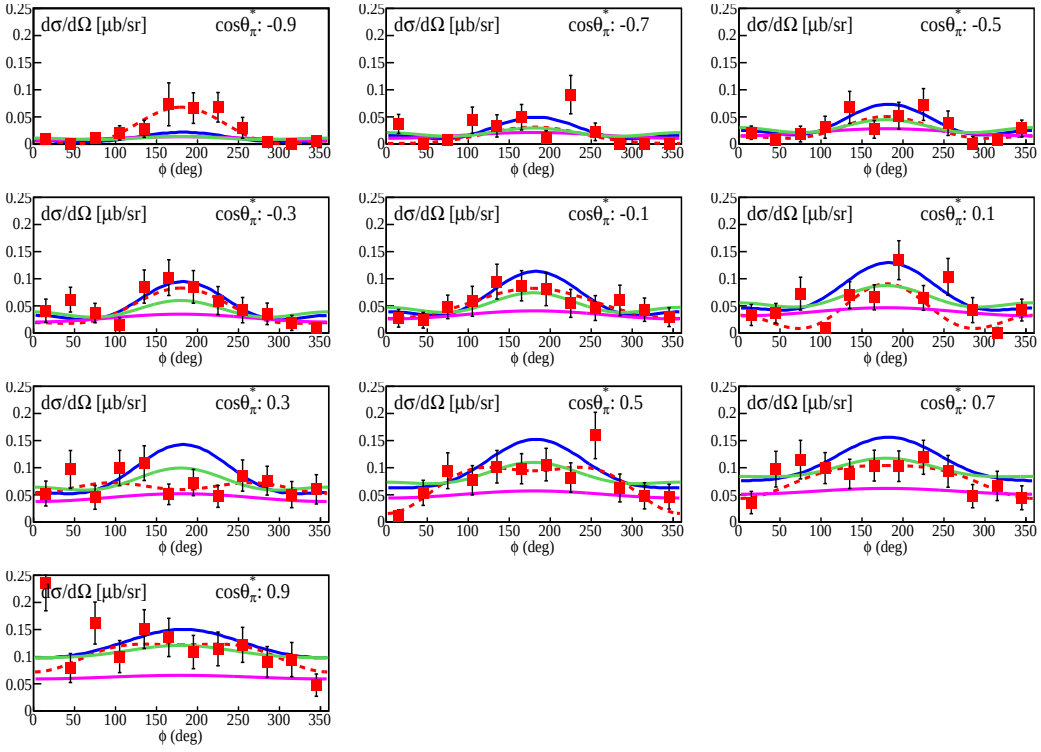


**Figure 6.1: The differential cross sections in $\mu$b/sr for $W = 1.09$ GeV and $Q^2 = 2.75\,\mathrm{GeV}^2$. Each subplot shows cross section for various $\cos\theta^*_\pi$ bin as a function of $\phi^*_\pi$. Experimental points (red) are shown with statistical errors only. The red dashed curve is a fit to the cross section as in Eq. 6.2. Predictions from Braun *et al* (magenta) as well as extrapolations of fit to world data at higher $W$ from MAID2007 (blue) and Aznauryan *et al* (green) are shown.**

in the previous chapters.

Fig. 6.1 shows the differential cross section for the kinematic bin nearest threshold, *viz.*, $W = 1.09$ GeV and $Q^2 = 2.75\,\mathrm{GeV}^2$. The results from experiment are shown as red points with statistical errors. One can observe that the cross section is more-or-less symmetric in $\phi_\pi^*$ but is reduced for backward angles in $\theta_\pi^*$. Some bins show large errors because of small statistical yield from experiment. Some bins have a yield of zero events from experiment but the acceptance is positive definite. For those bins an upper limit on the statistical uncertainty is estimated by assuming a yield of one event. The cross section for these bins is reported as zero with a statistical uncertainty for a experimental yield of one event.

The predictions from Braun *et al* [17] are shown as the magenta curves in the figure. The extrapolations of fit to world data at higher $W$ from MAID2007 [44] and Aznauryan *et al* [55] are shown as blue and green curves, respectively. One can observe a large discrepancy with the predictions of Braun near $\phi_\pi^* \sim 180^\circ$. This is because the predictions do not include enough P-wave contribution to the cross section. This should be reflected in the associated $\sigma_{LT}$ structure functions that can be extracted from the differential cross section via the following prescription as defined in Section 1.1.2:

$$\frac{d\sigma}{d\Omega_\pi^*} = \frac{p_\pi^*}{k_\gamma^*}\left(\frac{d\sigma_T}{d\Omega_\pi^*} + \varepsilon_L\frac{d\sigma_L}{d\Omega_\pi^*} + \varepsilon\frac{d\sigma_{TT}}{d\Omega_\pi^*}\cos 2\phi_\pi^* + \sqrt{2\varepsilon_L(\varepsilon+1)}\frac{d\sigma_{LT}}{d\Omega_\pi^*}\cos\phi_\pi^*\right). \tag{6.1}$$

Using this prescription, the differential cross section can be fitted with the following parameterization:

$$\frac{d\sigma}{d\Omega_\pi^*} = \frac{p_\pi^*}{k_\gamma^*}\left(A + \varepsilon B\cos 2\phi_\pi^* + \sqrt{2\varepsilon_L(\varepsilon+1)}C\cos\phi_\pi^*\right). \tag{6.2}$$

Here, $A$, $B$ and $C$ are the parameters of the fit and are equivalent to $\sigma_T + \varepsilon_L\sigma_L$, $\sigma_{TT}$ and $\sigma_{LT}$, respectively. The result of the fit is shown as the red dashed curves in Fig. 6.1. Please see Appendix D for differential cross sections for all kinematic bins in $W$ and $Q^2$.

Fig. 6.2 shows the $\chi^2$ distribution per number of degrees of freedom $\nu$ for the four $W$ bins near threshold obtained from the fitting result. The red curve is the expected distribution [36] based on the degrees of freedom for each fit. The expected distribution is a probability distribution function

$$f(x;\nu) = N\frac{x^{\nu/2-1}e^{-x/2}}{2^{\nu/2}\Gamma(\nu/2)} \tag{6.3}$$

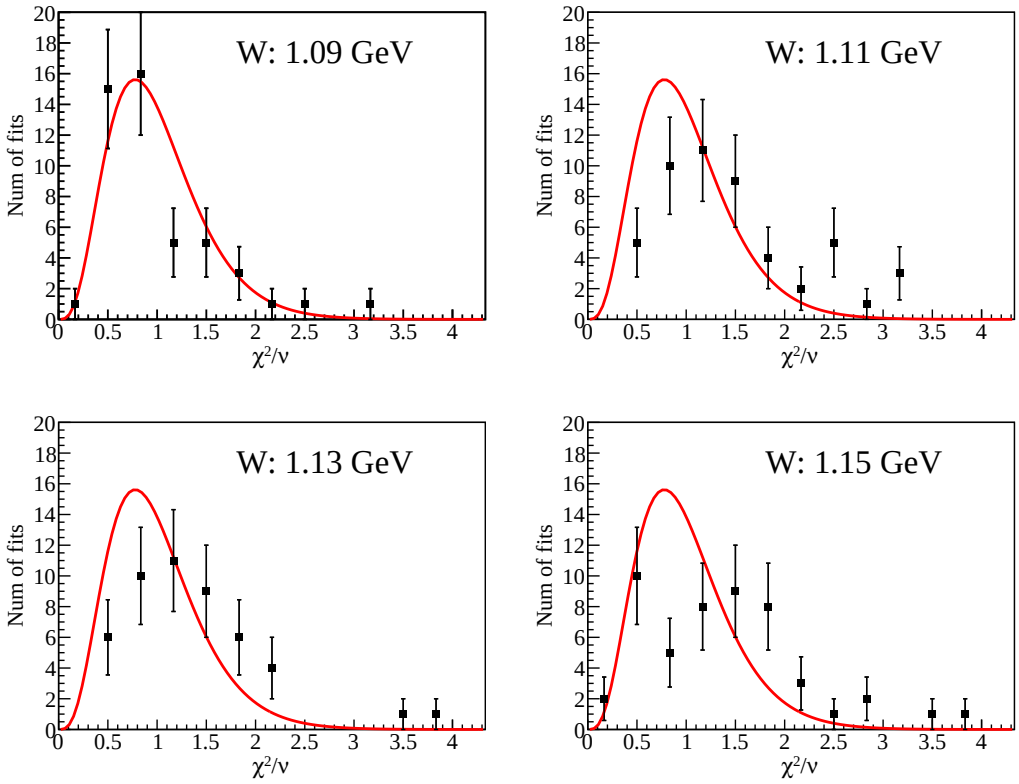


**Figure 6.2: The number of fits to the differential cross section using Eq. 6.2 are plotted as a function of the $\chi^2/\nu$. The expected $\chi^2$ distribution for 50 fits (5 $Q^2$ bins and 10 $\cos\theta^*_\pi$ bins) and $\nu = 9$ degrees of freedom is shown as the red curve.**

where $x$ is the value of $\chi^2$, $\nu$ is the number of degrees of freedom and $N$ is the normalization constant for the distribution. The differential cross section is fit using 3 parameters for each of the 10 $\cos\theta^*_\pi$ bins as a function of 12 $\phi^*_\pi$ bins. So, a total of 200 functions are fitted in $W$, $Q^2$ and $\cos\theta^*_\pi$ bins with the number of degrees of freedom $\nu = 9$ for each function.

## 6.3 Integrated Cross Sections

The integrated cross sections for the reduced process $\gamma^* p \rightarrow p\pi^0$ is obtained by integrating the fitted function Eq. 6.2 over the solid angle $d\Omega^*_\pi$. Fig. 6.3(a) shows the integrated cross sections as a function $Q^2$ for $W = 1.09$ GeV. The experimental results are shown as red points with associated statistical error bars. The gray band at the bottom shows the systematic error estimates for each kinematic bin. The predictions from Braun *et al* are shown as the magenta curve. One can observe a large discrepancy with these predictions. The extrapolations of fit to world data at higher $W$ from MAID2007 (blue)

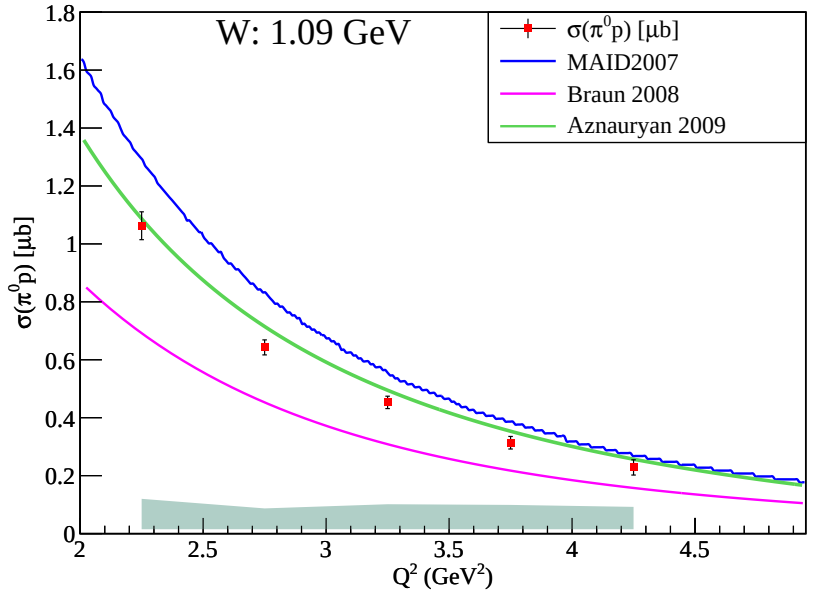


(a)

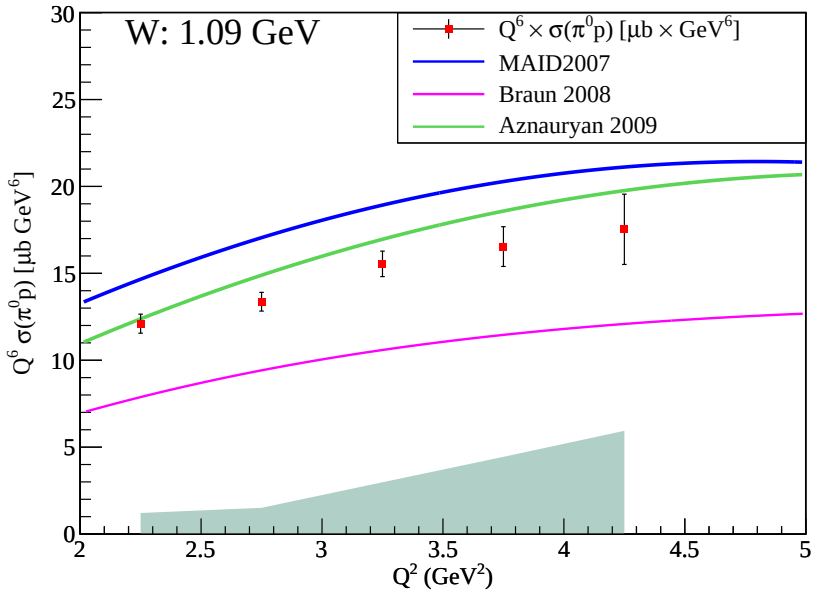


(b)

**Figure 6.3: (a) The integrated reduced cross sections are shown as a function of $Q^2$ for $W = 1.09$ GeV. (b) The integrated cross sections scaled by $Q^6$ at each bin. The results from experiment (red points) are shown along with predictions from Braun *et al* (magenta) and extrapolations of fit to world data at higher $W$ from MAID2007 (blue) and Aznauryan *et al* (green). The gray band at the bottom shows the systematic error estimates for each bin.**

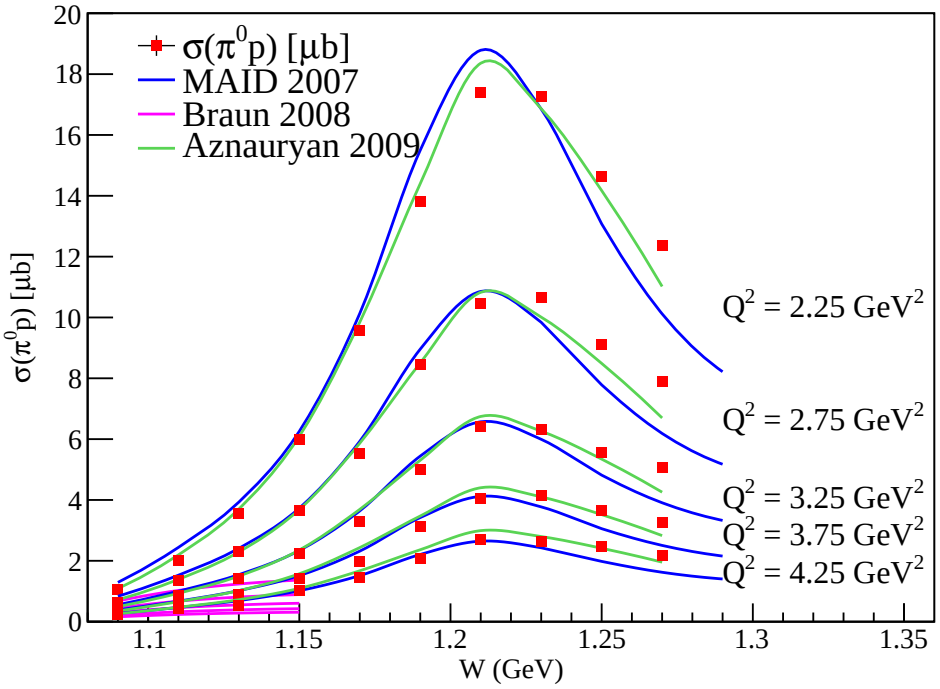


**Figure 6.4: The integrated reduced cross section as a function of $W$ for different values of $Q^2$. Experimental results (red points) are shown along with predictions from Braun *et al* (magenta) and extrapolations of fit to world data at higher $W$ from MAID2007 (blue) and Aznauryan *et al* (green). Predictions from Braun *et al* are only applicable for the near threshold region. The statistical errors are smaller than the data points.**

and Aznauryan *et al* (green) are also shown. Also shown are the same integrated cross sections scaled by $Q^6$ in Fig. 6.3(b).

The integrated cross sections can also be observed in another manner. Fig. 6.4 shows the integrated reduced cross section as a function of $W$ for various values of $Q^2$. For comparison predictions from Braun *et al* (magenta) and from MAID2007 (blue) and Aznauryan *et al* (green) are also shown. The predictions from Braun *et al* are only plotted up to $W = 1.16$ GeV as they are not applicable near the $\Delta(1232)$ resonance region. One can observe good agreement of the measurements at higher $W$ with the blue and green curves.

Fig. 6.5 shows the same information as Fig. 6.4 but zoomed into the near threshold region with each $Q^2$ bin separated into subplots. For the $W = 1.09$ GeV bin, the agreement with Braun *et al* is better than at higher $W$. One of the reasons could be the low estimation

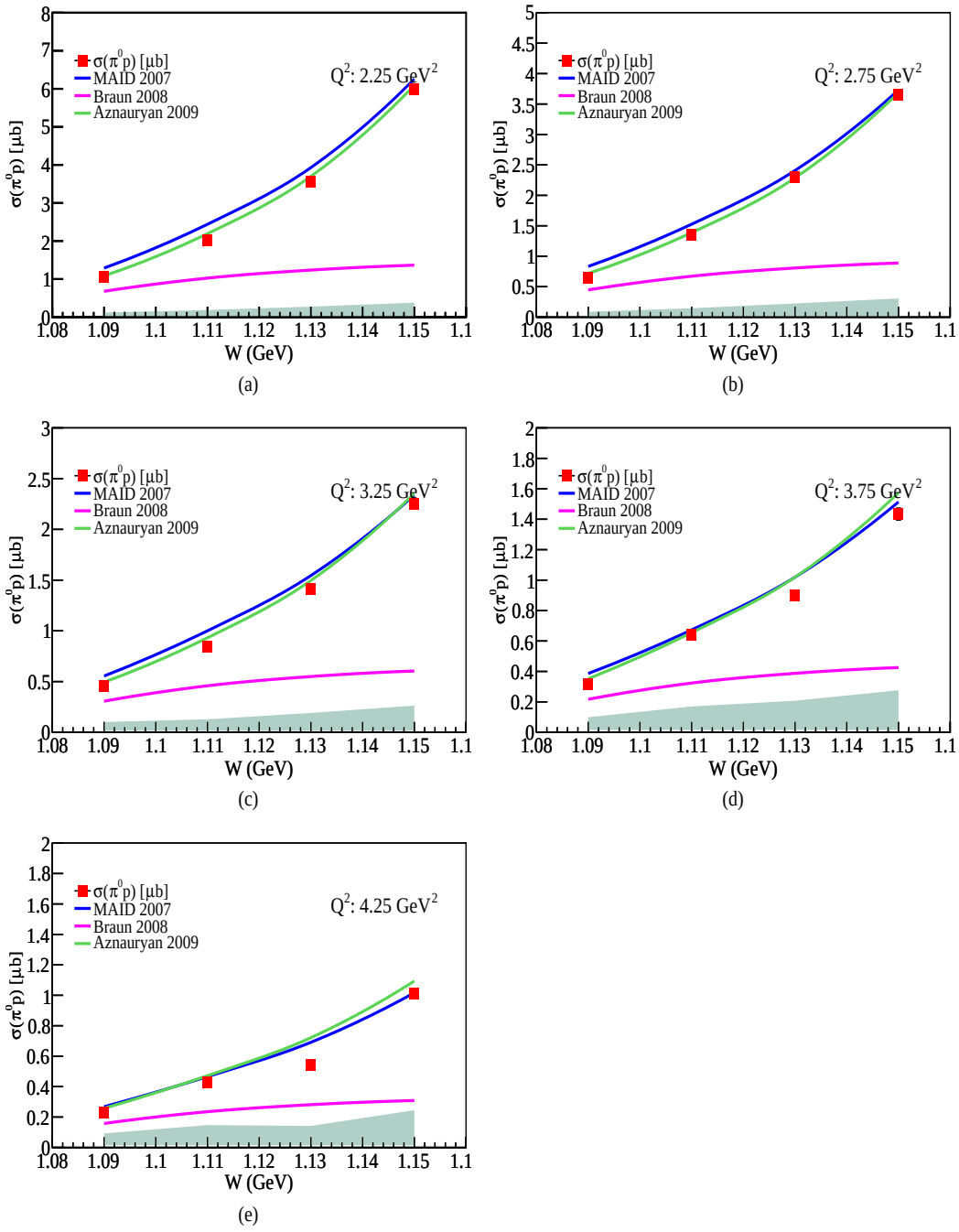


**Figure 6.5: The integrated cross section plotted as a function of $W$ for $Q^2 = 2.25\,\mathbf{GeV}^2$, (b) $Q^2 = 2.75\,\mathbf{GeV}^2$, (c) $Q^2 = 3.25\,\mathbf{GeV}^2$, (d) $Q^2 = 3.75\,\mathbf{GeV}^2$ and (e) $Q^2 = 4.25\,\mathbf{GeV}^2$. Experimental results (red points) are shown along with predictions from Braun *et al* (magenta) and extrapolations of fit to world data at higher $W$ from MAID2007 (blue) and Aznauryan *et al* (green). The statistical errors are smaller than the data points. The gray band at the bottom shows the systematic error estimates for each bin.**

of P-wave contribution to the cross section in the predictions.

## 6.4 Structure Functions

Now let us look at the extracted structure functions. Fig. 6.6 shows the structure functions for $W = 1.09$ GeV and different $Q^2$ bins. The left, middle and right columns show $\frac{d\sigma_T}{d\Omega} + \varepsilon_L \frac{d\sigma_L}{d\Omega}$, $\frac{d\sigma_{TT}}{d\Omega}$ and $\frac{d\sigma_{LT}}{d\Omega}$, respectively. The experimental results are shown in red with statistical error bars. The gray box indicates the systematic uncertainty estimates for each bin. The extrapolations of fit to world data at higher $W$ from MAID2007 (blue) and Aznauryan *et al* (green) are also shown.

In addition, predictions from Braun *et al* are shown as the magenta curves for $\frac{d\sigma_T}{d\Omega} + \varepsilon_L \frac{d\sigma_L}{d\Omega}$ and $\frac{d\sigma_{LT}}{d\Omega}$. Since Braun *et al* assume no D-wave contribution, the corresponding structure function $\frac{d\sigma_{TT}}{d\Omega}$ predictions are assumed to be zero and are not shown in the figure. One can observe that there is some $\frac{d\sigma_{TT}}{d\Omega}$ contribution present in our experimental results. Also, the results for $\frac{d\sigma_{LT}}{d\Omega}$, which correspond to the P-wave contributions, show inconsistency with the magenta curves. As hypothesized, the P-wave contribution predictions to the cross sections are smaller than observed.

## 6.5 Systematic Uncertainties

The systematic uncertainties are those uncertainties that are inherent in an experiment and cannot be remedied by repeating the experiment. They depend on the types of cuts used in the analysis to the calibration of the detectors. To determine these uncertainties, the parameters of the likely sources of these errors are varied within reasonable bounds and the sensitivity of the final result is checked against this variation. If the final

| **Source** | **Average Size %** |
|---|---|
| EC sampling fraction cuts | 0.4 |
| CC cuts | 0.1 |
| Vertex cuts | 0.1 |
| DC cuts | 1 |
| Proton ID | 1.1 |
| Bethe-Heitler subtraction | $\sim 7$ |
| $M_X^2$ | $\sim 5$ |
| Elastic normalization | 5 |
| Empty target | 2 |

**Table 6.1: The systematic errors for cross sections. The average size of the errors is the final estimated error on the experimental result.**

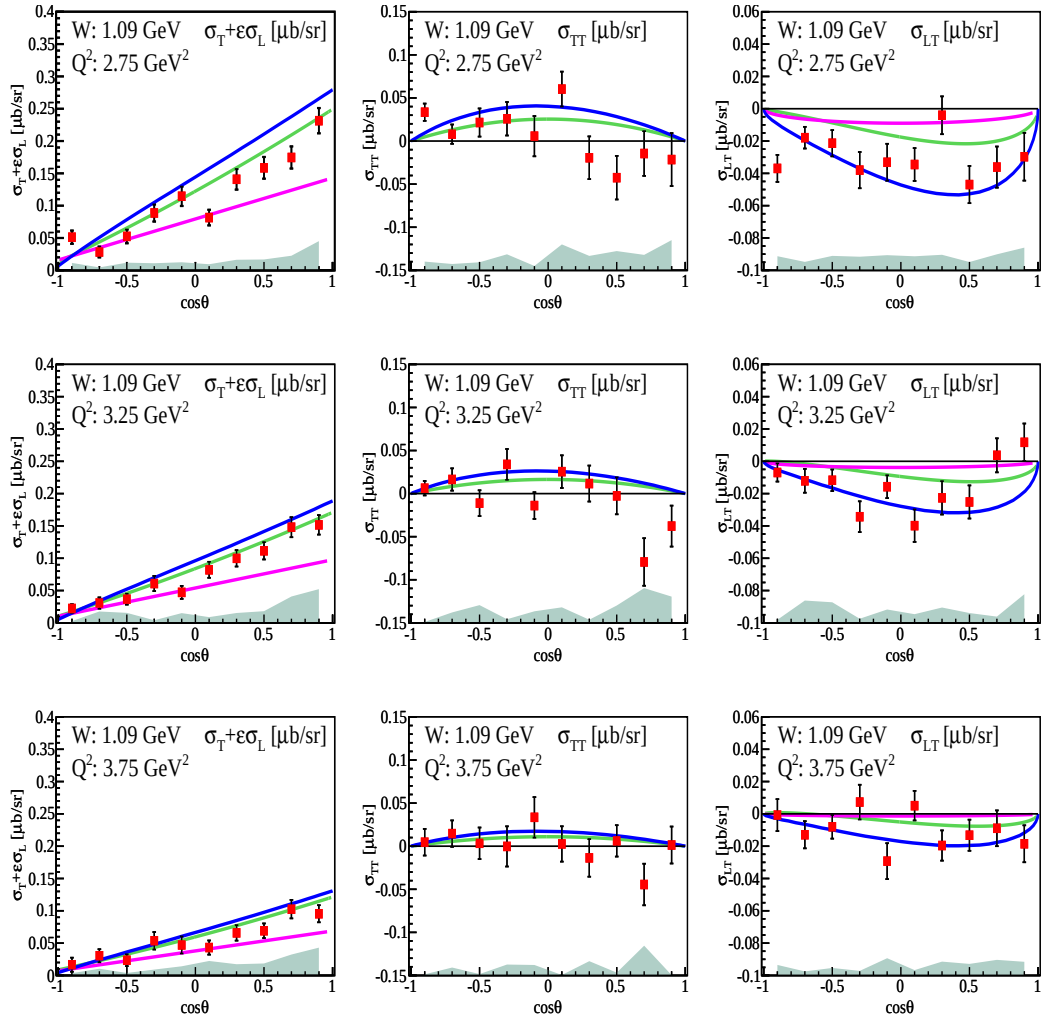


**Figure 6.6: The structure functions $\frac{d\sigma_T}{d\Omega} + \varepsilon_L \frac{d\sigma_L}{d\Omega}$ (left), $\frac{d\sigma_{TT}}{d\Omega}$ (middle) and $\frac{d\sigma_{LT}}{d\Omega}$ (right) as a function of $\cos\theta^*_\pi$ in $\mu$b/sr for $W = 1.09$ GeV and different $Q^2$ bins. Experimental results (red) are shown along with predictions from Braun *et al* (magenta) and extrapolations of fit to world data at higher $W$ from MAID2007 (blue) and Aznauryan *et al* (green). The Braun *et al* predictions do not include any $\sigma_{TT}$ contribution, so they are not shown. The gray band shows the systematic uncertainty estimates for each bin. Note the different scales for the $y$-axis for each column.**

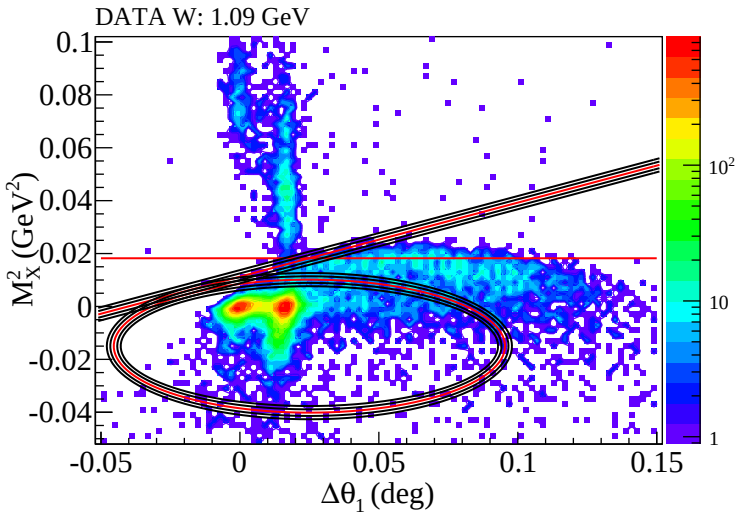


**Figure 6.7: The variations in the Bethe-Heitler subtractions cuts for $W = 1.09$ GeV. The $M_X^2$ is plotted as a function of $\Delta\theta_1$. The nominal cut is shown in red.**

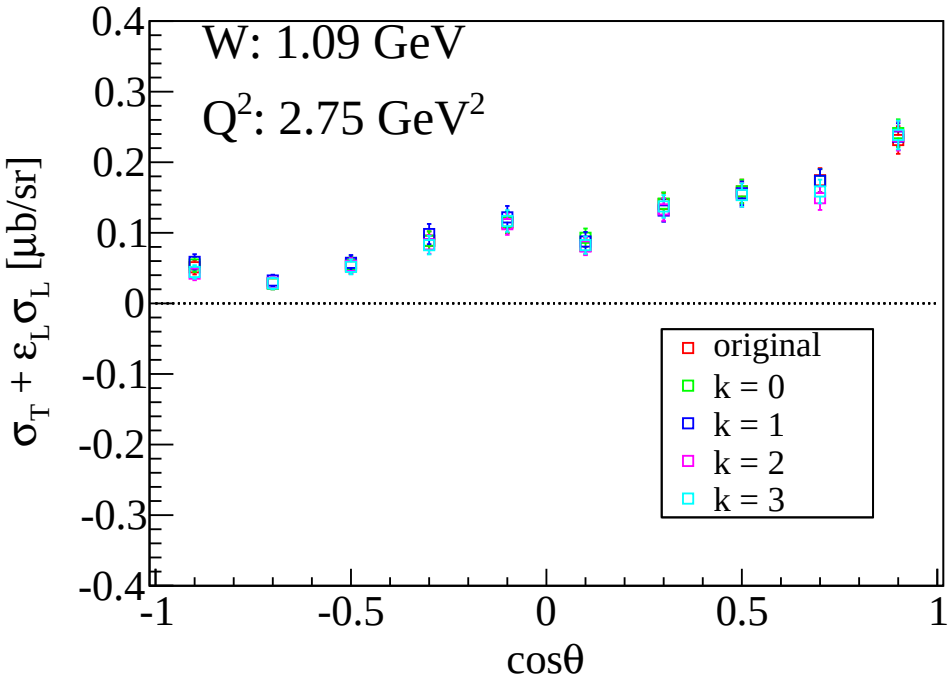


**Figure 6.8: The dependence of the Bethe-Heitler subtraction cuts is shown on the extracted $\sigma_T + \epsilon_L \sigma_L$ for $W = 1.09$ GeV and $Q^2 = 2.75\,\mathrm{GeV}^2$. The different colors indicate the variation in the cut. The results from the original cut are shown in red.**

result is not very sensitive to this variation then the systematic error due to this source can be considered to be small.

The structure functions were looked for sensitivity to these sources of errors. The results showed very little sensitivity to the sampling fraction cuts for the electromagnetic calorimeters (EC), the Cerenkov counter (CC) cuts, the drift chambers (DC) cuts, the cuts on the $z$-vertex of the electrons and protons, and the proton identification cuts. On average, these cuts had a systematic uncertainty of around 1%. The Bethe-Heitler subtraction cuts and the missing mass cuts were the sources of the largest errors in the experiment. Table 6.1 shows a summary of the average uncertainties for each source.

The largest source of the systematic uncertainty comes from the Bethe-Heitler subtraction cuts. Fig. 6.7 shows the variation of these cuts for the nearest threshold bin $W = 1.09$ GeV. The red curves are the nominal cuts. The result of the variation in these cuts is shown at the structure function level in Fig. 6.8. In this figure, the structure functions $\sigma_T + \varepsilon_L \sigma_L$ are plotted for varying Bethe-Heitler subtraction cuts. There is some kinematic dependence on this cut as can be observed from the plot. On average this cut gives about a 7% systematic uncertainty in the result.

The other large source of systematic uncertainty comes from the cut on the $M_X^2$ variable. The nominal cut is a $\pm 3\sigma$ cut from the mean value of the distribution and is a function of $W$ and $Q^2$. The cut is varied as shown in Fig. 6.9 for one of the $W$ and $Q^2$ bins. The result of these variations is seen in the Fig. 6.10 where the $\sigma_T + \varepsilon_L \sigma_L$ are plotted for the same kinematic bin. Once again there is some kinematic dependence on this cut. The average systematic uncertainty from this cut is about 5%.

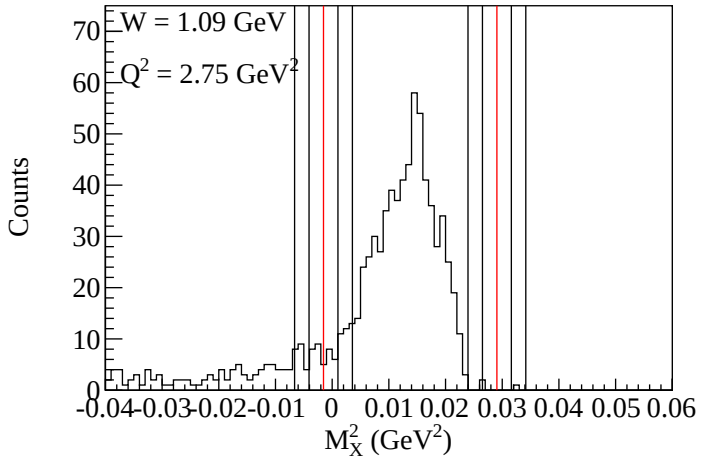


**Figure 6.9: The variations in the $M_X^2$ cuts for $W = 1.09$ GeV and $Q^2 = 2.75\,\mathrm{GeV}^2$. The nominal cut is shown in red.**

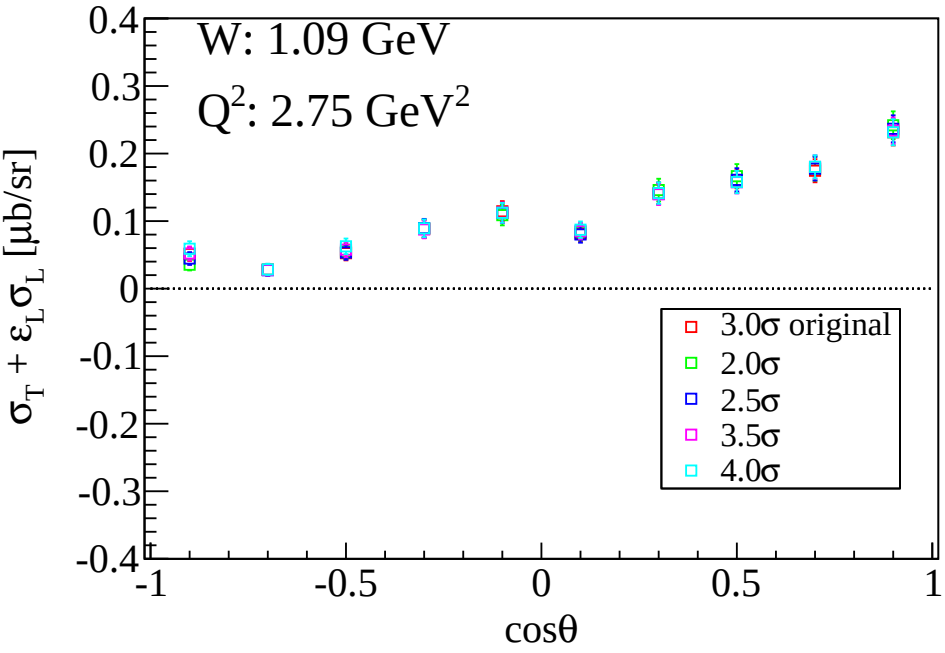


**Figure 6.10: The dependence of the $M_X^2$ cuts is shown on the extracted $\sigma_T + \epsilon_L\sigma_L$ for $W = 1.09$ GeV and $Q^2 = 2.75\,\mathrm{GeV}^2$. The different colors indicate the variation in the cut. The results from the original cut are shown in red.**

## 6.6 Multipoles

The parameters of the fit for the differential cross sections (Eq. 6.2) are functions of $\cos\theta_\pi^*$ and can be expressed in terms of Legendre polynomials:

$$\begin{aligned}
\frac{d\sigma_T}{d\Omega_\pi^*} + \varepsilon_L \frac{d\sigma_L}{d\Omega_\pi^*} &= A(\cos\theta_\pi^*) = \quad A_0 + A_1 P_1(\cos\theta_\pi^*) + A_2 P_2(\cos\theta_\pi^*) \\
\frac{d\sigma_{TT}}{d\Omega_\pi^*} &= B(\cos\theta_\pi^*) = \quad B_0 \sin^2\theta_\pi^* \\
\frac{d\sigma_{LT}}{d\Omega_\pi^*} &= C(\cos\theta_\pi^*) = \quad (C_0 + C_1\cos\theta_\pi^*)\sin\theta_\pi^*
\end{aligned} \tag{6.4}$$

The polynomials are expanded up to the second order to include terms only from $l = 0$ and $l = 1$ multipoles since these are the only multipoles expected to contribute in the near threshold region. The coefficients of the polynomials from Eq. 6.4 can be associated with these multipoles:

$$\begin{aligned}
A_0 &= |E_{0+}|^2 + |M_{1-}|^2 + \frac{5}{2}|M_{1+}|^2 + \frac{9}{2}|E_{1+}|^2 - 3Re(E_{1+}^* M_{1+}) + Re((3E_{1+} + M_{1+})M_{1-}^*) \\
&\quad + \varepsilon_L \frac{Q^2}{|\mathbf{q}^*|^2}(|S_{0+}|^2 + |S_{1-}|^2 + 4|S_{1+}|^2 - 4Re(S_{1+}S_{1-}^*)) \\
A_1 &= 2Re(E_{0+}(3E_{1+} + M_{1+} - M_{1-})^*) + \varepsilon_L \frac{Q^2}{|\mathbf{q}^*|^2} 2Re(S_{0+}(4S_{1+} + S_{1-})^*) \\
A_2 &= -\frac{3}{2}|M_{1+}|^2 + \frac{9}{2}|E_{1+}|^2 + 9Re(E_{1+}^* M_{1+}) - 3Re((3E_{1+} + M_{1+})M_{1-}^*) \\
&\quad + 12\varepsilon_L \frac{Q^2}{|\mathbf{q}^*|^2}(|S_{1+}|^2 + Re(S_{1+}S_{1-}^*)) \\
B_0 &= -\frac{3}{2}|M_{1+}|^2 + \frac{9}{2}|E_{1+}|^2 - 3Re(E_{1+}^* M_{1+}) + 3Re((E_{1+} - M_{1+})M_{1-}^*) \\
C_0 &= -\sqrt{\frac{2Q^2}{|\mathbf{q}^*|^2}} Re(S_{0+}(3E_{1+} - M_{1+} + M_{1-})^* - E_{0+}(2S_{1+} - S_{1-})^*) \\
C_1 &= -6\sqrt{\frac{2Q^2}{|\mathbf{q}^*|^2}} Re(S_{1+}(E_{1+} - M_{1+} + M_{1-})^* + S_{1-}E_{1+}^*).
\end{aligned} \tag{6.5}$$

We are interested in extracting the $E_{0+}$ and $S_{0+}$ ($l = 0$) multipoles. Here, we have associated the $L_{0+}$ with the $S_{0+}$ multipole

$$L_{0+} = \frac{\omega}{|\mathbf{q}^*|} S_{0+} \tag{6.6}$$

where $\omega$ and $\mathbf{q}^*$ are the virtual photon energy and 3-momentum in the center of mass frame.

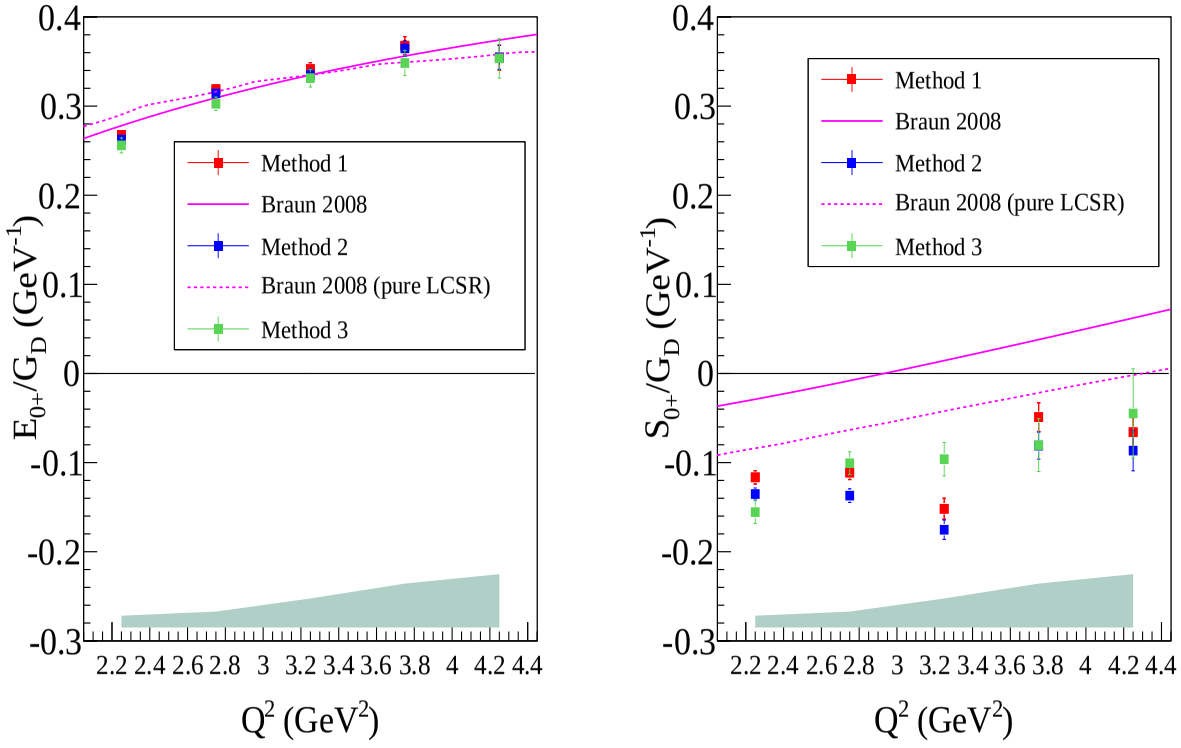


(a) (b)

**Figure 6.11: The S-wave multipoles (a) $E_{0+}$ and (b) $S_{0+}$ normalized to the dipole formula $G_D$ are plotted as a function of $Q^2$. The multipoles are extracted using three methods (red, blue and green points) as indicated in the text. The error bars include systematic and statistical uncertainties added in quadrature. The systematic uncertainties are shown separately as a gray band at the bottom. The LCSR based model predictions from Braun *et al* are shown (magenta) with minimized (solid) and unminimized (dashed) uncertainties in calculations.**

The S-wave multipoles were extracted by one of the CLAS collaborators, I. Aznauryan. Fig. 6.11(a) and Fig. 6.11(b) show the extracted S-wave multipoles $E_{0+}$ and $S_{0+}$ as a function of $Q^2$ using three different methods. These multipoles have been normalized to the dipole formula [50]:

$$G_D(Q^2) = \frac{1}{\left(1 + \frac{Q^2}{.71}\right)^2}. \tag{6.7}$$

The dipole formula is a fit to the electromagnetic form factors as a function of $Q^2$ that describes the shape for the charge distribution in the proton [58].

The three different fit methods include the following prescriptions. Only real parts of $E_{0+}$, $S_{0+}$, $M_{1-}$, $S_{1-}$, $E_{1+}$ and $S_{1+}$ are involved in the fitting. The first method (red points) includes a fit at all $W$ ranges ($W = 1.08 - 1.16$ GeV, current experiment) but $M_{1-}$, $S_{1-}$, $M_{1+}$, $E_{1+}$, and $S_{1+}$ were fitted to world data at higher $W$. The second method (blue points) includes a fit over all $W$ range as in the first method and $M_{1-}$, $M_{1+}$ and $S_{1+}$ were similarly obtained by fit to higher $W$ data. However, the ranges of the amplitudes $S_{1-}$ and $E_{1+}$ are increased by a factor of two to see their effect on current results. The third method (green points) is the same as the second one except that the fit is made only for $W = 1.09$ and 1.11 GeV, *i.e.*, very close to threshold. All three fit methods show consistent results.

The error bars on the points include systematic and statistical uncertainties added in quadrature. The systematic uncertainties are shown separately at the bottom of the plots as a gray band, which assume all systematic errors for all data points are entirely correlated. So, this gives an upper limit on the overall systematic uncertainty. The plots also show predictions from Braun *et al* as magenta curves. Braun *et al* have tried to minimize the uncertainties in their LCSR based model calculations by including electromagnetic form factor values known from experiment. The predictions from these calculations are shown as solid curves in the figure. The "pure" LCSR based models where the calculation uncertainties have not been minimized and the values for all form factors are obtained entirely from theoretical calculations are shown as dashed curves in the figure. One can observe that the experimental results for $E_{0+}$ are consistent with the predictions of Braun *et al* but there is discrepancy with the predictions for $S_{0+}$.

## 6.7 Generalized Form Factors $G_1$ and $G_2$

The S-wave multipoles $E_{0+}$ and $L_{0+}$ can be related to the generalized form factors $G_1^{\pi^0 p}$ and $G_2^{\pi^0 p}$ via Eq. 1.65. These equations can be re-written to obtain expressions of the generalized form factors in terms of the S-wave multipoles. The generalized form factors are thus extracted and plotted for each of the three different methods used to obtain the S-wave multipoles as discussed in the previous section.

Fig. 6.12(a) and (b) show the obtained form factors as a function of $Q^2$. The red, blue and green data points correspond to the three methods of fitting the multipoles. The systematic uncertainties are shown separately at the bottom of the plots as a gray band, which assume all systematic errors for all data points are entirely correlated. Also shown are the predictions from Braun *et al* in magenta for these form factors obtained from his LCSR based models. Similar to the predictions for the multipoles, the dashed curves reflect the calculations where the uncertainties have not been minimized by using experimental values of form factors and other parameters. The solid curves include predictions from the LCSR based model with minimized uncertainties. Additionally, the LET predictions in the chiral limit per Eq. 1.60 are also shown for comparison in blue where existing parameterizations for the elastic form factors [59, 60] have been used.

One can observe that the experimental results for $G_1$ are consistent with the predictions from Braun *et al*, but the results for $G_2$ show some discrepancy. In particular, one can observe a faster fall off than the dipole form for both $G_1$ and $G_2$. However, the zero crossing of $G_2$ is not observed as predicted. This faster than dipole form falling of the generalized form factors suggests a broadening of the spatial distribution of the correlated pion-nucleon system. It suggests that the correlated pion-nucleon system is broader than the nucleon itself because the nucleon follows the behavior of the dipole form factor.

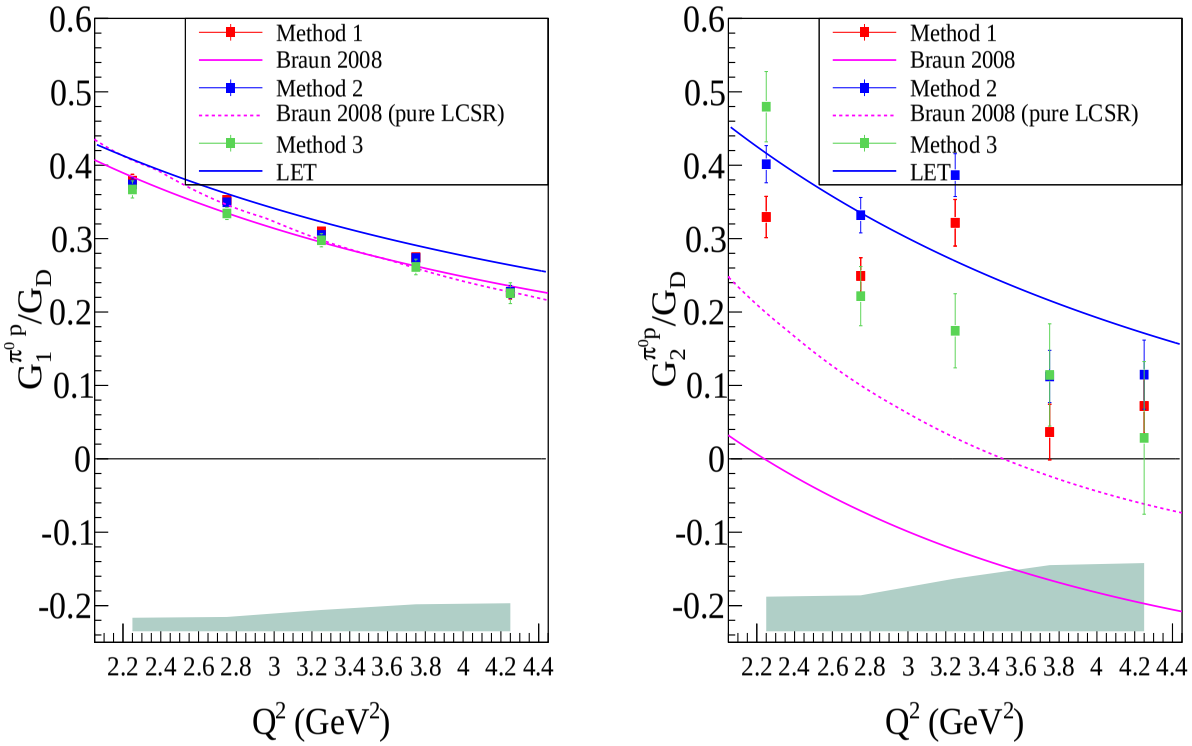


**Figure 6.12:** The generalized form factors (a) $G_1^{\pi^0 p}$ and (b) $G_2^{\pi^0 p}$ normalized to the dipole formula $G_D$ are plotted as a function of $Q^2$. The form factors are calculated from multipoles that are extracted using three methods (red, blue and green points) as indicated in the text. The error bars include systematic and statistical uncertainties added in quadrature. The systematic uncertainties are shown separately as a gray band at the bottom. The LCSR based model predictions from Braun *et al* are shown (magenta-solid) along with estimated uncertainties (magenta-dashed) in calculations. The LET predictions are also shown (blue).

## 7. Discussion and Conclusions

In this thesis, we set out to study the reaction $ep \to ep\pi^0$ in the near threshold region using CLAS data. The differential and integrated cross sections for this reaction are obtained for the reduced process $\gamma^* p \to p\pi^0$. The associated structure functions have also been extracted from the differential cross sections with appropriate systematic uncertainties estimates. Additionally, the S-wave multipoles $E_{0+}$ and $L_{0+}$ are extracted for $Q^2$ between $2-5\,\mathrm{GeV}^2$ by I. Aznuaryan who is one of the CLAS collaborators. From these multipoles the generalized form factors $G_1^{\pi^0 p}(Q^2)$ and $G_2^{\pi^0 p}(Q^2)$ are also extracted as prescribed by Braun *et al.*

The primary aim of the experiment was to test the applicability of the low energy theorems at high $Q^2$ per predictions of Braun *et al.* The structure functions are compared with these predictions. It is noted that the P-wave contribution to the near threshold transition amplitude is quite significant but its contribution is under-estimated by these predictions. The D-wave contribution near threshold was found to be negligible as predicted by Braun *et al.* The measured $E_{0+}$ and $G_1^{\pi^0 p}$ are consistent with the predictions from Braun *et al.* However, $L_{0+}$ and $G_2^{\pi^0 p}$ show discrepancy with these predictions. The faster than dipole form fall off is observed for both these form factors suggesting the broadening of the spatial distribution of the pion-nucleon system.

# REFERENCES


[1] M. Peskin and D. Schroeder. *An Introduction to Quantum Field Theory*. Westview Press, United States of America, 1995.

[2] E. Amaldi, S. Fubini, and G. Furlan. *Pion-Electroproduction*. Springer-Verlag, New York, 1979.

[3] G. F. Chew, M. L. Goldberger, F. E. Low, and Y. Nambu. Relativistic dispersion relation approach to photomeson production. *Phys. Rev.*, 106(6):1345–1355, Jun 1957.

[4] N. M. Kroll and M. A. Ruderman. A theorem on photomeson production near threshold and the suppression of pairs in pseudoscalar theory. *Phys. Rev.*, 93:233, 1954.

[5] D. Drechsel and L. Tiator. Threshold pion photoproduction on nucleons. *J. Phys. G*, 18:449, 1992.

[6] Y. Nambu and D. Lurié. Chirality conservation and soft pion production. *Phys. Rev.*, 125(4):1429, 1962.

[7] Y. Nambu and E. Shrauner. Soft pion emission induced by electromagnetic and weak interactions. *Phys. Rev.*, 128(2):862, 1962.

[8] E. Mazzucato et al. Precise measurement of neutral-pion photoproduction on the proton near threshold. *Phys. Rev. Lett.*, 57(25):3144–3147, Dec 1986.

[9] R. Beck et al. Measurement of the p($\gamma$,$\pi^0$) cross section at threshold. *Phys. Rev. Lett.*, 65(15):1841–1844, Oct 1990.

[10] A. I. Vainshtein and V. I. Zakharov. Low-energy theorems for photo- and electropion production at threshold. *Nucl. Phys. B*, 36:589, 1972.

[11] S. Scherer and J. H. Koch. Pion electroproduction at threshold and pcac. *Nucl. Phys. A*, 534:461, 1991.

[12] T. P. Welch et al. Electroproduction of $\pi^0$ on the proton near threshold. *Phys. Rev. Lett.*, 69(19):2761–2764, Nov 1992.

[13] P. V. Pobylitsa, M. V. Polyakov, and M. Strikman. Soft-pion theorem for hard near-threshold pion production. *Phys. Rev. Lett.*, 87(2):022001, Jun 2001.

[14] A. V. Efremov and A. V. Radyushkin. Factorization and asymptotic behaviour of pion form factor in qcd. *Phys. Lett. B*, 94(2):245–250, Jul 1980.

[15] G. Peter Lepage and Stanley J. Brodsky. Exclusive processes in perturbative quantum chromodynamics. *Phys. Rev. D*, 22(9):2157–2198, Nov 1980.

[16] V. M. Braun, D. Yu. Ivanov, A. Lenz, and A. Peters. Deep inelastic pion electroproduction at threshold. *Phys. Rev. D*, 75:014021, 2007.

[17] V. M. Braun, D. Yu. Ivanov, and A. Peters. Threshold pion electroproduction at large momentum transfers. *Phys. Rev. D*, 77(3):034016, 2008.

[18] A. Hosaka and H. Toki. *Quarks, Baryons and Chiral Symmetry.* World Scientific, New Jersey, 2001.

[19] S. Weinberg. *The Quantum Theory of Fields: Volume II Modern Applications.* Cambridge University Press, New York, 2005.

[20] P. Bopp et al. Beta-decay asymmetry of the neutron and $\frac{g_A}{g_V}$. *Phys. Rev. Lett.*, 56(9):919–922, Mar 1986.

[21] B. R. Holstein. How large is f(pi)? *Phys. Lett.*, B244:83–87, 1990.

[22] M. L. Goldberger and S. B. Treiman. Form factors in $\beta$ decay and $\mu$ capture. *Phys. Rev.*, 111(1):354–361, Jul 1958.

[23] V. Bernard, N. Kaiser, and U. G. Meissner. Chiral dynamics in nucleons and nuclei. *Int. J. Mod. Phys. E*, 4:193, 1995.

[24] V. Bernard, N. Kaiser, J. Gasser, and U. G. Meissner. Neutral pion photoproduction at threshold. *Phys. Lett.*, B268:291–295, 1991.

[25] F. Halzen and A. Martin. *Quarks and Leptons; An Introductory Course in Modern Particle Physics.* John Wiley, 1984.

[26] G. Peter Lepage and Stanley J. Brodsky. Exclusive processes in quantum chromodynamics: The form factors of baryons at large momentum transfer. *Phys. Rev. Lett.*, 43(8):545–549, Aug 1979.

[27] M. A. Shifman, A. I. Vainshtein, and V. I. Zakharov. Qcd and resonance physics. theoretical foundations. *Nuclear Physics B*, 147(5):385 – 447, 1979.

[28] B. A. Mecking et al. The CEBAF Large Acceptance Spectrometer (CLAS). *Nucl. Instrum. Meth.*, A503:513–553, 2003.

[29] B. A. Mecking. CEBAF at Jefferson Lab: An overview. Prepared for 3rd Workshop on Chiral Dynamics - Chiral Dynamics 2000: Theory and Experiment, Newport News, Virginia, 17-22 Jul 2000.

[30] M. D. Mestayer et al. The CLAS drift chamber system. *Nucl. Instrum. Meth.*, A449:81–111, 2000.

[31] G. Adams et al. The CLAS Cherenkov detector. *Nucl. Instrum. Meth.*, A465:414–427, 2001.

[32] E. S. Smith et al. The time-of-flight system for CLAS. *Nucl. Instrum. Meth.*, A432:265–298, 1999.

[33] M. Amarian et al. The CLAS forward electromagnetic calorimeter. *Nucl. Instrum. Meth.*, A460:239–265, 2001.

[34] J.J. Manak and E.S. Smith. *CLAS-NOTE 1999-016*. 1999.

[35] C. Smith. Private communication. 2008.

[36] C. Amsler et al. Particle Data Group. *Phys. Lett.*, B667:1, (2008) and 2009 partial update for the 2010 edition.

[37] V. Kubarovsky. Private communication. 2008.

[38] K. Park. Private communication. 2009.

[39] M. Ungaro. *PhD Thesis*. 2003.

[40] M. Osipenko, A. Vlassov, and M. Taiuti. *CLAS-NOTE 2004-020*: Matching between the electron candidate track and the cherenkov counter hit. 2004.

[41] F. X. Girod. Private communication. 2009.

[42] L. I. Schiff. Radiative correction to the angular distribution of nuclear recoils from electron scattering. *Phys. Rev.*, 87(5):750–752, Sep 1952.

[43] R. Ent et al. Radiative corrections for $(e, e'p)$ reactions at gev energies. *Phys. Rev. C*, 64(5):054610, Oct 2001.

[44] D. Drechsel, S. S. Kamalov, and L. Tiator. Unitary Isobar Model - MAID2007. *Eur. Phys. J.*, A34:69–97, 2007.

[45] O. Hanstein, D. Drechsel, and L. Tiator. Multipole analysis of pion photoproduction based on fixed t dispersion relations and unitarity. *Nucl. Phys. A*, 632(4):561 – 606, 1998.

[46] D. Lawrence and M. Mestayer. *CLAS-NOTE: 1999-018*: Clas drift chamber calibration: Software and procedures. 1999.

[47] M. Ungaro and J. Li. *CLAS-NOTE: 2003-006*: Procedure for drift chamber inefficiencies. 2003.

[48] A. Afanasev, I. Akushevich, V. Burkert, and K. Joo. Qed radiative corrections in processes of exclusive pion electroproduction. *Phys. Rev. D*, 66(7):074004, Oct 2002.

[49] M. Ungaro and K. Joo. *CLAS-NOTE: 2010-006*: Meson electro-production radiative corrections based on exclurad. 2010.

[50] B. Povh, K. Rith, C. Scholz, and F. Zetsche. *Particles and Nuclei: An Introduction to the Physical Concepts*. Springer, Germany, 2004.

[51] E. Smith and M. Garcon. Private communication: $http://clasweb.jlab.org/shifts/e1-6/target.html$. 2009.

[52] P. E. Bosted. Empirical fit to the nucleon electromagnetic form factors. *Phys. Rev. C*, 51(1):409–411, Jan 1995.

[53] K. Joo and L.C. Smith. *CLAS-NOTE: 2001-08*: Single $\pi^0$ electroproduction in the $\delta(1232)$ resonance from e1a data. 2001.

[54] M. Ungaro et al. Measurement of the $n \to \delta + (1232)$ transition at high-momentum transfer by $\pi$ electroproduction. *Phys. Rev. Lett.*, 97(11):112003, Sep 2006.

[55] I. G. Aznauryan et al. Electroexcitation of nucleon resonances from clas data on single pion electroproduction. *Phys. Rev. C*, 80(5):055203, Nov 2009.

[56] V. D. Burkert and T.-S. H. Lee. Electromagnetic meson production in the nucleon resonance region. *Int. J. of Mod. Phys. E*, 13(6):1035 – 1111, 2004.

[57] I. G. Aznauryan. Resonance contributions to $\eta$ photoproduction on protons found using dispersion relations and an isobar model. *Phys. Rev. C*, 68(6):065204, Dec 2003.

[58] G. L. Strobel. Proton dipole form-factor quark model. *Int. J. Theor. Phys.*, 35:2443–2454, 1996.

[59] E. J. Brash, A. Kozlov, Sh. Li, and G. M. Huber. New empirical fits to the proton electromagnetic form factors. *Phys. Rev. C*, 65(5):051001, Apr 2002.

[60] O. Gayou et al. Measurement of $gep/gmp$ in $e \to p \to ep \to$ to $q2 = 5.6gev2$. *Phys. Rev. Lett.*, 88(9):092301, Feb 2002.

# APPENDIX A
# Parameters and Plots

## A.1 Electron Sampling Fraction Parameters

The following table includes the parameterization used in Eqn. 3.1 for data.

| Parameters | Sector 1 | Sector 2 | Sector 3 | Sector 4 | Sector 5 | Sector 6 |
|---|---|---|---|---|---|---|
| $\alpha$ | -0.343817 | -0.335113 | -0.105147 | -0.530865 | -0.717546 | -0.539888 |
| $\beta$ | 0.621658 | 0.624218 | 0.419801 | 0.827726 | 0.983963 | 0.819236 |
| $\gamma$ | -0.058496 | -0.198127 | -0.424243 | -0.072115 | -0.062856 | -0.208550 |
| $\delta$ | -0.007746 | -0.041702 | -0.084225 | -0.021155 | -0.012791 | -0.058973 |

**Table A.1: The parameter values for the fit to the mean EC sampling fraction as a function of momentum as in Eq. 3.1 for experimental data.**

| Parameters | Sector 1 | Sector 2 | Sector 3 | Sector 4 | Sector 5 | Sector 6 |
|---|---|---|---|---|---|---|
| $\alpha$ | 0.008597 | 0.002634 | 0.004722 | -0.003629 | 0.025761 | 0.002631 |
| $\beta$ | 0.017859 | 0.037942 | 0.024008 | 0.038488 | -0.003984 | 0.032449 |

**Table A.2: The parameter values for the fit to the $\sigma$ EC sampling fraction as a function of momentum as in Eq. 3.1 for experimental data.**

## A.2 Proton Identification Parameters

The following table includes the parameterization used in Eqn. 3.5 for data.

| Sector | Mean (ns) | | | $\sigma$ (ns) | | |
|---|---|---|---|---|---|---|
| | a | b | c | a | b | c |
| 1 | -0.00402265 | 0.00551451 | 3.71989 | 0.2688910 | 0.1152970 | 2.009410 |
| 2 | -0.04468180 | 0.07991310 | 1.26776 | 0.2504400 | 0.0958828 | 2.259890 |
| 3 | -0.01711960 | 0.03245160 | 2.36276 | 0.2424720 | 0.1023070 | 2.087400 |
| 4 | 0.00217212 | 0.00767888 | 3.37383 | 0.2114360 | 0.1663010 | 1.689670 |
| 5 | -0.00169582 | 0.00109138 | 4.82923 | 0.1922650 | 0.1839430 | 1.613480 |
| 6 | 0.00840152 | 0.00253274 | 4.39880 | 0.0911354 | 0.4030660 | 0.918139 |

**Table A.3: The parameter values for the mean and sigma as in Eq. 3.5 used for proton ID for each sector for experimental data.**

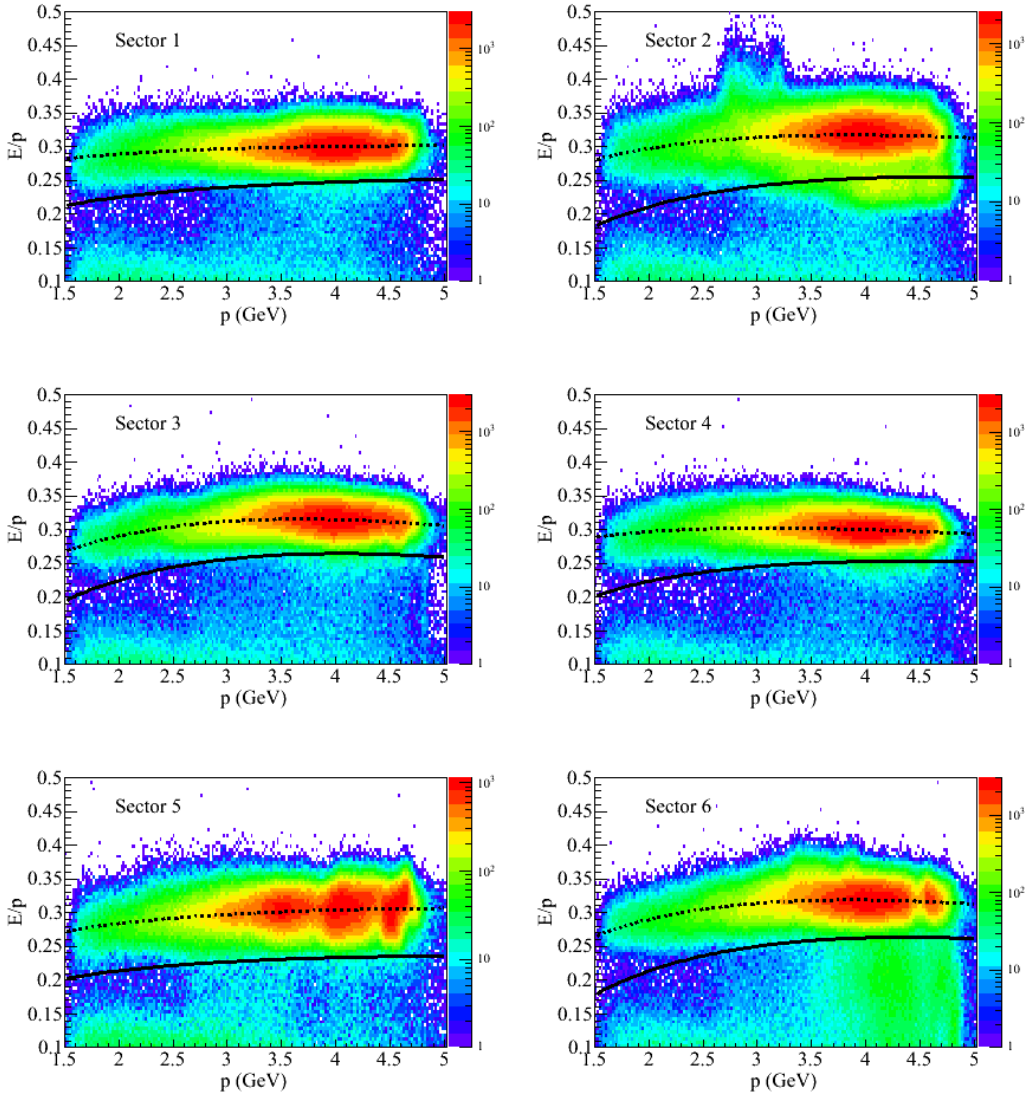


**Figure A.1: Sampling fraction $E/p$ for electron candidates plotted as a function of their momentum $p$ for the six sectors. The mean parameterization is shown as dashed curves and the solid curves indicate the cuts applied.**

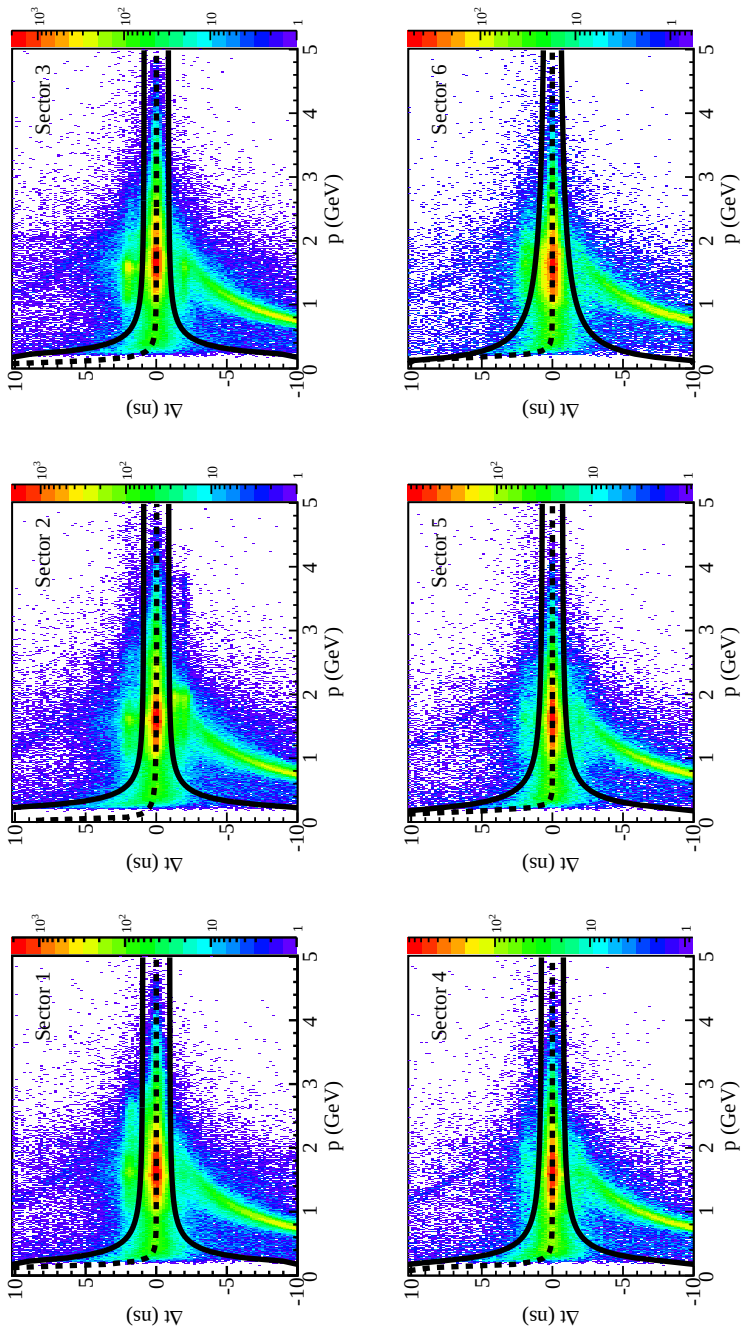


**Figure A.2:** $\Delta t$ **as a function of** $p$ **with curves of fit showing** $\pm 3.5\sigma$ **cut (solid lines) from the mean fit (dashed lines) for each sector.**

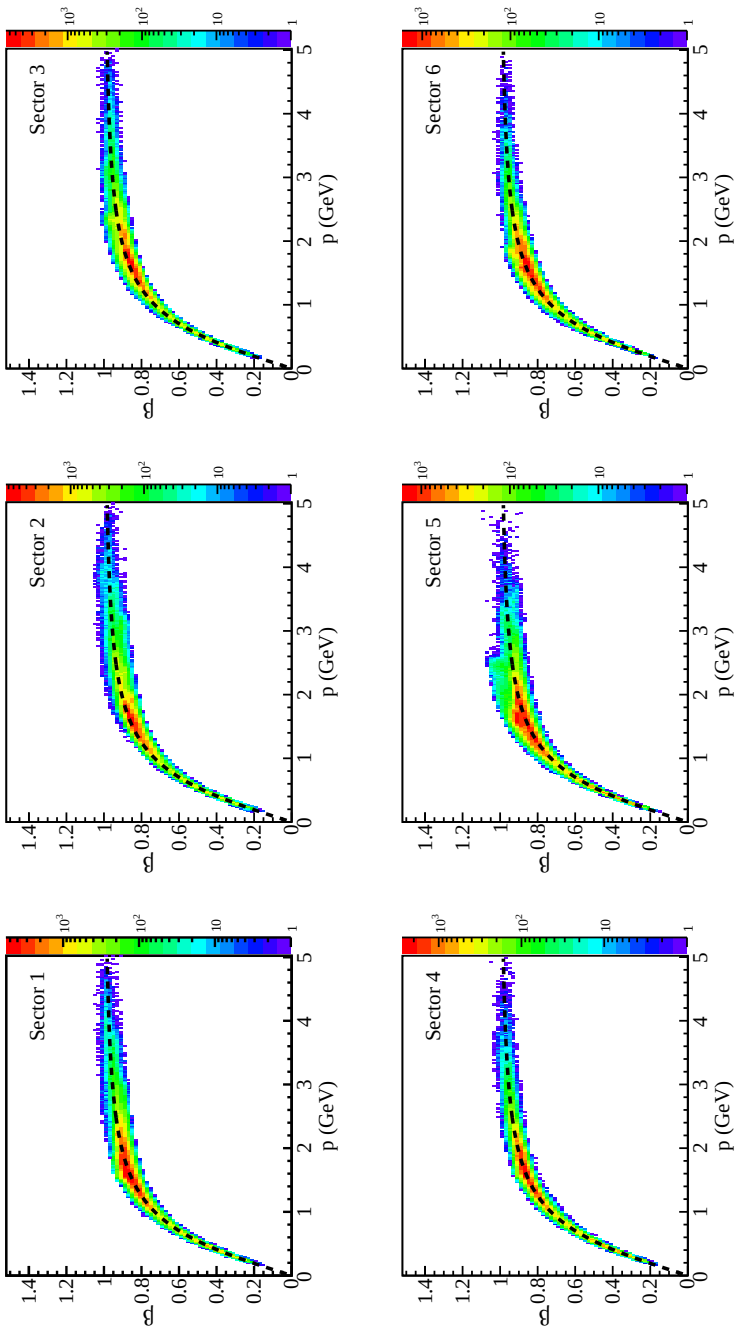


**Figure A.3: The measured $\beta$ as a function of $p$ after proton selection for each sector. The dashed curve is the expected theoretical proton profile.**

## A.3 DC Fiducial Cut Parameters

### A.3.1 DC Electron Fiducial Cuts

The following parameter values were used for electron fiducial cuts:

| Sector | $\alpha$ | $\beta$ | $\gamma$ | $\rho$ | $\kappa$ | $\xi$ |
|---|---|---|---|---|---|---|
| 1 | 12.0 | 20.0 | 0.32 | 32.0 | 0.416667 | 0.14 |
| 2 | 12.0 | 20.7 | 0.36 | 34.0 | 0.416667 | 0.14 |
| 3 | 12.0 | 20.2 | 0.32 | 32.0 | 0.416667 | 0.14 |
| 4 | 12.0 | 20.5 | 0.32 | 32.0 | 0.416667 | 0.14 |
| 5 | 12.0 | 20.5 | 0.29 | 32.0 | 0.416667 | 0.14 |
| 6 | 12.0 | 20.0 | 0.32 | 32.0 | 0.416667 | 0.14 |

**Table A.4: The electron fiducial cut parameters for each sector.**

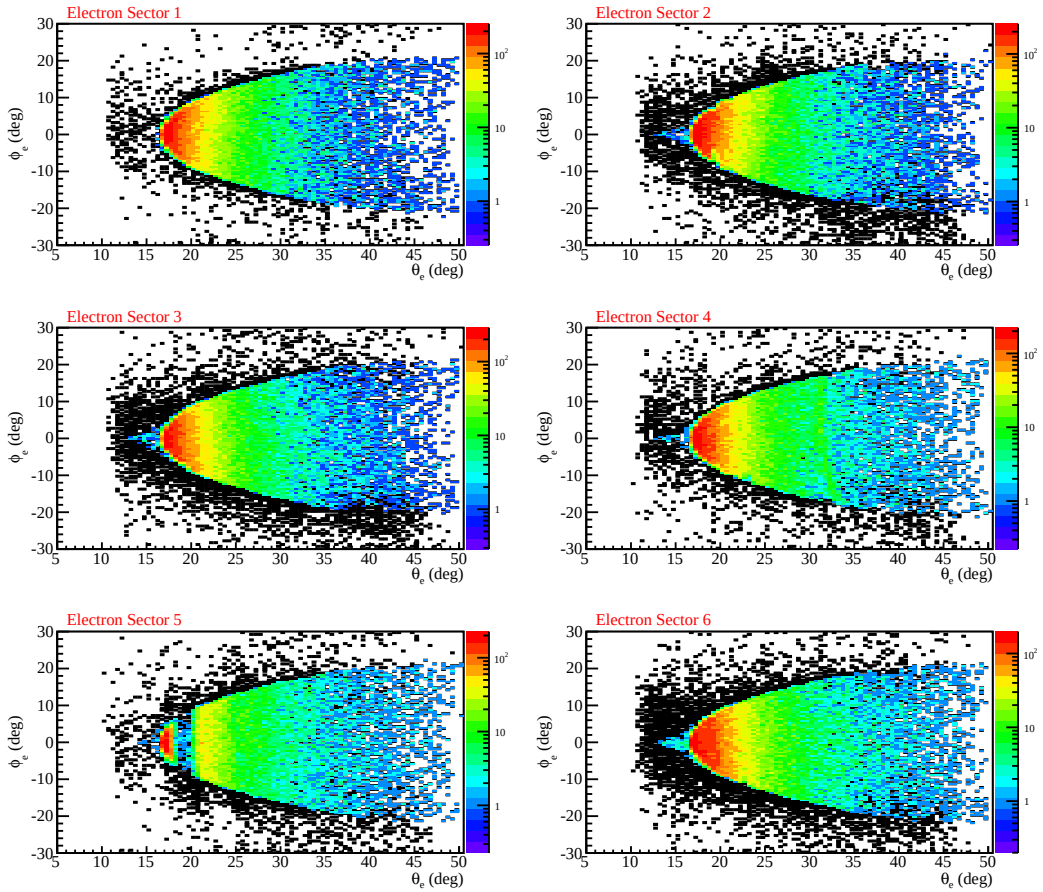


**Figure A.4: Electron DC fiducial cuts for all sectors integrated over all momentum. Rejected tracks are shown in black.**

### A.3.2 DC Proton Fiducial Cuts

The momentum dependent coefficients for the $\phi_{min}$ and $\phi_{max}$ are given by

$$a_i(p) = c_0 + c_1 p + c_2 p^2$$
$$b_i(p) = d_0 + d_1 p + d_2 p^2. \tag{A.1}$$

The following parameter values were used for proton fiducial cuts:

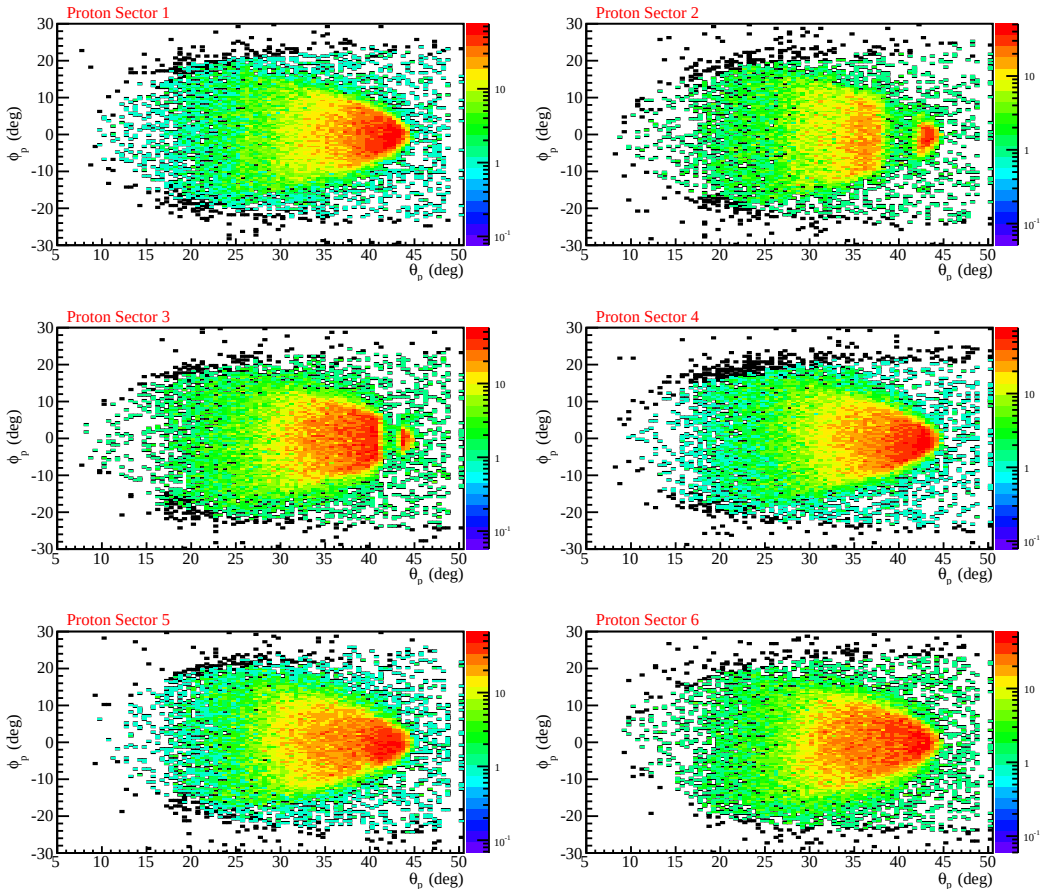


**Figure A.5: Proton DC fiducial cuts for all sectors integrated over all momentum. Rejected tracks are shown in black.**

## A.4 Proton Timing Correction Effects

The timing information for proton candidates in TOF paddles are corrected for all sectors. The effect of this correction is observed for each sector in Figs. A.6 and A.7.

| $i$ | $c_0$ | $d_0$ | $c_1$ | $d_1$ | $c_2$ | $d_2$ |
|---|---|---|---|---|---|---|
| 0 | 39.4471 | -1.42891 | -4.28941 | -20.8695 | 0.0910672 | 4.85237 |
| 1 | -5.95718 | -0.40323 | -0.0915413 | 4.15143 | 0.113486 | -0.873097 |
| 2 | 0.233019 | 0.0877448 | 0.010272 | -0.206594 | -0.00585689 | 0.0422065 |
| 3 | -0.0043921 | -0.00209527 | -4.57015e-05 | 0.0038365 | 8.66512e-05 | -0.000787643 |
| 4 | 3.22474e-05 | 1.40471e-05 | -1.63838e-06 | -2.40801e-05 | -2.99613e-07 | 5.06479e-06 |

**Table A.5: Sector 1 parameters used for proton fiducial cuts.**

| $i$ | $c_0$ | $d_0$ | $c_1$ | $d_1$ | $c_2$ | $d_2$ |
|---|---|---|---|---|---|---|
| 0 | 44.2525 | 4.94857 | -8.53036 | -20.3406 | 0.481749 | 4.03726 |
| 1 | -6.9053 | -1.97407 | 0.769652 | 4.2043 | 0.00638363 | -0.753544 |
| 2 | 0.281855 | 0.184416 | -0.0321893 | -0.218929 | -0.000844245 | 0.0372669 |
| 3 | -0.00536168 | -0.0045072 | 0.000722783 | 0.00432631 | 1.03893e-05 | -0.000703947 |
| 4 | 3.88746e-05 | 3.6027e-05 | -6.23593e-06 | -3.06811e-05 | 1.41789e-08 | 4.85139e-06 |

**Table A.6: Sector 2 parameters used for proton fiducial cuts.**

| $i$ | $c_0$ | $d_0$ | $c_1$ | $d_1$ | $c_2$ | $d_2$ |
|---|---|---|---|---|---|---|
| 0 | 48.8643 | 13.224 | -13.6046 | -22.7071 | 1.54434 | 3.47116 |
| 1 | -8.14818 | -2.07311 | 1.59337 | 3.88685 | -0.16267 | -0.529604 |
| 2 | 0.370884 | 0.177999 | -0.0920444 | -0.193177 | 0.01175 | 0.0225649 |
| 3 | -0.00764513 | -0.00419906 | 0.00230433 | 0.00365751 | -0.000322689 | -0.000357837 |
| 4 | 5.84148e-05 | 3.1048e-05 | -2.01461e-05 | -2.34094e-05 | 2.93282e-06 | 1.75395e-06 |

**Table A.7: Sector 3 parameters used for proton fiducial cuts.**

| $i$ | $c_0$ | $d_0$ | $c_1$ | $d_1$ | $c_2$ | $d_2$ |
|---|---|---|---|---|---|---|
| 0 | 42.7907 | -14.6804 | 0.557686 | -4.28155 | -1.93386 | 0.545166 |
| 1 | -7.06612 | 2.32197 | -0.589287 | 0.811594 | 0.366981 | -0.0287077 |
| 2 | 0.301463 | -0.0327651 | 0.0330414 | -0.0501169 | -0.0179363 | -0.000611366 |
| 3 | -0.00580282 | -0.000419906 | -0.000743318 | 0.00126087 | 0.000384465 | 2.22975e-05 |
| 4 | 4.16703e-05 | 8.18104e-06 | 5.97558e-06 | -1.03781e-05 | -3.01804e-06 | -2.27518e-07 |

**Table A.8: Sector 4 parameters used for proton fiducial cuts.**

| $i$ | $c_0$ | $d_0$ | $c_1$ | $d_1$ | $c_2$ | $d_2$ |
|---|---|---|---|---|---|---|
| 0 | 52.0838 | 4.57043 | -15.8603 | -17.2084 | 1.38223 | 2.43805 |
| 1 | -8.31577 | -0.143877 | 3.14067 | 2.7247 | -0.389671 | -0.325088 |
| 2 | 0.393192 | 0.0654633 | -0.22493 | -0.1203 | 0.0333465 | 0.00937443 |
| 3 | -0.00862513 | -0.00157316 | 0.00610496 | 0.00175928 | -0.000950539 | 1.01077e-05 |
| 4 | 7.12059e-05 | 1.11448e-05 | -5.65199e-05 | -7.58069e-06 | 8.93644e-06 | -1.50299e-06 |

**Table A.9: Sector 5 parameters used for proton fiducial cuts.**

| $i$ | $c_0$ | $d_0$ | $c_1$ | $d_1$ | $c_2$ | $d_2$ |
|---|---|---|---|---|---|---|
| 0 | 66.7155 | -4.17306 | -22.5136 | -17.1484 | 4.17892 | 3.71364 |
| 1 | -10.6179 | -0.407384 | 4.06603 | 4.34246 | -0.859252 | -0.834831 |
| 2 | 0.47953 | 0.122555 | -0.249083 | -0.258914 | 0.0558406 | 0.0479698 |
| 3 | -0.00970942 | -0.00360644 | 0.00620864 | 0.00583929 | -0.00141667 | -0.00107312 |
| 4 | 7.30481e-05 | 3.08354e-05 | -5.37051e-05 | -4.52976e-05 | 1.23011e-05 | 8.33686e-06 |

**Table A.10: Sector 6 parameters used for proton fiducial cuts.**

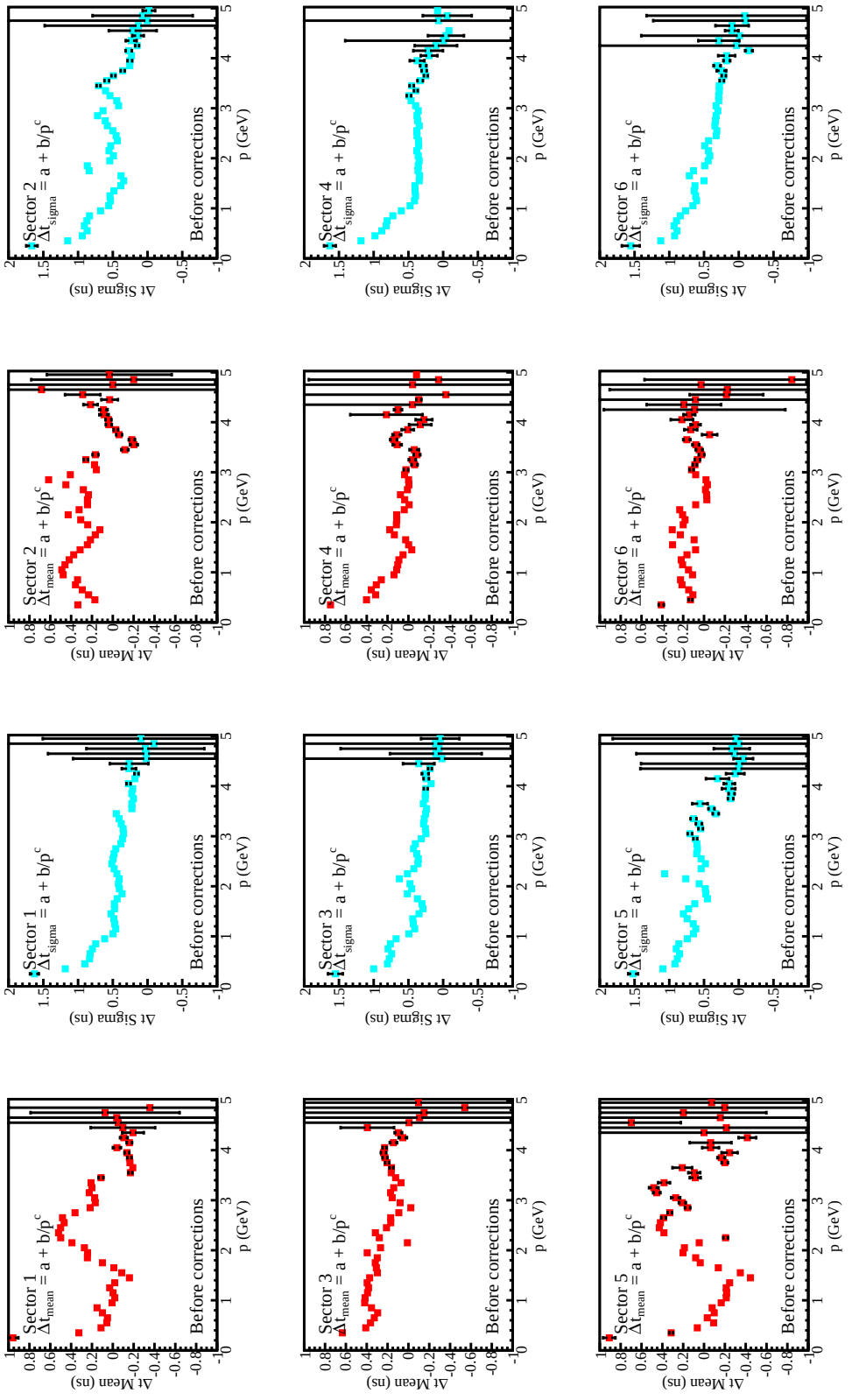


**Figure A.6: The mean and $\sigma$ of $\Delta t$ as functions of particle momenta for proton candidates in each sector for all TOF paddles before TOF corrections.**

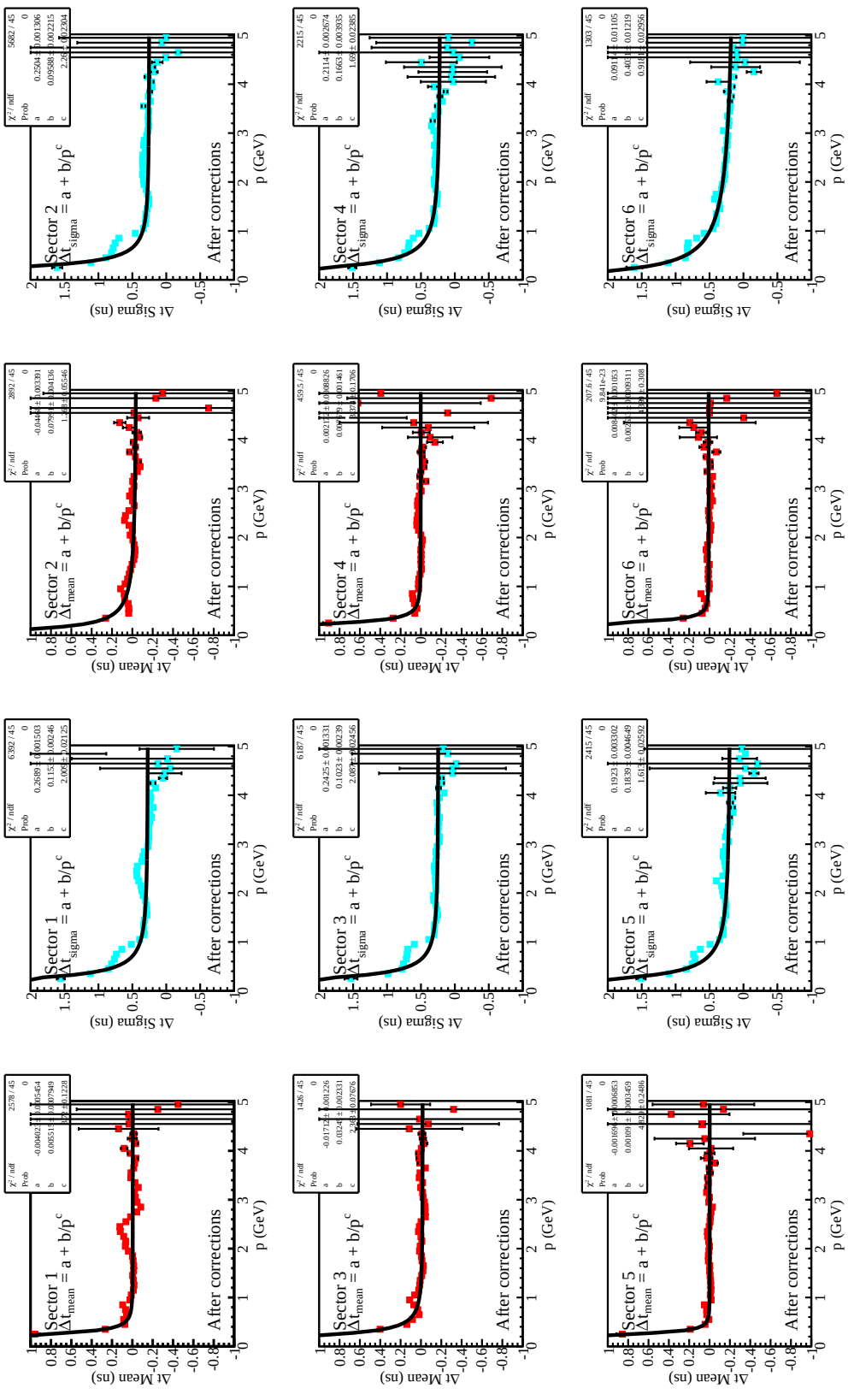


**Figure A.7: The mean and $\sigma$ of $\Delta t$ as functions of particle momenta for proton candidates in each sector for all TOF paddles after TOF corrections.**

## A.5 Electron and Proton Angle Corrections

The coefficients of the electron angle correction are given by

$$a_i(\theta) = c_0 + c_1\theta + c_2\theta^2. \tag{A.2}$$

The parameters of the correction are

| $i$ | $c_0$ | $c_1$ | $c_2$ |
|---|---|---|---|
| 0 | -2.09355677 | -3.31684806E-02 | -1.13440559E-03 |
| 1 | 1.31174283 | 2.07143724E-01 | 6.37836137E-04 |
| 2 | -2.44489241 | -1.221424E-01 | -5.16479755E-03 |
| 3 | -2.8053815E-01 | 2.24826958E-01 | 2.72359806E-03 |
| 4 | 4.07094475E-01 | 4.20764036E-02 | -5.1299142E-03 |

**Table A.11: The parameters for electron angle corrections for sector 1.**

| $i$ | $c_0$ | $c_1$ | $c_2$ |
|---|---|---|---|
| 0 | 5.64114112E-01 | 1.2504244E-02 | 4.10083333E-03 |
| 1 | -5.1219438E-01 | -4.2716178E-02 | -3.910457E-04 |
| 2 | -1.0028315 | 5.6957746E-02 | 8.16171478E-04 |
| 3 | 1.66281611 | 9.0687908E-02 | -1.8383547E-03 |
| 4 | -6.89544888E-02 | -1.61183679E-01 | -2.0352014E-03 |

**Table A.12: The parameters for electron angle corrections for sector 2.**

| $i$ | $c_0$ | $c_1$ | $c_2$ |
|---|---|---|---|
| 0 | -7.70204323E-01 | -5.12792186E-02 | 1.1502628E-02 |
| 1 | 3.5334639E-01 | 1.09249069E-01 | 1.17432835E-03 |
| 2 | -2.7030428E-01 | -6.00117927E-02 | -3.45627949E-03 |
| 3 | 3.4657869 | 1.7845019E-02 | 1.71147716E-03 |
| 4 | 5.47101163E-01 | -4.27954855E-01 | -2.826383E-04 |

**Table A.13: The parameters for electron angle corrections for sector 3.**

| $i$ | $c_0$ | $c_1$ | $c_2$ |
|---|---|---|---|
| 0 | -1.14963156 | -3.6355055E-02 | 8.71534207E-03 |
| 1 | 1.62542337E-01 | 1.0517602E-01 | 7.9181789E-04 |
| 2 | -9.95714015E-01 | -1.39340483E-02 | -2.6545698E-03 |
| 3 | 2.3246248 | 8.09892278E-02 | 8.92225567E-05 |
| 4 | 4.23272698E-01 | -3.10226155E-01 | -1.58515365E-03 |

**Table A.14: The parameters for electron angle corrections for sector 4.**

| $i$ | $c_0$ | $c_1$ | $c_2$ |
|---|---|---|---|
| 0 | -5.01741685E-01 | -1.08187405E-01 | 6.3294693E-04 |
| 1 | -1.77085757 | -2.003366E-02 | 2.44439224E-03 |
| 2 | -6.3760666E-01 | 1.72421567E-01 | 1.33297453E-03 |
| 3 | 4.5728914E-02 | 4.9708738E-02 | -4.205488E-03 |
| 4 | 1.20123351 | -1.8280028E-02 | -9.6490117E-04 |

**Table A.15: The parameters for electron angle corrections for sector 5.**

| $i$ | $c_0$ | $c_1$ | $c_2$ |
|---|---|---|---|
| 0 | -1.83039564 | -7.9916894E-03 | 1.38427978E-02 |
| 1 | 9.3981116E-01 | 1.59486435E-01 | 3.71918054E-05 |
| 2 | -6.0376152E-01 | -1.28512835E-01 | -3.70724347E-03 |
| 3 | 4.00965538 | 4.63797833E-02 | 3.39126187E-03 |
| 4 | 1.41910734E-01 | -5.06583454E-01 | -8.60422808E-04 |

**Table A.16: The parameters for electron angle corrections for sector 6.**

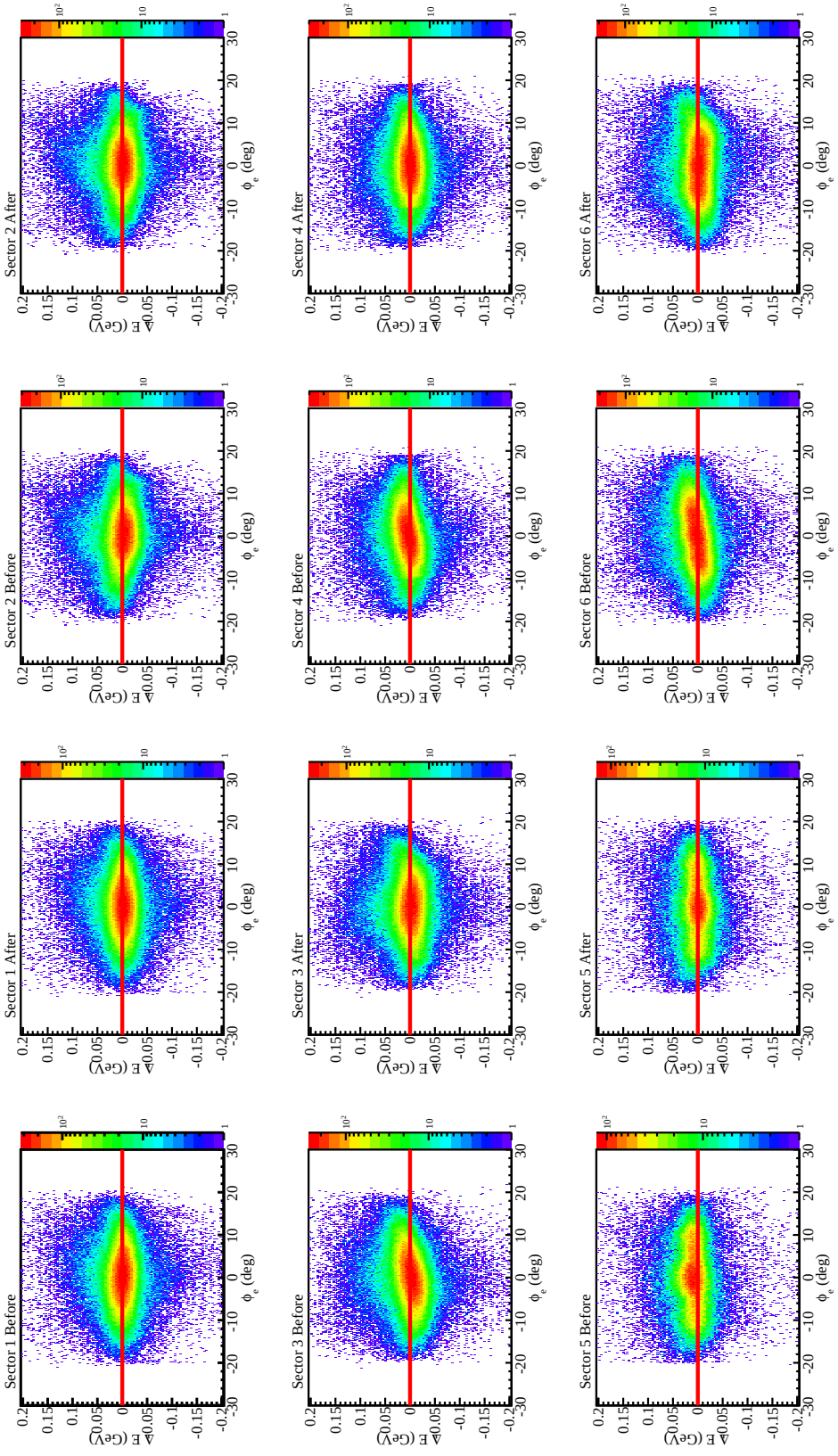


**Figure A.8:** $\Delta E$ vs $\phi_e$ distributions before and after electron angle corrections for each of the CLAS sectors. Red line indicates expected peak position.

## A.6 Electron Momentum Corrections

The coefficients of the electron momentum correction are given by

$$a_i(\theta_e) = c_0 + c_1\theta_e + c_2\theta_e^2. \tag{A.3}$$

The parameters of the correction are

| $i$ | $c_0$ | $c_1$ | $c_2$ |
|---|---|---|---|
| 0 | 1.0176579118581E-02 | -7.9599239534114E-06 | 9.5112707858653E-08 |
| 1 | -0.20495101625537 | 7.9655917387783E-03 | -6.9400370675523E-05 |
| 2 | -0.15348562918845 | 1.0743244205188E-02 | -1.8086561701112E-04 |
| 3 | 0.11761993283213 | -7.9967328974761E-03 | 1.3019443527636E-04 |

**Table A.17: The parameters of electron momentum corrections for sector 1.**

| $i$ | $c_0$ | $c_1$ | $c_2$ |
|---|---|---|---|
| 0 | 1.0087801836821E-02 | -5.6599480422299E-06 | 1.0033722952831E-07 |
| 1 | -0.22412829804132 | 1.1661447536158E-02 | -1.5960488468465E-04 |
| 2 | -0.15076163008159 | 1.0942470368942E-02 | -1.8929500388527E-04 |
| 3 | 0.11317471787380 | -7.6499984847730E-03 | 1.2506972055652E-04 |

**Table A.18: The parameters of electron momentum corrections for sector 2.**

| $i$ | $c_0$ | $c_1$ | $c_2$ |
|---|---|---|---|
| 0 | 1.0073933449548E-02 | -5.0800069598611E-06 | 1.0797150380251E-07 |
| 1 | -1.0019870422334E-01 | 1.1211638296420E-02 | -2.1899832926782E-04 |
| 2 | -9.9580311244930E-02 | 6.8099881808583E-03 | -1.1416945384378E-04 |
| 3 | -1.2820491669835E-04 | 2.5650746001025E-04 | -7.3395343512598E-06 |

**Table A.19: The parameters of electron momentum corrections for sector 3.**

| $i$ | $c_0$ | $c_1$ | $c_2$ |
|---|---|---|---|
| 0 | 1.0221497899831E-02 | -1.1728924887767E-05 | 1.7100120165989E-07 |
| 1 | -2.0318433751035E-02 | 2.4612021589962E-03 | -6.3507481408119E-05 |
| 2 | -7.6365686745569E-02 | 5.2998598339562E-03 | -9.1297828333589E-05 |
| 3 | 4.7326314122685E-04 | 4.7628893452639E-04 | -1.4020818540861E-05 |

**Table A.20: The parameters of electron momentum corrections for sector 4.**

| $i$ | $c_0$ | $c_1$ | $c_2$ |
|---|---|---|---|
| 0 | 1.0110107335248E-02 | -2.4757597510374E-06 | 1.3082672597941E-08 |
| 1 | -0.11955549846234 | 6.1878054901081E-03 | -9.3393940238598E-05 |
| 2 | -9.6360858729669E-02 | 6.8477708809656E-03 | -1.1784209351117E-04 |
| 3 | 3.9383613408158E-02 | -2.7046265634257E-03 | 4.4662480048095E-05 |

**Table A.21: The parameters of electron momentum corrections for sector 5.**

| $i$ | $c_0$ | $c_1$ | $c_2$ |
|---|---|---|---|
| 0 | 1.0112945449548E-02 | -5.3018979653485E-06 | 8.7085945937647E-08 |
| 1 | -1.8772394756644E-02 | 4.6198689235790E-03 | -1.0356199140906E-04 |
| 2 | 3.1792598257448E-02 | -3.2324591761590E-03 | 5.3194937440755E-05 |
| 3 | 2.6160738941275E-02 | -1.3819042499386E-03 | 1.8214642092420E-05 |

**Table A.22: The parameters of electron momentum corrections for sector 6.**

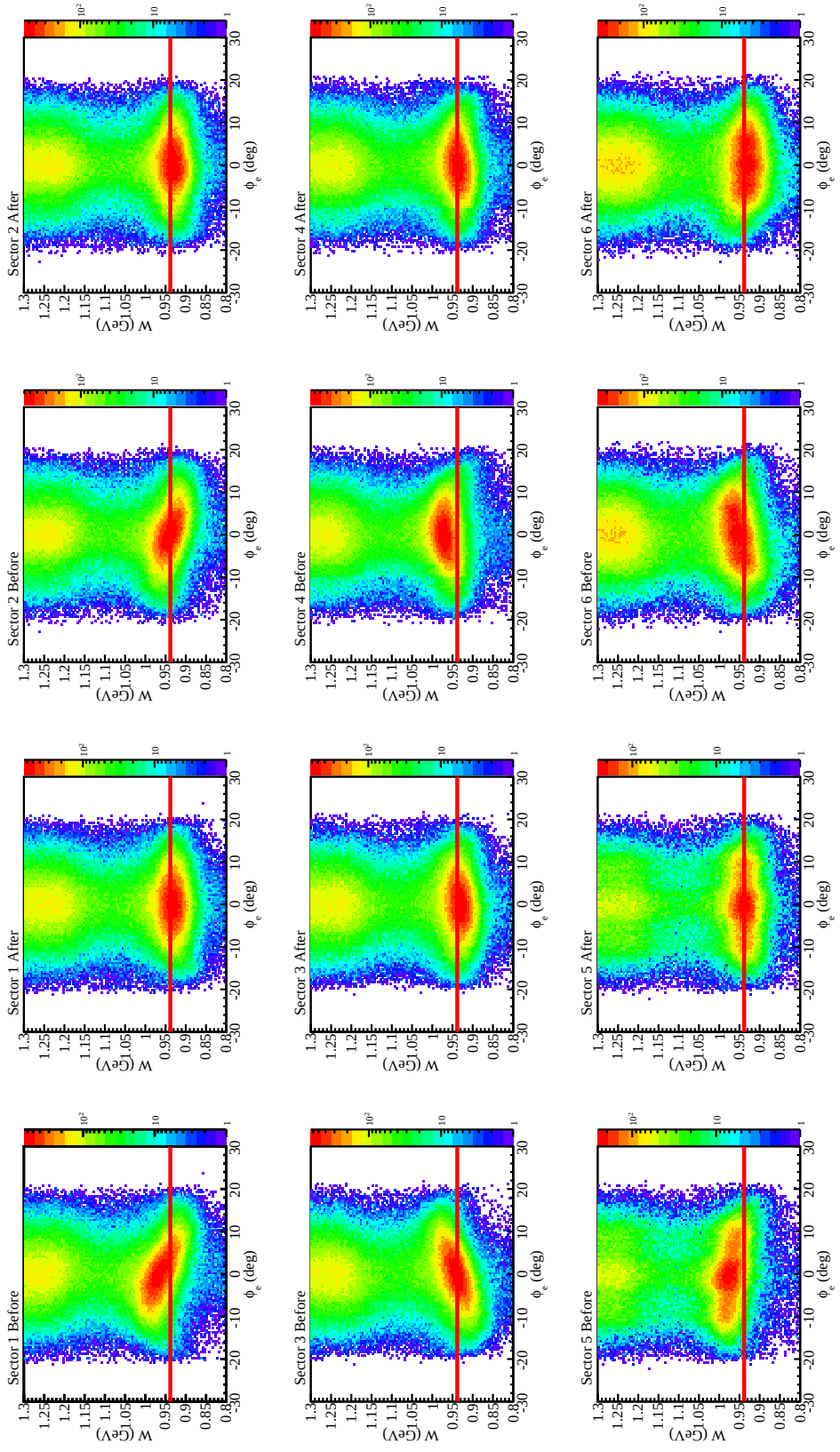


**Figure A.9:** $W$ vs $\phi_e$ for each of the CLAS sectors before and after electron momentum corrections. Red line indicates expected elastic peak position ($M_p$).

## A.7 Bethe-Heitler Subtraction Parameters

We first define a variable to indicate the offset from the lower edge of the first $W$ bin:

$$W_0 = W - 1.08 \tag{A.4}$$

such that the parameters for the linear polynomial are:

$$b_0(W) = 0.01 + 0.125W_0 \tag{A.5}$$

$$a_0(W) = 0.25 + 3.0W_0. \tag{A.6}$$

Also, the parameters for the ellipse are:

$$r_1(W) = 0.07 + 0.04W_0 \tag{A.7}$$

$$r_2(W) = 0.025 + 0.015W_0 \tag{A.8}$$

with the center fixed at

$$x_0 = 0.025 \tag{A.9}$$

$$y_0 = -0.015. \tag{A.10}$$

Fig. A.10 shows the effect of the Bethe-Heitler subtraction cuts for all bins near threshold, $W \in (1.08, 1.16)$ GeV.

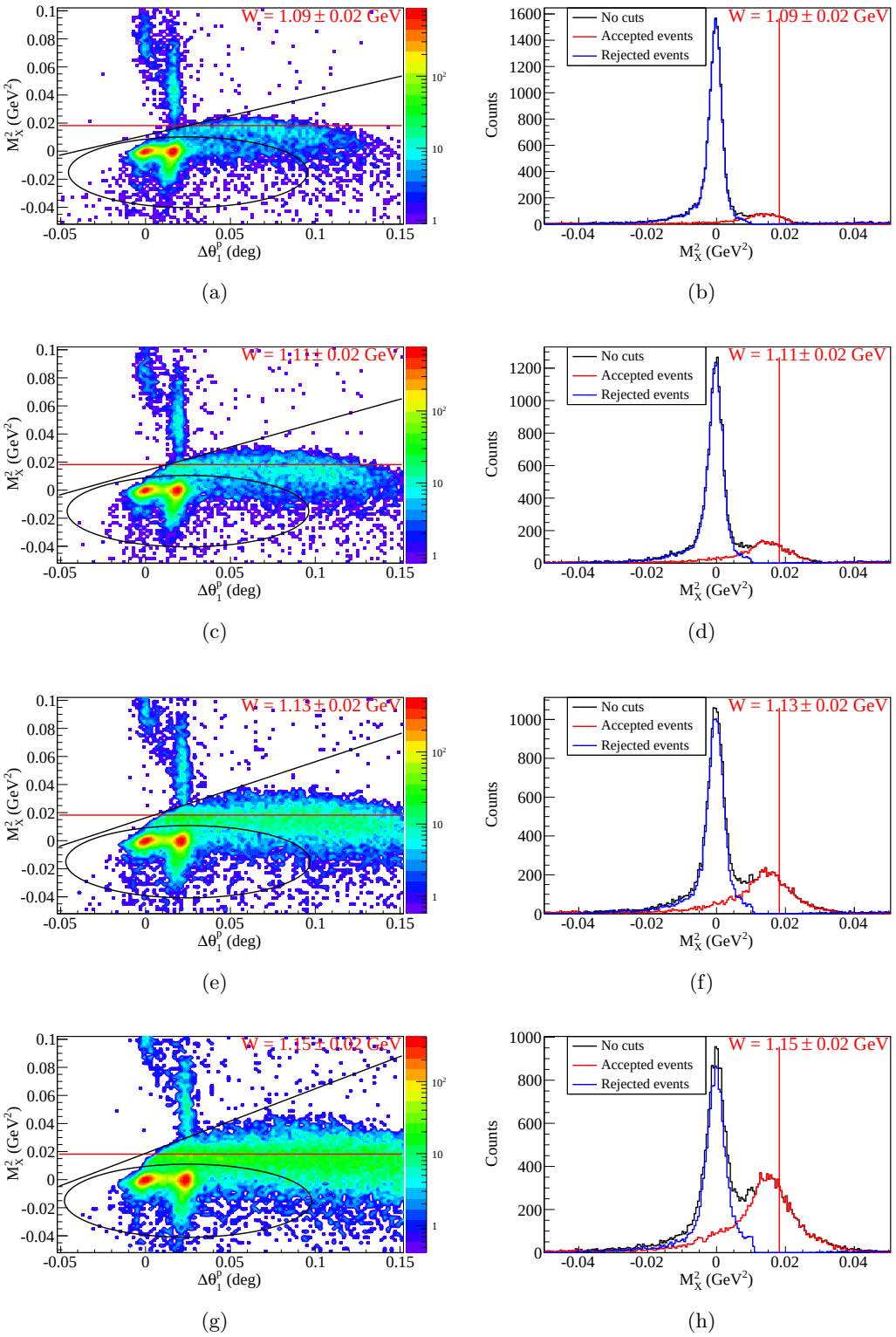


**Figure A.10:** $M_X^2$ **vs** $\Delta\theta_1^p$ **(a, c, e, g) for all near threshold bins in** $W \in (1.08, 1.16)$ **GeV and the corresponding** $M_X^2$ **projections (b, d, f, h) showing accepted and rejected cuts after Bethe-Heitler subtraction cuts.**

# APPENDIX B
# EC Coordinates

The transformation from CLAS coordinates $(X, Y, Z)$ of tracks on the EC plane to native EC coordinates $(U, V, W)$ or $(X_{EC}, Y_{EC}, Z_{EC})$ is described as follows.

First we obtain a rotation matrix $R$ to rotate from CLAS coordinates to EC plane coordinates:

$$R = \begin{bmatrix} \cos\theta\cos\phi & \cos\theta\sin\phi & -\sin\theta \\ -\sin\phi & \cos\phi & 0 \\ \sin\theta\cos\phi & \sin\theta\sin\phi & \cos\theta \end{bmatrix}. \tag{B.1}$$

Here $\theta = 25^\circ$ is the polar angle from the CLAS center to the EC plane and $\phi$ is the azimuthal angle to the center of the EC plane for a given sector. The azimuthal separation between the center of any two neighboring EC sectors is $60^\circ$. This rotation matrix is thus different for each sector of CLAS and needs to be constructed on an event-by-event basis. We use this matrix to rotate the CLAS coordinates $(X, Y, Z)$ to the EC coordinates $(X_{EC}, Y_{EC}, Z_{EC})$:

$$\vec{X}_{EC} = R\vec{X}. \tag{B.2}$$

After the rotation, we still need to translate the $Z$-coordinate to the EC plane. So,

$$Z_{EC} \rightarrow Z_{EC} - 510.32\,\text{cm}. \tag{B.3}$$

Here, 510.32 cm is the distance from the CLAS center to the EC plane.

Now, we can get the $(U, V, W)$ coordinates for the tracks. These coordinates in essence give us the distance from the corner of the scintillator in the EC to the point of hit for each of the three different orientations of the scintillators. On the EC plane, the minimum and maximum value of $Y_{EC}$ from the center is $(-182.974, 189.956)$ cm. Using this range and the angular separation of $\rho = 62.889^\circ$ between each side of the EC triangle these distances can be computed using the following prescription:

$$\begin{aligned} U &= \frac{Y_{EC} - Y_{MIN}}{\sin\rho} \\ V &= \frac{Y_{MAX} - Y_{MIN}}{\tan\rho} - X_{EC} + \frac{Y_{MAX} - Y_{EC}}{\tan\rho} \\ W &= \frac{Y_{MAX} - Y_{MIN}}{\tan\rho} + X_{EC} + \frac{Y_{MAX} - Y_{EC}}{2\cos\rho\tan\rho}. \end{aligned} \tag{B.4}$$

# APPENDIX C
## Elastic Normalizations

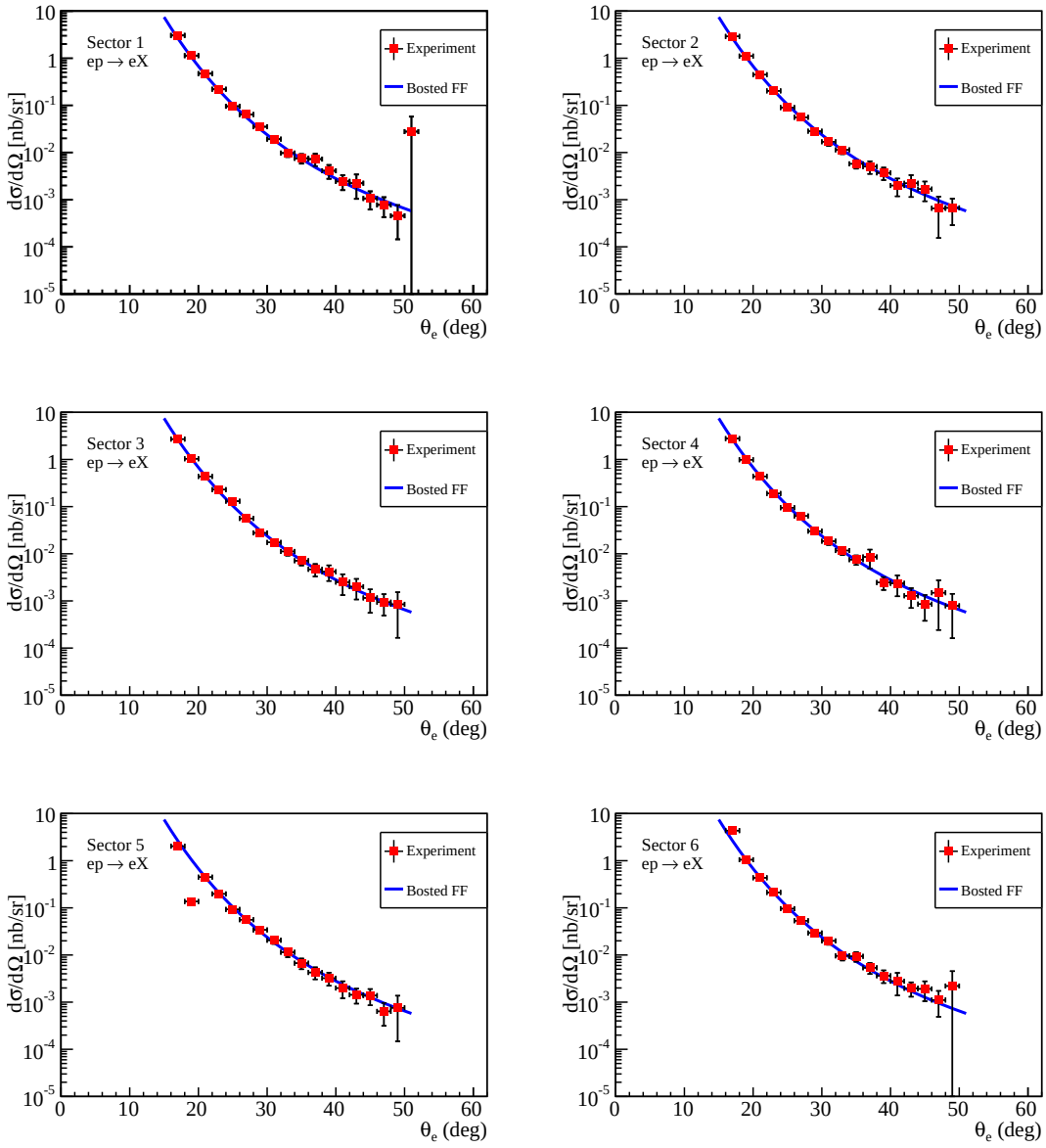


**Figure C.1: Differential cross section for the inclusive reaction $ep \rightarrow eX$ as a function of $\theta_e$ for each of the CLAS sectors. Measured cross section is shown in red and the blue curve shows the expected cross section.**

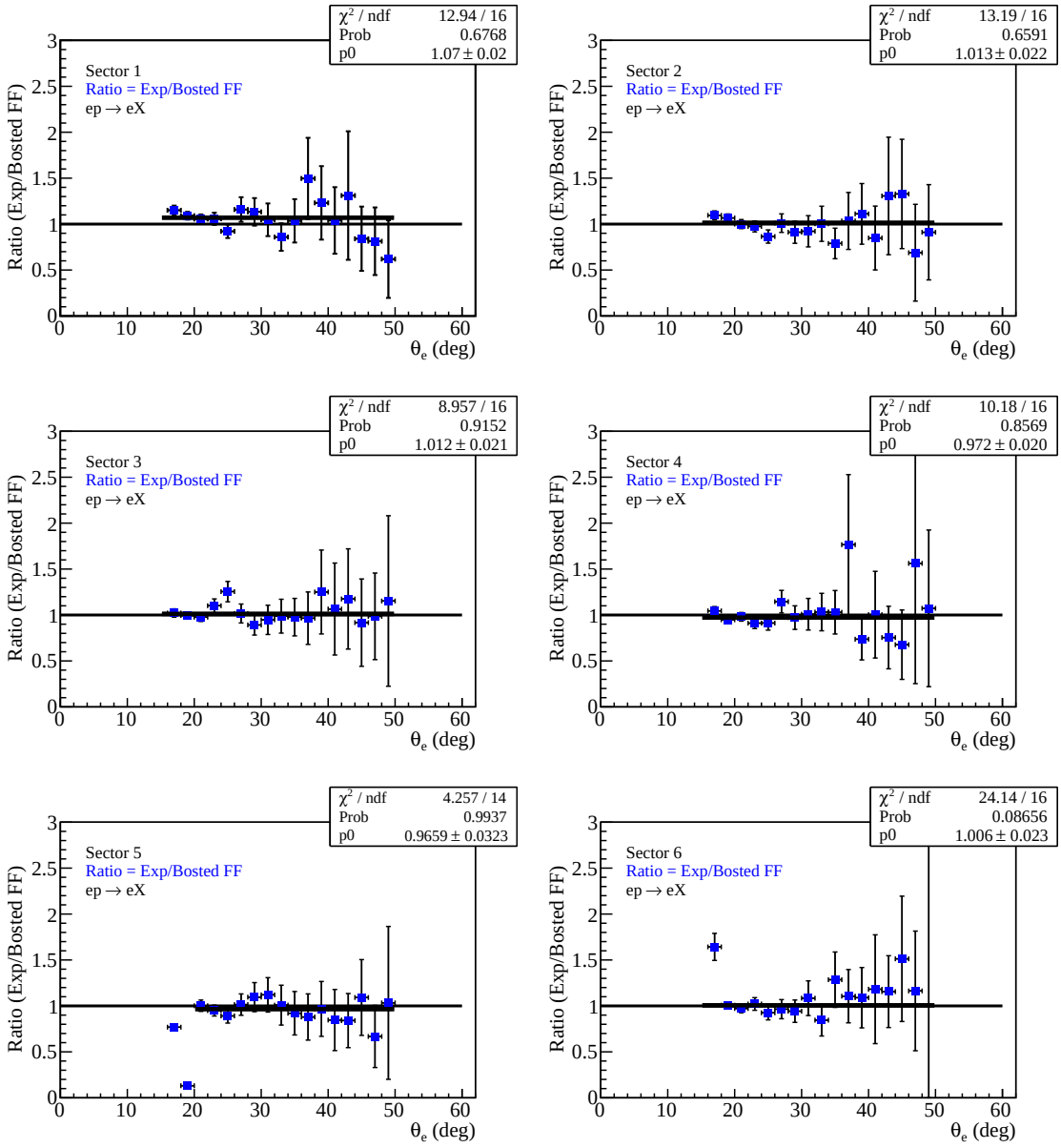


**Figure C.2: The ratio of the measured to expected cross section as a function of $\theta_e$ for each of the CLAS sectors for the inclusive reaction $ep \rightarrow eX$. Thick black line shows the zeroth polynomial fit to the points.**

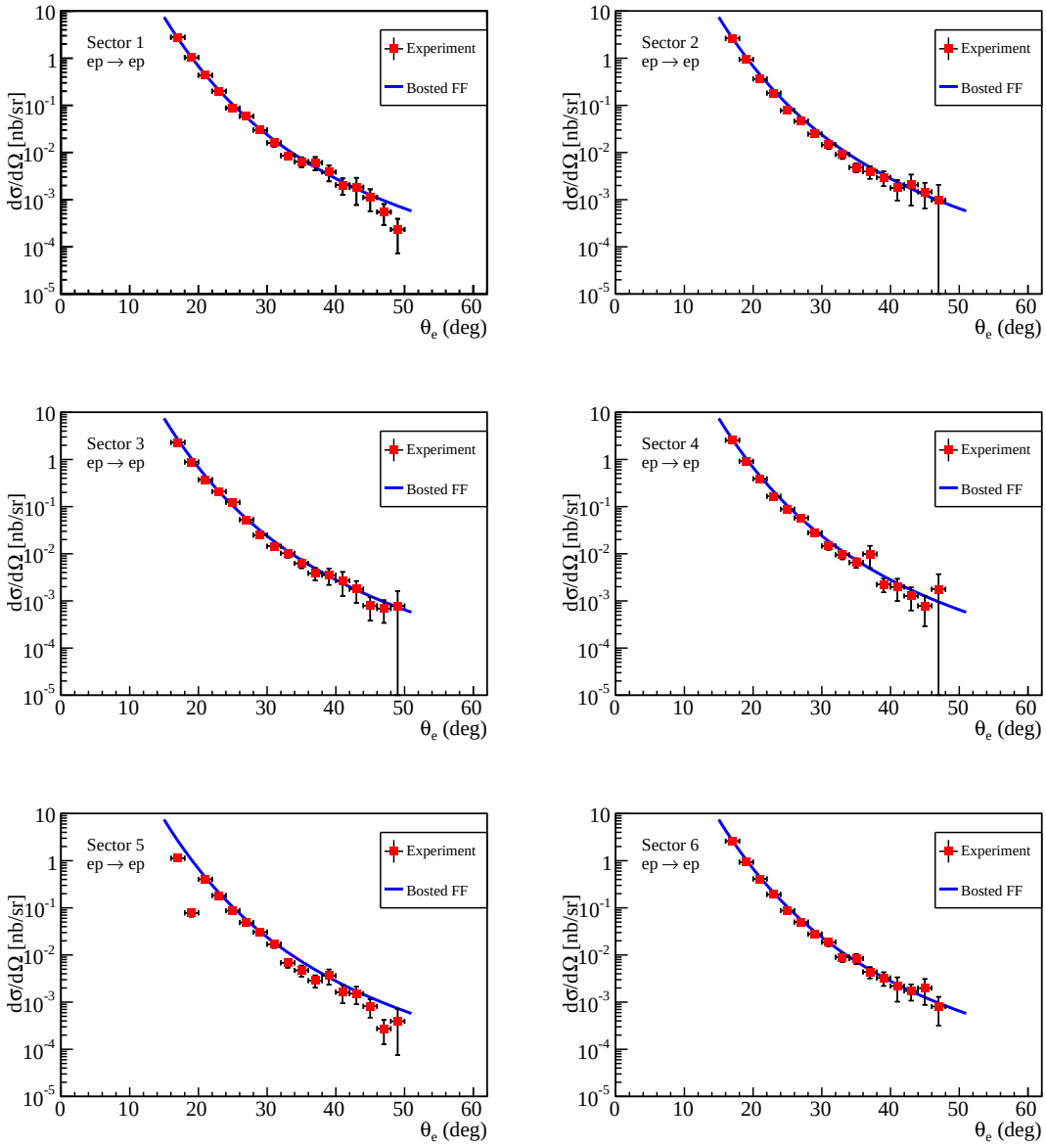


**Figure C.3: Differential cross section for the exclusive reaction $ep \rightarrow ep$ as a function of $\theta_e$ for each of the CLAS sectors. Measured cross section is shown in red and the blue curve shows the expected cross section.**

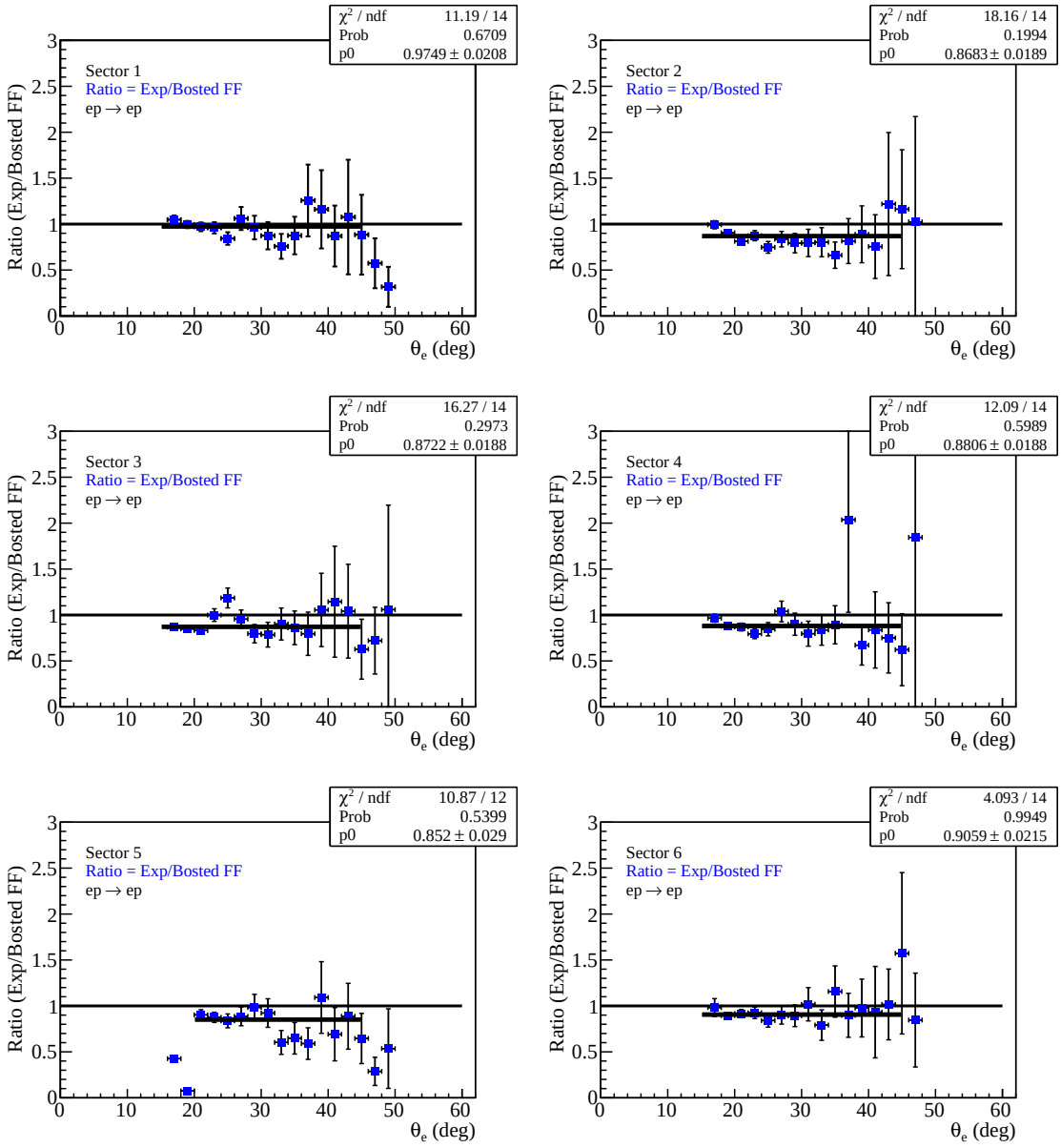


**Figure C.4: The ratio of the measured to expected cross section as a function of $\theta_e$ for each of the CLAS sectors for the exclusive reaction $ep \rightarrow ep$. Thick black line shows the zeroth polynomial fit to the points.**

# APPENDIX D
## Differential Cross Sections

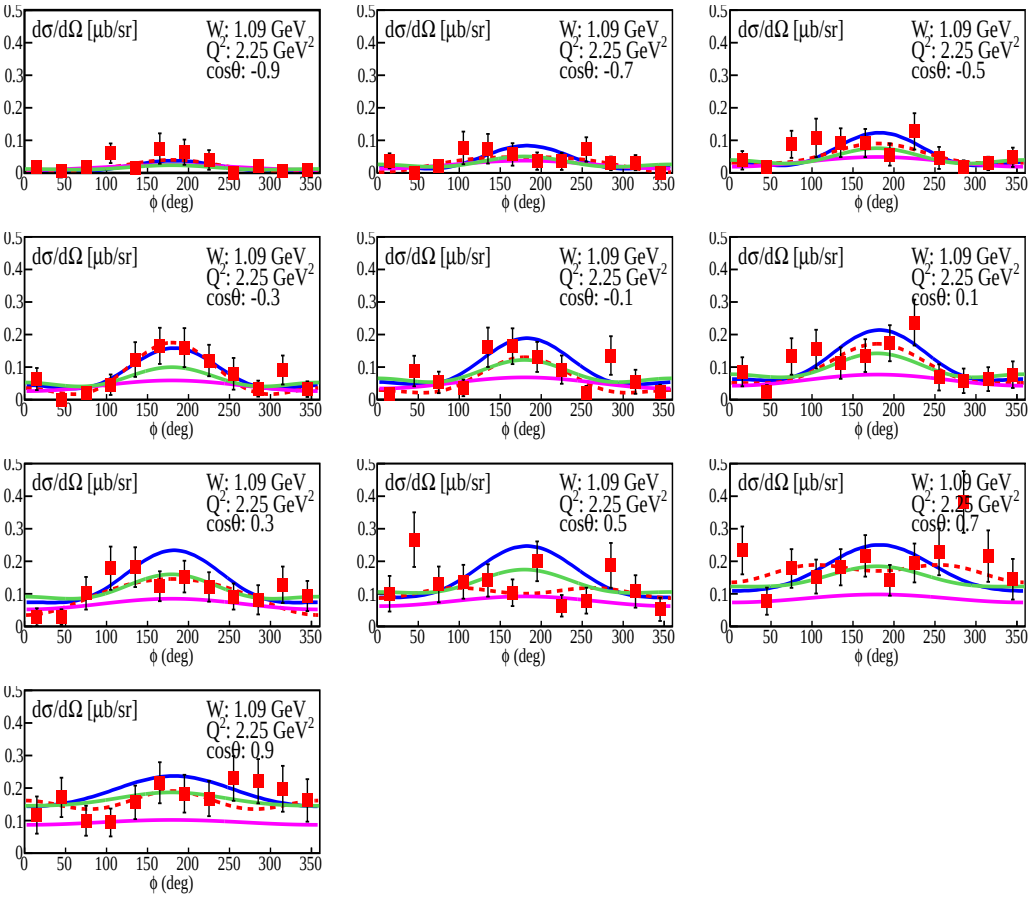


**Figure D.1: The differential cross sections in $\mu$b/sr for $W = 1.09$ GeV and $Q^2 = 2.25\,\mathrm{GeV}^2$. Each subplot shows cross section for various $\cos\theta^*_\pi$ bin as a function of $\phi^*_\pi$. Experimental points (red) are shown with statistical errors only. The red dashed curve is a fit to the cross section as in Eq. 6.2. Predictions from Braun *et al* (magenta) as well as extrapolations of fit to world data at higher $W$ from MAID2007 (blue) and Aznauryan *et al* (green) are shown.**

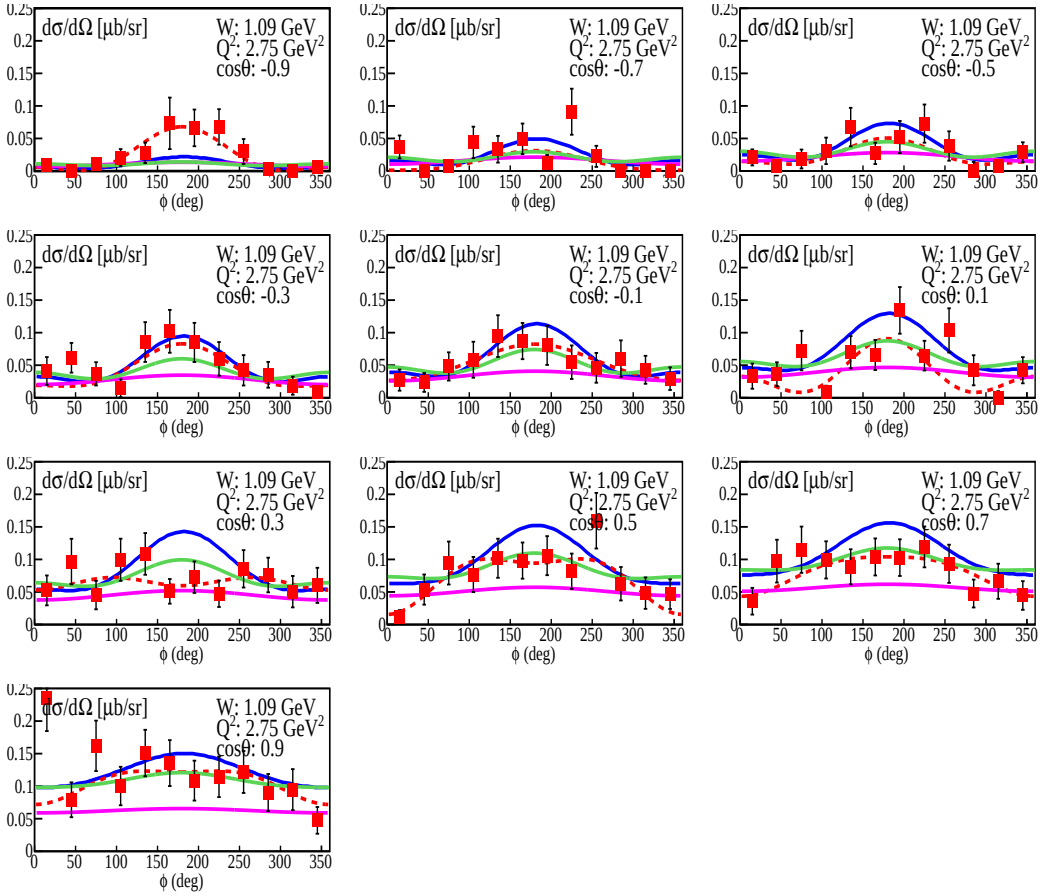


**Figure D.2: The differential cross sections in $\mu$b/sr for $W = 1.09$ GeV and $Q^2 = 2.75\,\mathrm{GeV}^2$. Each subplot shows cross section for various $\cos\theta^*_\pi$ bin as a function of $\phi^*_\pi$. Experimental points (red) are shown with statistical errors only. The red dashed curve is a fit to the cross section as in Eq. 6.2. Predictions from Braun *et al* (magenta) as well as extrapolations of fit to world data at higher $W$ from MAID2007 (blue) and Aznauryan *et al* (green) are shown.**

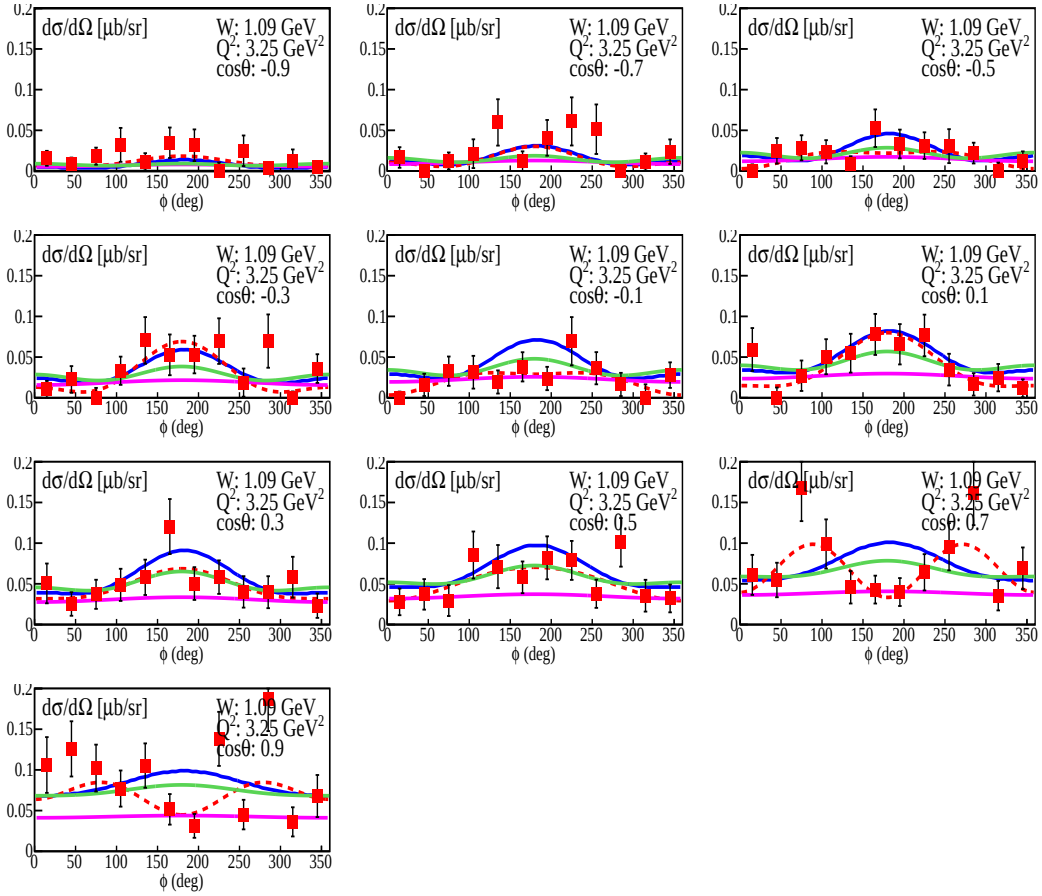


**Figure D.3: The differential cross sections in $\mu$b/sr for $W = 1.09$ GeV and $Q^2 = 3.25\,\mathrm{GeV}^2$. Each subplot shows cross section for various $\cos\theta^*_\pi$ bin as a function of $\phi^*_\pi$. Experimental points (red) are shown with statistical errors only. The red dashed curve is a fit to the cross section as in Eq. 6.2. Predictions from Braun *et al* (magenta) as well as extrapolations of fit to world data at higher $W$ from MAID2007 (blue) and Aznauryan *et al* (green) are shown.**

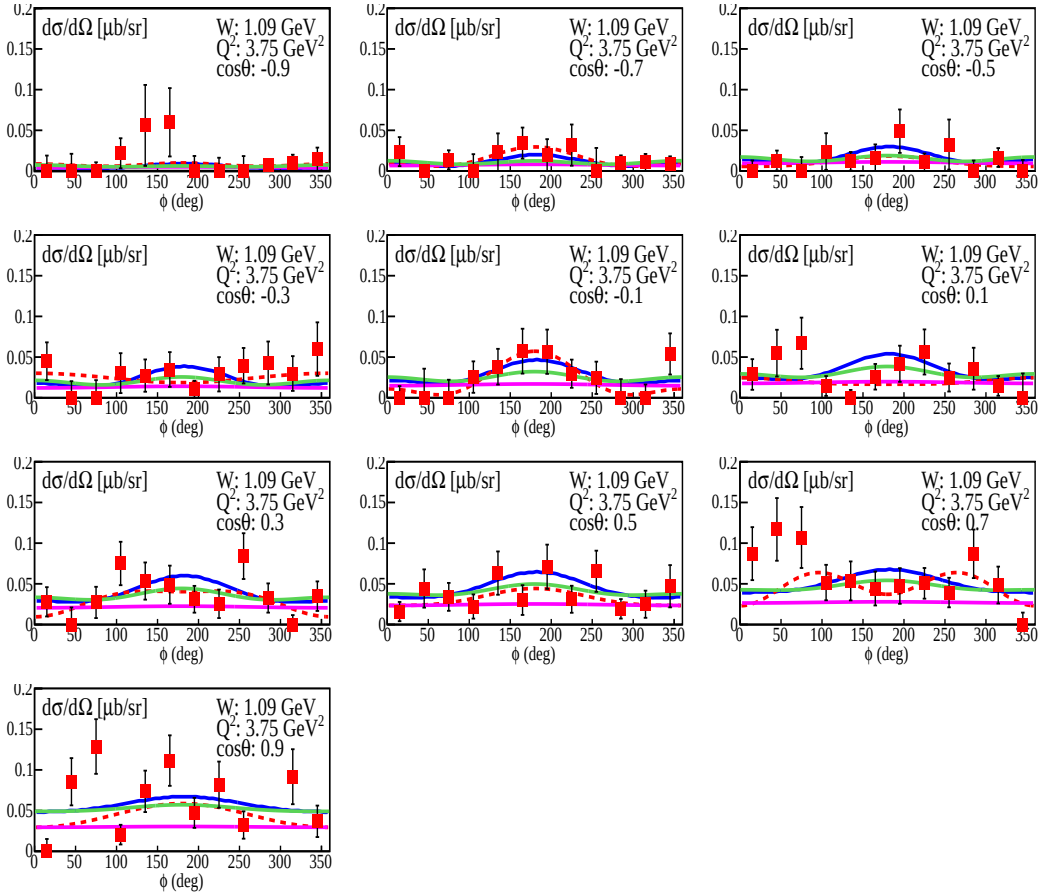


**Figure D.4: The differential cross sections in $\mu$b/sr for $W = 1.09$ GeV and $Q^2 = 3.75\,\mathrm{GeV}^2$. Each subplot shows cross section for various $\cos\theta^*_\pi$ bin as a function of $\phi^*_\pi$. Experimental points (red) are shown with statistical errors only. The red dashed curve is a fit to the cross section as in Eq. 6.2. Predictions from Braun *et al* (magenta) as well as extrapolations of fit to world data at higher $W$ from MAID2007 (blue) and Aznauryan *et al* (green) are shown.**

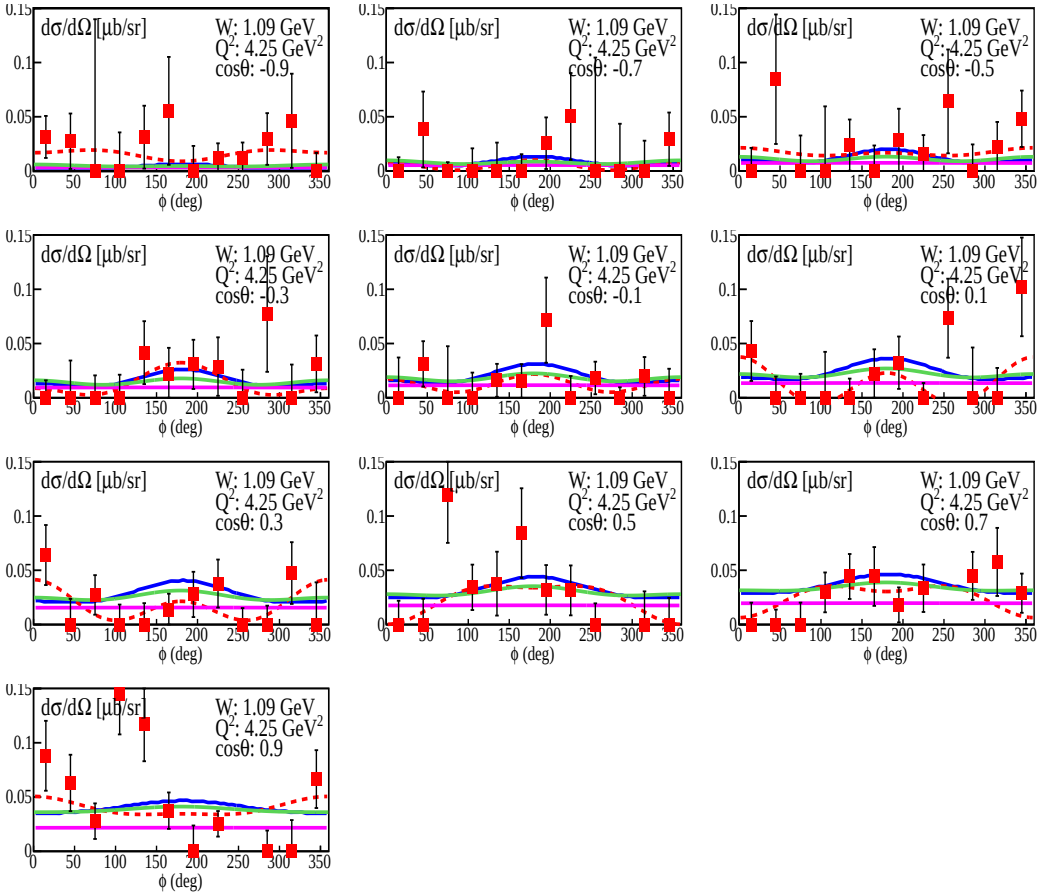


**Figure D.5: The differential cross sections in $\mu$b/sr for $W = 1.09$ GeV and $Q^2 = 4.25\,\mathrm{GeV}^2$. Each subplot shows cross section for various $\cos\theta^*_\pi$ bin as a function of $\phi^*_\pi$. Experimental points (red) are shown with statistical errors only. The red dashed curve is a fit to the cross section as in Eq. 6.2. Predictions from Braun *et al* (magenta) as well as extrapolations of fit to world data at higher $W$ from MAID2007 (blue) and Aznauryan *et al* (green) are shown.**

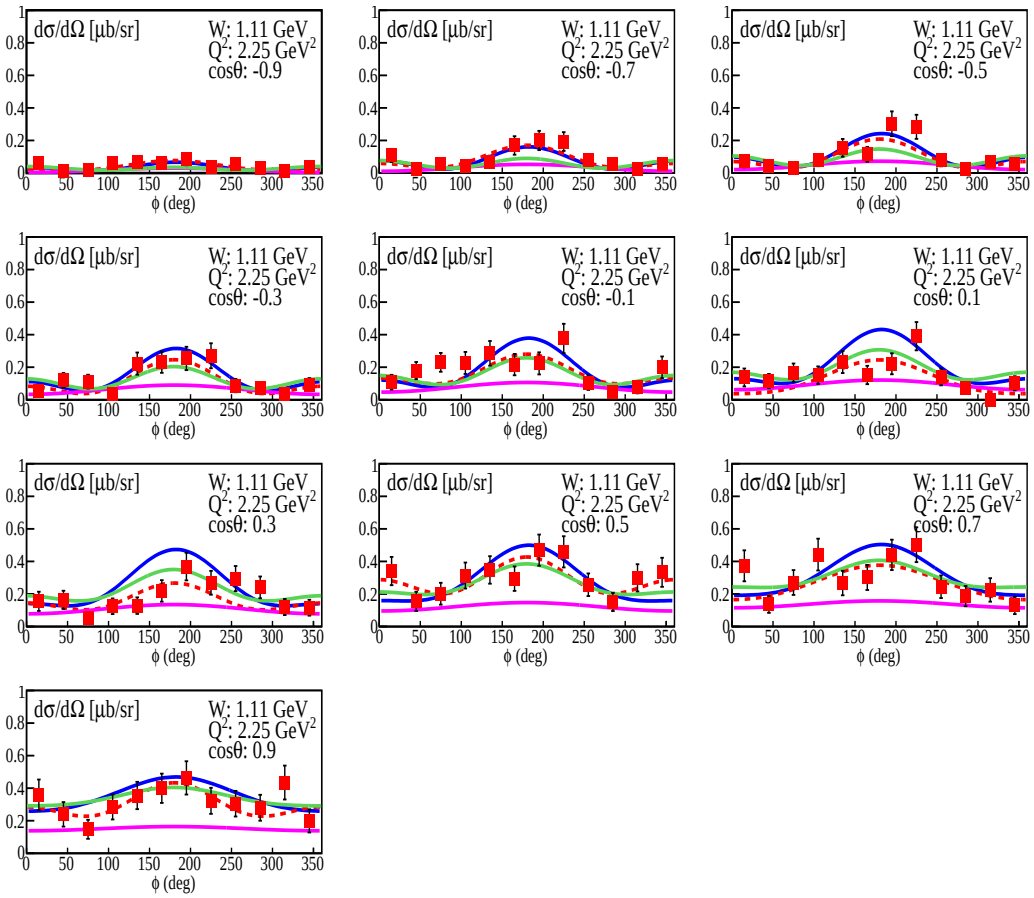


**Figure D.6: The differential cross sections in $\mu$b/sr for $W = 1.11$ GeV and $Q^2 = 2.25\,\mathrm{GeV}^2$. Each subplot shows cross section for various $\cos\theta^*_\pi$ bin as a function of $\phi^*_\pi$. Experimental points (red) are shown with statistical errors only. The red dashed curve is a fit to the cross section as in Eq. 6.2. Predictions from Braun *et al* (magenta) as well as extrapolations of fit to world data at higher $W$ from MAID2007 (blue) and Aznauryan *et al* (green) are shown.**

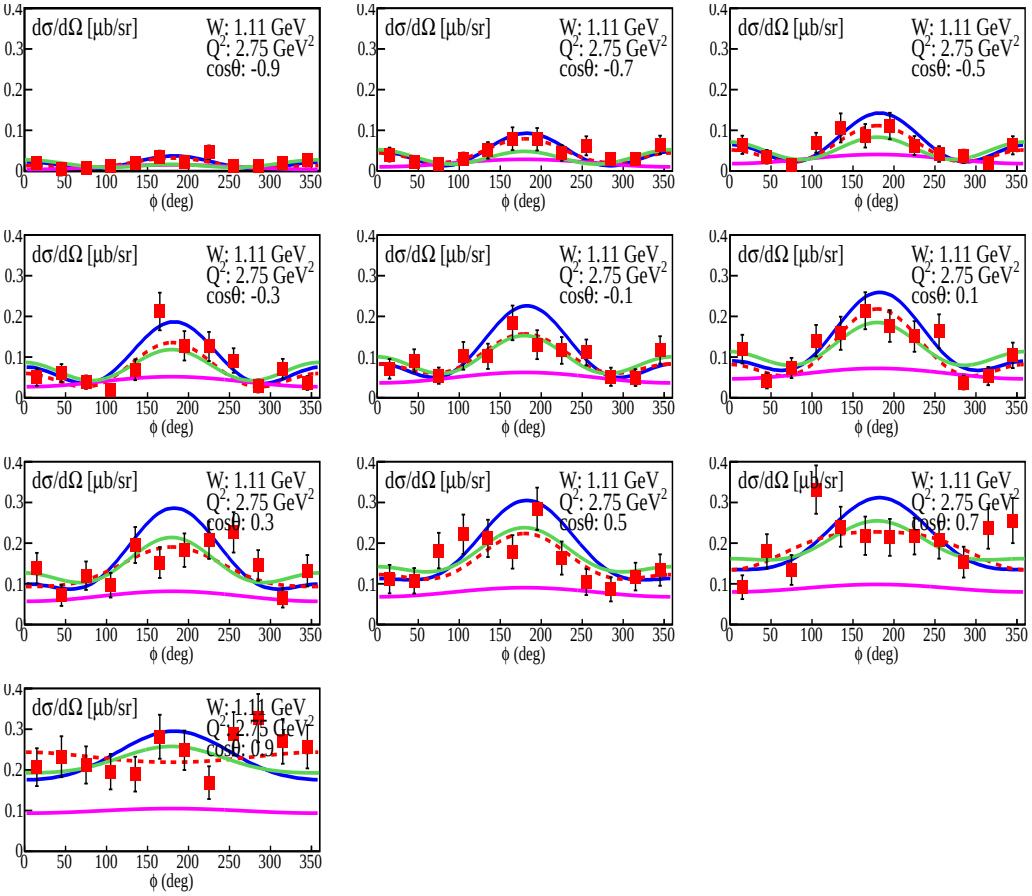


**Figure D.7: The differential cross sections in $\mu$b/sr for $W = 1.11$ GeV and $Q^2 = 2.75\,\mathrm{GeV}^2$. Each subplot shows cross section for various $\cos\theta^*_\pi$ bin as a function of $\phi^*_\pi$. Experimental points (red) are shown with statistical errors only. The red dashed curve is a fit to the cross section as in Eq. 6.2. Predictions from Braun *et al* (magenta) as well as extrapolations of fit to world data at higher $W$ from MAID2007 (blue) and Aznauryan *et al* (green) are shown.**

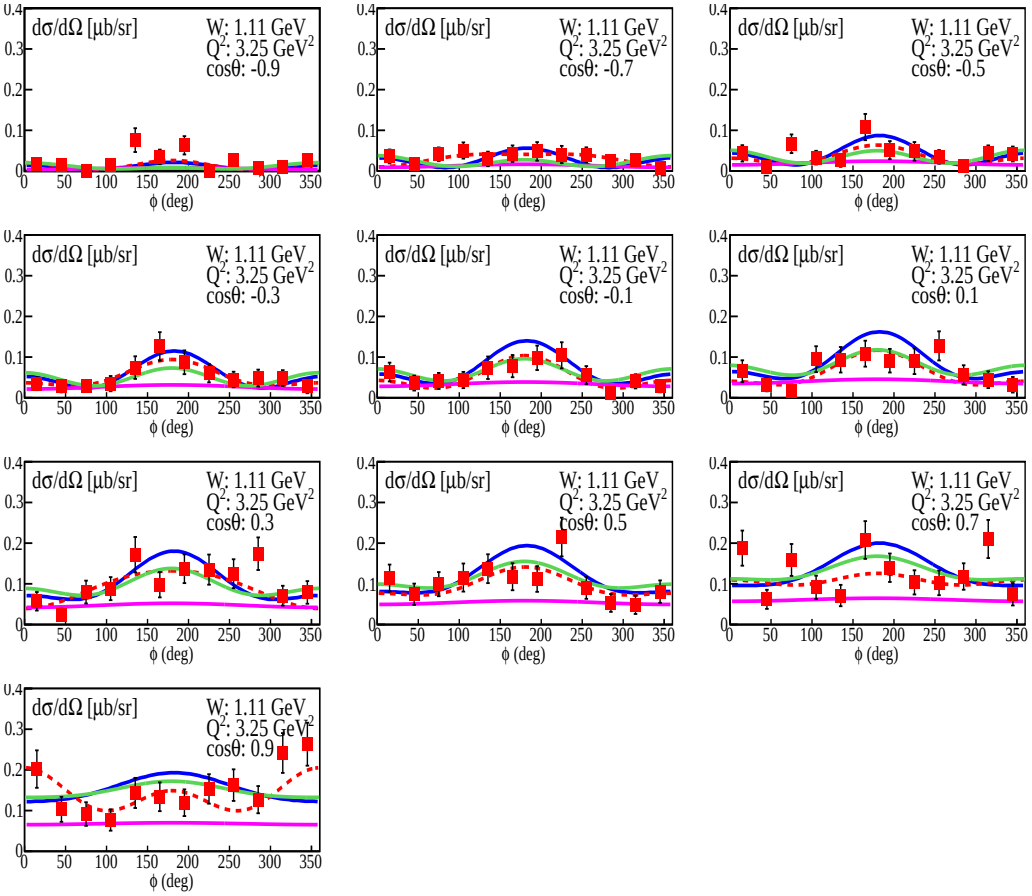


**Figure D.8: The differential cross sections in $\mu$b/sr for $W = 1.11$ GeV and $Q^2 = 3.25\,\mathrm{GeV}^2$. Each subplot shows cross section for various $\cos\theta^*_\pi$ bin as a function of $\phi^*_\pi$. Experimental points (red) are shown with statistical errors only. The red dashed curve is a fit to the cross section as in Eq. 6.2. Predictions from Braun *et al* (magenta) as well as extrapolations of fit to world data at higher $W$ from MAID2007 (blue) and Aznauryan *et al* (green) are shown.**

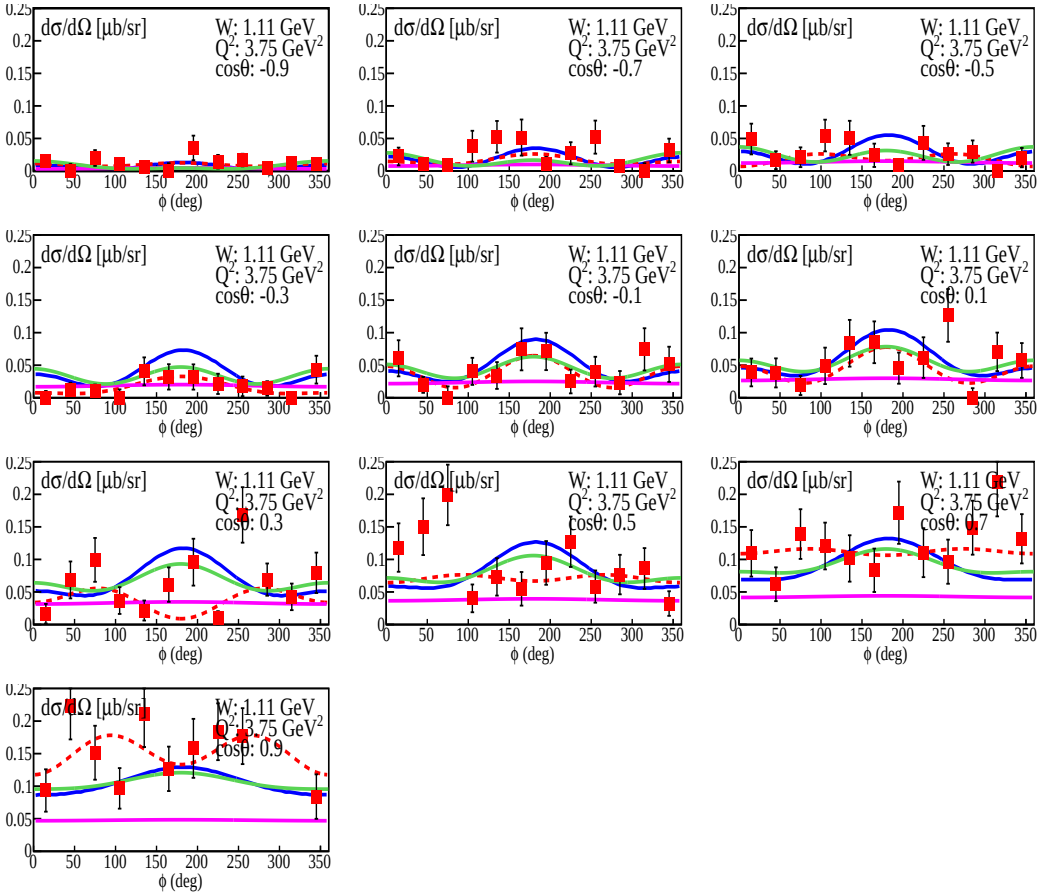


**Figure D.9: The differential cross sections in $\mu$b/sr for $W = 1.11$ GeV and $Q^2 = 3.75\,\mathrm{GeV}^2$. Each subplot shows cross section for various $\cos\theta^*_\pi$ bin as a function of $\phi^*_\pi$. Experimental points (red) are shown with statistical errors only. The red dashed curve is a fit to the cross section as in Eq. 6.2. Predictions from Braun *et al* (magenta) as well as extrapolations of fit to world data at higher $W$ from MAID2007 (blue) and Aznauryan *et al* (green) are shown.**

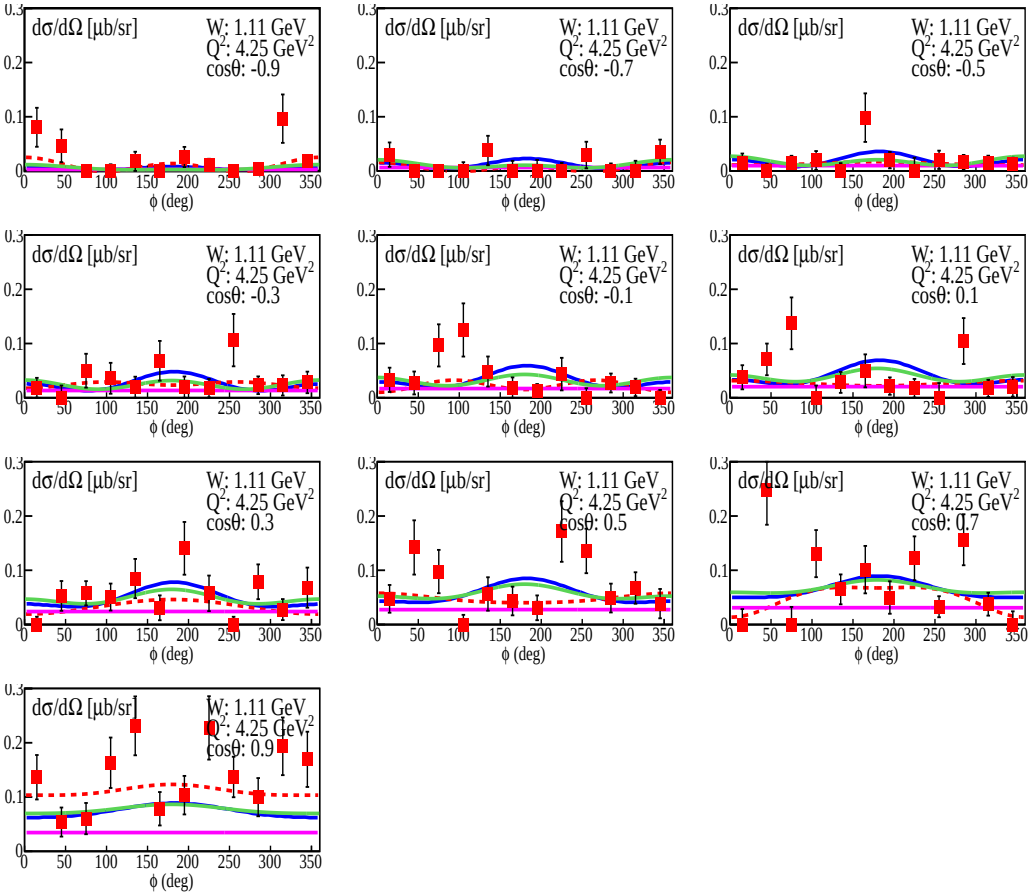


**Figure D.10: The differential cross sections in $\mu$b/sr for $W = 1.11$ GeV and $Q^2 = 4.25\,\mathrm{GeV}^2$. Each subplot shows cross section for various $\cos\theta^*_\pi$ bin as a function of $\phi^*_\pi$. Experimental points (red) are shown with statistical errors only. The red dashed curve is a fit to the cross section as in Eq. 6.2. Predictions from Braun *et al* (magenta) as well as extrapolations of fit to world data at higher $W$ from MAID2007 (blue) and Aznauryan *et al* (green) are shown.**

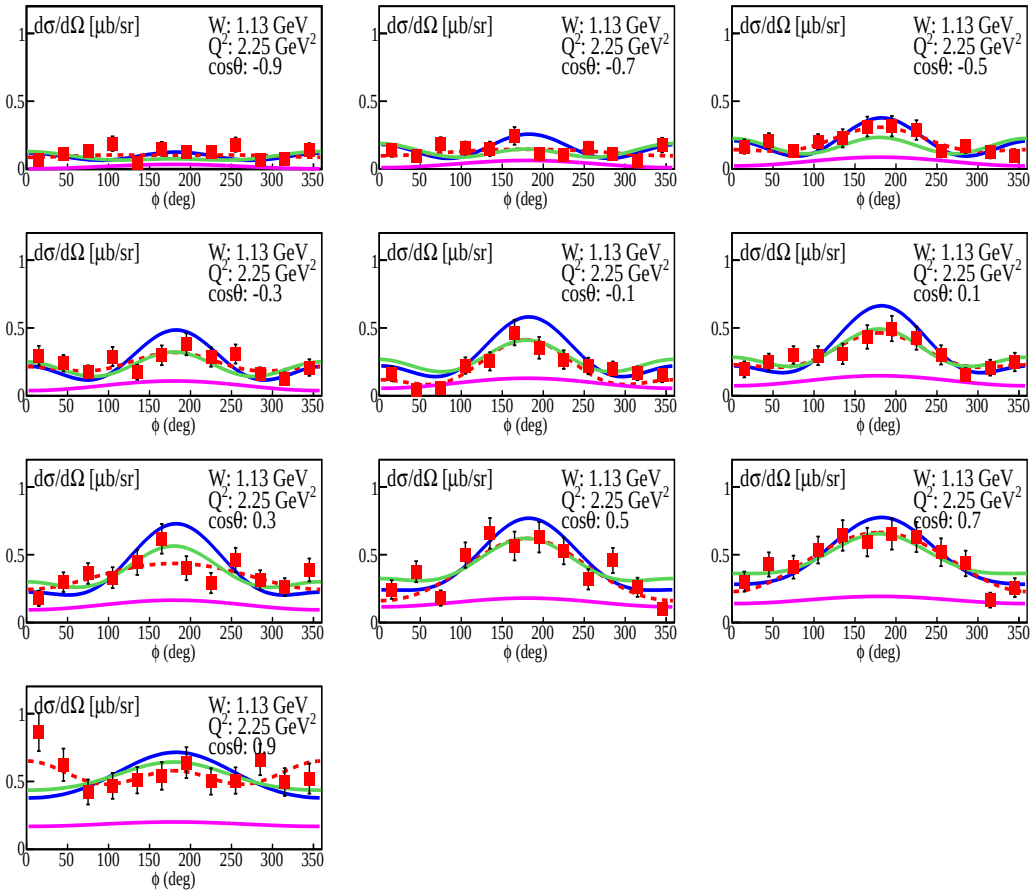


**Figure D.11: The differential cross sections in $\mu$b/sr for $W = 1.13$ GeV and $Q^2 = 2.25\,\mathrm{GeV}^2$. Each subplot shows cross section for various $\cos\theta^*_\pi$ bin as a function of $\phi^*_\pi$. Experimental points (red) are shown with statistical errors only. The red dashed curve is a fit to the cross section as in Eq. 6.2. Predictions from Braun *et al* (magenta) as well as extrapolations of fit to world data at higher $W$ from MAID2007 (blue) and Aznauryan *et al* (green) are shown.**

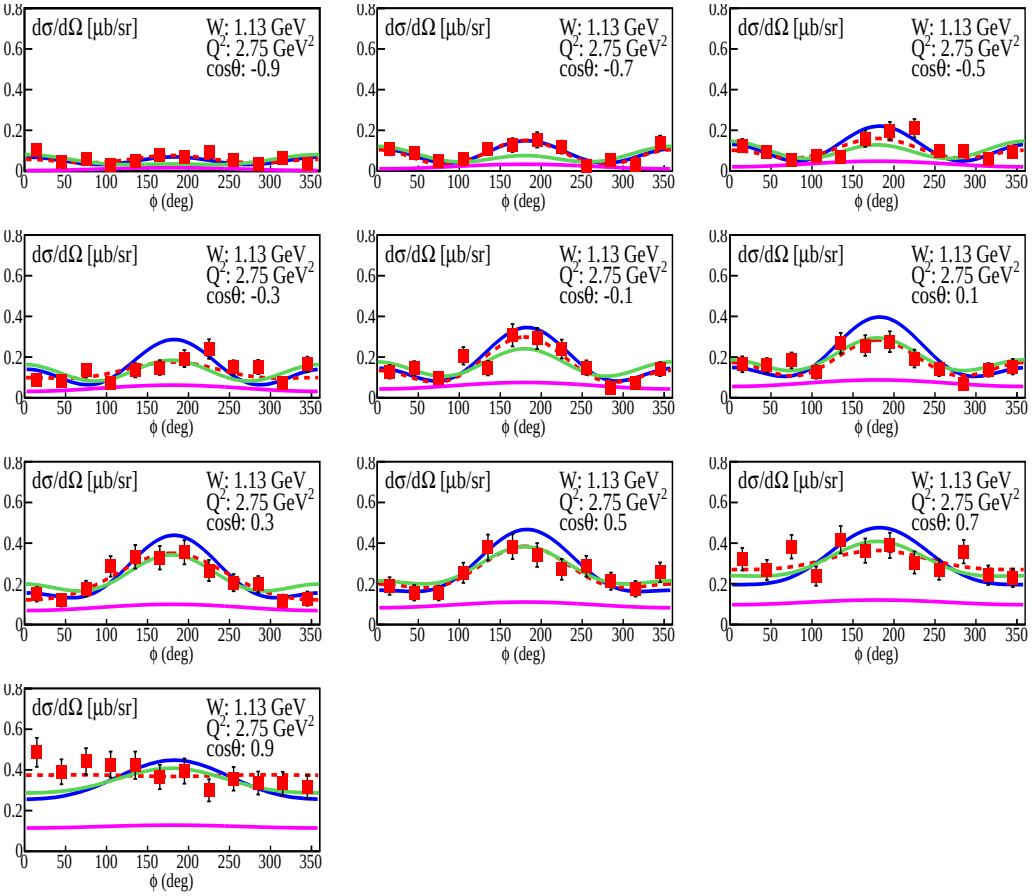


**Figure D.12: The differential cross sections in $\mu$b/sr for $W = 1.13$ GeV and $Q^2 = 2.75\,\mathrm{GeV}^2$. Each subplot shows cross section for various $\cos\theta^*_\pi$ bin as a function of $\phi^*_\pi$. Experimental points (red) are shown with statistical errors only. The red dashed curve is a fit to the cross section as in Eq. 6.2. Predictions from Braun *et al* (magenta) as well as extrapolations of fit to world data at higher $W$ from MAID2007 (blue) and Aznauryan *et al* (green) are shown.**

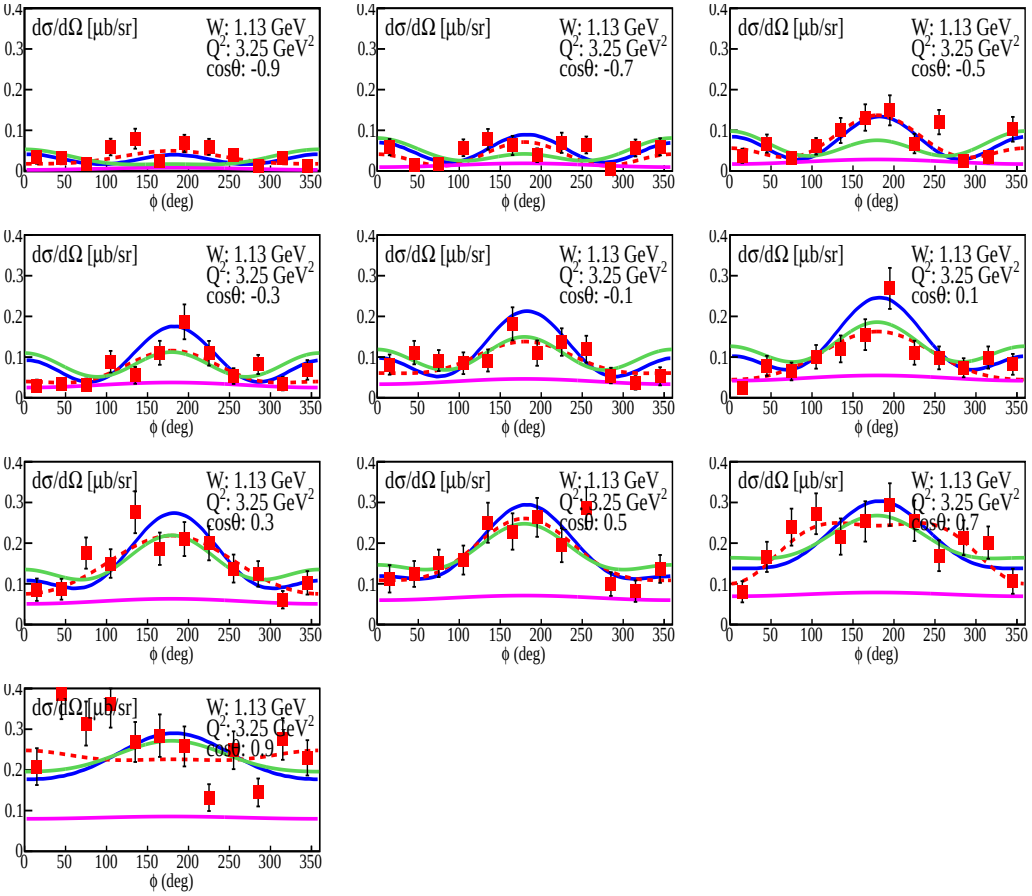


**Figure D.13: The differential cross sections in $\mu$b/sr for $W = 1.13$ GeV and $Q^2 = 3.25\,\mathrm{GeV}^2$. Each subplot shows cross section for various $\cos\theta^*_\pi$ bin as a function of $\phi^*_\pi$. Experimental points (red) are shown with statistical errors only. The red dashed curve is a fit to the cross section as in Eq. 6.2. Predictions from Braun *et al* (magenta) as well as extrapolations of fit to world data at higher $W$ from MAID2007 (blue) and Aznauryan *et al* (green) are shown.**

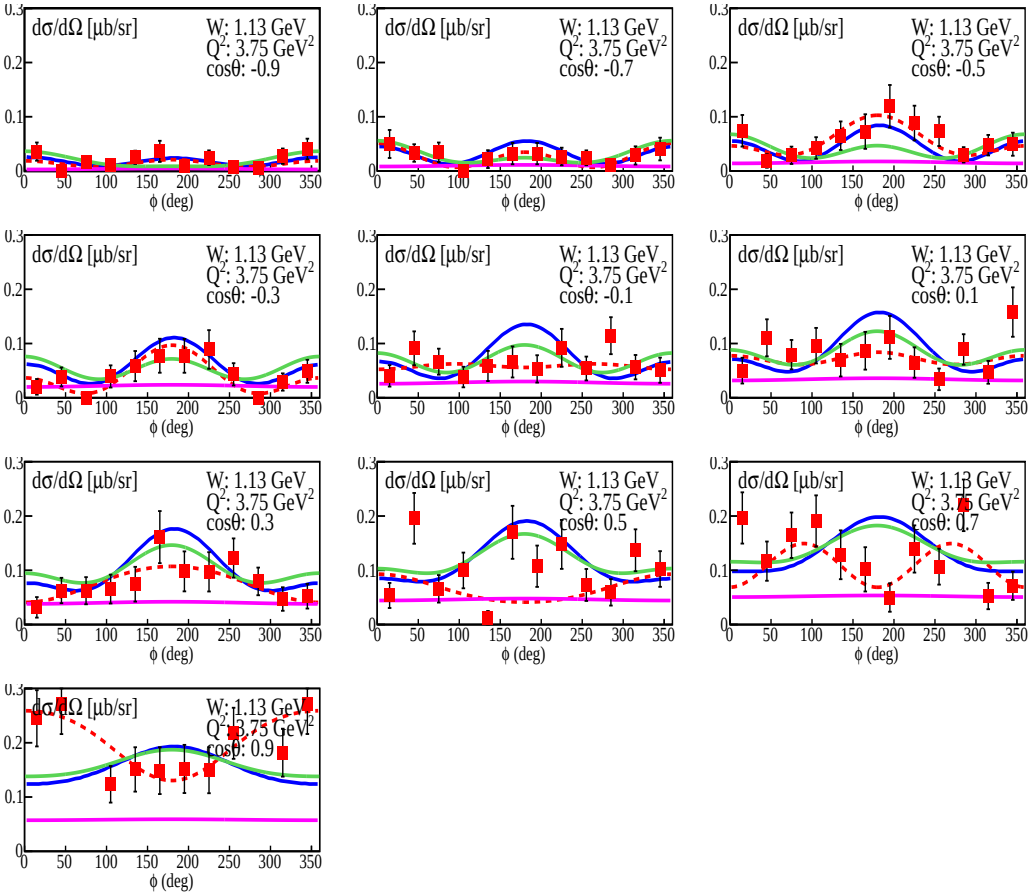


**Figure D.14: The differential cross sections in $\mu$b/sr for $W = 1.13$ GeV and $Q^2 = 3.75\,\mathrm{GeV}^2$. Each subplot shows cross section for various $\cos\theta^*_\pi$ bin as a function of $\phi^*_\pi$. Experimental points (red) are shown with statistical errors only. The red dashed curve is a fit to the cross section as in Eq. 6.2. Predictions from Braun *et al* (magenta) as well as extrapolations of fit to world data at higher $W$ from MAID2007 (blue) and Aznauryan *et al* (green) are shown.**

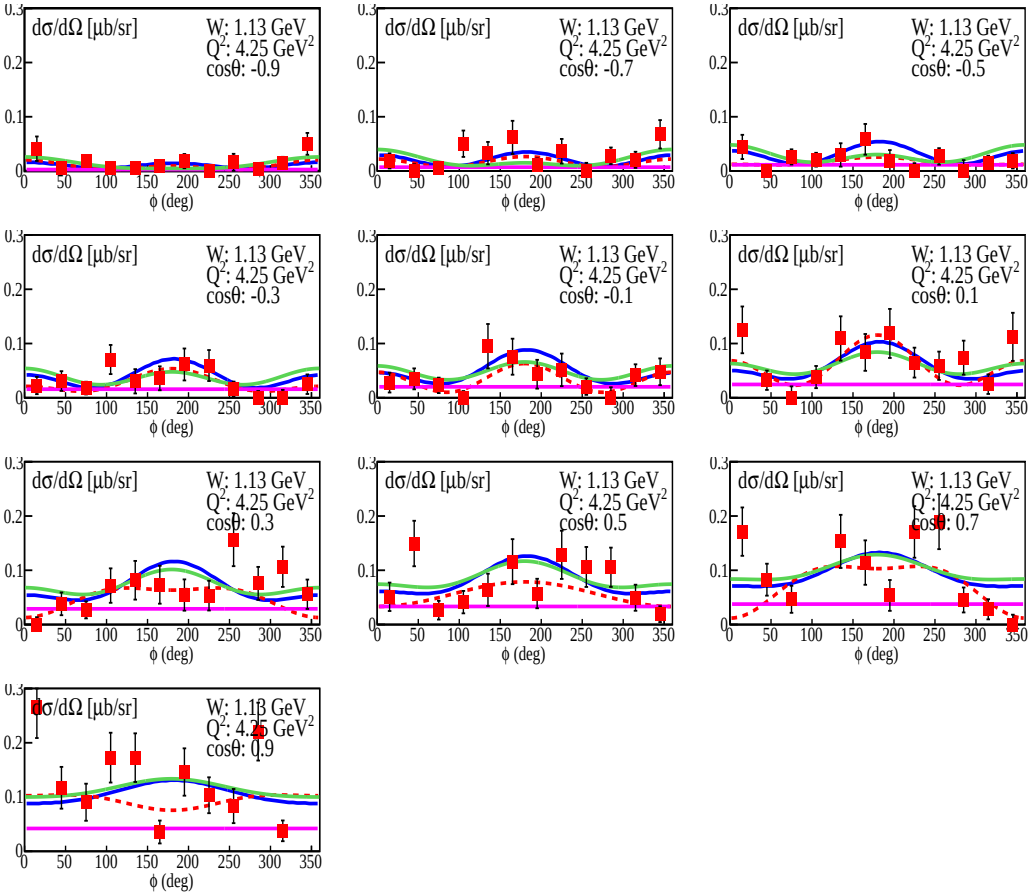


**Figure D.15: The differential cross sections in $\mu$b/sr for $W = 1.13$ GeV and $Q^2 = 4.25\,\mathrm{GeV}^2$. Each subplot shows cross section for various $\cos\theta^*_\pi$ bin as a function of $\phi^*_\pi$. Experimental points (red) are shown with statistical errors only. The red dashed curve is a fit to the cross section as in Eq. 6.2. Predictions from Braun *et al* (magenta) as well as extrapolations of fit to world data at higher $W$ from MAID2007 (blue) and Aznauryan *et al* (green) are shown.**

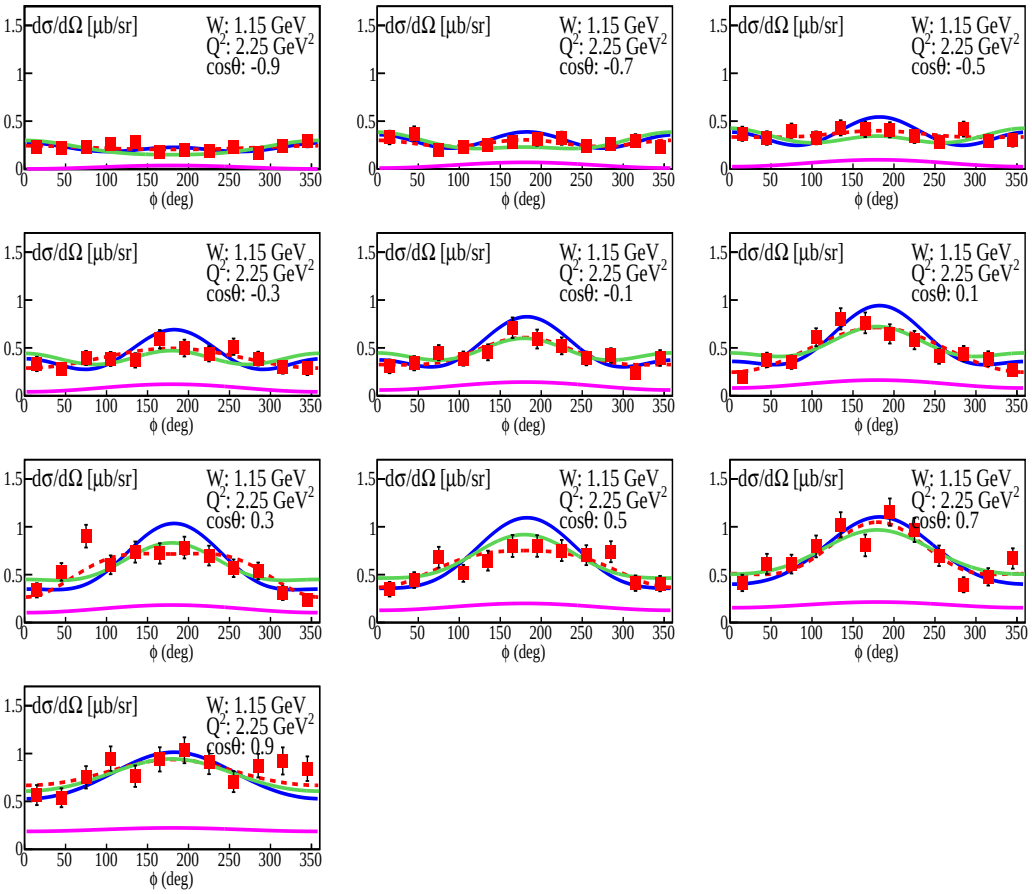


**Figure D.16: The differential cross sections in $\mu$b/sr for $W = 1.15$ GeV and $Q^2 = 2.25\,\mathrm{GeV}^2$. Each subplot shows cross section for various $\cos\theta^*_\pi$ bin as a function of $\phi^*_\pi$. Experimental points (red) are shown with statistical errors only. The red dashed curve is a fit to the cross section as in Eq. 6.2. Predictions from Braun *et al* (magenta) as well as extrapolations of fit to world data at higher $W$ from MAID2007 (blue) and Aznauryan *et al* (green) are shown.**

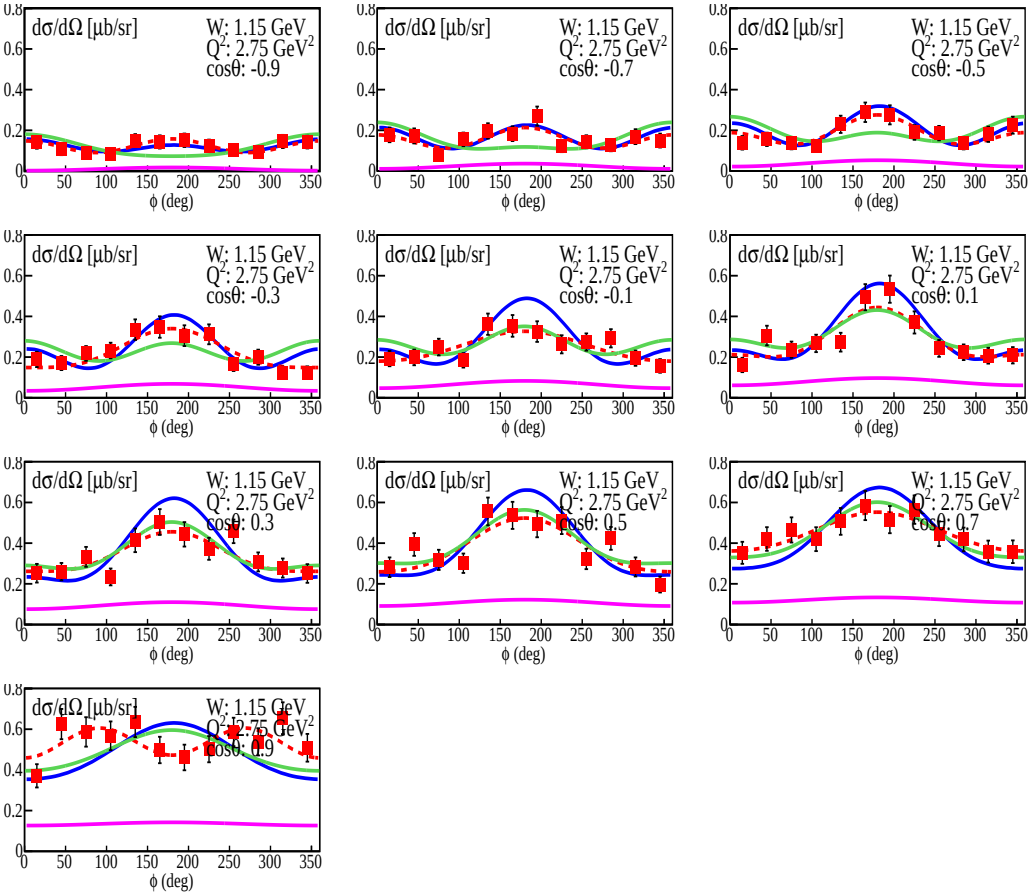


**Figure D.17: The differential cross sections in $\mu$b/sr for $W = 1.15$ GeV and $Q^2 = 2.75\,\mathrm{GeV}^2$. Each subplot shows cross section for various $\cos\theta^*_\pi$ bin as a function of $\phi^*_\pi$. Experimental points (red) are shown with statistical errors only. The red dashed curve is a fit to the cross section as in Eq. 6.2. Predictions from Braun *et al* (magenta) as well as extrapolations of fit to world data at higher $W$ from MAID2007 (blue) and Aznauryan *et al* (green) are shown.**

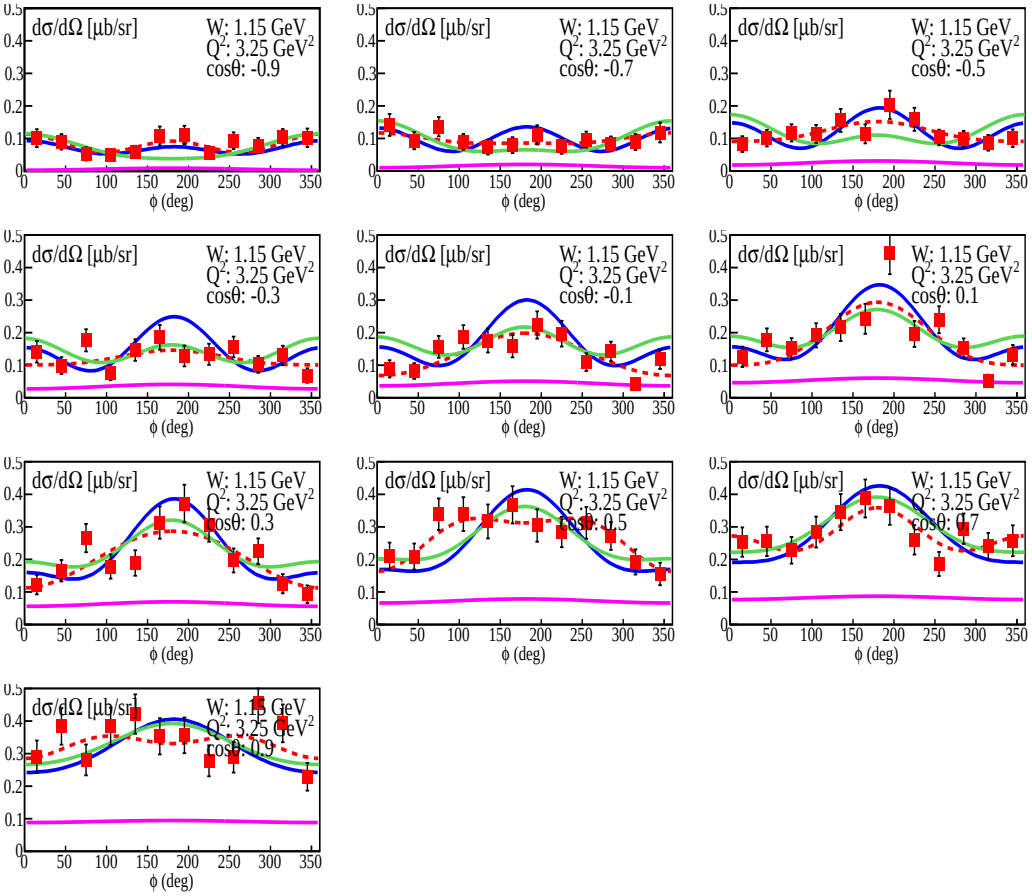


**Figure D.18: The differential cross sections in $\mu$b/sr for $W = 1.15$ GeV and $Q^2 = 3.25\,\mathrm{GeV}^2$. Each subplot shows cross section for various $\cos\theta^*_\pi$ bin as a function of $\phi^*_\pi$. Experimental points (red) are shown with statistical errors only. The red dashed curve is a fit to the cross section as in Eq. 6.2. Predictions from Braun *et al* (magenta) as well as extrapolations of fit to world data at higher $W$ from MAID2007 (blue) and Aznauryan *et al* (green) are shown.**

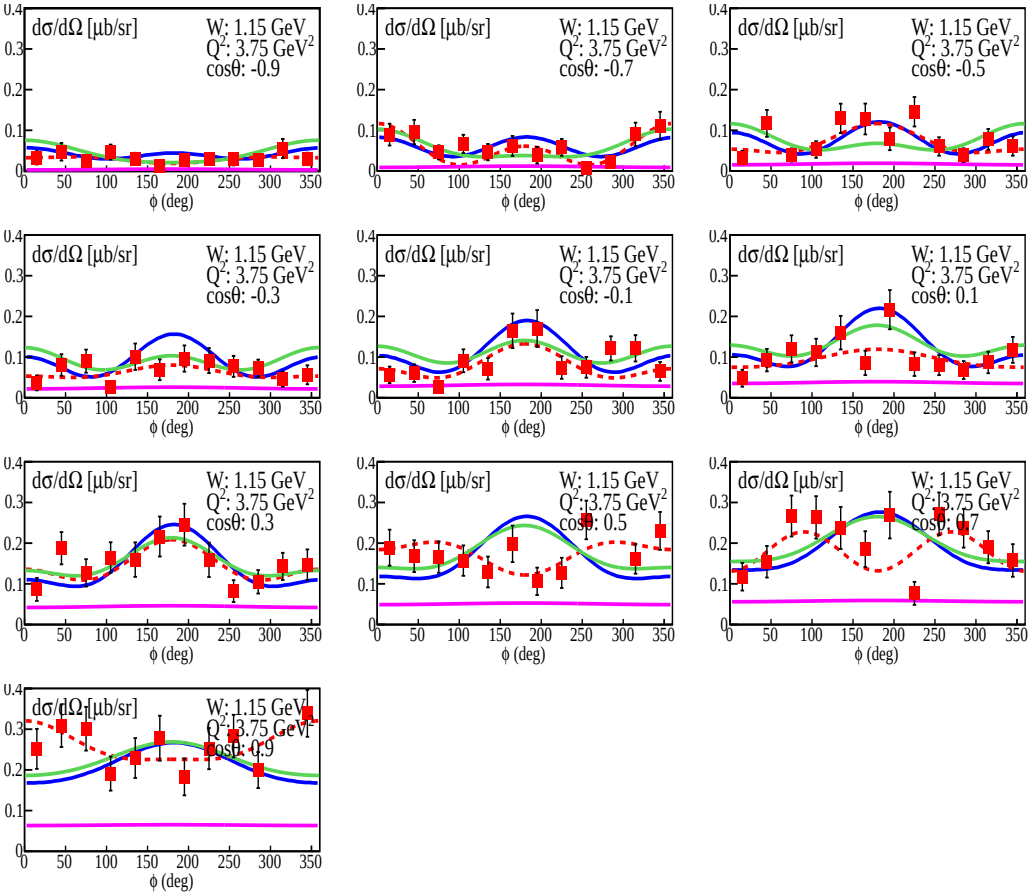


**Figure D.19: The differential cross sections in $\mu$b/sr for $W = 1.15$ GeV and $Q^2 = 3.75\,\mathrm{GeV}^2$. Each subplot shows cross section for various $\cos\theta^*_\pi$ bin as a function of $\phi^*_\pi$. Experimental points (red) are shown with statistical errors only. The red dashed curve is a fit to the cross section as in Eq. 6.2. Predictions from Braun *et al* (magenta) as well as extrapolations of fit to world data at higher $W$ from MAID2007 (blue) and Aznauryan *et al* (green) are shown.**

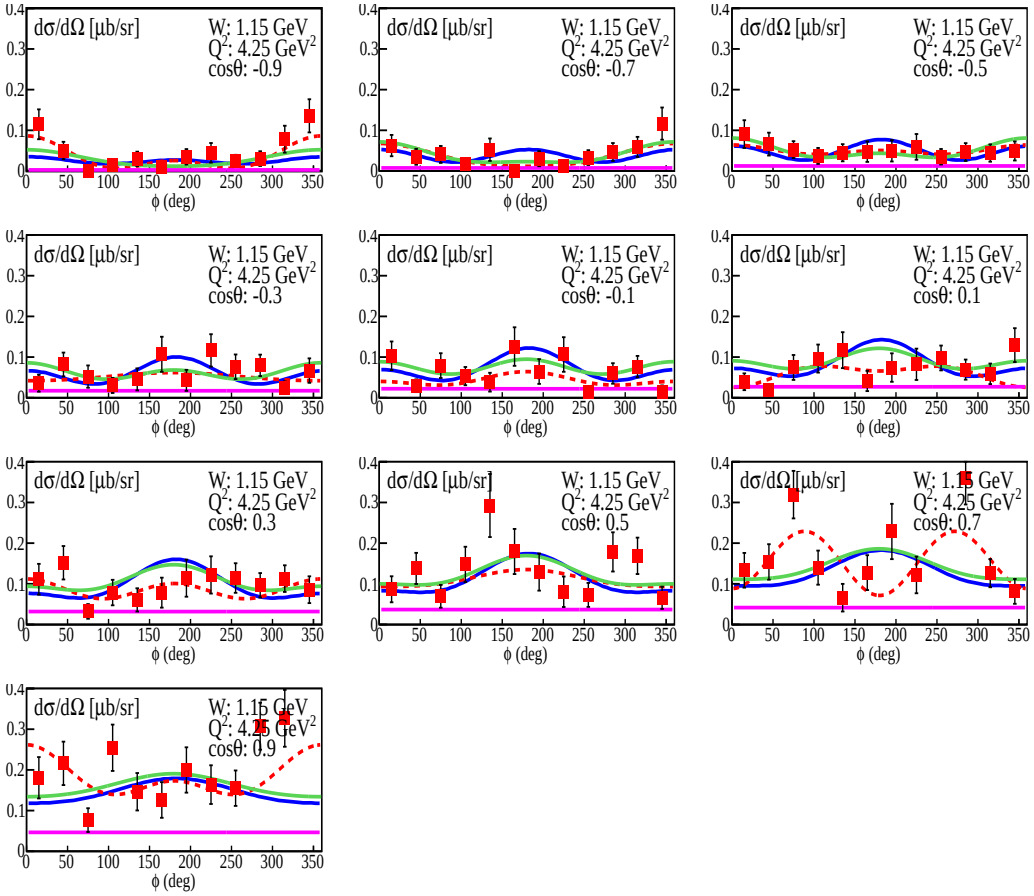


**Figure D.20: The differential cross sections in $\mu$b/sr for $W = 1.15$ GeV and $Q^2 = 4.25\,\mathrm{GeV}^2$. Each subplot shows cross section for various $\cos\theta^*_\pi$ bin as a function of $\phi^*_\pi$. Experimental points (red) are shown with statistical errors only. The red dashed curve is a fit to the cross section as in Eq. 6.2. Predictions from Braun *et al* (magenta) as well as extrapolations of fit to world data at higher $W$ from MAID2007 (blue) and Aznauryan *et al* (green) are shown.**